



HAL
open science

Etude de l'effet de l'addition de gaz sur l'équilibre de phases en mélanges pétroliers dans des conditions de haute pression et haute température.

José Francisco Romero Yanes

► To cite this version:

José Francisco Romero Yanes. Etude de l'effet de l'addition de gaz sur l'équilibre de phases en mélanges pétroliers dans des conditions de haute pression et haute température.. Génie des procédés. Université de Pau et des Pays de l'Adour; Universidade federal do Cear , 2021. Franais. NNT : 2021PAUU3011 . tel-03340202

HAL Id: tel-03340202

<https://theses.hal.science/tel-03340202>

Submitted on 10 Sep 2021

HAL is a multi-disciplinary open access archive for the deposit and dissemination of scientific research documents, whether they are published or not. The documents may come from teaching and research institutions in France or abroad, or from public or private research centers.

L'archive ouverte pluridisciplinaire **HAL**, est destin e au d p t et   la diffusion de documents scientifiques de niveau recherche, publi s ou non,  manant des  tablissements d'enseignement et de recherche franais ou  trangers, des laboratoires publics ou priv s.



UNIVERSIDADE
FEDERAL DO CEARÁ



IVERSITÉ
DE PAU ET DES
PAYS DE L'ADOUR

JOSÉ FRANCISCO ROMERO YANES

**STUDY OF GAS ADDITION EFFECTS ON THE PHASE BEHAVIOR OF
PETROLEUM MIXTURES AT HIGH PRESSURE AND HIGH TEMPERATURE
CONDITIONS**

Doctorate Thesis

Thesis presented to the Post-Graduation Program in Chemical Engineering at the Federal University of Ceará, in cotutelle with Université de Pau et des Pays de l'Adour as a partial requirement to obtain the degree of Doctor in Science.

Advisors:
Prof. Dr. Hosiberto Batista de Sant'Ana
Prof. Dr. Jean Luc-Daridon

FORTALEZA (BRAZIL) / PAU (FRANCE)

2021

JOSÉ FRANCISCO ROMERO YANES

STUDY OF GAS ADDITION EFFECTS ON THE PHASE BEHAVIOR OF
PETROLEUM MIXTURES AT HIGH PRESSURE AND HIGH TEMPERATURE
CONDITIONS

Tese apresentada ao Programa de Pós-Graduação em Engenharia Química da Universidade Federal do Ceará, em cotutela com a Université de Pau et des Pays de l'Adour como requisito parcial à obtenção do título de Doutor em Engenharia Química, na área de concentração de Processos Químicos e Bioquímicos pela UFC, e Doutor em Engenharia de Petróleo pela UPPA.

Orientadores:
Prof. Dr. Hosiberto Batista de Sant'Ana
Prof. Dr. Jean-Luc Daridon

FORTALEZA (BRAZIL) / PAU (FRANCE)

2021

JOSÉ FRANCISCO ROMERO YANES

STUDY OF GAS ADDITION EFFECTS ON THE PHASE BEHAVIOR OF
PETROLEUM MIXTURES AT HIGH PRESSURE AND HIGH TEMPERATURE
CONDITIONS

Thesis presented to the Post-Graduation Program in Chemical Engineering at the Federal University of Ceará (UFC), in cotutelle with Université de Pau et des Pays de l'Adour (UPPA) as a partial requirement to obtain the title of Doctor in Chemical Engineering by UFC, and Doctor in Petroleum Engineering by UPPA.

EXAMINATION BOARD

Prof. Dr. Hosiberto Batista de Sant'Ana (Advisor)
Universidade Federal do Ceará

Prof. Dr. Jean-Luc Daridon (Advisor)
Université de Pau et des Pays de l'Adour

Prof. Dr. Harvey W. Yarranton (Reviewer)
University of Calgary

Prof. Dr. Simon Ivar Andersen (Reviewer)
Technical University of Denmark

Dra. Magali Pujol (Jury)
TOTAL S. A.

Dr. Felipe Fleming (Jury)
Petróleo Brasileiro S.A. – Petrobras

Prof. Dr. Moises Bastos Neto (Jury)
Universidade Federal do Ceará

Prof. Dr. Guillaume Galliéro (Jury)
Université de Pau et des Pays de l'Adour

Dedicated to my family

ACKNOWLEDGMENTS

After this 3-year PhD journey, a time that seemed long at the beginning, but that passed incredibly fast, numerous and diverse people were involved directly or indirectly. To avoid disremembering any person, I would like to express my deepest gratitude to all who contributed to the success of each step of this work.

I would like to give special thanks to three persons who influenced, guided, and motivated this work. The first of them is our Project Manager from Petrobras, Dr. Felipe Fleming, his company and compromise during the project were invaluable. After every meeting, his many feedbacks give us a lot to work with, and a lot to rethink! Thank you for the interest, involvement, and for pushing all the critical details of the work.

From my stage in France, I would like to thank Prof. Dr. Jean-Luc Daridon. His reception, support, ideas, and interest in work from day one made us keep going in the best way even in a world pandemic. Many thanks for all the considerations and guidance during this time.

Finally, I would like to give special thanks to Prof. Dr. Hosiberto Batista de Sant'Ana, who always motivates us to obtain the best results of our work. Many thanks for taking not only a Venezuelan in your lab, but two! Especially during a time that was life changing. Thank you for all your trust and all the support during this thesis.

I would like to extend my gratitude to Prof. Dr. Harvey Yarranton and Dr. Simon Ivar Andersen for accepting the revision of this thesis, and for their invaluable contributions. Both were an inspiration even before considering to pursuit my master and doctorate degree.

Also, I acknowledge to Dra. Magali Pujol, Prof. Dr. Guillaume Gallièro, and Prof. Dr. Moises Bastos Neto for accepting to participate in the jury committee, and their appreciated contributions.

Special thanks to Prof. Dr. François Montel for his support in modeling and results evaluation. Every meeting was enriching and motivating by his unique perspective of petroleum and thermodynamics.

From the Laboratory of Complex Fluids and their Reservoirs (LFCR) of l'Université de Pau, I would to express my gratitude for the support to all the team of Thermophysical Properties, Jean-Patrick Bazile, Djamel Nasri, Prof. Dr. Hervé Carrier.

Also, to all PhD students and personnel from LFCR, thank you for the shared time, and good moments!

From Grupo de Pesquisa em Termofluidodinâmica Aplicada (GPTA) of Universidade Federal do Ceara, I would like to thank Prof. Dra. Regianne Pinheiro, Prof. Dra. Aline M. Bessa, Prof. Dr. Filipe Feitosa, and Profa. Dra. Rílvia S. De Aguiar, for all the shared work, support and time! Also, thank to my lab colleagues Ailton, Raissa, Peterson and all undergraduate students Joao, Moacir, Caiua, Gutembergue, Brenno, Marina. Thank you for the shared coffees, cakes, your company on the long days working in the lab, and the good times. Being witness of all the group's success was always a motive of joy during these times.

I would like to express all my gratitude to my family and specially to my beloved Angelica, without all their support this work would never be done. Thank you for making all our journeys always lighter and better than we ever imagined.

Thank you to God, for the beginnings and ends of every road that we have overcome, and the blessing of the company of invaluable persons and friends.

ABSTRACT

Phase behavior of reservoir fluids is a crucial information for an efficient production development project. Depending on fluid characteristics, their phase behavior can vary from simple to complex multiphasic equilibria. Moreover, multiphasic equilibria may be encountered by natural occurrence under reservoir conditions or induced during production operations. Recently, complex phase behavior has been reported for Brazilian Pre-Salt crude oils, especially for medium crude oil fluids associated with high gas oil ratios. Specifically, evidence of complex liquid – liquid equilibria have been reported at high pressure and high temperature conditions. However, the study and detection of this equilibrium have been limited by the crude oil characteristics, high opacity, and low phase segregation, that limits conventional PVT laboratorial analysis. For that reason, it is proposed in this work a systematic study of phase behavior of Pre-Salt crude oils mixed with gases at high proportion. Phase transitions were investigated by a combination of PVT techniques providing visualization and detection of phase transitions in opaque fluids under high pressure. Through these studies, non-typical phase transitions were detected for systems involving high methane content, when analyzed using conventional PVT techniques (near-infrared light scattering and high-pressure microscopy). Results show the formation of a high dispersed second liquid phase, no fractal, with fast redissolution at high pressure. Bulk fluid analyses were also made by intermediate of a new full visual PVT technique, using a short-wave infrared fluid imaging designed for opaque crude oil evaluation. This test confirms a second dense liquid phase that can be formed when crude oil is mixed at a high gas oil ratio, especially with methane. Thermodynamic modelling and solubility analysis suggest that this second phase formed could be a heavy and aromatic dominated phase, but its behavior is far from typical asphaltenes. Based on the formed second phase characteristics, a wide biphasic liquid – liquid region is then identified for mixtures of crude oil and gas, especially for low molecular weight gases at high gas oil proportion.

Keywords: phase behavior; PVT; hydrocarbons; liquid-liquid equilibria; crude oil; methane; carbon dioxide.

RESUMO

O comportamento de fases dos fluidos do reservatório é uma informação fundamental para um projeto de produção petrolífera eficiente. Dependendo das características do fluido, seu comportamento da fase pode variar de equilíbrios líquido – vapor simples a sistemas multifásicos complexos. Recentemente, transições de fases complexas foram reportadas para petróleo produzido do Pré-sal brasileiro, especialmente para fluidos envolvendo óleos médios associados a altas proporções de gás. Especificamente, um tipo de equilíbrio líquido – líquido complexo foi encontrado em condições atípicas de alta pressão e alta temperatura. No entanto, o estudo e a detecção desse equilíbrio têm sido limitados pelas características do petróleo, sua alta opacidade e a baixa segregação de fase, que limita a análise laboratorial PVT convencional. Por esse motivo, é proposto neste trabalho um estudo sistemático do comportamento de fase de petróleos do Pré-Sal Brasileiro misturados com gases em alta proporção. As transições de fase foram investigadas por uma combinação de técnicas PVT, proporcionando visualização e detecção de diferentes transições de fase em fluidos opacos sob alta pressão. Por meio desses estudos, transições de fase atípicas foram detectadas para sistemas envolvendo alto teor de metano, quando analisadas por técnicas convencionais de PVT (espalhamento de luz no infravermelho próximo e microscopia de alta pressão). Os resultados mostram a formação de uma segunda fase líquida altamente dispersa, não fractal, com rápida redissolução a pressões elevadas. Análises integrais do fluido foram feitas por meio de uma nova técnica PVT de visualização total, usando inspeção do fluido no infravermelho próximo, projetadas para a avaliação de petróleos opacos. Este teste confirma que uma segunda fase líquida densa é formada quando o óleo cru é misturado a uma alta proporção de gás, especialmente com metano. Resultados de modelagem termodinâmica e de análises de solubilidade indicam que esta segunda fase formada pode ser uma fase pesada e dominada por aromáticos, mas seu comportamento fuje dos asfaltenos típicos. Com base nas características da segunda fase formada, uma ampla região bifásica líquido - líquido é identificada para misturas de petróleo bruto e gás, especialmente para gases de baixo peso molecular em alta proporção de gás.

Palavras-chave: comportamento de fase; PVT; hidrocarbonetos; equilíbrio líquido-líquido; petróleo; metano; dióxido de carbono.

RÉSUMÉ

Le comportement de phase des fluides de réservoir est une information cruciale pour prévoir des procédés de production pétrolière efficace. Selon les caractéristiques du fluide, le comportement de phase peut varier de simples équilibres liquide-vapeur à des systèmes multiphasiques plus complexes. Ces équilibres multiphasiques peuvent être rencontrés naturellement dans les conditions de réservoir ou induits par les procédés de production. Récemment, des comportements de phase complexes ont été observés dans des champs d'huile Brésiliens situés sous une croûte saline et appelés « Pre-Salt » contenant des fluides de réservoir moyens caractérisés par rapports gaz liquide (GOR) élevés. Plus précisément, des équilibres liquide-liquide et liquide-liquide-vapeur ont pu être observés dans des conditions de haute pression et de haute température. Cependant, l'étude et la détection de ces équilibres ont été limitées par les caractéristiques de ces pétroles bruts et en particulier leur opacité élevée ainsi que par la faible ségrégation de phase rencontrées dans ces équilibres entre phases denses sous haute pression, qui limitent l'analyse par les techniques PVT conventionnelles. Pour cette raison, il a été proposé dans ce travail une étude systématique du comportement de phase des huiles brutes Pre-Salt Brésiliennes recombinaées avec de fortes teneurs en gaz. Les transitions de phase ont été étudiées par une combinaison de techniques PVT novatrices offrant une visualisation et une détection des transitions de phase dans les fluides opaques sous haute très haute pression. Des transitions de phase atypiques ont été mises à jour dans des systèmes ayant une forte teneur en méthane par de premières études menées avec des techniques PVT conventionnelles par dispersion de lumière dans l'infrarouge proche et par microscopie haute pression dans le visible. Ces résultats ont montré la formation d'une phase liquide non fractale fortement dispersée dans une seconde phase liquide, avec une faible cinétique de redissolution sous haute pression. Pour confirmer ces observations, nouvelles analyses ont été effectuées par l'intermédiaire d'une nouvelle technique PVT à visibilité intégrale. Cette technique utilise une imagerie infrarouge dans le domaine des ondes courtes (SWIR) qui permet de rendre visible les pétroles bruts opaques. Ces nouveaux tests ont permis de confirmer la présence d'une phase dispersée qui peut se former lorsque le pétrole brut est recombinaé avec un GOR important avec un gaz léger tel que du méthane mais aussi avec du dioxyde de carbone. Les résultats de la modélisation thermodynamique associée à ces observations expérimentales indiquent que cette seconde phase liquide formée pourrait correspondre à une phase lourde fortement

aromatique, mais son comportement est éloigné des phases asphaltènes typiques. Sur la base des caractéristiques de la seconde phase formée, une large région liquide-liquide biphasique est donc identifiée pour les mélanges de pétrole brut et de gaz, en particulier pour les gaz de faible poids moléculaire à forte proportion de gaz.

Mots clés : comportement de phase; PVT; hydrocarbures; équilibre liquide-liquide ; huile brute ; méthane ; gaz carbonique.

LIST OF FIGURES

Figure 1.1 Schematic representation of different types of binary phase diagrams.....	30
Figure 1.2 L1 (oil-rich)–L2 (CO ₂ -rich)–V equilibria for crude oil and CO ₂ mixture in a full visual PVT cell. Adapted from Lindeloff et al., 2013.	34
Figure 1.3 Light absorption spectra of different reservoir fluids and water (VENKATARAMANAN et al., 2006).....	41
Figure 1.4 NIR SDS response for two crude oils during expansion, adapted from Hammami et al. (2000).....	42
Figure 2.1 Schematic diagram of PVT, HPM and sample injection ensemble.	56
Figure 2.2 Relative volume and saturation pressures (●) of crude oil and methane systems during CCE depletions.	60
Figure 2.3 Saturation pressure and isothermal compressibility for the overall system and the gas phase after the bubble point for crude oil and methane mixtures.	61
Figure 2.4 NIR transmittance signal for equilibrium steps (solid symbols) and continue depressurization (lines) during CCE test. Saturation pressures marked (●) for crude oil and methane mixtures.....	62
Figure 2.5 NIR transmittance comparison during CCE and system re-pressurization for all crude oil and methane mixtures (65.0, 67.5, 70.0, 72.5, and 75.0 methane mol%). .	64
Figure 2.6 NIR transmittance, HPM particle count and micrographs for crude oil and methane mixtures with 65.0, 67.5 and 70.0 methane mol% during HPM test.....	66
Figure 2.7 NIR transmittance and HPM particle count for 72.5 methane mol% crude oil and methane mixture during HPM test.....	67
Figure 2.8 Micrographs for 72.5 methane mol% mixture with crude oil during HPM..	67
Figure 2.9 NIR transmittance and HPM particle count for 75.0 methane mol% mixture with crude oil during HPM test.	69
Figure 2.10. Micrographs for 75.0 methane mol% mixture with crude oil during HPM test.....	69

Figure 2.11 SDS variation during AOP-monophasic pressurization test and micrographs for from pressures above the AOP to monophasic condition, for 75.0 methane mol% mixture with crude oil.	70
Figure 2.12. Filtration element after isobaric filtration test (A) at pressures bellow AOP, and (B) at 80 MPa and 313.15 K.	71
Figure 2.13. P-composition diagram for methane and crude oil mixtures at reservoir conditions (343.15 K).	72
Figure 3.1. Schematic diagram of PVT, HPM and sample injection ensemble.	76
Figure 3.2. Relative volume, saturation pressure (red marked) and NIR transmittance from CCE test for the RC1 system (66.0% mol gas, 100.0 mol% CO ₂ content in gas).	77
Figure 3.3. Micrographs, particles count and SDS signal for RC1 system (66.0% mol gas, 100.0 mol% CO ₂ content in gas).	78
Figure 3.4. Relative volume, saturation pressure (red marked) and NIR transmittance during CCE test for the RC2 system (73.1% mol gas, 52.1 mol% CO ₂ content in gas).	79
Figure 3.5. Micrographs, particles count and SDS signal for RC2 system (73.1% mol gas, 52.1 mol% CO ₂ content in gas).	79
Figure 3.6. Relative volume, saturation pressure (red marked) and NIR transmittance (continue and equilibrium steps) during CCE test for the RC3 (75.8 mol% gas, 37.6 mol% CO ₂ content in gas), RC4 (78.0 mol% gas, 26.6 wt% CO ₂ content in gas), RC5 (78.9 mol% gas, 22.0 mol% CO ₂ content in gas), and RC6 (79.8 wt% gas, 17.9 mol% CO ₂ content in gas) systems.	81
Figure 3.7. Particles count and SDS signal for RC3 (75.8 mol% gas, 37.6 mol% CO ₂ content in gas), RC4 (78.0 mol% gas, 26.6 wt% CO ₂ content in gas), RC5 (78.9 mol% gas, 22.0 mol% CO ₂ content in gas), and RC6 (79.8 wt% gas, 17.9 mol% CO ₂ content in gas) systems during HPM test.	83
Figure 3.8 Micrographs for RC3 (75.8 mol% gas, 37.6 mol% CO ₂ content in gas), RC4 (78.0 mol% gas, 26.6 wt% CO ₂ content in gas), RC5 (78.9 mol% gas, 22.0 mol% CO ₂ content in gas), and RC6 (79.8 wt% gas, 17.9 mol% CO ₂ content in gas) systems during HPM depletion test.	84

Figure 3.9 Particle size distribution during depletion for RC5 system (78.9 mol% gas, 22.0 mol% CO ₂ content in gas) obtained by HPM.....	85
Figure 3.10 Particle size distribution during depletion for RC6 system (79.8 wt% gas, 17.9 mol% CO ₂ content in gas) obtained by HPM.....	85
Figure 3.9. Bubble point pressure and AOP diagram as function of the total gas volume fraction for crude oil and gas mixtures at reservoir conditions (343.15 K).	87
Figure 4.1. Relative volume and saturation pressures (yellow markers) for the different crude oils and methane mixtures during CCE depletions.	93
Figure 4.2. Bubble point identification on PVT head visor for the different crude oil and methane mixtures during CCE test.....	94
Figure 4.3 NIR transmittance signal during CCE test for the different crude oil and methane mixtures. (Evident phase transitions at pressures above the bubble point for medium oils was marked with dashed lines for better visualization).....	95
Figure 4.4. NIR transmittance, HPM particle count and micrographs for the different crude oil and methane mixtures during HPM test.	96
Figure 4.5 Micrographs for the different crude oil and methane systems during HPM depletion test.....	98
Figure 4.6 SDS variation during AOP-monophasic pressurization test and micrographs for from pressures above the AOP to monophasic condition, for 75.0 methane mol% mixture with P2 crude oil.	99
Figure 5.1. Schematic diagram of PVT, sample injection ensemble, and near-infrared (NIR) solid detection system (SDS).	105
Figure 5.2 Density data crosschecking between PVT cell and HPHT densimeter for BR1 crude oil + methane for a medium methane content (around 50.0 mol%), solid marks; and, higher methane content (around 75.0 mol%), empty marks, for a temperature range of 313.15 to 373.15 K.....	109
Figure 5.3 PVT density measurements for BR1 crude oil + methane mixtures for three different methane composition: (i) 26.5 mol% (solid marks), (ii) 52.6 mol% (empty marks), and (iii) 74.7 mol% (half-filled marks), at temperatures from 313.15 K to 373.15 K.	110

Figure 5.4. Solubility parameter as function of temperature and pressure for BR1 crude oil + methane mixtures (26.5 mol%, black points; 52.6 mol% blue points; and 74.7 mol%, red points).....	112
Figure 5.5 Solubility parameter for BR1 dead oil (δ_{BR1-DO}) and methane (δ_{CH_4}) as function of pressure, for temperatures from 313.15 to 373.15 K.	113
Figure 5.6 Cohesive energy ratio for BR1+methane mixtures (E_{mix}) and BR1 dead oil (E_{DO}) as a function of methane content, calculated at bubble point pressures for 313.15 K, 323.15 K, 333.15 K, and 314.15 K.....	114
Figure 5.7 Molar volume ratios for BR1 + methane mixtures (v_{mix}) and BR1 dead oil (v_{DO}) as function of methane content, calculated at bubble point pressures for 313.15 K, 323.15 K, 333.15 K, and 314.15 K.....	115
Figure 5.8 Solubility parameter ratio for BR1 + methane mixtures (δ_{mix}) and BR1 dead oil (δ_{DO}) as function of methane content, calculated at bubble point pressures for 313.15 K, 323.15 K, 333.15 K, and 314.15 K.....	115
Figure 5.9 NIR transmittance measurements during CCE for BR2 + 75 %mol gas with (A) 0 %mol CO ₂ (100 % methane); (B) 26.3 % mol CO ₂ ; (C) 37.5 % mol CO ₂ ; (D) 100 % mol CO ₂ at temperatures of 343.15, 363.15 and 383.15 K.	117
Figure 5.10 Solubility parameter as function of temperature and pressure for BR2 crude oil + methane + CO ₂ mixtures. (A) 0.0 %mol CO ₂ (100 % methane); (B) 26.3 % mol CO ₂ ; (C) 37.5 % mol CO ₂ ; (D) 100 % mol CO ₂ , at temperatures of 343.15 K, 363.15 K, and 373.15 K.	120
Figure 5.11. Solubility parameter for BR2 dead oil (δ_{BR2-DO}), methane (δ_{CH_4}), and CO ₂ (δ_{CO_2}) as a function of pressure, for temperatures from 343.15 K to 383.15 K.....	120
Figure 5.12. (A) Bubble point pressure; (B) AOP, (C) solubility parameter at bubble point pressure; (D) solubility parameter at AOP; (E) cohesive energy at bubble point pressure; and (E) cohesive energy at AOP, for BR2 + 75.0 mol% gas mixtures, as function of CO ₂ composition, at 343.15 K, 363.15 K, 383.15 K.....	122
Figure 6.1 Schematic diagram of the PVT cell, SWIR camera, and sample injection ensemble.	127
Figure 6.2 Cell inspection using SWIR camera. (A) stirrer impeller with empty cell; and (B) stirrer impeller with cell filled with black crude oil.....	128

Figure 6.3 PVT with QCR assemble diagram (adapted from DARIDON; ORLANDI; CARRIER, 2016).	130
Figure 6.4 Crude oil + CO ₂ phase diagrams obtained for carbon dioxide composition of 20.0, 40.0, 60.0, and 70.0 mol%, at T = (293.15 to 378.15). Adjusted lines for eye-guide.	134
Figure 6.5 PV curves for the crude oil + CO ₂ systems for four CO ₂ different composition (20.0, 40.0, 60.0, and 70.0 mol%), at 293.15 K (dashed lines) and 323.15 K (continuous lines).	136
Figure 6.6 Different phase transitions detected by SWIR camera, as follows: (A) Liquid-vapor transition, for crude oil + 60.0 CO ₂ mol% at 338.15 K; (B) Liquid-liquid transition, for crude oil + 70.0 CO ₂ mol% at 323.15 K; and (C) liquid-liquid-vapor transition, for crude oil + 70.0 CO ₂ mol% at 308.15 K.....	137
Figure 6.7 Crude oil + CO ₂ systems phase diagrams obtained for a CO ₂ composition of 78.0, 84.0, and 86.0 mol%, at a temperature range of T = (293.15 to 378.15) K. Adjusted lines for eye-guide.	139
Figure 6.8 Crude oil + CO ₂ liquid-liquid phase transition for 78.0 mol% CO ₂ at 338.15 K (A) and 84.0 mol% CO ₂ at 358.15 K (B), during constant composition expansion.....	140
Figure 6.9 Crude oil + CO ₂ liquid-liquid phase transition for 86.0 mol% CO ₂ at T = 378.15 K (A) and at T = 358.15 K (B), during constant composition expansion.	142
Figure 6.10 QCR dissipation during CCE for crude oil + 78.0 mol% CO ₂ systems at 105 °C (solid symbols) and 85 °C (unfilled symbols).....	143
Figure 6.11 7th overtone QCR frequency and dissipation during CCE for crude oil and CO ₂ systems at 378.15 K.....	144
Figure 6.12. Phase diagram obtained using SWIR imaging and QCR analysis for crude oil and CO ₂ mixtures.	145
Figure 6.13. Crude oil + methane phase diagrams obtained for methane composition of 30.0, 45.0, 60.0, 70.0, 78.0 and 80.0 mol%, at T = (293.15 to 378.15). Adjusted lines for eye-guide.	146

Figure 6.14. Crude oil + methane mixtures pressure-composition diagram for T = (323.15 and 378.15) K. Adjusted continuous lines for eye-guide. Dashed line indicates experimental LL region.	148
Figure 6.15 PV curves for the crude oil + methane systems for four methane different composition (30.0, 45.0, 60.0, 70.0, 78.0, and 80.0 mol%), at 338.15 K (dashed lines) and 378.15 K (continuous lines).	148
Figure 6.16. Crude oil + methane phase transition detected by SWIR camera for different methane content, as follows: (A) 30.0 mol%; (B) 45.0 mol%, (C), 60.0 mol%, (D) 70.0 mol%, (E) 78.0 mol%, and (F) and 80.0 mol%, at a referential T = 358.15K, during constant composition expansion.....	149
Figure 6.17. Phase diagrams obtained for crude oil + methane + CO ₂ systems, with 20.0, 40.0, 60.0, 70.0, 78.0, 80.0 and 84.0 gas mol% from 293.15 to 378.15 K (adjusted lines for eye-guide).	151
Figure 6.18. Different phase transitions detected by SWIR camera for crude oil + methane + CO ₂ , as follows: (A) L→LV transition at 40.0 gas mol%; (B) LL→LLV transition at 40.0 gas mol%, and (C) LL→LLV transition at 80.0 gas mol%; and (D) AsphL→AsphLLV transition at 84.0 gas mol%.	152
Figure 6.19 Asphalt phase in sapphire windows at 358.15 K (A), and 338.15 K (B) detected by SWIR camera for crude oil + methane + CO ₂	153
Figure 6.20. Phase diagram obtained using SWIR imaging and QCR analysis for crude oil + CO ₂ + methane mixtures.	154
Figure 6.21. SWIR microscopy (50x) for (A) LL and (B) LL + asphaltene equilibria for 82.0 gas mol % mixture at 358.15 K.	154
Figure 6.22 P-T diagrams for the crude oil + CO ₂ systems, at 20.0, 40.0, 60.0, 78.0, 84.0, and 86.0 CO ₂ mol%. Experimental data in black squares, and PR EOS in continuous line.	158
Figure 6.23 P-T diagrams for the crude oil + methane systems, at 30.0, 45.0, 60.0, 78.0, and 80.0, methane mol%. Experimental data in black squares, and PR EOS in continuous line.	160

Figure 6.24 Modeled composition of the L2 phase for the systems crude oil + methane, with methane content of 60.0, 70.0, 78.0, and 80.0 methane mol%, together with the CNA extraction percent, at a referential condition of 100 MPa and 338.15 K.....	161
Figure 6.25 P-T diagrams for the crude oil + methane + CO ₂ systems, at 40.0, 60.0, 70.0, 78.0, 80.0, and 84.0, gas mol%. Experimental data in black squares, and PR EOS in continuous line.....	162
Figure 6.26 Modeled composition of the L2 phase for the systems crude oil + methane + CO ₂ , with gas content of 60.0, 70.0, 78.0, 80.0 and 84.0 gas mol%, together with the CNA extraction percent, at a referential condition of 100 MPa and 338.15 K.....	163
Figure 7.1 Schematic figure of Liquid-Solid determination test.....	170
Figure 7.2 LLVE for the mixture of CO ₂ , diphenylmethane and 2,2,4,4,6,8,8-heptamethylnonane at 89.925 mol% gas, 293.42 K, and pressures bellow 5.23 MPa.	173
Figure 7.3 Fluid inspection using a magnification lent for the mixture of methane, diphenylmethane and 2,2,4,4,6,8,8-heptamethylnonane at 40.326 mol% gas, at (A) 308.15 K (immiscibility as bright droplets), and (B) 328.15 K (totally homogeneous) at 40.0 MPa.....	175
Figure 7.4 Micrography for LL condition of 60.3 methane mol % mixture with diphenylmethane and 2,2,4,4,6,8,8-heptamethylnonane at 308.15 K and 70 MPa.	178
Figure 7.5 Pictures from PVT frontal camera (A) and micrography (B) for LL condition of 83.37 CO ₂ mol % mixture with <i>o</i> -terphenyl and 2,2,4,4,6,8,8-heptamethylnonane at 325.15 K and 70 MPa.	178
Figure 7.6 Images of different fluid condition obtained by full visual PVT for systems including heptamethylnonane, <i>o</i> -terphenyl and gases: (A) monophasic condition for mixture with 50.0 mol% CO ₂ at 358.15 K and 12.0 MPa, (B) LV condition for mixture with 50.0 mol% CO ₂ at 358.15 K and 9.7 MPa, (C) LL condition for mixture with 60.0 mol% methane at 358.15 K and 60.0 MPa, (D) LLV condition for mixture with 60.0 mol% methane at 358.15 K and 50.0 MPa, (E) LL condition for mixture with 83.3 mol % CO ₂ at 338.15 K and 32.5 MPa, and (F) LS condition for mixture with 60.9 mol % methane at 324.19 K and 73.0 MPa.	183
Figure 7.7 P-T diagrams for 2,2,4,4,6,8,8-heptamethylnonane + diphenylmethane + CO ₂ systems, at (A) 14.896, (B) 50.403, (C) 73.174, (D) 78.205, (E) 81.980, (F) 85.993, (G)	

89.925, and (H) 92.575, gas mol%. Experimental LVE data in black squares, LLE in red squares, LLVE data in blue squares, and PPR EOS in continuous line.	185
Figure 7.8 P-T diagrams for 2,2,4,4,6,8,8-heptamethylnonane + diphenylmethane + methane systems, at (A) 20.6190, (B) 40.326, (C) 60.376, and (D) 70.807 gas mol%. Experimental LVE data in black squares, LLVE data in blue squares, and PPR EOS in continuous line.....	186
Figure 7.9 P-T diagrams for 2,2,4,4,6,8,8-heptamethylnonane + diphenylmethane + methane + CO ₂ systems, at (A) 20.125, (B) 36.862, (C) 59.972, (D) 69.961, and (E) 80.021 gas mol% (gas 1:1 molar CO ₂ /methane). Experimental LVE data in black squares, LLVE data in blue squares, and PPR EOS in continuous line.	187
Figure 7.10 P-T diagrams for 2,2,4,4,6,8,8-heptamethylnonane + <i>o</i> -terphenyl + CO ₂ systems, at (A) 14.704, (B) 31.407, (C) 50.424, (D) 61.497, (E) 73.167, (F) 78.174, (G) 83.375, and (H) 88.649, gas mol%. Experimental LVE data in black squares, LLE in red squares, LLVE data in blue squares, LSE data in black diamonds, and PPR EOS in continuous line.....	189
Figure 7.11 P-T diagrams for 2,2,4,4,6,8,8-heptamethylnonane + <i>o</i> -terphenyl + methane systems, at (A) 20.380, (B) 40.395, (C) 60.903, and (D) 70.4585 gas mol%. Experimental LSE data in black diamonds, LLVE data in blue squares, and PPR EOS in continuous line.	190
Figure 7.12 P-T diagrams for 2,2,4,4,6,8,8-heptamethylnonane + <i>o</i> -terphenyl + methane + CO ₂ systems, at (A) 20.700, (B) 39.315, (C) 59.411, (D) 70.037, (E) 79.993, and (G) 84.003 gas mol% (gas 1:1 molar CO ₂ /methane). Experimental LSE data in black diamonds, LLVE data in blue squares, and PPR EOS in continuous line.....	191
Figure 7.13 Sensibility study of P-T diagrams for 2,2,4,4,6,8,8-heptamethylnonane + <i>o</i> -terphenyl + methane systems, at (A) 20.380, (B) 40.395, (C) 60.903, and (D) 70.4585 gas mol%. Experimental LSE data in black diamonds, LLVE data in blue squares, and PPR EOS in continuous line considering $k_{\text{heptamethylnonane, } o\text{-terphenyl}} = 0$	192

LIST OF TABLES

Table 1.1 Multiphasic LLV for CO ₂ and crude oil mixtures reported in literature.....	33
Table 2.1 Density, average molar weigh, SARA analysis, and water content for the oil.	54
Table 2.2 Compositional analysis of the dead crude oil.....	55
Table 2.3 Saturation pressure and AOP determined for the evaluated system of methane and dead crude oil at reservoir condition (343.15 K).....	72
Table 3.1. Experimental carbon dioxide (CO ₂) and methane (CH ₄) content for crude oil and gas mixtures, and total gas volume fraction ^a	75
Table 3.2. Bubble point pressure P^{bubble} and AOP for studied systems at 343.15 K ^a	87
Table 4.1 Crude oil samples characterization by °API, SARA composition, average molecular weight, WAT and wax content.	92
Table 4.2 Compositional analysis of the dead crude oils.	92
Table 5.1 Experimental methane and CO ₂ composition for crude oil + gas mixtures. .	105
Table 5.2 Solubility parameters and internal pressures comparison from literature data and values obtained from NIST density, at 303.15 K and 0.1 MPa.	107
Table 5.3 Density data deviation (%AARD) between PVT cell and HPHT densimeter for a temperature domain of 313.15 K and 373.15 K.	110
Table 5.4 Bubble point pressures for BR1 crude oil + methane mixtures at a temperature range of 313.15 K to 373.15 K.	111
Table 5.5 Tamman–Tait equation fitting parameters, along with SSE values for BR1 crude oil + methane mixtures (x_1 is the methane mol percent)	111
Table 5.6 Tamman–Tait equation fitting parameters and SSE for BR1 dead oil.....	113
Table 5.7 Bubble point pressures (P^b) for BR2 crude oil + methane + CO ₂ mixtures, AOP, and asphaltene existence region (AOP- P^b) at a temperature range of 343.15 K to 383.15 K.....	118

Table 5.8 Tamman–Tait equation fitting parameters, along with SSE values for BR2 crude oil + methane + CO ₂ mixtures and BR2 dead oil (x_{CO_2} is the carbon dioxide mol percent).....	119
Table 6.1 Compositional analysis of the crude oil sample.....	126
Table 6.2 Molecular weight, critical temperature, critical pressure, and acentric factor for gases and crude oil cuts for condensed model.....	132
Table 6.3 Experimental phase transition data for crude oil + CO ₂ systems ^a	135
Table 6.4 Experimental phase transition data for crude oil + methane systems ^a	147
Table 6.5 Fitted binary interaction parameter between crude oil fractions/carbon dioxide (k_{CO_2-i}), and crude oil fraction/methane (k_{CH_4-i}) for condensed model.	156
Table 7.1 CAS registry number, molecular structure, mass fraction purity, and suppliers of the chemicals.....	167
Table 7.2 Chemicals molecular weight, fusion temperature (T_f), and normal boiling temperature (T_b) ^a	167
Table 7.3 System molar composition for different aromatics and gases used.	168
Table 7.4 Critical temperature, critical pressure, and acentric factor for chemical compounds.....	171
Table 7.5 Binary interaction parameter matrix for systems compounds.....	172
Table 7.6 Experimental phase transition data for mixtures of carbon dioxide (1), diphenylmethane (2) and 2,2,4,4,6,8,8-heptamethylnonane.	174
Table 7.7 Experimental phase transition data for mixtures of methane (1), diphenylmethane (2) and 2,2,4,4,6,8,8-heptamethylnonane.	176
Table 7.8 Experimental phase transition data for mixtures of methane/CO ₂ (1:1 molar) (1), diphenylmethane (2) and 2,2,4,4,6,8,8-heptamethylnonane.....	176
Table 7.9 Experimental LV and LLV phase transition data for mixtures of carbon dioxide (1), <i>o</i> -terphenyl (2), and 2,2,4,4,6,8,8-heptamethylnonane.....	179
Table 7.10 Experimental LS phase transition data for mixtures of carbon dioxide (1), <i>o</i> -terphenyl (2), and 2,2,4,4,6,8,8-heptamethylnonane.....	180

Table 7.11 Experimental phase transition data for mixtures of methane (1), <i>o</i> -terphenyl (2), and 2,2,4,4,6,8,8-heptamethylnonane.	181
Table 7.12 Experimental LS phase transition data for mixtures of methane (1), <i>o</i> -terphenyl (2), and 2,2,4,4,6,8,8-heptamethylnonane.	181
Table 7.13 Experimental phase transition data for mixtures of methane/CO ₂ (1:1 molar) (1), <i>o</i> -terphenyl (2), and 2,2,4,4,6,8,8-heptamethylnonane.	182
Table 7.14 Experimental LS phase transition data for mixtures of methane/CO ₂ (1:1 molar) (1), <i>o</i> -terphenyl (2), and 2,2,4,4,6,8,8-heptamethylnonane.	182

SUMMARY

1	CHAPTER I: INTRODUCTION	27
1.1.	Introduction.....	27
1.2.	Fundamentals on fluid phase behavior	28
1.2.1.	Phase behavior of binary asymmetric hydrocarbon mixtures	31
1.2.2.	Phase behavior of binary carbon dioxide and hydrocarbons mixtures.....	32
1.3.	Multiphase equilibria in crude oil mixtures	32
1.3.1.	Liquid-Liquid-Vapor equilibria in crude oil mixtures.....	32
1.3.2.	Asphaltenes precipitation	35
1.3.3.	Wax precipitation	36
1.3.4.	The case of Brazilian Pre-Salt fluids	37
1.4.	Analytical methods for phase behavior study of crude oil fluids	38
1.4.1.	Light scattering technique	41
1.4.2.	High pressure microscopy (HPM).....	43
1.4.3.	Quartz crystal resonator.....	44
1.4.4.	Spectrometric fluid evaluation.....	46
1.5.	Aim of this project	48
1.5.1.	General objective.....	48
1.5.2.	Specific objectives.....	48
1.6.	Thesis structure	48
1.7.	Scientific production during this thesis	49
2	CHAPTER II: PHASE BEHAVIOR OF METHANE AND PRE-SALT CRUDE OILS USING HPM AND NIR SDS TECHNIQUES	52
2.1.	Introduction.....	52
2.2.	Materials and Methods.....	53
2.2.1.	Crude oil sample.....	53
2.2.2.	PVT apparatus	55
2.2.3.	PVT sample preparation and CCE test	57
2.2.4.	Isothermal depressurization HPM analysis	58
2.2.5.	Isothermal redissolution analysis.....	59

2.3.	Results and Discussion	59
2.3.1.	CCE tests results	59
2.3.2.	Isothermal depressurization HPM results	64
2.4.	Conclusions.....	72
3	CHAPTER III: MEASUREMENT OF FLUID PHASE EQUILIBRIA FOR HIGH GAS RATIO MIXTURES OF CARBON DIOXIDE, METHANE, AND BRAZILIAN PRE-SALT CRUDE OIL	74
3.1.	Introduction.....	74
3.2.	Materials and Methods.....	75
3.2.1.	Crude oil and gas mixtures preparation and phase behavior analysis procedure.....	75
3.3.	Results and discussions.....	77
3.3.1.	Low gas volume fraction systems	77
3.3.2.	High gas volume fraction systems.....	80
3.4.	Conclusions.....	88
4	CHAPTER IV: PHASE BEHAVIOR EVALUATION FOR DIFFERENT PRE-SALT CRUDE OIL MIXTURED WITH METHANE AT HIGH GAS RATIO... ..	89
4.1.	Introduction.....	89
4.2.	Material and Methods	90
4.2.1.	Crude oils characterization	90
4.2.2.	PVT sample preparation and CCE test.....	90
4.3.	Results and Discussion	91
4.3.1.	Crude oils characterization and CCE test results.....	91
4.3.2.	Isothermal depressurization HPM results.....	95
4.4.	Conclusions.....	99
5	CHAPTER V: EXPERIMENTAL PHASE BEHAVIOR AND SOLUBILITY PARAMETER FOR CRUDE OIL + METHANE (T = [311.15 – 373.15] K) AND CRUDE OIL + METHANE + CO ₂ MIXTURES (T = [343.15 – 383.15] K).....	101
5.1.	Introduction.....	101
5.2.	Materials and Methods.....	104
5.2.1.	Crude oil samples	104
5.2.2.	Phase behavior and PVT tests	104
5.2.3.	Density measurements at high pressure using vibrating tube.....	107

5.3.	Results and Discussion	109
5.3.1.	BR1 crude oil + methane mixtures	109
5.3.2.	BR2 crude oil + methane mixtures + CO ₂	116
5.4.	Conclusions.....	122
6	CHAPTER VI: STUDY OF LIQUID–LIQUID AND LIQUID–LIQUID–VAPOR EQUILIBRIA FOR CRUDE OIL MIXTURES WITH CARBON DIOXIDE AND METHANE USING SHORT-WAVE INFRARED IMAGING: EXPERIMENTAL AND THERMODYNAMIC MODELING.....	124
6.1.	Introduction.....	124
6.2.	Materials and Methods.....	125
6.2.1.	Crude oil sample.....	125
6.2.2.	Full visibility PVT tests	127
6.2.3.	QCR Asphaltene flocculation test	129
6.2.4.	Thermodynamic Modelling	130
6.3.	Results and Discussion	134
6.3.1.	Mixtures of crude oil and CO ₂	134
6.3.2.	Mixtures of crude oil and methane	145
6.3.3.	Mixtures of crude oil + methane + CO ₂	150
6.3.4.	Thermodynamic modelling.....	155
6.4.	Conclusions.....	163
7	CHAPTER VII: Study of HIGH-PRESSURE PHASE EQUILIBRIA (LVE, LLE, LSE, AND LLVE) for MODEL SYSTEMS INCLUDING HIGH CARBON NUMBER BRANCHED PARAFINS, POLYAROMATICS, METHANE AND CARBON DIOXIDE.	165
7.1.	Introduction.....	165
7.2.	Material and Methods	166
7.2.1.	Chemicals	166
7.2.2.	Systems preparation and phase behavior study	167
7.2.3.	Thermodynamic Modelling	170
7.3.	Results.....	173
7.3.1.	Experimental phase behavior results	173
7.3.2.	Thermodynamic modeling results	184
7.4.	Conclusions.....	192

8	GENERAL CONCLUSIONS	193
9	RECOMMENDATIONS FOR FUTURE RESEARCH	196
10	REFERENCES.....	196
APPENDIX		
	APPENDIX A: D Uncertainty, repeatability, and validation analysis.....	210
	APPENDIX B: Derivative PVT properties for crude oil and gas mixtures.....	218

1 CHAPTER I: INTRODUCTION

1.1. Introduction.

One of the crucial parts that determine the feasibility when developing a petroleum reservoir is the phase behavior of the produced fluid. As expected for heterogeneous mixtures such as petroleum fluids, their phase behavior is complex and still represents a challenge from experimental and modeling perspectives. As commented by Shaw and Zou (2007), phase behavior of petroleum fluids is influenced by a continuum of thousands mixed hydrocarbons. Besides the innumerable quantity of compounds in the mixture, their chemical diversity goes from light, simple molecules as methane, to heavy, intricate and complex chemical species as asphaltenes. The variety on physicochemical characteristics among petroleum compounds could lead to complex multiphasic conditions, that occur naturally in reservoir conditions, or induced during reservoir development (SHAW; DELOOS; ARONS, 1997; SHELTON; YARBOROUGH, 1977).

From an initial reservoir evaluation, simple biphasic vapor – liquid equilibria (VLE) is used for the assessment of oil reserves in place, as well as for the preliminary study of extraction technologies. However, multiphasic equilibria involving three, four, or more coexisting phases could define the final reservoir development strategy (COUTINHO; JØRGENSEN; STENBY, 1995; KHAN; POPE; SEPEHRNOORI, 1992; OKUNO; XU, 2014a). Operational pressure and temperature variations during oil extraction can intercept the multiphasic domain, especially during fluid depletion and cooling until surface facilities conditions.

Moreover, compositional changes on the reservoir fluid can promote complex multiphasic scenarios. A common practice for enhanced oil recovery (EOR) is the addition of low molecular weight fluids, e.g., methane, carbon dioxide, nitrogen, or natural gas, to the reservoir fluid. This process allows the reservoir pressurization, and/or to improve the flowability characteristics after miscible flooding. However, compositional changes of reservoir fluid can lead to different types of phase equilibria. For example, one type can be related to heavy organic separation, thus leading to the formation of an asphaltenic dominated phase (CAO; GU, 2013; MCKEAN et al., 1999). Other type can be associated to the formation of liquid – liquid equilibria (LLE), where one liquid phase is rich in hydrocarbons, and the other is mainly composed by the EOR

fluid. Moreover, during depletion, a vapor phase is formed and, under specific conditions, a triphasic liquid – liquid – vapor equilibria (LLVE) can be reached (ORR; YU; LIEN, 1981; TUREK; METCALFE; FISHBACK, 1988). This triphasic condition is typically observed at temperatures near the critical temperature of the EOR fluid. In general, this condition is below wax crystallization temperatures of crude oils, and a paraffinic dominated phase can also be formed at reduced temperatures. As result, a combination of multiphase scenarios can be obtained depending on the fluid characteristics and the faced operational conditions.

Recently, complex multiphase equilibria have been observed during Brazilian Pre-Salt reservoir developments. These reservoirs are located in the ultradeep South-east coast of Brazil and are characterized by a high Gas-to-Oil ratio (GOR), high carbon dioxide content, high paraffinic content, with a non-neglectable amount of asphaltenes, and also by producing light to medium crude oils. Laboratorial PVT studies during live oil analysis have evidenced atypical and challenging phase transitions, in which a kind of liquid – liquid immiscibility was detected in a wide temperature and pressure domain above the classical LV phase envelope (CARDOSO et al., 2015; DARIDON et al., 2020). The study of this type of equilibria is limited by conventional PVT techniques, mainly because of the crude oil opacity and the uncommon equilibrium characteristics. Therefore, different analytical approaches are required for an appropriate fluid phase behavior assessment.

In this thesis, systematic study of phase behavior of Pre-Salt crude oil (dead oils) mixed with different gases was developed. This approach aims to reproduce the live oil fluids behavior, but controlling systems variables, such as type of gas in the mixture, gas ratio, and type of crude oil. Phase equilibria characteristics were evaluated by different analytical PVT techniques and procedures, aiming to better identify the different transitions, and the potential immiscibility causes.

1.2. Fundamentals on fluid phase behavior

For any system, the number of possible phases in equilibrium are established by the phase rule. As the number of components increase in the system, the degree of freedom and the number of multiphase equilibria can rise over specific ranges of temperature, pressure, and composition. However, the interpretation of these systems is typically made based on binary systems (SHAW; DELOOS; ARONS, 1997).

For simple binary systems, up to four phases can be obtained in equilibrium if the phases are noncritical. For organic mixtures, a classification of phase equilibrium and critical locus typologies has been made by Van Konynenburg and Scott (1980), based on the topology and number of critical lines projected on pressure-temperature diagrams. These critical lines can connect the critical points of the pure components, here denoted Cl and Ch for the lower and the higher critical temperature component, respectively. In this classification, six types of binary phase behavior are presented, as depicted in Figure 1.1.

Accordingly, Type I diagrams present an uninterrupted liquid – vapor (LV) critical line between Cl and Ch . This type of phase behavior is obtained for mixtures of chemically similar compounds, with no marked difference on critical properties. When the chemical differences increase, a liquid – liquid insolubility can be seen at lower temperatures. In these conditions, a Type II diagram is obtained, where a second critical locus is formed from a liquid – liquid (LL) critical point and sharply increases to high pressures. This critical line intercepts the liquid – liquid – vapor (LLV) line, forming an Upper Critical End Point (UCEP) at lower temperatures and pressures. For systems with a high liquid – liquid insolubility, the critical line linking Cl and Ch is broken and divided in two branches and the diagram becomes Type III. One of the critical lines goes from the Ch and increases to higher pressures, while the other critical line connects Cl to a three phase LLV line through a UCEP. Type IV has three critical lines: one LV critical line that links Cl to a UCEP, a second that connects Ch to a lower critical end point (LCEP), and a third LL critical line that goes from a low pressure UCEP and sharply increases to higher pressures. Type V exhibits only the high temperature behavior of Type IV diagrams, while Type VI is similar to Type I, but an LLV region is presented between a low pressure LCEP and a UCEP.

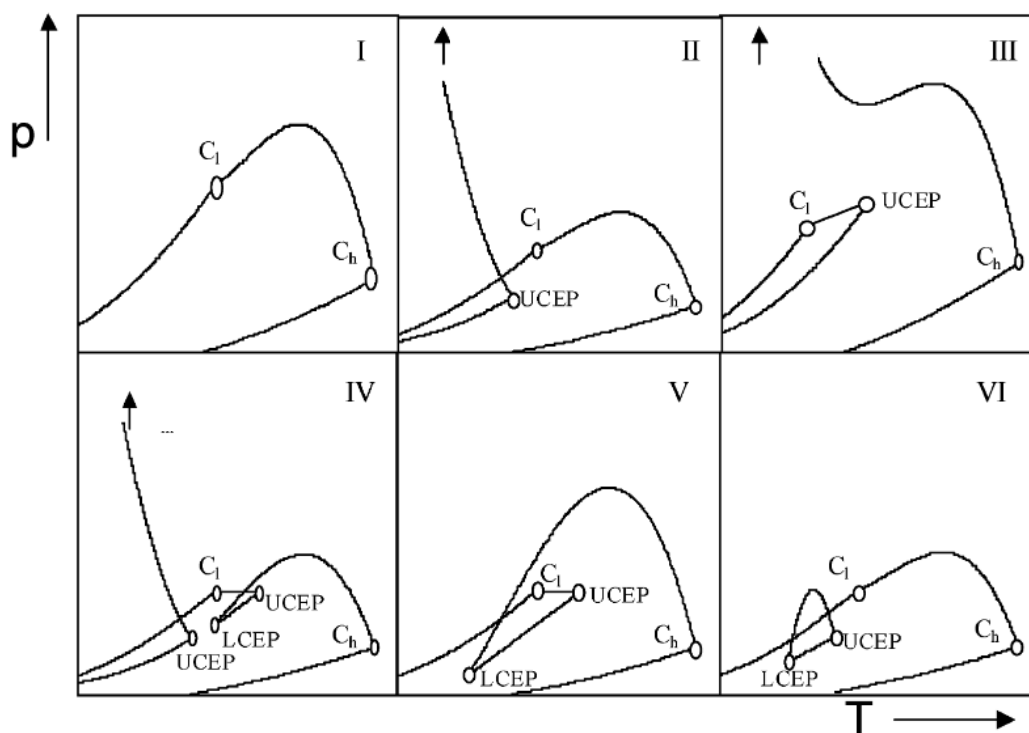


Figure 1.1 Schematic representation of different types of binary phase diagrams (Adapted from García et al. 2004).

These different types of phase behavior can be found in mixtures of industrial interest, and in petroleum mixtures. It can be noted that when the chemical difference in the mixture or system asymmetry increases, multiphasic equilibria are favored (GARCÍA; LUGO; FERNÁNDEZ, 2004; QUINTEROS-LAMA; LLOVELL, 2016, 2018). Consequently, liquid – liquid – vapor triphasic regions can be formed, commonly at temperature and pressure near the critical point of the lighter compound. When this temperature is lower than the crystallization temperature of one of the components of the mixture, a solid phase formation may appear, and the phase projection diagrams can be altered significantly (SHAW; BÉHAR, 2003). The solid equilibria line can intercept the liquid – liquid – vapor line, forming a solid – liquid – liquid – vapor quadruple point, normally defined as *Q*-point. Examples of this type of phase behavior are described in the next section for asymmetric mixtures of organic compounds and methane or carbon dioxide.

1.2.1. Phase behavior of binary asymmetric hydrocarbon mixtures

Several efforts have been made to better understand the phase behavior of low molecular weight gases and crude oil mixtures. Fundamental research of binary mixtures phase behavior for gases and paraffins, aromatics, and typical crude oils molecules, demonstrate complex phase behavior as the molecular size differences increase. Accordingly, when the asymmetry of the system increases, multiphase transitions can be observed under specific pressure and temperature conditions.

For methane and *n*-paraffins systems, multiphase LLV equilibria (LLVE) is formed only when methane is mixed with *n*-hexane or *n*-heptane at low temperatures (CHEN; CHAPPELEAR; KOBAYASHI, 1976). For the case of mixtures with *n*-hexane, a Type II phase diagram is observed, with a small LLV region between a LCEP and a UCEP around the critical point of pure methane. For methane and *n*-octane (or higher *n*-alkanes) mixtures, LLV was not observed because of paraffin crystallization (HOTTOVY; KOHN; LUKS, 1982; KOHN; BRADISH, 1964). However, the addition of ethane to the methane and *n*-octane mixture causes the formation of a LLV region, as demonstrated by Hottovy and collaborators (1981).

For ethane and *n*-alkane mixtures, LLV E is formed for paraffins with chain length from 18 to almost 25 carbons (ESTRERA; LUKS, 1987; KOHN; KIM; PAN, 1966; PETERS; DE ROO; LICHTENTHALER, 1991; PETERS; SPIEGELAAR; DE SWAAN ARONS, 1988). Further investigations have revealed that aromatic compounds enhanced liquid immiscibility when mixed with ethane (ESTRERA; ARBUCKLE; LUKS, 1987; JANGKAMOLKULCHAI; ARBUCKLE; LUKS, 1988). Additionally, an interesting behavior was observed for *n*-alkanols and ethane mixtures with LLVE existence from methanol to *n*-decanol, with a minimum LLV region for *n*-butanol. This phenomenon has been related to polar-non-polar interactions (LAM; JANGKAMOLKULCHAI; LUKS, 1990).

For mixtures of propane and *n*-alkanes, LLV immiscibility is observed only for heavy paraffins (carbon number above 37) (HOTTOVY; KOHN; LUKS, 1981, 1982; ROWLINSON; SWINTON, 1982). In all cases, LLV regions are bounded by two critical end points (*CEP*) or by *Q*-type point, formed by the interception of the solid – liquid – vapor line and the LLV loci (HOTTOVY; KOHN; LUKS, 1982; JANGKAMOLKULCHAI; ARBUCKLE; LUKS, 1988).

1.2.2. Phase behavior of binary carbon dioxide and hydrocarbons mixtures

Multiphasic equilibria is also observed for carbon dioxide (CO₂) and hydrocarbons mixtures (GARCÍA; LUGO; FERNÁNDEZ, 2004; QUINTEROS-LAMA; LLOVELL, 2018). A Type II phase diagram is observed for CO₂ and *n*-paraffins mixtures between *n*-heptane and *n*-undecane. For larger paraffins, with carbon numbers between 14 and 21, the phase behavior changes to Type III diagram (FALL; FALL; LUKS, 1985; HOTTOVY; LUKS; KOHN, 1981). A special case is obtained for the mixture of CO₂ and *n*-tridecane (C13) where a Type IV LLV is observed (ENICK; HOLDER; MORSI, 1985; FALL; LUKS, 1985b; HOTTOVY; LUKS; KOHN, 1981). To obtain the triphasic condition high CO₂ ratios are necessary, CO₂ content represents typically more than 65.0 mol % in the mixture for LLVE formation.

Considering these phase behavior scenarios, boundaries of LL and LLV equilibria could be either separated or follow a continuous critical locus. The heaviest *n*-alkane that presents LLV equilibria when mixed with CO₂ is the *n*-heneicosane (*n*-C21). For *n*-docosane (*n*-C22), the SLV boundary is obtained at higher temperatures than the expected LLV (FALL; LUKS, 1984). Additionally, for CO₂ and aromatics solvent mixtures, *n*-alkylbenzenes systems presented a similar LLV behavior to the homologous *n*-alkane (FALL; LUKS, 1985a; LANSANGAN; JANGKAMOLKULCHAI; LUKS, 1987).

1.3. Multiphase equilibria in crude oil mixtures

High asymmetrical mixtures can be encountered naturally in crude oil reservoirs or can be generated during reservoir development, especially during gas injection. In this section, reported types of multiphasic equilibria for crude oil mixtures are presented, along with phase transitions characteristics.

1.3.1. Liquid-Liquid-Vapor equilibria in crude oil mixtures

Similar to the described for binary mixtures of low molecular weight gases and heavy hydrocarbons, multiphasic behavior is also observed for crude oil and gas mixtures, e.g., CO₂, methane, and enriched separator gas. This condition is achieved especially at high gas composition, low temperatures, and pressures around the gas-solvent critical point. The LLVE occurrence has been widely reported for reservoir fluids ranging from light to heavy crude oil. Table 1.1 consolidates some studies reported in the literature for

LLVE of crude oil and CO₂ mixtures. It can be noted that LLVE formed by CO₂ addition in crude oil is normally observed for gas composition above 60 mol%, a comparable condition to those of binary mixtures.

Table 1.1 Multiphasic LLV for CO₂ and crude oil mixtures reported in literature.

Reference	Type of oil	C7+, mol%	C7+ °API	C7+ MW	CO ₂ for LLVE mol%	studied T, K
Huang, 1974	WTO _a	57.92	32.1	323	77.8	305.4
Shelton, 1977	-	54.93	27.3	243	75 - 95	313.7
Shelton, 1977	WTO	65.41	33.9	227	78-95	307.6
Orr, 1981	Maljamar	41.65	36.1	199.3	79.3	305.4
Yellig, 1982	Levelland	54.93	-	-	65	314.3
Orr, 1984	Wasson	-	-	-	70	319.3
Turek, 1984	WTO A	57.74	27.7	226	65-95	314.2
		26.39-	32.9-	215-		
Turek, 1988	WTO	66.93	27.2	247	70	316.2
Winzinger, 1991	North Ward Estes Field	52.34	31.1	229	57	301.5
Khan, 1992	JEMA WTO	54.29	27.5	248	60	316.5
Khan, 1992	BSB WTO	56.28	29.3	229	59	313.7
Creek, 1993	WTO	41.62	34.6	215	58	307.6
Creek, 1993	WTO	66.34	24.7	252	60	304.3
	Middle East					
Lindeloff, 2013	Oil A	47.644	25.7	271	70	310.9

^a WTO: West Texas Oil

The highest temperature reported for LLVE crude oil mixtures with CO₂ is 319.3 K. Above this temperature, and at higher pressures, a LL region could be extended almost 6 K from the LLV upper critical end point (UCEP). Finally, if the temperature is higher, these systems present only LV equilibrium regions whichever the nature and composition of the oil is (AL GHAFRI; MAITLAND; TRUSLER, 2014; HUANG; TRACHT, 1974; ORR; YU; LIEN, 1981). LLE evaluation for high gas content systems is impeded by the lack of density difference between phases, especially when fluids are visually opaque.

The influence of these LLV and LL phase equilibria on crude oil recovery (OKUNO; XU, 2014a, 2014b), along with their proper representation by process simulators, is still a scientific challenge. It has been reported that the second liquid phase can extract valuable, light fractions of crude oil compounds, even if it is mainly composed by CO₂ (COUTINHO; JØRGENSEN; STENBY, 1995; IMAI et al., 2019; LINDELOFF et al., 2013; MOHEBBINIA; SEPEHRNOORI; JOHNS, 2013; NEGAHBAN et al., 2020; PAN et al., 2015).

Multiphasic LLVE has also been reported for mixtures of crude oil and ethane (MEHROTRA, 1985), propane (DINI; BECERRA; SHAW, 2016), and higher molecular weight solvents when mixed with crude oil (JOHNSTON et al., 2017). In some cases, the immiscibility is related to a solvent-rich phase, or to a heavy-asphaltic-rich phase, each one in equilibrium with an oil-rich phase and a vapor phase mainly composed by the lighter compound in the mixture.

The existence of LL and LLVE has been proved experimentally by visual static PVT tests, or by typical miscibility slim tube tests. Through these analyses, the formation of two independent liquid phases can be observed, one of them oleic and the other rich in lighter compound, such as CO₂. An example of an LLVE is presented in Figure 1.2. In this picture, a clear interphase is observed between the gas and the two liquid phases. However, it has been reported that as the CO₂-rich phase solubilizes some crude oil compounds, the mixture becomes denser, viscous, and darker, limiting visual identification of interphases, especially at elevated gas content (EGHBALI; DEHGHANPOUR, 2019; LINDELOFF et al., 2013; OKUNO; XU, 2014b; ORR; YU; LIEN, 1981).

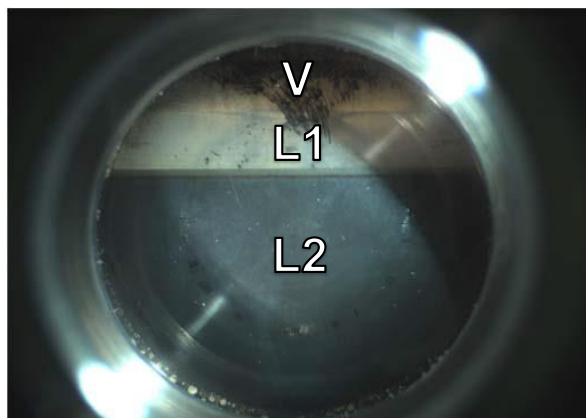


Figure 1.2 L1 (CO₂-rich)–L2 (oil-rich)–V equilibria for crude oil and CO₂ mixture in a full visual PVT cell. Adapted from Lindeloff et al., 2013.

For this reason, one of the main problem for multiphasic equilibria studies is the opaque nature of the system and the poor phases segregation due to density similarities of the different liquids (AL GHAFRI; MAITLAND; TRUSLER, 2014; OKUNO; XU, 2014a; ORR; YU; LIEN, 1981; WANG et al., 2003). Consequently, different PVT analyses are recommended for opaque crude oils phase behavior characterization, as described in next sections (DARIDON et al., 2020; DINI; BECERRA; SHAW, 2016).

1.3.2. Asphaltenes precipitation

Asphaltenes are recognized by their complex molecular structure and intricate phase behavior. Additionally, they have a critical influence in crude oil quality and flowability characteristics during oil production. Asphaltenes are commonly identified as the heaviest, aromatic and the most polar group among crude oil components (SPEIGHT, 2004), and their precipitation is normally associated with changes in pressure (DÍAZ et al., 2011), temperature (CALLES et al., 2008; MAQBOOL; SRIKIRATIWONG; FOGLER, 2011), and compositional variations in the crude oil (GONZALEZ et al., 2005; RAMOS et al., 2013; ROGEL; MOIR, 2017; YARRANTON, 2005).

Commonly during reservoir development, asphaltenes destabilization is mainly promoted by fluid depletion, also by solvent injection in Enhanced Oil Recovery (EOR) methods. In both cases, volumetric fraction of light compounds play an important role on the oil solvency towards asphaltenes (CARDOSO et al., 2014). Accordingly, fluid expansion during lifting increases the volumetric fraction of compressible compounds in the oil mixture (JOSHI et al., 2001; GARCÍA; LUGO; FERNÁNDEZ, 2004). Thus, as consequence of these effects, minimum solubility conditions could be achieved and asphaltenes could be destabilized.

Multiphasic equilibria involving LLV and precipitated asphaltene is recognized to be scarce in literature (GODBOLE; THELE; REINBOLD, 1995). However, almost the totality of studies cited in Table 1.1, documented the formation of a macroscopic and probably asphaltenic dense phase in systems with high gas content. LLV + asphalt equilibria has been reported for crude oil mixtures with CO₂, and separator ethane-rich gas for low temperature reservoirs (SHELTON; YARBOROUGH, 1977), especially for heavy crude oil samples (DERUITER; NASH; SINGLETARY, 1994; GODBOLE; THELE; REINBOLD, 1995; KHATANIAR et al., 1999; SHARMA et al., 1989).

Similarly, it has been demonstrated that heavy crude oil, bitumen, and heavy oil fractions concentrated in asphaltenes, as vacuum residues, can form a multiphasic LLV+asphaltene equilibria when mixed with propane or pentane (DINI; BECERRA; SHAW, 2016; ZOU; SHAW, 2004). For these systems, two liquid phases are formed, one rich in crude oil, and a second one asphaltene dominated, both in equilibrium with a vapor phase rich in light alkanes. For this type of complex equilibria, characterized by the crude oil opacity, the implementation of spectrometric analysis involving X-ray studies becomes necessary to visualize the phase separation and dispersion in the dark crude oil.

Because of experimental difficulties encountered in studying asphaltene precipitation in live oil reservoir conditions, asphaltene destabilization is mainly investigated under atmospheric pressure by using alkanes with carbon number higher than five. Dead oil samples are titrated with paraffinic solvents to promote asphaltene phase separation at atmospheric conditions (MAQBOOL; SRIKIRATIWONG; FOGLER, 2011; THARANIVASAN; YARRANTON; TAYLOR, 2012). This procedure aims to reproduce the destabilization effects caused by fluid depletion from reservoir, allowing to perform reference studies of destabilization, aggregation, and deposition mechanisms (ANDERSEN, 1999b; CASAS et al., 2019; DURAN; SCHOEGGL; YARRANTON, 2019).

1.3.3. Wax precipitation

For simple binary mixtures, the quadruple Q -point normally delimits the temperature at which multiphasic SLLVE is observed (FALL; LUKS, 1984). This point is influenced by the melting temperature of the heavier compound in the mixture. In some cases, this temperature is high enough to radically modify the phase diagram, and a solid dominated region is obtained in a wide temperature range (SHAW; ZOU, 2007).

In the case of crude oil mixtures, paraffinic compounds, also known as saturates or waxes, can form a solid phase when the temperature is reduced. These compounds include typically n -alkanes and cycloalkanes species. Large paraffinic solids can be formed if the crude oil is cooled below their wax appearance temperature (WAT). This phase behavior is recognized as one of the most important flow assurance issues during reservoir production, especially for offshore risers with large thermal gradients (COUTINHO et al., 2006; COUTINHO; DARIDON, 2001).

For paraffinic reservoir fluids with high gas content, and no neglectable content of asphaltenes, the phase behavior becomes more interesting and complex. As aforementioned, lower temperatures induce liquid – liquid insolubilities for crude oil mixtures and gases, which can also promote the wax solid formation. However, scarce data has been openly published for this type of SLLVE.

Alongside, simultaneous wax and asphaltenes precipitations are a classical unresolved question (GARCÍA; CARBOGNANI, 2001). The interception of the asphaltene precipitation onset pressure (AOP) line and the WAT in a PT diagram is the initial and final point for this type of solid – solid equilibria study. At lower temperatures, no analytical techniques have been developed to experimentally detect the AOP changes when waxes go out of solution.

1.3.4. The case of Brazilian Pre-Salt fluids

Brazilian Pre-Salt crude oils represent one of the typical natural platforms for multiphase equilibria studies. Produced from oil fields in the ultradeep offshore South east coast of Brazil, they are characterized by a combination of light to medium crude oils (between 28 to 30 °API); with high Gas-to-Oil ratio (GOR), spanning from 200 to 350 m³/m³; high CO₂ content, from 1 to 45 mol%; high pressure, and medium temperatures (DA COSTA FRAGA et al., 2015). Their discovery promoted a vast technology development, specially related to remote reservoir locations (below 2000 m of water column and more than 5000 m of carbonate formations), focused on well construction, flow assurance, fluid treatment, and transportation (BELTRAO et al., 2009). Besides these technical challenges for reservoir development, the fluid complexity was an additional variable regarding multiphase behavior.

In terms of liquid composition, crude oil from Brazilian Pre-Salt is characterized by a relatively high paraffinic content. This chemical characteristic is widely known in Pre-Salt fluids for their impact on reservoir operations, flow assurance and transportation, regarding wax solid formation and gelification (GONCALVES et al., 2013). Among the saturates fraction, the content of *n*-paraffins is predominant in medium crude oils over the *iso*-paraffins content; and they have a higher naphthenic compounds content than other lighter Brazilian crudes (FRANÇA et al., 2018). A second important fraction of crude oil compounds include branched aromatics, as alkyl-benzenes and alkyl-naphthalenes, as described by Vanini and collaborators, 2018. They identified more than 2700 compounds

for Brazilian crude oils, including Pre-Salt samples, by using high-resolution analytical techniques, concluding on the paraffinic nature of these crude oils (VANINI et al., 2018).

Medium and ever lighter crude oils produced from Brazilian Pre-Salt reservoirs also have a non-neglectable amount of heavy and asphaltenic compounds. Considering the high GOR of the reservoirs, heavy compounds stability and the possibility of multiphasic equilibria are matters of high relevance, especially if any gas injection method is considered for EOR.

Recently, phase behavior studies for Brazilian Pre-salt reservoir fluids presented an atypical complex and multiphasic equilibria. Specially, an uncommon liquid-liquid-vapor type equilibrium was observed, but differently than classical LLV discussed above, this liquid immiscibility is detected at much higher temperatures and pressures than the critical condition of solubilized gases (CARDOSO et al., 2015). The assessment of this type of phase behavior has not been extensively studied, mainly due to the limitations of classical PVT techniques and protocols (DARIDON et al., 2020). As commented by Cardoso and collaborators (2015), the combination of different analytical techniques is necessary for the proper evaluation of these complex phase equilibria, especially because of the high fluid opacity and the poor phase segregation. In this regard, this thesis aims to contribute to the interpretation of this phenomena by the evaluation of classical and new experimental techniques, used to investigate complex phase behavior for highly asymmetrical mixtures as encountered on Pre-Salt fluids. Some of the PVT techniques used in this thesis for fluid evaluation are described in the next section.

1.4. Analytical methods for phase behavior study of crude oil fluids

Several analytical techniques have been developed for the study and assessment of phase behavior of complex mixtures as crude oil. In general, they follow the same principles of phase behavior analysis of simple fluids, which are based on: (i) how the compositions of the phases are determined (analytical methods); and, (ii) how the phase transitions are detected (synthetic techniques) (FORNARI; ALESSI; KIKIC, 1990). System compositions can be determined by the individual analysis of every formed phase after equilibration, splitting, and settling. On the other hand, overall composition can be estimated by recombination using synthetic approaches, where target mixtures are prepared by knowing the precise amount of their constituents. This methodology is also

used in swelling tests for both industrial and research purposes by adding gas and solvents to live oil or degasified oil, aiming to evaluate its effect in their phase behavior.

Moreover, analytical methods involve the determination of the compositions of the phases once the system is brought to equilibrium. The composition of the phases is analyzed by either taking samples or in-situ techniques like gravimetric or optical methods. On the opposite side, synthetic methods do not need sampling and analysis of the phases but the exact feed composition of the system must be known prior to its loading into the equilibrium cell. Synthetic methods can operate with or without a phase transition. However synthetic methods with a phase transition detection are more often used than synthetic methods without a phase transition (DOHRN; PEPER; FONSECA, 2010).

Regarding the methods for phase transition determination, several techniques have been proposed to better assess the different phase transitions that could occur for a crude oil sample. Depending on the type of measurement used for the phase transition detection, they can be classified as direct or indirect methods. The most common and easy direct technique for phase transition determination is the visual fluid inspection, normally used for simple synthetic mixtures. Indeed, in most of the cases, synthetic fluids are translucent and phase separations can be visually determined with analytical precision. However, as the crude oil is dark and complex, this method may lose its application. Even for a simple equilibrium such as liquid – vapor transitions, visual fluid inspection can be prevented due to its high opacity and also because of poor phase segregation. This is a common case in extra heavy crude oils, for example. Formation of high dispersed phases and microscopical phases, such as asphaltene flocs and wax crystals, are also not detected by simple visual inspection.

The use of visual PVT cells allows the possibility of simultaneous fluid inspection along with, in most of the cases, measurements of compressibility changes during fluid expansion. Compressibility changes indirectly permit the determination of vapor phase formation, which can be visually confirmed by phase splitting in the PVT cell (AGRAWAL et al., 2012). When near-critical fluids are analyzed, i.e. fluids with no evident change on overall volume after vapor evolution, is recommended the treatment of compressibility data by using the Y_{exr} -function (HOSEIN; MAYRHOO; MCCAIN, 2014).

$$Y_{ext} = \frac{-V_i}{P_i} \left(\frac{P-P_i}{V-V_i} \right) \quad \text{Eq. 1.1}$$

where P_i and V_i are the initial PVT pressure and volume, respectively, and P and V are the measured values during the pressure depletion experiment.

This function describes the fluid gas availability, given by the Eq. 1.1. For pressures above the bubble point, the Y_{ext} -function has minor variation with pressure. However, if pressure is reduced below the fluid's bubble point, Y_{ext} -function decrease evidently by the gas release, and this change helps to identify vapor phase formation. However, if the fluid is analyzed near its critical point, no information can be provided by this function, and the visual fluid inspection is, if possible, the only method to detect the phase transition.

In order to overcome limitations during PVT tests, the study of different fluid properties can be measured to indirectly determine phase transitions occurrence in crude oil. They include thermal properties (calorimetry, transitiometry) (ANDERSEN; BIRDI, 1991; JUYAL et al., 2011; WILKEN; FISCHER; GMEHLING, 2002), mechanical and transport properties (viscosity, density) (ESCOBEDO; MANSOORI, 1995; SHADMAN et al., 2012), electromagnetic properties (conductivity, permittivity) (FOTLAND; ANFINDSEN; FADNES, 1993), optical properties (refractive index, light absorption) (ANDERSEN, 1999b; CASTILLO et al., 2006; HAMMAMI et al., 2000) and acoustic properties (velocity, attenuation) (CARRIER et al., 2000; YARRANTON; CHEN; THOMAS, 2000). Accordingly, a specific fluid property is monitored while pressure, temperature, or volume is varied, and the formation phase is indirectly detected when a change in the measured property occurs. This approach has been especially useful for the study of microscopic phase transitions as asphaltene formation, and wax precipitation.

Similarly, some analytical methods for fluid phase behavior evaluation use changes in the properties of an external sensor or materials in contact with the fluid. For example, changes on the electrical response of an acoustic sensor (DARIDON; CARRIER, 2017) and, pressure losses through a filter (ANDERSEN; LINDELOFF; STENBY, 1998; FIROOZINIA; FOULADI HOSSEIN ABAD; VARAMESH, 2016; YONEBAYASHI et al., 2018) have been used for fluid phase transition determination at high pressure conditions.

In the following sections a detailed description of analytical techniques used in this thesis for fluid phase evaluations is presented. Among these methods, conventional

and well-established procedures were used in chapter II to IV for the assessment of multiphase fluid equilibria of Pre-Salt crude oil and gas mixtures. Moreover, no conventional PVT techniques implemented in chapter VI are also detailed.

1.4.1. Light scattering technique

One of the most common techniques used for phase transition determination in crude oil systems is the light scattering technique. When fluids are irradiated with a source of light, any phase transition, e.g., gas or solid phase formation, can impact in fluid light transmittance. For heavy crude oils, that are normally opaque and adsorb most of the visible light, a near-infrared (NIR) light is commonly used. At this wavelength, minimum absorbance is observed for oils ranging from light to heavy crude oils, as depicted in Figure 1.3 (VENKATARAMANAN et al., 2006).

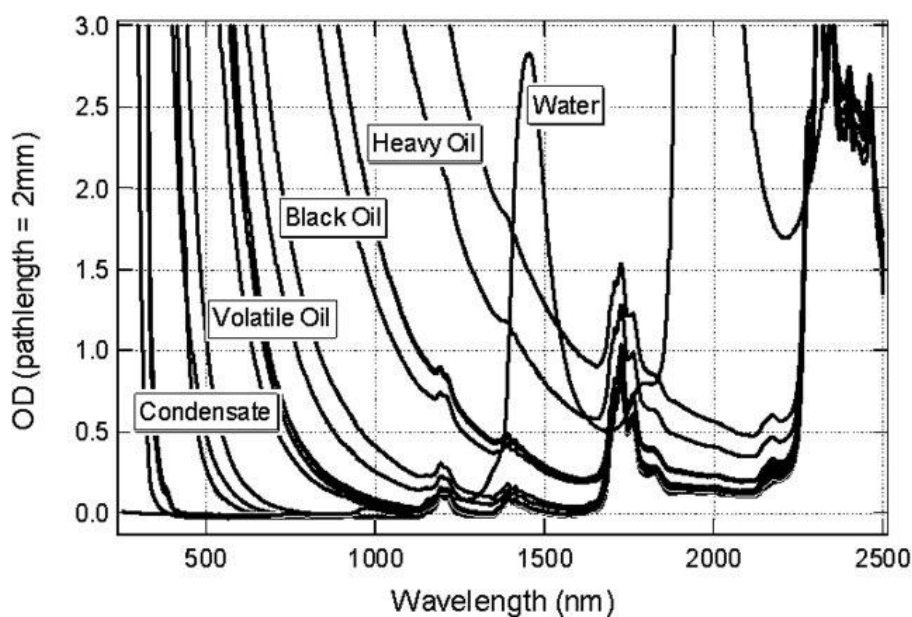


Figure 1.3 Light absorption spectra of different reservoir fluids and water (VENKATARAMANAN et al., 2006).

The use of NIR for phase behavior studies of petroleum fluids is well established in literature for low and high pressure applications (FUHR et al., 1991; FUHR; KLEIN; REICHERT, 1986; HOTIER; ROBIN, 1983). The typical usage of NIR scattering is presented by Hammami and collaborators (2000), where a NIR based solid detection system (SDS) is used for asphaltene onset pressure (AOP) determination on live oils, a

method that was widely adopted by industrials and researchers. Specifically, crude oil NIR transmittance is monitored during isothermal constant composition expansion (CCE) tests, and the phase transitions are detected as changes in the transmitted light power. This change in fluid transmissibility is then associated to: (i) scattering by solid formations, as asphaltenes or waxes, or (ii) light scattering by bubbles formation, as a vapor phase emerges. This last has a dramatic effect on the fluid NIR transmittance, as depicted in Figure 1.4.

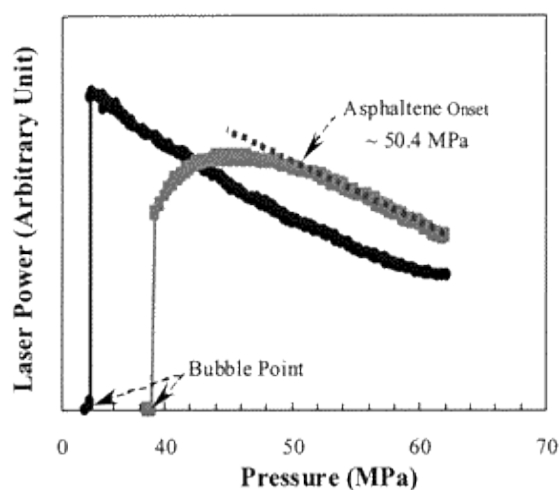


Figure 1.4 NIR SDS response for two crude oils during expansion, adapted from Hammami *et al.* (2000).

Consequently, this method allows the evaluation of phase transitions and the differentiation of asphaltenes or vapor phase formation, in most of the cases. Also, it can be used as a guide for phase dissolution scanning, especially for solids and asphaltene formations with an important dissolution hysteresis (ASKE *et al.*, 2002; HAMMAMI *et al.*, 2000). NIR light scattering has been applied in the study of asphaltene precipitation of heavy and opaque crude oil, especially for temperature effects on asphaltene precipitation envelope (TAVAKKOLI *et al.*, 2014a). Also, it was implemented to the study of heavy and opaque live oils, with reported asphaltene precipitation problems during production (LEI *et al.*, 2015). Attempts were also made to obtain the asphaltene redissolution point below the bubble point pressure, or lower asphaltene precipitation onset, by using NIR measurements. However, results are still not accurate when using this technique. Moreover, it is important to mention that fluid depressurization rate can

affect the results of asphaltene precipitation onset detected by NIR SDS; lower onset can be obtained at faster depletion rates (JOSHI et al., 2001).

NIR SDS technique is inoperative when multiphasic equilibria are studied. In most of the cases, it is not possible to identify the cause of the light scattering when two or more phases are present. Furthermore, this method is also limited by the analysis of a specific region of the fluid. In general, only the small region where the NIR laser passes is measured. Also, it does not allow the assessment of the initial condition of the fluid, it only gives information of fluid changes from a referential initial state. Then, if the fluid is multiphasic since the beginning of the test, the NIR light scattering technique will not provide any information about this condition.

1.4.2. High pressure microscopy (HPM)

A complementary analytical technique that can be used for fluid phase behavior analysis is the optical microscopy. This technique has been widely used at atmospheric condition for asphaltene flocculation analysis by solvents addition, and for wax precipitation, as a prominent method when cross polarized light is used (BUCKLEY, 2007; HIRSCHBERG et al., 1984; TAVAKKOLI et al., 2014a). Their study is limited to particles analysis above micrometrical size. However, it still is an accepted technique that provides not only the visual confirmation of the formed phase, but also their morphological features.

For high pressure analysis, specific microscopic cells have been designed and applied for the visual inspection of pressurized crude oil fluids (DARIDON; PAULY; MILHET, 2002; JOHNSTON et al., 2017; MANCILLA-POLANCO et al., 2017). In this type of analysis, a small fluid sample is flowed through a channel composed by two optical sapphires, within a path of some hundreds of microns. While the fluid is depressurized, visual inspection can be performed in the fluid, and microscopic phase transitions can be detected. In some cases, the HPM cell is coupled with a NIR SDS laser, that allows the simultaneous measurement of transmitted light power during microscopy analysis.

By using this technique, asphaltenes and wax behavior has been studied at reservoir conditions. Microscopic analysis has been used as basis to propose aggregation and flocculation mechanisms (JOSHI et al., 2001; MOHAMMADI et al., 2015, 2016). Zhou and Sarma (2012) investigated by HPM the effect of different gases on asphaltene

precipitation, concluding that the depressurization rate has an important influence on the asphaltene onset precipitation determination. HPM analysis was also used for testing of asphaltene inhibitors, thus being useful for the screening of flocculant retardants for live oils. HPM allowed not only the analysis of AOP variation after use of chemical inhibitors, but also the morphological changes of precipitated solid (KARAN et al., 2003).

HPM fluid visualization overcomes some limitations of light scattering technique. For instance, it can be used to define a reference state, or to verify an initial monophasic fluid condition, before a NIR scanning during depletion. However, it is limited because: (i) analysis of submicrometric phases is not possible, (ii) only a small sample of the overall fluid is analyzed, with limitation on fluid isotropy conclusions, (iii) heavy and opaque crude oils cannot be analyzed by classical optical microscopy and (iv) fluid opacity, pressure range and objective magnification are highly inter-correlated. Precisely, when higher optical magnification is used, minimal focal length is reached. Then, thinner sapphire windows must be used, limiting their pressure range. Also, the quantity of light collected by a microscope depends on the magnification objective used, thus restraining the application for opaque fluids study.

1.4.3. Quartz crystal resonator

To overcome limitations on particles size determination, and the limitations of *ex-situ* analysis, high-precision acoustic techniques have been developed to study phase transitions in fluids and in particular asphaltene destabilization (ABUDU; GOUAL, 2009; DARIDON et al., 2013). One prominent technique is based on the use of piezoelectric resonators immersed in the fluid, that allows the resonation frequency measurements while the system conditions change, e.g., pressure, temperature, or composition.

This type of resonator is denominated quartz crystal resonator (QCR) and consists of a AT-cut polished quartz sensor, placed between two metallic electrodes, that oscillates in specific frequencies under an electric potential. The oscillation frequency of the quartz sensor is measured by an acoustic analyzer (in MHz), and related to fluid properties when the quartz is immersed on it. It was demonstrated that changes in frequency (Δf) and dissipation ($\Delta \Gamma$) of quartz oscillation peaks, when the sensor is immersed on liquids, can be related to viscous dissipation for Newtonian fluids (KEIJI KANAZAWA; GORDON, 1985). When no mass deposition is considered in the sensor, Δf and $\Delta \Gamma$ are proportional to the product of the viscosity and density of the contacting liquid ($\mu_l \rho_l$), according to

Kanazawa and Gordon (1985) equations (DARIDON et al., 2013; DARIDON; CARRIER, 2017), as follows:

$$\Delta f_n = -\sqrt{n} \frac{C_m}{\sqrt{\pi f_0}} \sqrt{\mu_l \rho_l} \quad (\text{Eq. 1.2})$$

$$\Delta \Gamma_n = +\sqrt{n} \frac{C_m}{\sqrt{\pi f_0}} \sqrt{\mu_l \rho_l} \quad (\text{Eq. 1.3})$$

$$C_m = \frac{2f_0^2}{\sqrt{\mu_q \rho_q}} \quad (\text{Eq. 1.4})$$

where C_m is the Sauerbrey constant defined by Eq. 1.4, f_0 is the fundamental resonance frequency of the quartz crystal used, ρ_q and μ_q are the density and the shear modulus of the quartz material, respectively, and n is the investigated overtone.

This type of sensor is also sensitive to molecular deposition in their surface, with an influence on their oscillation response. Finally, deposited mass in the quartz resonator can be related to changes in their oscillation behavior as follows:

$$\Delta f_n = -n(2C_m \rho h) - \sqrt{n} \frac{C_m}{\sqrt{\pi f_0}} \sqrt{\mu_l \rho_l} \quad (\text{Eq. 1.5})$$

$$\Delta \Gamma_n = +\sqrt{n} \frac{C_m}{\sqrt{\pi f_0}} \sqrt{\mu_l \rho_l} (1 + R) \quad (\text{Eq. 1.6})$$

where R is an empirical correction for viscous friction on rough surfaces, and ρh is the mass (per unit of area) that represent mass deposition in the sensor, and accounts for interfacial effects such as slippage.

When the sensor is immersed in a crude oil sample, any change in oil properties will result in a shift in resonant behavior of the sensor according to the above equations. Dissipation and frequency variations will account for alterations on the product of density and viscosity, and phase transitions can be detected when this product is affected. Phase transitions with obvious discontinuity of these properties, e.g., bubble point pressure of black oil fluids, will have a marked variation in oscillation response. Formation of slurries, dispersed phases, as asphaltenes, can also affect the $\mu_l \rho_l$ factor, with a slighter sensor response. Also, the shift in oscillation frequency can also account for solid deposition in the quartz sensor (DARIDON; CARRIER, 2017).

The sensibility of this technique for particles detection has been reported to be below $0.6 \mu\text{m}$ (DARIDON et al., 2013). Accordingly, it has been successfully used for

the determination of high dispersed particles, as occurs in the asphaltene flocculation studies (GOUAL et al., 2014). The use of QCR has been proved efficient for asphaltene precipitation onset studies during titration experiment at atmospheric condition (SAIDOUN et al., 2019; TAVAKKOLI et al., 2014b), or in pressurized systems and live oil testing (DARIDON; ORLANDI; CARRIER, 2016; DARIDON et al., 2020; DARIDON; CARRIER, 2017). Also, it has been widely implemented for the study of precipitation mechanisms (GOUAL et al., 2005), considering different oil/sensor surfaces (ABUDU; GOUAL, 2009), and flocculation times (TAVAKKOLI et al., 2014a). The high precision of the QCR analysis has also favored precipitation kinetic studies, by reducing the flock detection time compared to other techniques (VILAS BÔAS FÁVERO et al., 2017a).

Features of QCR technique overcome the limitations of HPM in both particle size, and the overall bulk fluid analysis. However, similar to the NIR light scattering, the QCR test is performed relative to an initial referential state. For that reason, the fluid condition at this referential point needs to be well defined beforehand. Ideally, a monophasic condition is necessary to detect subsequent phase transitions by the QCR. Then, to obtain information of the fluid referential state, more specialized techniques are required for heavy and opaque crude oils.

1.4.4. Spectrometric fluid evaluation

The techniques above mentioned are almost incomplete if they are used individually. It can be noted that they are complementary, in terms of the information quality and the type that each one can provide. However, when heavy and opaque crude oils are analyzed, the tests are biased without the confirmation of the initial state of the fluid, a crucial data required before any PVT test. For that reason, specialized visualization techniques have been developed to allow dark fluid inspection.

Similar to the principle of light scattering, the main goal of full fluid visualization technique is to irradiate/detect the transmitted light through the fluid bulk, using a radiation with low absorption on crude oil. In this sense, a complete visualization of the fluid can be obtained, and the information of number of phases, volumes, and segregation can be more easily addressed.

Following this idea, efforts have been made to fully visualize complex phase behaviors of heavy crude oils and bitumen. However, instead of using visual light

imaging, fluid inspection was made through transmitted X-rays images (ABEDI et al., 1999). The X-ray source acts in the same way as a conventional light bulb in classical full visual PVT tests, with the advantage that it has minimum absorption on heavy and asphaltenic crude oils. Then, transmitted X-rays through fluid and walls of the PVT are measured, treated, and converted to high-resolution visual images.

Using this technique, complex phase behavior has been observed by the first time for mixtures of bitumen and pentane (ZOU; SHAW, 2004), and propane (DINI; BECERRA; SHAW, 2016). Correspondingly, it was determined that a heavy asphaltenic liquid phase is formed when mixed with pentane. This heavy phase can stay dispersed in the fluid's bulk or settle as a separate phase. After their formation by propane addition, the biphasic region goes from a very high pressure until the bubble point pressure. Additionally, over a broad range of conditions, adherent deposits (solids or liquids) were observed in equilibria with the second liquid and/or vapor phase. Similar results were observed for mixture of bitumen and propane, with the formation of heavy and dispersed phases, which cannot be confirmed by using conventional PVT techniques (DINI; BECERRA; SHAW, 2016). HPM studies coupled with fluid compositional analysis were also made for the evaluation of heavy phase distribution between liquid phases (JOHNSTON et al., 2017).

Most recently, a new full visualization assembly was developed based on the low crude oil absorbance of short wave near-infrared (SWIR) radiation (DARIDON et al., 2020). As previously depicted in Figure 1.3, crude oil has a reduced absorption in the wavelength range from 1000 to 1600 nm. Accordingly, a SIWR digital camera can be readily adapted in a full visual PVT for the analysis of opaque crude oils. This type of camera works in a spectral range of 900 to 1700 nm, and has been successfully used for determination of complex multiphasic LLE, LLVE, and asphaltene precipitation in heavy crude oils, including Brazilian Pre-Salt samples (DARIDON et al., 2020). Additionally, this visualization assembly can also be adapted to HPM cells, allowing the detection of microscopic dispersions in opaque and heavy crude oils.

A combination of these techniques will be necessary to properly address the phase behavior of high asymmetric mixtures, asphaltenic containing crude oils, and low molecular weight gases, representative of their reservoir fluids. In this thesis, the full visual PVT-SIWR analysis will be fundamental in chapter VI for the experimental and modeling study of atypical high pressure – high temperature (HP-HT) LLVE of Pre-Salt fluids.

1.5. Aim of this project

This thesis project was motivated by complex multiphase equilibria phenomena observed during Brazilian Pre-Salt crude oil production. The particular compositional properties of these fluids, i.e., high GOR, high CO₂ content, high wax content, asphaltene presence, and high opacity, have been a challenge for proper fluid phase behavior study. Accordingly, the following objectives have been defined to investigate complex phase behavior of Pre-Salt crude oils:

1.5.1. General objective

Study gas addition effect on the phase behavior of Brazilian Pre-Salt dead oil mixtures at high pressure and temperature conditions.

1.5.2. Specific objectives

- Study the phase behavior of methane and carbon dioxide mixtures with Brazilian Pre-Salt dead oil samples using conventional PVT techniques.
- Identify the characteristics of formed phases in Brazilian Pre-Salt and gas mixtures in terms of morphology, redissolution, and dispersion.
- Compare the phase behavior of highly asymmetric mixtures of different Pre-Salt crude oils.
- Implement new visualization techniques for the analysis of the phase behavior of gas mixtures with Brazilian Pre-Salt crude oil.
- Implement thermodynamic models to describe and aid to understand the observed multiphase behavior for crude oil and gas mixtures.
- To investigate simpler model-systems that could present similar phase behavior to the obtained for Brazilian Pre-Salt crude oil mixed with gas.

1.6. Thesis Structure

In chapter I, the fundamentals of fluid phase behavior of multicomponent mixtures are introduced. Limitations on phase behavior analysis of complex mixtures and reservoir fluids are also addressed. Different PVT analytical techniques are described for phase behavior evaluation of reservoir fluids.

These techniques are applied in the analysis of crude oil from Brazilian Pre-Salt mixed with gases. In chapter II the effect of methane addition on the phase behavior of Brazilian Pre-Salt crudes was studied and analyzed by intermediate of conventional PVT techniques. Subsequently, chapter III and chapter IV extend the discussion by focusing on gas composition, and the crude oil characteristics, respectively.

In chapter V, volumetric and fluid phase behavior data were utilized to calculate derivative properties for crude oil and gas mixtures. Through this analysis, it is intended to obtain information about the possible causes of mixtures' phase immiscibility.

Later, in chapter VI, new analytical techniques are presented to assess complex phase behavior of dead Pre-Salt oil, methane, and/or carbon dioxide mixtures. Precisely, SWIR fluid inspection and QCR analysis were implemented to study LLVE and SLE for these systems. Besides, available thermodynamics models were tested for phase behavior representation.

Lastly, in chapter VII, a fundamental study of phase behavior of high asymmetrical systems, involving heavy branched paraffins, aromatics, and gases is presented. This study aims to compare the behavior of simple systems with those observed in crude oil.

1.7. Scientific production during this thesis

The results presented in this thesis have been part of different type of scientific publications. Details of these works will be presented in individual chapters of this thesis. Precisely, the papers published in international scientific journals are:

1. Romero Yanes, J. F., Feitosa, F. X., Fleming, F. P., de Sant'Ana, H. B., Experimental study of the phase behavior of methane and crude oil mixtures. *Fuel* 2019, 255, 115850. <https://doi.org/10.1016/j.fuel.2019.115850>.
2. Romero Yanes, J. F., Ferreira, A. F. B., Gomes de Medeiros, P. Y., Bassani, G. S., Fleming, F. P., Feitosa, F. X., de Sant'Ana, H. B., 2019. Phase Behavior for Crude Oil and Methane Mixtures: Crude Oil Property Comparison. *Energy Fuels*. <https://doi.org/10.1021/acs.energyfuels.9b03560>.
3. Romero Yanes, J. F.; de Sant'Ana, H. B.; Feitosa, F. X.; Pujol, M.; Collell, J.; Pauly, J.; Fleming, F. P.; Montel, F.; Daridon, J.-L. Study of Liquid–Liquid and Liquid–Liquid–Vapor Equilibria for Crude Oil Mixtures with Carbon Dioxide and

- Methane Using Short-Wave Infrared Imaging: Experimental and Thermodynamic Modeling. *Energy Fuels* 2020. <https://doi.org/10.1021/acs.energyfuels.0c03064>.
4. Romero Yanes, J. F.; da Costa, M. F. L.; Sampaio, J. P. G.; Chacón Valero, A. M.; Feitosa, F. X.; de Sant'Ana, H. B. Experimental Phase Behavior and Solubility Parameter for Crude Oil + Methane [T = 311.15–373.15 K] and Crude Oil + Methane + CO₂ Mixtures [T = 343.15–383.15 K]. *Fuel* 2020, 119675. <https://doi.org/10.1016/j.fuel.2020.119675>.
 5. Romero Yanes, J. F., Feitosa, F. X., Fleming, F. P., de Sant'Ana, H. B., Measurement of Fluid Phase Equilibria for High Gas Ratio Mixtures of Carbon Dioxide, Methane, And Brazilian Pre-Salt Crude Oil, *Journal of Chemical and Engineering Data*, <https://doi.org/10.1021/acs.jced.0c00988>.

Some of these works have been selected for publication from International Congress. The works sent to international congresses are presented below:

1. Romero Yanes, J.F., Feitosa, F.X., de Sant'Ana, H.B. "Effect of carbon dioxide in crude oil + methane mixtures at temperature from 343.15 to 383.15 K". CBTERMO 2019. Nova Friburgo. RJ – Brazil.
2. Romero Yanes, J.F., Feitosa, F.X., Fleming, F.P., de Sant'Ana, H.B. "Experimental study of the effect of methane on the phase behavior of recombined crude oil". Petrophase 2019.
3. Romero Yanes, J.F., Ferreira, A.F.B., Gomes de Medeiros, P.Y., Fleming, F.P., Feitosa, F.X., de Sant'Ana, H.B. "Phase behavior comparison for different recombined reservoir fluids with methane". Petrophase 2019.
4. Romero Yanes, J.F., Feitosa, F.X., Fleming, F.P., de Sant'Ana, H.B. "Phase behavior of crude oil recombined with CO₂ and methane". Petrophase 2019.
5. Alves, C.A., Romero Yanes, J.F., Feitosa, F.X., de Sant'Ana, H.B., 2019. "Effect of Temperature on Asphaltenes Precipitation: Direct and Indirect Analyses and Phase Equilibrium Study". Petrophase 2019.
6. Soares, M; Romero Yanes, J.F., de Sant'Ana, H.B. "Density and viscosity of saturates, aromatics, and resins from Brazilian crude oils". Petrophase 2019.

Some of the last-mentioned works have been part of collaborative projects, involving undergraduate student's works, and graduate colleagues' research. Some of them, have also been selected for publication in international journals, as follows:

1. Alves, C.A., Romero Yanes, J.F., Feitosa, F.X., de Sant'Ana, H.B., 2019. Effect of Temperature on Asphaltene Precipitation: Direct and Indirect Analyses and Phase Equilibrium Study. *Energy Fuels* 33, 6921–6928. <https://doi.org/10.1021/acs.energyfuels.9b00408>.

2 CHAPTER II: PHASE BEHAVIOR OF METHANE AND PRE-SALT CRUDE OILS USING HPM AND NIR SDS TECHNIQUES

Results published in: *Experimental Study of the Phase Behavior of Methane and Crude Oil Mixtures*. Fuel 2019, 255, 115850. <https://doi.org/10.1016/j.fuel.2019.115850>.

2.1. Introduction.

In this chapter, it is studied the phase behavior of Brazilian Pre-Salt dead crude oil + methane mixtures, at different methane ratio. This study is a first approximation to simulate the Pre-Salt reservoir fluid and their complex phase behavior. It is important to remember the unusual characteristics observed for these fluids, described by Cardoso (2015), precisely: (i) there is some evidence of a LL immiscibility formed at HPHT conditions above the LV locus, (ii) the phases are characterized by their high dispersity, and (iii) the second liquid phase present a rapid redissolution with pressure.

Mixtures of methane and asphaltic crude oil represent one of the most asymmetrical systems that can be encountered at reservoir conditions. Critical properties of methane are wide different from those of heavy asphaltenic compounds in crude oil. Additionally, mixtures of methane and crude oil can have a dramatical effect on the solvency capacity towards asphaltenes. For this study, it is important to remark some typical characteristics of asphaltenes, such as: (i) their slow kinetic, for both aggregates formation, or redissolution, (ii) fractal morphology, and (iii) aggregative capacity (CHAISSONTORNYOTIN; BINGHAM; HOEPFNER, 2017; HAMMAMI et al., 2000; MOHAMMADI et al., 2015; VILAS BÔAS FÁVERO et al., 2017). Some of these phenomenological conclusions depends on the experimental observations of asphaltene flocks formation at reservoir conditions and their flocculation envelope (ARTOLA et al., 2011).

Most of the literature data for mixtures of methane or natural gas with crude oil shows an identification of the phase boundaries, i.e., bubble point pressure and asphaltene onset pressure, specially used to fit models' parameters, validate phase behavior predictive methods, and the further calculation of derivative thermodynamic properties (GONZALEZ et al., 2005; TING; HIRASAKI; CHAPMAN, 2003; VARGAS et al., 2009a). Nevertheless, characteristics of the phase transitions for these systems is scarce

in open literature, especially for asphaltenes and related equilibria at higher pressures than the bubble pressure point (ALHAMMADI; VARGAS; CHAPMAN, 2015).

For that reason, the main goal of this chapter is to better describe the phase transition for Pre-Salt crude oil at high pressure condition. Specially, focused on phase characteristics as morphology, dispersion, and redissolution, to better assess the observation that have been reported for live oil systems. Phase boundaries were determined by using different conventional PVT techniques combined: pressure-volume measurements, coupled with a NIR probe for solid detection system (SDS), together with HPM analysis. These techniques were used to identify liquid-vapor (LV) transitions and any other transition above the LV locus, as asphaltene precipitation, as function of methane content. Phases redissolution was also evaluated by system pressurization from pressures above their appearance onset to monophasic region.

2.2. Materials and Methods

Mixtures of a Brazilian Pre-Salt dead oil and methane systems were made for PVT studies. Systems were prepared through synthetic method, i.e. mixtures of known composition were prepared and their phase behavior studied in a variable volume cell (AL GHAFRI; MAITLAND; TRUSLER, 2014; GUI et al., 2017). Crude oil and methane mixtures (65.0, 67.5, 70.0, 72.5 and 75.0 mol% of methane) were studied, and their phase behavior was analyzed in a motorized PVT cell. Two different tests were performed for each composition: a constant composition expansion (CCE) test, and an isothermal expansion for high pressure microscopy (HPM) analysis, detailed described in Sections 2.2.3 and 2.2.4. Both tests were made at reported reservoir temperature of 343.15 K (70.0 °C).

2.2.1. Crude oil sample

Dead crude oil sample was supplied by Petrobras, and collected during a well-test at stock tank condition. After received in our laboratory, sample storage was made at room conditions. Before any experiment using the crude oil, the overall sample was heated at 65 °C and stirred to dissolve waxes. Table 2.1 depicts crude oil characterization, i.e., density, SARA (saturates, aromatics, resins and asphaltene) analysis, molar weight,

and water content. Additionally, compositional analysis of the crude oil is presented in Table 2.2.

Density measurements were carried out by using an Anton Paar SVM 3000 viscodensimeter, based on a U-tube principle. Standard oils (CN-6773, Anton Paar) were used for calibration procedure, with an uncertainty $u(\rho) = 0.0001 \text{ g/cm}^3$.

Asphaltene content was measured following a single stage *n*-heptane addition, as stated by Alboudwarej et al. (ALBOUDWAREJ et al., 2002) and described elsewhere (ROMERO YANES et al., 2018a). Crudes SAR (saturates, aromatics, and resins) content was also determined by liquid chromatography fractionation, following ASTM D2007M procedure (KHARRAT et al., 2007). Analytical grade (> 99.8 %) solvents (*n*-heptane, toluene, dichloromethane and methanol) supplied by Sigma-Aldrich were used. It is important to mention all chemicals were used with no further purification processes. Water content was determined by using a Karl-Fischer titration (Metrohm, Brazil).

Table 2.1 Density, average molar weigh, SARA analysis, and water content for the oil.

crude oil properties	
API gravity, °API	28.0
density at 40 °C, kg/m ³	889.1
average molar weight, kg/kmol	250
saturates content ± 1, wt%	59
aromatic content ± 1, wt%	22
resins content ± 1, wt%	18
asphaltenes content ± 0.05, wt%	0.68
water content, wt%	0.49

Crude oil SARA fractionation was used to investigate its asphaltene stability by intermediate of the Sepúlveda's Criteria, i.e., Qualitative-Quantitative Analysis (QQA), and Stability Cross Plot (SCP) test (GUZMÁN et al., 2017; KUMAR; VOOLAPALLI; UPADHYAYULA, 2018). These asphaltene stability criteria are based in a series of relations between crude oil SARA fractions, the use of both tests is recommended to better results in asphaltene stability evaluation (GUZMÁN et al., 2017). Details about the criteria are presented elsewhere (GUZMÁN et al., 2017; KUMAR; VOOLAPALLI; UPADHYAYULA, 2018).

Table 2.2 Compositional analysis of the dead crude oil.

Carbon number	wt %	mol %
C3	0.00	0.00
iC4	0.01	0.04
nC4	0.06	0.28
iC5	0.13	0.53
nC5	0.27	1.10
C6	0.95	3.31
C7	2.15	6.51
C8	3.09	8.43
C9	2.90	6.98
C10	2.58	5.61
C11	2.47	4.91
C12	2.35	4.26
C13	2.68	4.47
C14	2.41	3.70
C15	2.55	3.61
C16	2.09	2.74
C17	2.04	2.51
C18	2.23	2.59
C19	2.10	2.33
C20+	66.93	36.09
C20+ molar weight		541

2.2.2. PVT apparatus

In this part, PVT analysis have been performed by using a Fluid-Eval PVT cell (Vinci Technologies, France), with a maximum operational condition of 100 MPa and 473.15 K, with a maximum capacity of 2000 cm³. cell operational uncertainties (u) have been determined as: $u(P) = 0.1$ MPa for pressure; $u(T) = 0.1$ K for temperature; and, $u(V) = 1 \cdot 10^{-8}$ m³ (0.01 cm³) for volume. A schematic diagram of the high-pressure system is presented in Figure 2.1, with a detailed description made below.

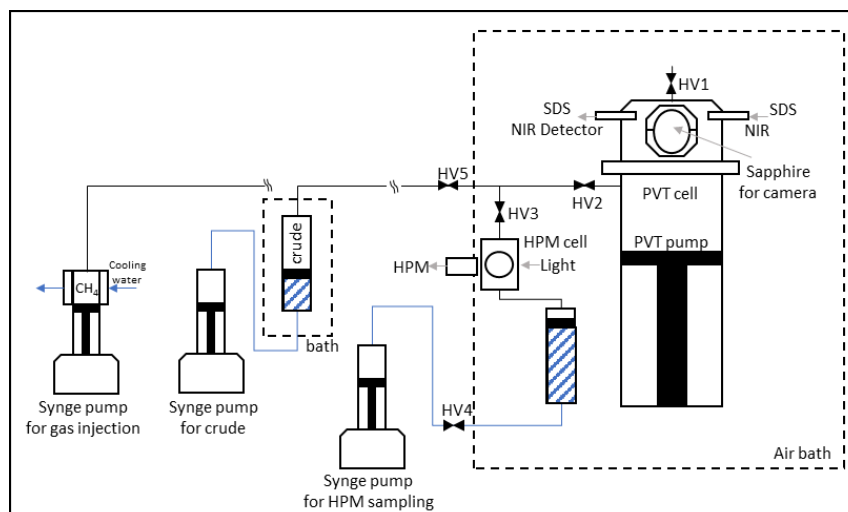


Figure 2.1 Schematic diagram of PVT, HPM and sample injection ensemble.

The apparatus consists of a variable volume Hastelloy cell, embedded with a high-pressure pump (with a pressure accuracy of 0.1 % of their high limit pressure). This system is also equipped with a magnetic driven stirrer for homogenization of the fluid sample.

Vapor phase could be visually identified through two sapphire windows placed at the top of the cell. Through these windows, volumetric measurements of the formed phase (with an accuracy of 0.02 cm^3) can be made using a video camera. Vinci VisionACq V1.5[®] software was used for image processing and volume calculation.

Near Infrared (NIR) transmittance through the crude sample was measured continuously during depletion using a Solid Detection System (SDS) provided by Vinci Technologies. A NIR laser source was connected to the PVT cell through an optic fiber. NIR transmittance was analyzed in the wavelength of 1,500 nm by an optical power meter with a minimal sensitivity of 1 pW.

HPM analysis were also performed for phase identification during the depressurization process. HPM cell consist of a high-pressure arrangement with two sapphires distanced by 100- μm where sample from the PVT flows through. HPM cell is connected between PVT cell and a high-pressure reservoir. Vinci HPM V1.0.11[®] software was used for micrograph analysis. From these analyses, it could be possible to detect the presence of particles, their counting, along with their size, with a lower detection of 1 μm diameter.

2.2.3. PVT sample preparation and CCE test

Crude oil and gas were precisely introduced to the PVT cell, previously vacuumed at 1 kPa, by using high-pressure syringe pumps. Firstly, a volume of crude oil (80.00 mL) was injected in the PVT cell, at 40.0 °C and 690 kPa. Secondly, a required amount of methane (White Martins, 99.995 wt%) was injected by using a Teledyne Isco 260D syringe pump $u(V) = 1 \cdot 10^{-8} \text{ m}^3$ (0.01 cm³), at 13.79 MPa. Gas temperature during injection procedure was controlled by intermediate of the cooling jacket of the syringe pump, by using a PolyScience AD07R-40 chiller, at 20.0 °C.

Temperature and pressure during injection were monitored to calculate the mass amount of each fluid introduced in the PVT cell. Density and molecular mass of crude oil were previously determined, as described in Table 1. Methane density was taken from NIST REFPROP V7 database (112.17 kg/m³ at 20.0 °C and 13.79 MPa). Mass of crude oil and gas were calculated from volumetric displacement of the pumps, and their respective density. The expanded uncertainty for gas molar composition was $u(x) = 0.89$ mol %, details for uncertainty calculation are given in Appendix A.

After the desired amount of crude oil and gas were injected to the PVT, the cell content was continuously stirred and pressurized with a rate of 415 kPa/min (60 psi/min) until at least 14 MPa above the bubble point. It was kept under stirring, at least, 12 h before the CCE test.

CCE test was performed by a controlled depressurization following equilibrium steps until at least 20 MPa below the detection of first bubbles. Depressurization steps were kept at 3,400 kPa for pressures far from bubble point; and 690 kPa for pressures near the bubble point. Depressurization rate between equilibrium steps was 208 kPa/min (30 psi/min), at a minimal equilibrium time of 15 min. After this time, a three parameter criterium was adopted to ensure equilibrium was achieved, as follow: no variations on pressure higher than 35 kPa; 0.03 cm³ of volume change; and, 1.0 °C temperature variation for at least 5 min. Only when this criterion is attained, pressure, temperature and volume values are taking by intermediate of a data acquisition software (AppliLab). It is important to mention that for each depressurization step; the system was stirred constantly. On the other hand, equilibrium steps were taken without stirring.

Phase transitions were identified by intermediate of three different techniques, as follow: (i) pressure-volume (PV curve) slope variation against pression (AGRAWAL et al., 2012; JOHNSTON et al., 2017); (ii) visual identifications; and, (iii) variations on

sample NIR transmittance (HAMMAMI et al., 2000; LEI et al., 2015). For instance, bubble point pressure was determined by the changing on the slope for PV curves (AGRAWAL et al., 2012; JOHNSTON et al., 2017). Uncertainty of each method is detailed in Appendix A. Visual identification of the first bubbles was recorded by the camera located in front of sapphire windows in the head cell. This analysis was important to the confirmation of the saturation pressure. Gas phase volume was determined by using the coupled camera. From these data, isothermal compressibility for the gas phase was also calculated. Monophasic isothermal compressibility at high pressures was determined by volumetric measurements from PVT embedded pump. Relative volume was calculated by dividing system volume (at each equilibrium step) by the interpolated volume at the saturation pressure. Uncertainty of bubble point pressure obtained by changes on PV slope was estimated as 0.624 MPa.

NIR transmittance were recorded continuously during depressurization and at the equilibrium stages. It is important to state that NIR transmittance at saturation pressure is close to zero (10^{-8} W). Nevertheless, above bubble point pressure, a decreasing in NIR transmittance, could be related to disperse phases, slurries, or solid formations, e.g., asphaltene onset pressure (AOP) (HAMMAMI et al., 2000; LEI et al., 2015). Uncertainty of bubble point pressure and AOP determination using NIR was estimated in 0.629 and 0.634 MPa, respectively.

After the last stage of equilibrium, the entire system was repressurized (at a rate of 415 kPa/min) to get the initial pressure of the test. After that, the system remains at rest during at least 12 h under stirring (750 rpm). Next, NIR transmittance before and after recombination was compared to assure the return to initial state. This sample was used then for isothermal depressurization HPM analysis.

2.2.4. Isothermal depressurization HPM analysis

Isothermal depressurization HPM analysis was conducted under a depressurization ramp of 208 kPa/min and equilibrium steps of 5 min. Simultaneously, a flowrate of 0.1 cm³/min was set in the syringe pump to flow fresh fluid from the PVT cell to the HPM cell. During the depressurization and equilibrium steps, phase formation, e.g. asphaltenes, were identified by particle count, aggregates size and relative coverage area, by using microscope camera and Vinci HPM V1.0.11[®] software. Micrographs were taken every 2 sec. NIR transmittance measurements in the PVT cell during HPM test were also

registered during both depletion and equilibrium steps. Uncertainty of HPM analysis for bubble point pressure and AOP was 0.647 MPa, as detailed in Appendix A.

2.2.5. Isothermal redissolution analysis

Phase insolubilities were also evaluated in terms of dissolution by repressurizing the system from the AOP, or appearance onset pressure, to the monophasic pressure. Pressurization was made by increasing PVT pressure with the HPM connected, at a rate of 415 kPa/min. Then, NIR transmittance in bulk fluid, and HPM information were recorded simultaneously during fluid compression.

2.3. Results and Discussion

2.3.1. CCE tests results

Relative volumes against pressure for all the crude oil + methane systems are depicted in Figure 2.2. From these curves, saturation pressure was determined from the inflection point of the relative volume. It was observed that increasing methane molar content this inflection point is less evident, as expected. For methane compositions of 72.5 and 75.0 mol%, PV curve plots show a continuous shape, with no clear discontinuity (AMJAD et al., 2016). For this reason, bubble point pressure is better determined by both visual observation of the first bubbles in the PVT cell sapphire windows and by the sharp decrease of SDS NIR signal.

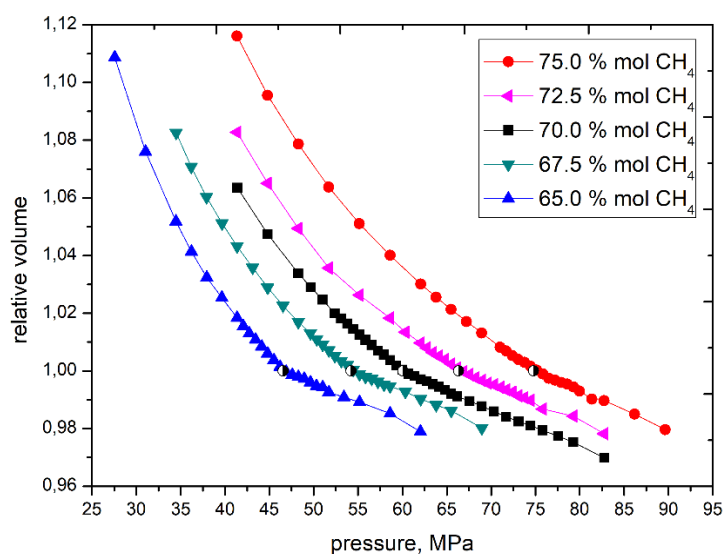


Figure 2.2 Relative volume and saturation pressures (●) of crude oil and methane systems during CCE depletions.

Compressibility calculation of each measured phase are presented in Figure 2.3. Overall compressibility was directly calculated from the volumetric measurements of the cell content. These measurements are coincident to the monophasic compressibility at pressures above the saturation pressure. Below saturation pressure, two different compressibilities were calculated, one from the gas phase, obtained from frontal camera; and another from volumetric measurements of the embedded pump. From these data, it could be observed a compressibility difference over 100-fold for the gas phase compared to the dense phase. This difference in compressibility confirms the measured bubble point and denotes the LV equilibrium for all the systems. It was observed that as methane content increases, the overall system compressibility variation becomes less evident, when saturation pressure is reached. For systems above 70.0 mol% of methane, the identification of the bubble point pressure was possible by means of a visual observation of the cell content and the NIR transmittance response.

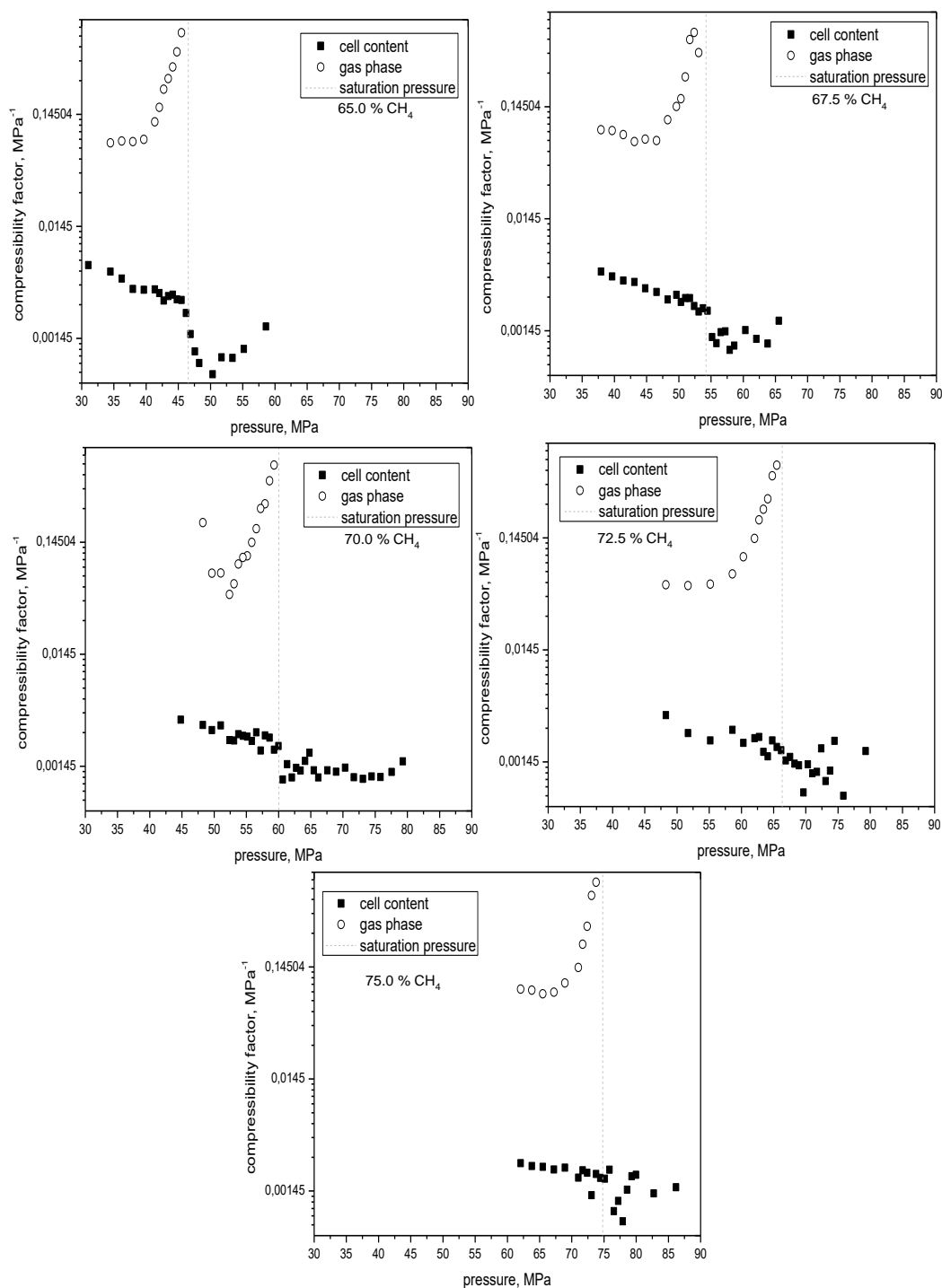


Figure 2.3 Saturation pressure and isothermal compressibility factor at 343.15 K for the overall system and the gas phase after the bubble point for crude oil and methane mixtures.

Figure 2.4 shows NIR signal measurements for equilibrium steps and the continue measurement during system depletion. It can be noted that a sharp NIR transmittance

reduction was attained when bubble point was reached. It could be related to the bubbles formation leading to a high laser dispersion or density changes in the continuous oil phase that contributes to the increase of sample absorbance (HAMMAMI et al., 2000; LEI et al., 2015). For system composition below 70.0 mol% of methane, a monotonic increase in NIR transmittance was detected during depletion until the saturation pressure. This behavior could be related to the reduction of the system density due to the depressurization.

For systems with higher methane content, NIR transmittance variations were detected indicating a possible phase transition at pressure above the LV locus. This variation is normally related to asphaltenes when the AOP was reached, and NIR SDS is used. Additionally, for mixtures with high methane content, phase transition occurs at higher pressures, possibly due to solvency variation in crude oil toward heavy compounds (CARDOSO et al., 2014). NIR transmittance oscillation for 72.5 and 75.0 methane mol% were observed under stirring, between equilibrium steps, probably indicating a segregation process of the phase formed. Additionally, it could be observed that, during the equilibration of the stages, when PVT cell stirrer is turn off, NIR transmittance signal increases. These observations could indicate that the formed phase may distribute in PVT cell when system is not stirred, leaving the NIR laser path and consequently the SDS detection zone.

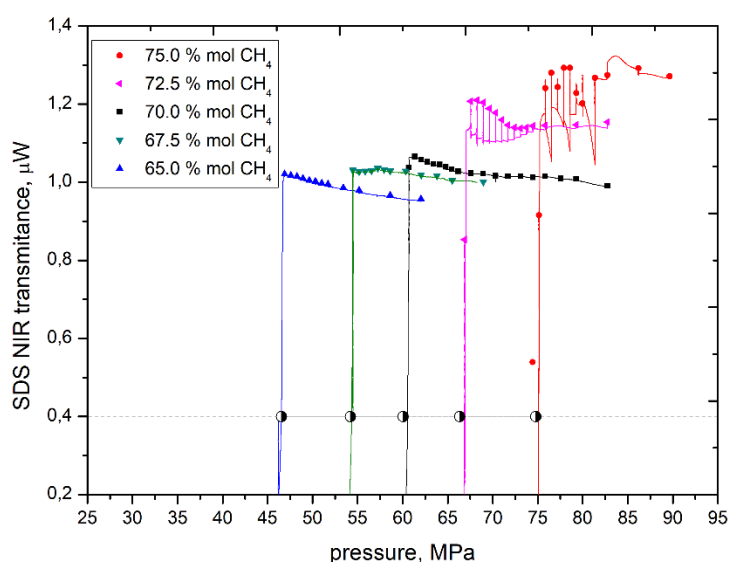


Figure 2.4 NIR transmittance signal for equilibrium steps (solid symbols) and continue depressurization (lines) during CCE test. Saturation pressures marked (●) for crude oil and methane mixtures.

NIR transmittance signal comparison between sample depletion and repressurization process is shown in Figure 2.5. It was noticed that all systems required a stabilization time to reach the initial transmittance, possible due to the delay in phase equilibrium caused by mass transfer limitations. For mixtures with methane content below 70.0 mol%, systems without apparent AOP, NIR transmittance was higher during recompression, and then decrease to the initial value after the equilibration time (12 hours). Samples NIR transmittance could be related inversely with density (HAMMAMI et al., 2000; LEI et al., 2015), and the decreasing of NIR transmittance after the stabilization time could indicate the stabilization in mixture density until reach equilibrium. Nevertheless, for systems with higher methane content, 72.5 and 75.0 mol%, NIR transmittance were lower during the pressurizing process and could be related to heavy phase redissolution. After equilibration time, NIR transmittance reaches initial CCE NIR value. It important to mention, that no considerable hysteresis was detected for phase redissolution after the pressurizing process, at least by using NIR SDS measurements.

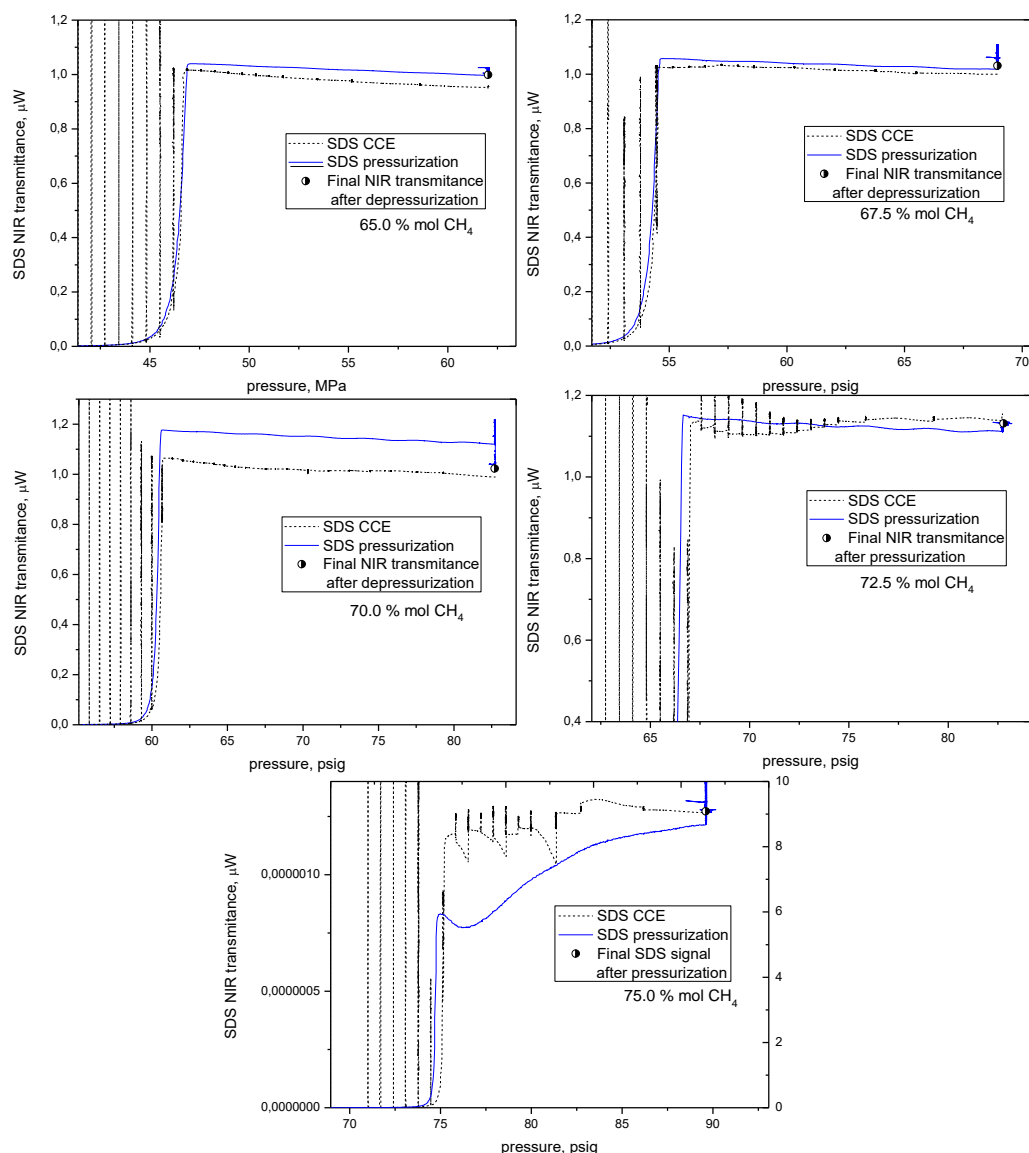


Figure 2.5 NIR transmittance comparison during CCE and system re-pressurization for all crude oil and methane mixtures (65.0, 67.5, 70.0, 72.5, and 75.0 methane mol%).

2.3.2. Isothermal depressurization HPM results

It is important to emphasize that all NIR transmittance data were investigated by HPM test to corroborate the phase transitions characteristics, described in the last Section. NIR transmittance, HPM particle count and micrographs for crude oil mixtures with 65.0, 67.5 and 70.0 methane mol% were presented in Figure 2.6. It was noted that NIR transmittance behaviors in the same way of CCE test. It means, with a monotonal increase during depletion until reach bubble point pressure. Micrographs analysis can confirm that there is not any asphaltene precipitation, no particles appearing were detected during

depletion. Only LV transition is observed when saturation pressure was attained. It is important to mention that the constant response of SDS and HPM during depletion, i.e., constant particles count, no observation of particulate appearing, and SDS monotonal behavior, allows to confirm the absence of any other phases at pressure above the bubble point pressure. The difference on particle count between the systems could be associated with the initial estate of the HPM sapphire windows that represent a base line for each analysis.

Moreover, for these systems, bubble point maximum difference obtained by using CCE and HPM was observed for 70.00 methane mol%, with a value of 2.05 MPa, with a 3.42 % difference. It is interesting to remember that bubble point from CCE is always lower than HPM analysis. These differences could be associate to the accuracy techniques. During HPM test, the systems depletion is performed continuously, in difference to the equilibrium steps considered in CCE analysis. It has been reported in the literature that the depressurization rate could have influence in the bubble point pressure (ZHOU et al., 2017), and it could be related to the difference obtained by the two methods. It is expected that the CCE results were more accurate, by the consideration of the equilibrium steps during depletion (ZHOU et al., 2017). The approximate error for the bubble pressure points determination, by intermediate of each technique, is within 100 psi (0.69 MPa).

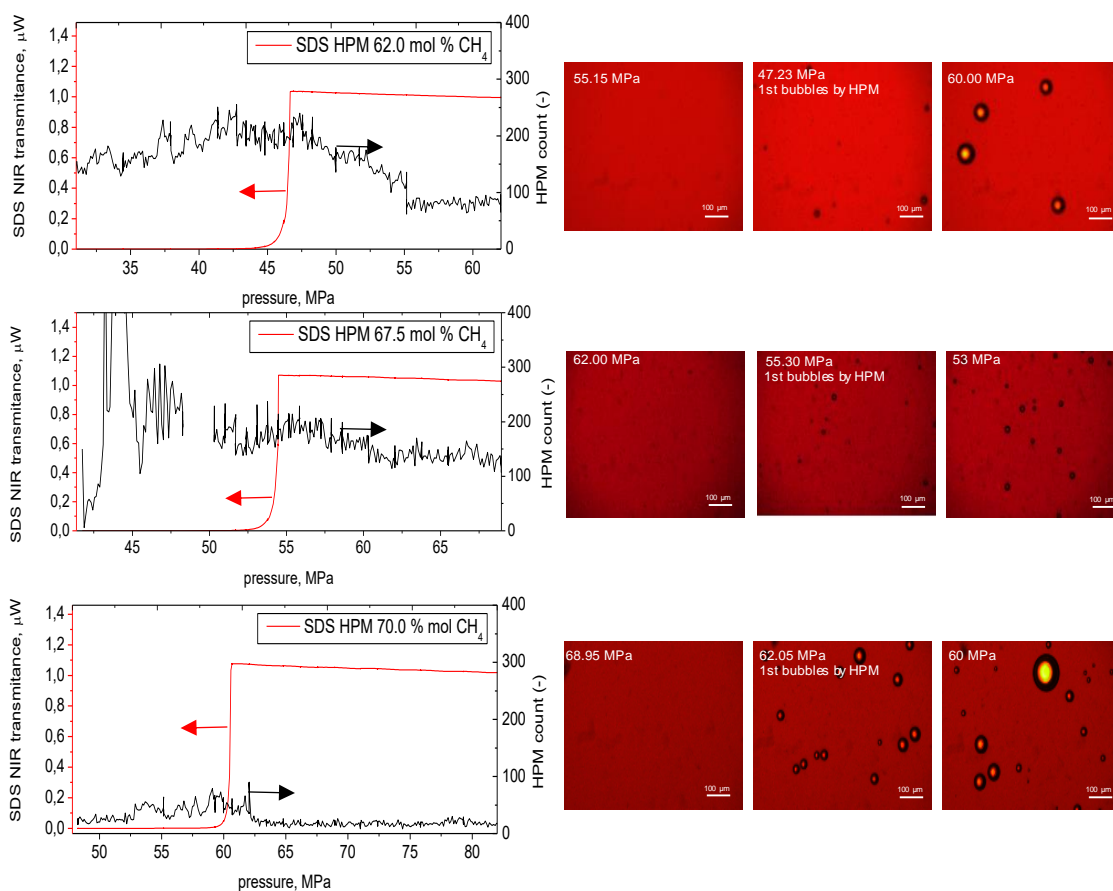


Figure 2.6 NIR transmittance, HPM particle count and micrographs for crude oil and methane mixtures with 65.0, 67.5 and 70.0 methane mol% during HPM test.

Figures 2.7 to 2.10 present HPM results for systems with higher methane content (72.5 and 75.0 mol%). Micrographs and particles count confirm the appearance of a second phase during depressurization. Its appearance onset was identified in the pressure at which the insolubility was visually observed in the HPM. This result is in accordance with SDS NIR transmittance, where there is a decrease on this signal when phase transition is observed. Figure 2.7 shows SDS NIR transmittance along with HPM count for the system with 72.5 methane mol %. It is shown that there is an increase in HPM count during depletion, at the same pressure (75.15 MPa) SDS NIR decreases in the CCE test. This event could be related to a phase transition, typically associated with asphaltene flocculation that contribute to decrease NIR transmittance. Likewise, Figure 2.8 shows the formation of a fine dispersed phase, around 75.15 MPa. This phase shows no tendency to aggregate to form clusters. Also, it is remarkable that the phase disappeared entirely when the system reached bubble point pressure. Although asphaltene are recognized to

form fractal aggregates or flocs (MOHAMMADI et al., 2015), micrographs do not show any fractal agglomeration even at 7.0 MPa below their onset pressure.

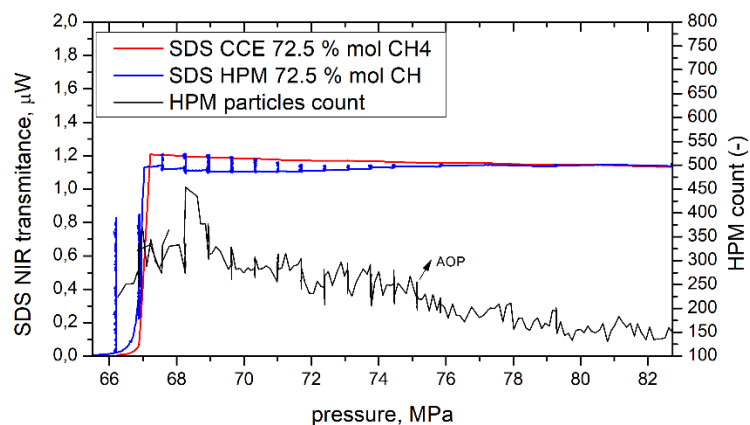


Figure 2.7 NIR transmittance and HPM particle count for 72.5 methane mol% crude oil and methane mixture during HPM test.

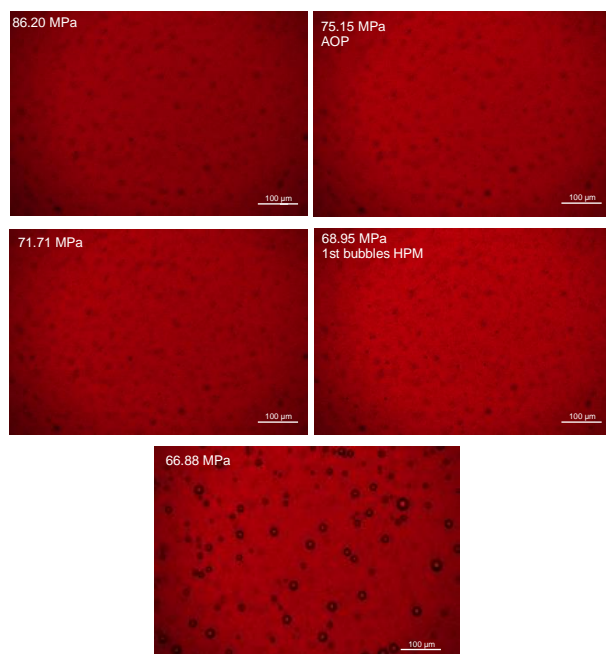


Figure 2.8 Micrographs for 72.5 methane mol% mixture with crude oil during HPM test.

Same behavior was obtained for 75.0 methane mol% system, as presented in Figures 2.9 and 2.10. Nevertheless, phase transition event was more evident, for HPM test, and for SDS analysis. Figure 2.9 depicts a sharp increase in HPM particles count. Once again, SDS NIR transmittance is in accordance with HPM results, i.e., SDS signal

decrease at the same pressure where phase transition was detected by HPM test. Figure 2.10 shows that this phase is characterized by form a fine particulate dispersed phase with no fractal aggregates despite their higher particles count. No growing effects were observed, even reducing the pressure 8 MPa below phase appearance onset. Additionally, it was observed that when near saturation pressure was reached, there is a decreasing in dispersed phase count.

The non-typical morphology observed for this disperse phase, compared to classical asphaltene microscopy results, where big fractal aggregates are formed, could be associated to (i) incipient heavy phase destabilization is attained, (ii) crude oil presents high solvency over heavy compounds (high asphaltene stability), or (iii) the insolubility is not a classical asphaltenic precipitation. From these criteria, the only readily assessed is the crude oil stability.

Highly dispersed asphaltenic phase has been observed for stable crude oils with no problems of asphaltene precipitations (ABUTAQIYA et al., 2019a; MOHAMMADI et al., 2015). The crude stability could be verified using models that consider crude oil composition, based in SARA fractionation (GUZMÁN et al., 2017; KUMAR; VOOLAPALLI; UPADHYAYULA, 2018; YEN; YIN; ASOMANING, 2001). It has been reported that combined Sepúlveda's criterions, i.e., Quantitative-Qualitative analysis (QQA), and Stability Cross Plot (SCP), results in better prediction of asphaltene stability for crude oils. When QQA and SCP method was applied, based on SARA composition of the used crude oil presented in Table 2.1, stable asphaltene were predicted by both methods.

Then, crude oil properties and the resulted asphaltene stability, could be related with the observed fine dispersion, low aggregation and fast dissolution of the particulate observed by the HPM. However, there is no possible to conclude with these results that the formed phase is a fine asphaltenic solid dispersion, or it is other type of phase equilibria. For that reason, and to better understand these atypical results, more tests have been done for the system with 75.0 methane mol%.

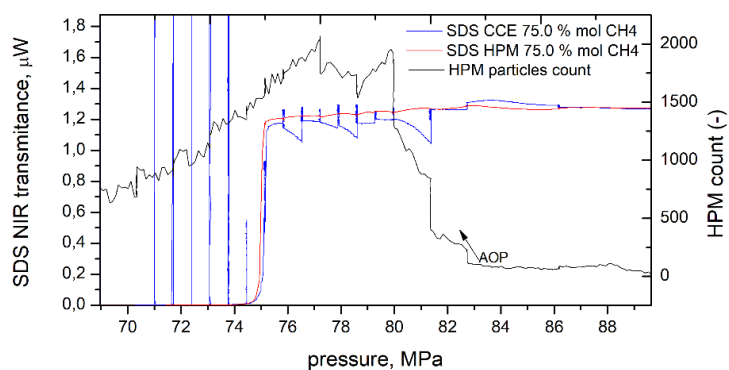


Figure 2.9 NIR transmittance and HPM particle count for 75.0 methane mol% mixture with crude oil during HPM test.

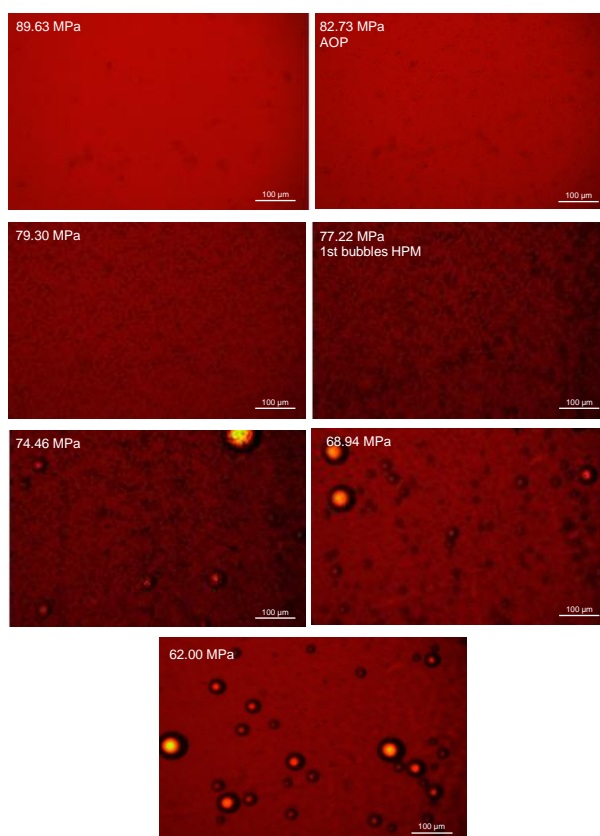


Figure 2.10. Micrographs for 75.0 methane mol% mixture with crude oil during HPM test.

Firstly, the phase heterogeneity redissolution was evaluated. Precisely, system was depressurized until AOP, then, after the phase is formed, system is compressed until monophasic condition. Results of this test is showed in Figure 2.11. This figure presents the variation of SDS signal when system is depressurized to the AOP from the monophasic condition, and compared with the SDS response when compressed. During

the expansion, SDS signal increases due to the reduction in system density until the AOP was reached and the signal sharply decrease by phase formation light scattering. After 5 minutes, a micrograph was taken and it shows a fine dispersion, as described previously.

After that, the system was repressurized until initial monophasic condition. During this compression, it was observed a decreasing in SDS signal that could be related to the increasing on the system density, until the monophasic pressure was reached. At this point, SDS signal recovers almost the original NIR transmittance, i.e., $1.044 \mu\text{W}$ vs $1.056 \mu\text{W}$ at the beginning of the test almost instantaneously. This small difference could be caused by some fractions that require more time to dissolve. At the same time, with less than 5 minutes of equilibration, no asphaltenes were detected by HPM as one can note in the Figure 2.11.

Redissolution of the dispersed phase appears to be achieved with no kinetic restrictions. Although reports about slow redissolution of asphaltenes (CHAISSONTORNYOTIN; BINGHAM; HOEPFNER, 2017; HAMMAMI et al., 2000; MOHAMMADI et al., 2015), the observed asphaltenes behavior support a thermodynamic phase transition with specific dependence of system states variables. It is important to mention that the used techniques do not allow to conclude about the type of phase transition, and furthers analysis need to be done to verify the phase composition, quantity, and phase properties (polarity, density, viscosity). However, it is evident that addition of methane to Pre-Salt fluids can induce to atypical phase separations, detected by conventional PVT techniques.

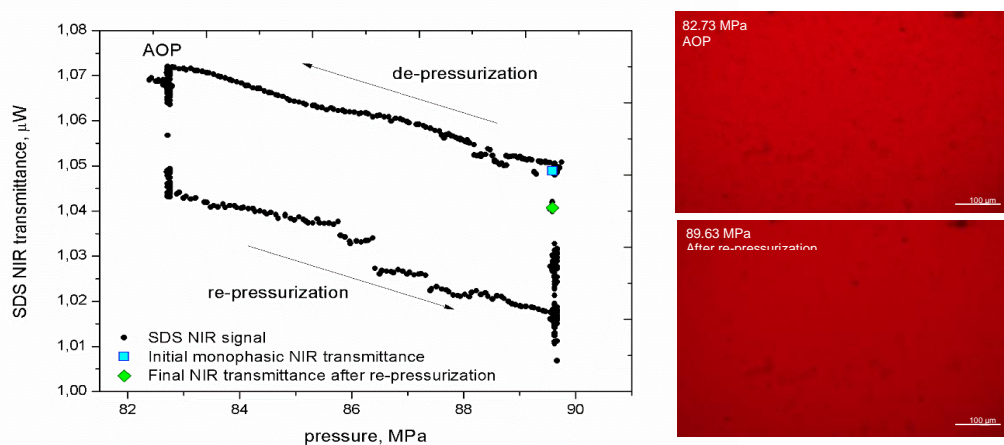


Figure 2.11 SDS variation during AOP-monophasic pressurization test and micrographs for from pressures above the AOP to monophasic condition, for 75.0 methane mol% mixture with crude oil.

The high phase dispersity limits the individual sampling of the two observed phases. However, the size of the observed dispersion is at least bigger than $1\ \mu\text{m}$ (minimal HPM detection size). For that reason, it is reasonable to think that the dispersed phase, if solid, could be separated by using a micrometric mesh filter. Then, fluid was filtered at isobaric and isothermal conditions, at 5 MPa below the AOP. Used filter has a porosity of $0.5\ \mu\text{m}$, then it can retain any non-extrudable solid bigger than this size. Figure 2.12 (A) present the filtration element after passing 50 mL of the heterogeneous sample through. No solid retention was observed, along with no changes of pressure drop in filter. The filtration was totally different when it was performed at temperatures below mixture WAT, with high solid retention, as depicted in Figure 2.12 (B), with a pressure drop that can 10 MPa. After these results, the observed phase insolubility may not be related to typical asphaltenes solids formation.

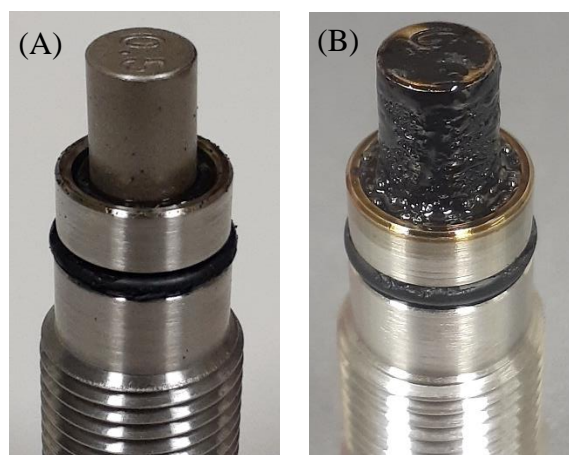


Figure 2.12. Filtration element after isobaric filtration test (A) at pressure below AOP, and (B) at 80 MPa and 313.15 K.

Summarizing, phase transitions (saturation pressure and AOP) for the system crude oil + methane at different methane content were listed in Table 2.3. Also, a pressure against composition diagram is presented in Figure 2.13. From these data, it could be stated that there is a slightly different on saturation pressure obtained by two different methods. Nevertheless, these results are in a good agreement between them. In addition, there is an increasing in saturation pressure with the increasing on methane content, as expected. For

the higher methane content systems (72.5 and 75.0 methane mol%), phase transition was observed with the formation of non-aggregative fine-dispersed phase.

Table 2.3 Saturation pressure and AOP determined for the evaluated system of methane and dead crude oil at reservoir condition (343.15 K).

methane content ± 0.89 , % mol	CCE bubble point pressure \pm 0.62, MPa	AOP ± 0.63 , MPa
65.02	46.5	-
67.51	54.2	-
70.05	60.1	-
72.51	66.3	75.2
75.00	74.8	82.7

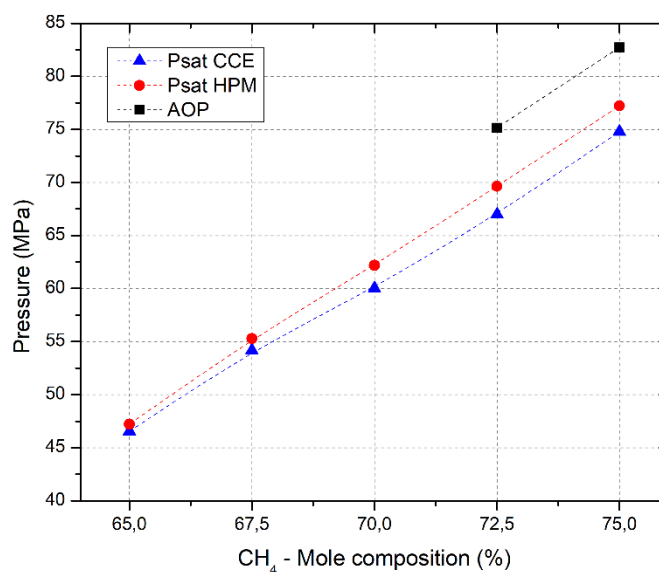


Figure 2.13. *P*-composition diagram for methane and crude oil mixtures at reservoir conditions (343.15 K). Phase transitions uncertainties within 0.62 MPa for bubble point pressure and 0.65 MPa for AOP.

2.4. Conclusions

Brazilian Pre-Salt crude oil phase transitions were studied by intermediate of the addition of methane (from 65.0 to 75.0 methane mol%). Pressure-volume curves show a slight phase transition, by increasing methane molar content, along with the increasing of

saturation pressure. For systems with higher methane molar content (72.5 and 75.0 methane mol %) a phase transition was detected by CCE test and HPM analysis. CCE test shows an SDS NIR transmittance variation during phase transition that could be normally associate with asphaltenes. This phase is characterized as a fine non-aggregative dispersion, with no fractal geometry. Asphaltenes solubility test reveals that there is a dissolution phenomenon of these particulate phase, with no hysteresis in NIR transmittances during depletion and compression cycling. This behavior could indicate a pure thermodynamic phase transition, with diminutive kinetic restriction for phase dissolution. Additionally, dispersed phase separation by filtration was unsuccessful, that could suggest that the formed phase is not a typical solid asphaltenic phase. The high dispersity observed for the second phase avoided its individual sampling for chemical analysis. To promote the dispersed phase coalescence, it could be tested the effect of surfactants or interfacial active compounds that could promote the phase separation.

3 CHAPTER III: MEASUREMENT OF FLUID PHASE EQUILIBRIA FOR HIGH GAS RATIO MIXTURES OF CARBON DIOXIDE, METHANE, AND BRAZILIAN PRE-SALT CRUDE OIL

Results published in: *Measurement of Fluid Phase Equilibria for High Gas Ratio Mixtures of Carbon Dioxide, Methane, And Brazilian Pre-Salt Crude Oil*, Journal of Chemical and Engineering Data, <https://doi.org/10.1021/acs.jced.0c00988>

3.1. Introduction

Brazilian Pre-Salt Reservoir fluids are particularly known by their high gas ratio and high carbon dioxide content. Carbon dioxide can constitute more than 30.0 mol% of produced of Pre-Salt fluids, and more than 50.0 mol% of produced gas (DA COSTA FRAGA et al., 2015). Physicochemical properties of CO₂, as their high critical conditions, can induce complex multiphasic phase behavior in reservoir fluids. In chapter I, several examples are presented where LLVE is a common feature for CO₂ + crude oil mixtures, specially at low temperature and pressures around the critical pressure of CO₂. Additionally, CO₂ can also affect the solvency of the crude oil mixture towards asphaltenic fractions. Carbon dioxide can act as a precipitant or enhance the solubility of heavy crude oil fractions, depending added quantity, temperature, and crude oil characteristics (GONZALEZ et al., 2008b).

In the past chapter, phase behavior of Pre-Salt crude oil and pure methane mixtures was investigated, aiming to better understand the complex fluid phase equilibria observed in the synthetic mixture. Despite the high flocculation capacity of methane, no typical asphaltic phase was observed. Also, limitations on methane content were attained by the high recombination pressure of the mixtures with crude oil. Addition of CO₂ to the mixtures can increase the compositional span of gas addition for the synthetic crude oil + gas mixtures. Accordingly, gas composition and gas addition effect can be studied by using CO₂ in the recombination gas.

For that reason, in this chapter a new experimental dataset of a low asphaltene Brazilian pre-salt crude oil + carbon dioxide + methane mixtures were studied to evaluate phase behavior at reservoir conditions for six different compositions, by focusing on phase insolubility characteristics, as morphology, and dissolution, along with compressed-fluid behavior at pressures higher than saturation pressure.

3.2. Materials and Methods

Phase behavior of CO₂ + CH₄ + crude oil mixtures were studied. Same crude oil than chapter II was used. It is important to stress that Pre-Salt reservoir fluids are characterized by their high gas-oil ratio, and by their associated gas mainly composed of methane and carbon dioxide, with minor proportion of other light-ends compounds. Specifically, this crude oil presented originally a composition of 8.48 CO₂ mol % and 50.59 methane mol %. Table 3.1 shows experimental composition of the synthetic mixtures, along with the volumetric ratio of total gas mixed with oil. A constant mass proportion for gas to oil ratio of 25:75 (w/w) was fixed for all systems, with methane content from 0 wt% for RC1 to 62.5 wt% for RC6 mixture.

Table 3.1. Experimental carbon dioxide (CO₂) and methane (CH₄) content for crude oil and gas mixtures, and gas-oil volume ratio ^a.

System	RC1	RC2	RC3	RC4	RC5	RC6
CO ₂ content in gas / wt %	100.0	74.9	62.4	49.9	43.6	37.5
CH ₄ content in gas / wt %	0.0	25.1	37.6	50.1	56.4	62.5
CO ₂ content in gas / mol %	100.0	52.1	37.6	26.6	22.0	17.9
Crude oil / wt %	74.5	75.1	75.0	75.0	74.9	74.9
Gas-oil ratio / m ³ /m ³	154.6	216.2	250.2	282.4	299.2	315.3
Gas mol content / mol %	66.0	73.1	75.8	78.0	78.9	79.8

^a Combined uncertainty for composition $u_c(x_i) = 0.1$ wt%, or 0.89 mol %.

3.2.1. Crude oil and gas mixtures preparation and phase behavior analysis procedure

Systems preparation was made as described in chapter II. Briefly, calculated volumes for gas and crude oil were measured and injected to the PVT cell by using a D Series Teledyne Isco syringe pumps (volume accuracy of 0.01 cm³). Crude oil was firstly charged in a Teledyne Isco 100DM syringe pump and equilibrated at 40.0 °C and 689.5 KPa (100 psig). Sistem adaptation was depicted in Figure 3.1.

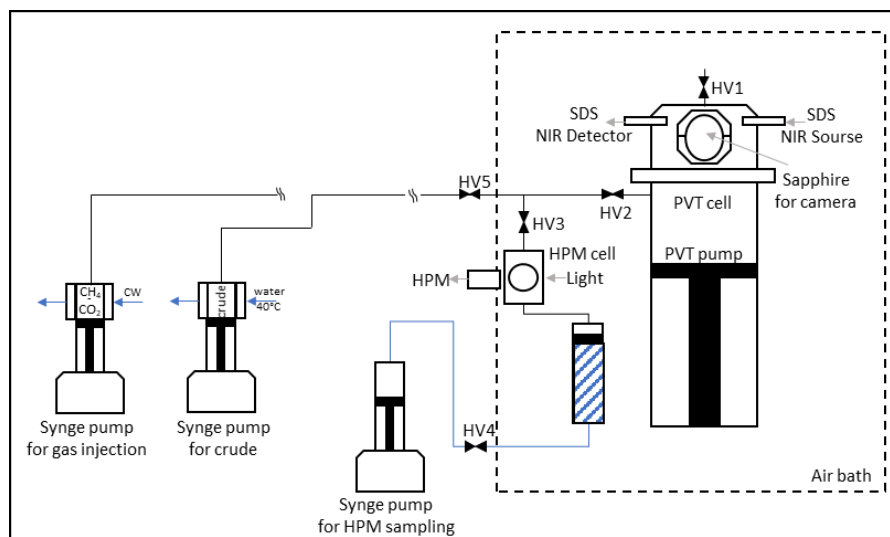


Figure 3.1. Schematic diagram of PVT, HPM and sample injection ensemble.

For phase behavior analysis, same recombination, CCE, and HPM test were made than described in chapter II. From volumetric data during CCE, PV diagrams were constructed and saturation pressure was identified by the interception of two linear fits, one in the incompressible region at high pressures and a second one fit after the visual observation of the first bubbles in the PVT-cell head windows (AGRAWAL et al., 2012; JOHNSTON et al., 2017). NIR-SDS system helps to detect density variations and the occurrence of phase transitions by a sharply change of the transmitted power. Primary phase insolubility detection and verification of saturation pressure was obtained with this technique.

After CCE test, system was recompressed and homogenized during 12 h. Then, HPM tests were performed. NIR transmittance was measured directly to the PVT-cell and it was compared with the CCE equilibrium steps measurements. NIR transmittance and HPM observations will be integrated to the CCE results to better describe phase transitions for all the prepared crude oil and gas mixtures. Special details were made to near saturation pressure, to evaluate redissolution of any dispersed phase at bubble point pressure.

3.3. Results and discussions

From data described in Table 3.1, it could be observed that gas volume fraction of the system rises as the methane/CO₂ proportion increase, as expected. Our database was splitted in two groups, as follows: low gas volume ratio and high gas volume ratio systems, with a referential of 250 m³/m³.

3.3.1. Low gas volume fraction systems

Two cases were evaluated for fluids with gas-oil ratio below 250 m³/m³ (RC1 and RC2). RC1 is constituted only for CO₂ and represents a typical black oil PV behavior, i.e., saturation pressure is easily identified from the sharp break in the PV curve slope. PV curve from CCE analysis and SDS measurements were shown in Figure 3.2.

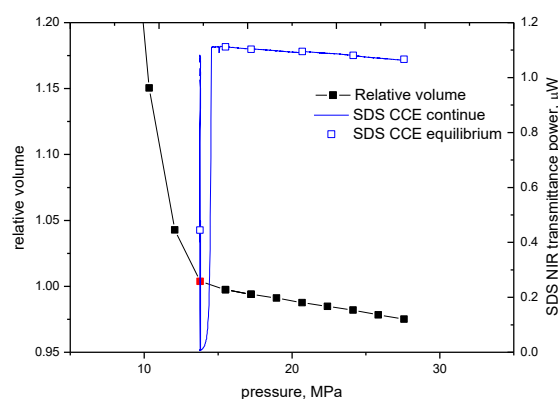


Figure 3.2. Relative volume, saturation pressure (red marked) and NIR transmittance from CCE test for the RC1 system (66.0% mol gas, 100.0 mol% CO₂ content in gas).

Figure 3.3 shows results for HPM test for RC1 (66.0% mol gas, 100.0 mol% CO₂ content in gas). It could be seen that there is no detection of asphaltenes precipitation from the micrographs. This result can be confirmed by a slight monotonal increase in SDS signal during depletion, caused by fluid density decreases. When saturation pressure was achieved, the SDS signal drops (red line) to zero by diffraction on formed bubbles.

As expected, a minimum gas quantity in the crude oil mixture is required to promote asphaltene destabilization during depletion. For this first system tested, a molar ratio of 66.0 CO₂ mol% was obtained. This same molar gas composition was tested in the past chapter. Similarly, no asphaltene precipitation or phase separation was observed. It is important to mention that CO₂ is considered to have less influence on asphaltene

precipitation than methane, related to their higher solubility parameter (GONZALEZ et al., 2005).

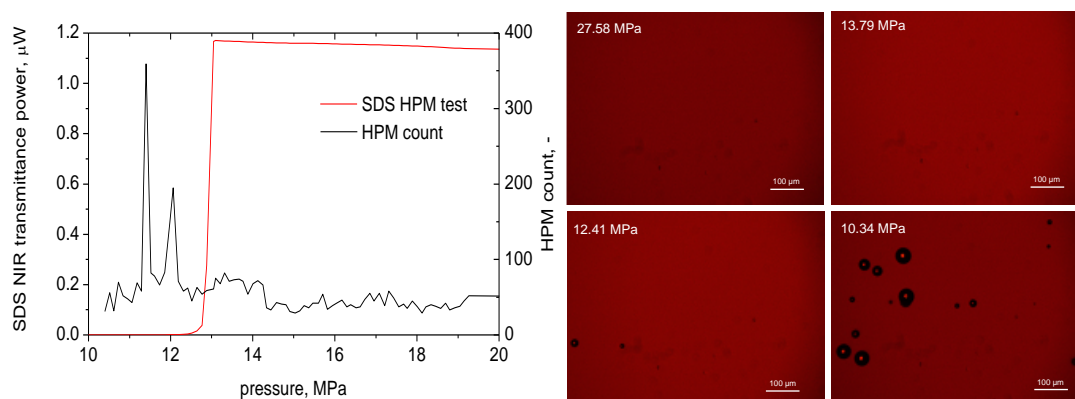


Figure 3.3. Micrographs, particles count and SDS signal for RC1 system (66.0% mol gas, 100.0 mol% CO₂ content in gas).

For RC2 (73.1% mol gas, 52.1 mol% CO₂ content in gas) methane notably affect saturation pressure, increasing from 12.3 to 40.6 MPa, by comparison to RC1, as shown in Figure 3.4. When compared to RC1, RC2 PV plot presents a continuous shape with no sharp PV slope change. This result is expected for mixtures of medium crude oil with high gas content. For this reason, it should be employed two different techniques to confirm saturation pressure, as follows: (i) visual identification of gas phase in the cell content from sapphire windows, and (ii) NIR transmittance measurements. It is important to point out that at 41.3 MPa, few KPa above bubble point pressure, a small change on SDS signal is observed. At this pressure, the equilibrium measurement of the SDS decreases and reach a plateau. This plateau and the decreasing in the SDS signal could be an indicative of the presence of asphaltenes, that have been also confirmed by HPM.

During the HPM test it was verified a phase immiscibility formation just above the bubble point pressure, as one can note in Figure 3.5. At the same time, the SDS signal showed a slight decrease in the transmitted power due to a phase heterogeneity detection. After that, it falls to zero in the saturation pressure.

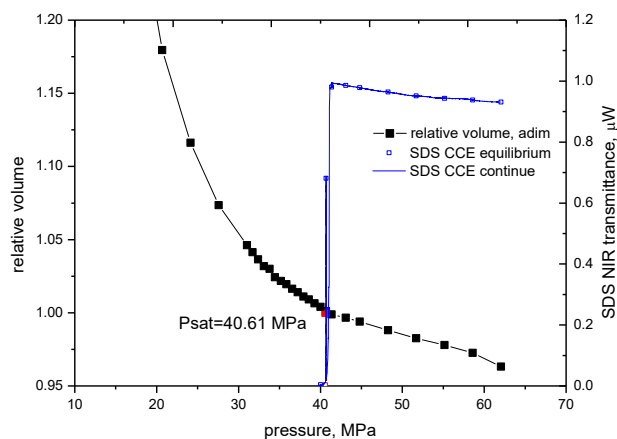


Figure 3.4. Relative volume, saturation pressure (red marked) and NIR transmittance during CCE test for the RC2 system (73.1% mol gas, 52.1 mol% CO₂ content in gas).

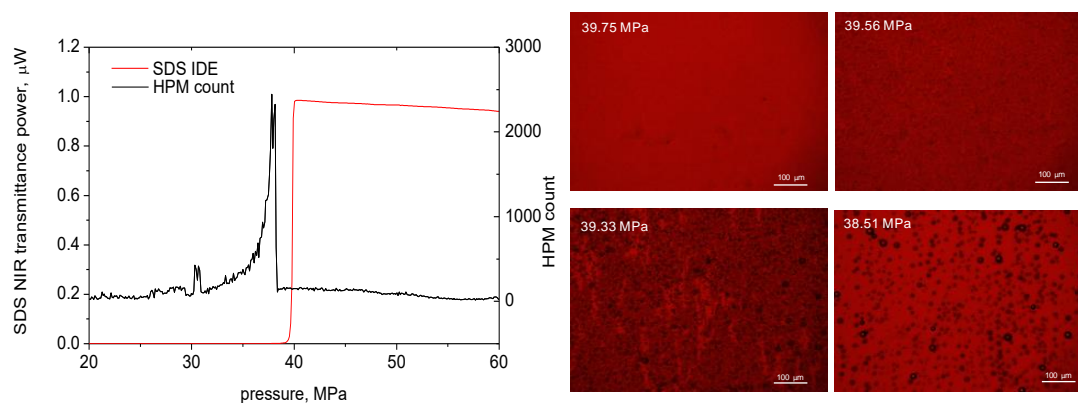


Figure 3.5. Micrographs, particles count and SDS signal for RC2 system (73.1% mol gas, 52.1 mol% CO₂ content in gas).

The addition of methane could induce the formation of an insoluble phase a few kPa above the bubble point pressure. This phase seems to appear as a fine particles dispersion and it was noted that before gas complete release below saturation pressure, the phase dissolves immediately in oil phase. For stable crude oils, fine and powdery asphaltenes dispersion can be observed (JOSHI et al., 2001; MOHAMMADI et al., 2015, 2016). Especially for pressures near their AOP, powdery and no sticking material asphaltene formation is favored, with also rapid redissolution (JOSHI et al., 2001).

It is worth noting that this system has a total gas molar content of 73.0 mol%, divided in 38.0 mol% of CO₂ and 35.0 mol% of methane. From chapter II results, a similar phase heterogeneity was observed when this crude oil was mixture with pure methane at 72.5 mol%. Then, even with a minor methane content, RC2 system starts to present a

phase insolubility that could be related to the total molar gas content added to the crude oil. Also, phase transitions, i.e. bubble point pressure and insolubility onset pressure, are observed at lower pressures when compared to pure methane mixture. This result is expected because of solubility contribution of CO₂ addition.

A similar system has been studied by using full observation NIR PVT for pre-salt crude oils + separator gas mixtures (DARIDON et al., 2020). At a condition of 78.0 mol % of gas, a phase separation was detected and associated to LLE. From our results, a phase immiscibility was obtained even at lower gas addition when only methane and CO₂ was mixed, that could be associated to the lack of light-ends in the synthetic mixture.

3.3.2. *High gas volume fraction systems*

As mentioned previously, here high gas volume fraction fluids are defined as mixtures presenting a gas-oil volume ratio higher than 250 (m³/m³), that is the case studies of fluids RC3 to RC6 (Table 4). Figure 6 depicts PV diagrams for mixtures RC3 to RC6, together with the SDS signal during depletion and equilibrium steps. From these plots, it can be stated that all samples present a similar shape of pressure-volume (PV) curve. Moreover, saturation pressure increases as methane composition increases, as expected.

Also, from Figure 3.6, it could be observed that NIR measurements during depletion show a more evident phase transitions at higher pressures than the bubble point pressure. Generally, NIR transmittance signal decays are associated with asphaltene onset pressure (AOP), at pressures higher than the bubble point pressure. As the methane/CO₂ ratio increases, this NIR signal reduction occurs at higher pressures. NIR transmittance signal difference between equilibration steps (red dots) and continuous measurements (blue line) is due to cell stirring and equilibration time. Possible phases segregation in the PVT cell during the equilibration time could result in an increased NIR transmittance signal in each equilibrium step, also observed for mixtures of crude oil and pure methane.

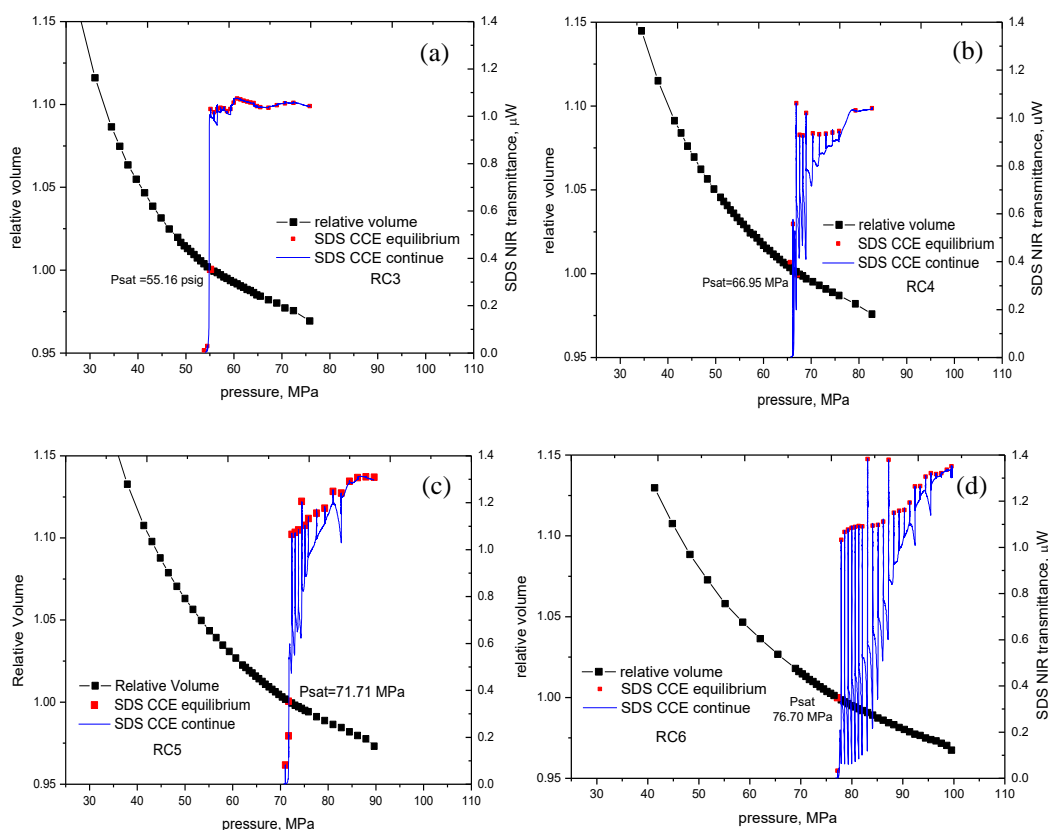


Figure 3.6. Relative volume, saturation pressure (red marked) and NIR transmittance (continue and equilibrium steps) during CCE test for (a) RC3 (75.8 mol% gas, 37.6 mol% CO₂ content in gas); (b) RC4 (78.0 mol% gas, 26.6 wt% CO₂ content in gas); (c) RC5 (78.9 mol% gas, 22.0 mol% CO₂ content in gas); and (d) RC6 (79.8 wt% gas, 17.9 mol% CO₂ content in gas) systems.

One can note in Figure 3.6 that NIR transmittance variation becomes prominent from the system with higher methane ratio. For instance, as methane mass content on the gas mixtures is higher than 50.0 mol% from RC4 to RC6 systems. Respectively, asphaltene onset pressure varies from 62.0 MPa to 86.2 MPa for the RC3 to RC5 systems. For RC6, it can be stressed that NIR transmittance signal drops from near initial pressure test. Correspondingly, these systems have a total gas content between 75.8 and 79.0 mol%, molar compositions that were not possible to study with pure methane due to their high recombination pressure, above 90 MPa. Therefore, it can be noted that CO₂ physicochemical properties allowed the solubilization of more gas in crude oil at lower pressures. Also, phase transitions were detected at lower pressures compared to pure

methane systems. To verify phases characteristics, fluid inspection was made during the HPM tests.

Figure 3.7 shows the HPM particles count and the SDS transmitted power during depletion for systems RC3 to RC6. Simultaneously, the SDS signal falls for all tests when the HPM count starts to increase, indicating a dispersed phase formation. To better understand the nature of the phase transitions observed above the bubble point pressure, Figure 3.8 depicts high-pressure micrographs for RC3 to RC6 mixtures. These results emphasize the correlation between the phase heterogeneity and NIR transmittance signal. It could be seen the formation of fine dispersed phase that becomes more evident as the pressure decreases in all systems. From these micrographs, it can be noted that the phase insolubility seems to form small and not fractal aggregates.

Even at high gas fraction, as RC5 and RC6, the dispersed phase does not aggregate to form fractal flocks but remains as a fine dispersion as one can see in Figure 3.8. From these micrographs, particles size distributions were generated during depletion, as depicted in Figure 3.9 and 3.10. It can be noted a minimal particle size grow for both systems. This behavior is not typically reported in literature, normally asphaltenes are morphologically described as fractal solids that aggregates to form bigger flocks, as the pressure is reduced from the AOP (CHAISSOONTORNYOTIN; BINGHAM; HOEPFNER, 2017; MOHAMMADI et al., 2015). For this studied crude oil, no fractal particles aggregation is observed still at high gas volume content. For RC5 and RC6 systems, a wide asphaltene dominated region is observed, their pressure domain – i.e., the difference between AOP and bubble point pressure, goes from 14.5 to 22.9 MPa, respectively. Even at pressure far below the AOP, asphaltenes seems to remain as a disperse and no sticking powder, maybe related to high solubility in crude oil. Moreover, it is interesting to mention that the disperse phase almost totally disappears when bubble point pressure is reached.

These results are similar to previous observations for the phase transitions of same crude oil when mixed with pure methane, also presenting a rapid redissolution of the dispersed phase at higher pressures than the asphaltene onset. As previously commented, CO₂ addition allowed the solubilization of higher quantity of gas in crude oil. However, phase transitions present same morphological characteristics than those observed when pure methane is used as solvent, i.e., a high and fine dispersed phase that no aggregates to form fractal flocks. Even considering pressures of almost 22.9 MPa below the AOP, the phase remains as a fine powdery and no-sticking material. That could suggest a minimal

enrichment of the asphaltenic phase on other classes of heavy oil compounds (JOSHI et al., 2001).

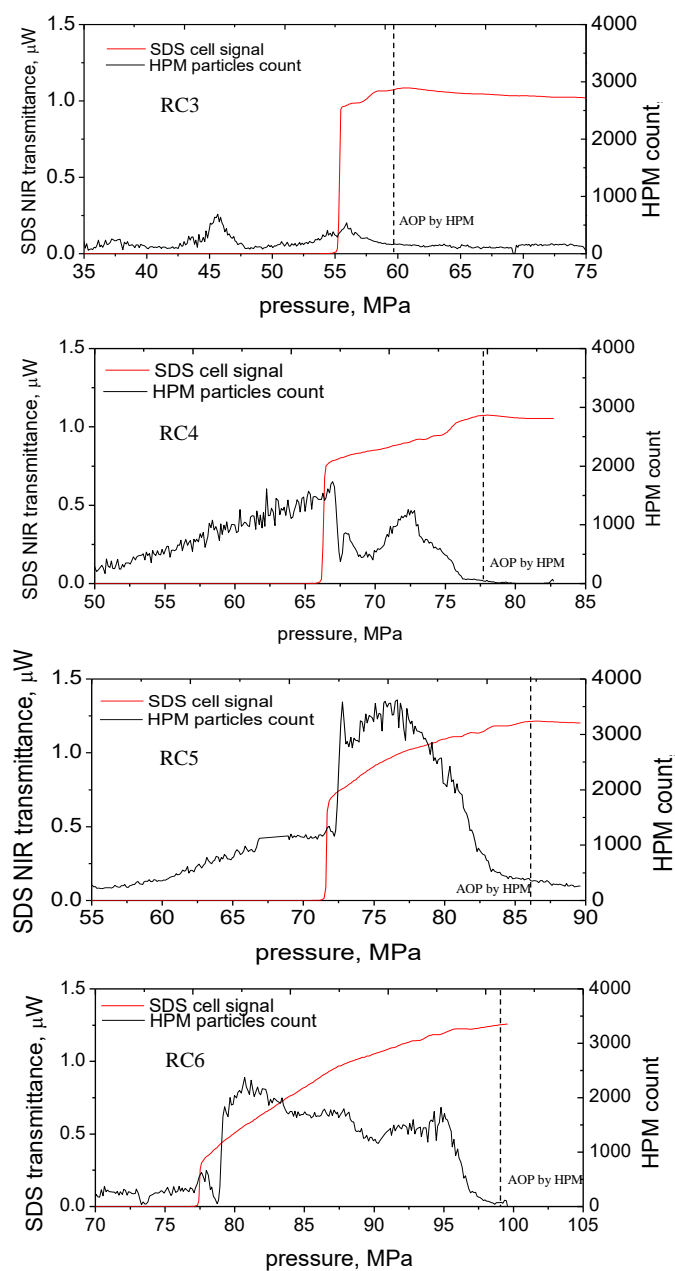


Figure 3.7. Particles count and SDS signal for RC3 (75.8 mol% gas, 37.6 mol% CO_2 content in gas), RC4 (78.0 mol% gas, 26.6 wt% CO_2 content in gas), RC5 (78.9 mol% gas, 22.0 mol% CO_2 content in gas), and RC6 (79.8 wt% gas, 17.9 mol% CO_2 content in gas) systems during HPM test.

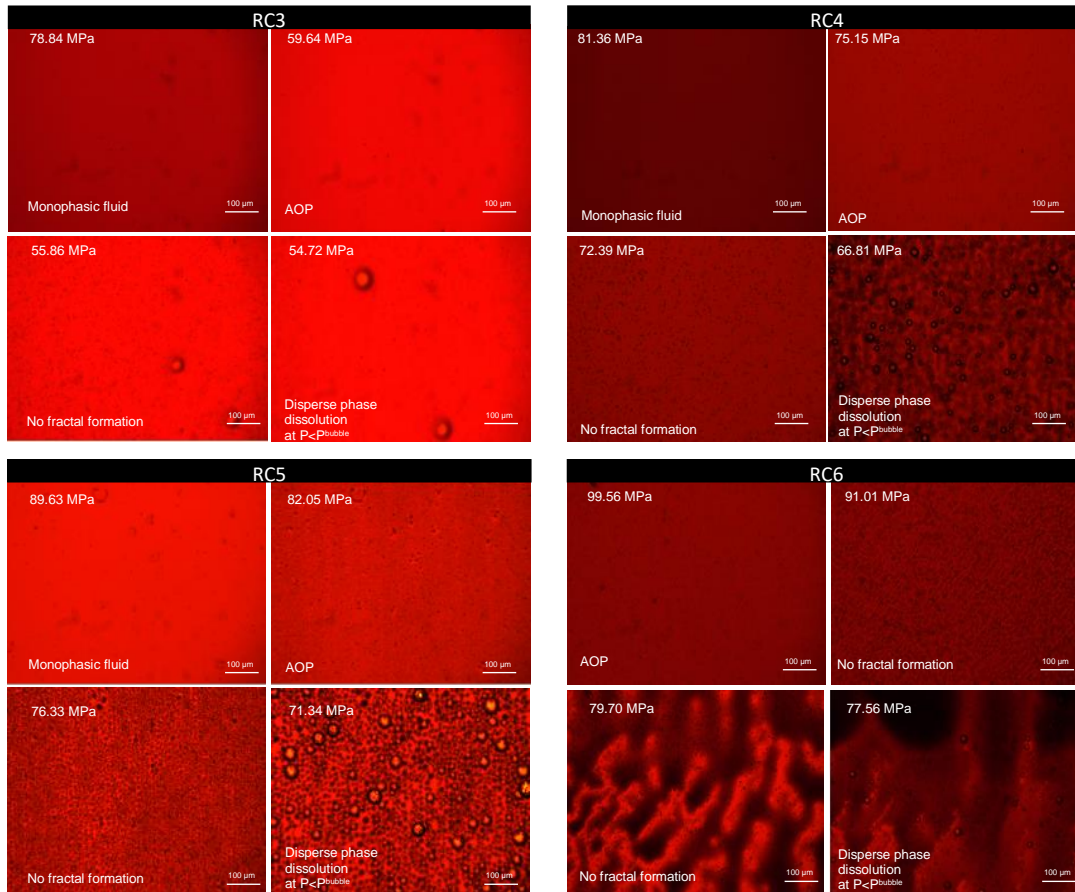


Figure 3.8 Micrographs for RC3 (75.8 mol% gas, 37.6 mol% CO₂ content in gas), RC4 (78.0 mol% gas, 26.6 wt% CO₂ content in gas), RC5 (78.9 mol% gas, 22.0 mol% CO₂ content in gas), and RC6 (79.8 wt% gas, 17.9 mol% CO₂ content in gas) systems during HPM depletion test.

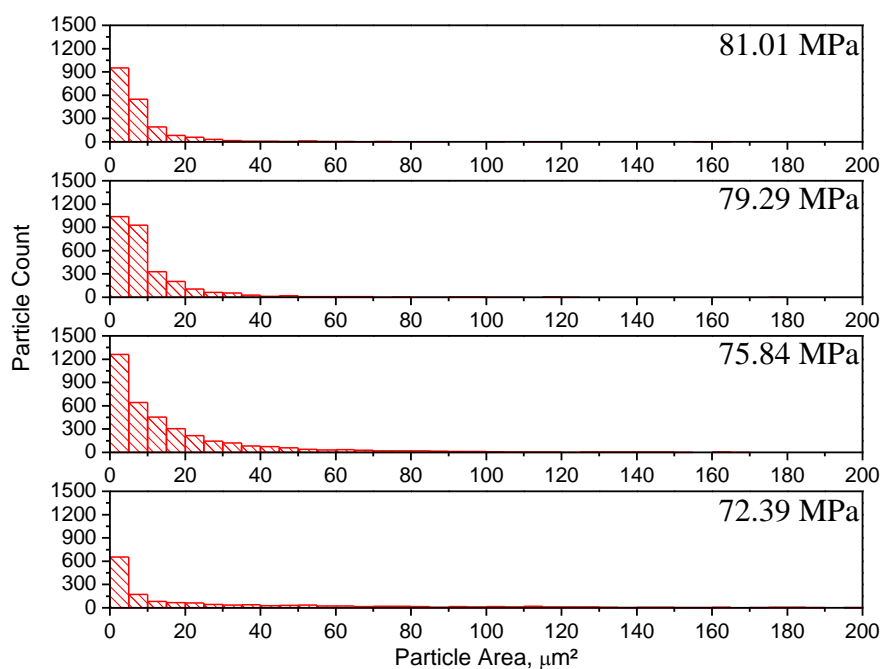


Figure 3.9 Particle size distribution during depletion for RC5 system (78.9 mol% gas, 22.0 mol% CO_2 content in gas) obtained by HPM.

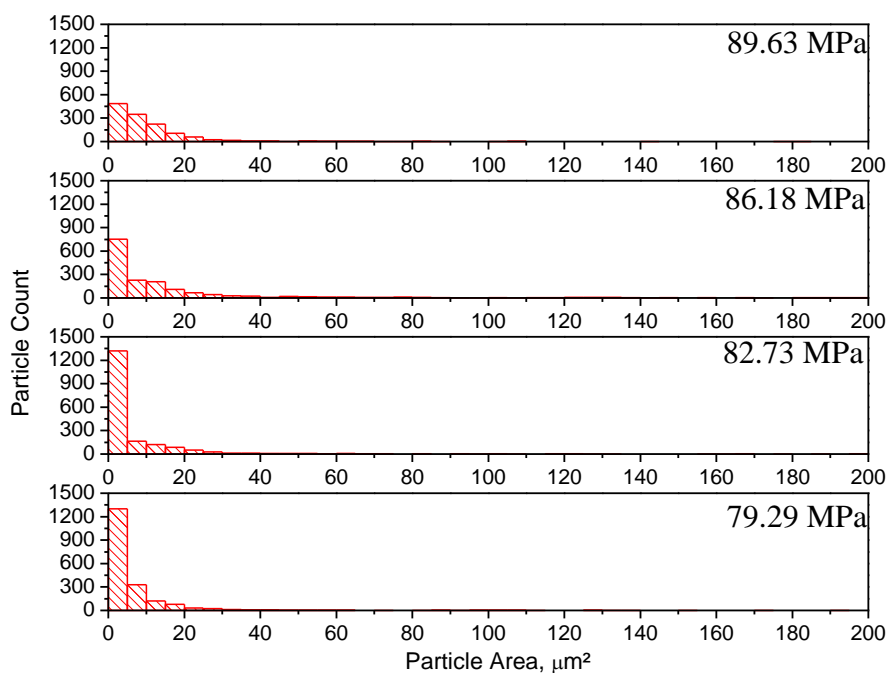


Figure 3.10 Particle size distribution during depletion for RC6 system (79.8 wt% gas, 17.9 mol% CO_2 content in gas) obtained by HPM.

From the used techniques in this chapter, it was not possible conclude other phase transition than asphaltene precipitation, as usually made in the literature (MOHAMMADI et al., 2015). The high dispersion of the detected insolubility, together with its no evident phase segregation, avoided its sampling for chemical characterization. However, it could not be discarded other types of phase transition, like LL transition that we also reported for crude oil + methane + CO₂ systems (AL GHAFRI; MAITLAND; TRUSLER, 2014; CARDOSO et al., 2014; DARIDON et al., 2020).

This LLE has been found in pre-salt reservoirs fluids at high temperatures and pressures, presenting low density differences that difficult their separation (DARIDON et al., 2020). Additionally, the LLE boundaries determination can be limited when used indirect phase transition detection techniques, i.e., techniques that measure fluid properties changes to determine phase transitions. These techniques include NIR laser-SDS, quartz crystal resonator, HPM, among others. However it has been reported that the atypical dispersed phase has a rapid redissolution at their phase boundaries (CARDOSO et al., 2014), specially noted in this work at the LV transition point.

From the literature, it is well known that asphaltenes precipitation depends on crude oil properties and composition, that could affect their solubility and stability. Aggregates formed during asphaltenes precipitation are expected to present themselves as a large fractal aggregates flocks, characterized by having a slow kinetic of redissolution. Crude oil used to formulate the samples in this chapter has a low asphaltene content. Also, the asphaltenes are classified as stable when evaluated the crude oil SARA composition by using Sepúlveda criterions, and presented a high asphaltene precipitation onset in n-heptane at 100 KPa and 25 °C, as stated in Table 2. Possibly, for these reasons, no typical asphaltene dispersions were observed even reaching elevated gas content as 79.8 mol% for RC6 system.

A general overview of all crude oil and gas mixtures studied in this chapter is presented in Figures 3.11, experimental phase transition data is presented in Table 3.2. As expected, saturation pressure increases as the gas volume fraction and methane/CO₂ ratio increase. From Figure 3.11, it could be seen that for medium to high gas ratio samples there is a phase transition at pressures above bubble point pressure. This phase transition is associate to a heavy asphaltic phase formation despite their non-conventional behavior, characterized by fine particles dispersion and no fractal morphology. Additionally, their formation was favored at high CH₄/CO₂ ratio, as observed in Figure 3.10. However, systems with CO₂ presented lower asphaltene precipitation pressures than

previous results in chapter II for crude oil mixtures with only methane at same gas fraction. Specifically, for 75.0 mol% methane mixtures, asphaltene onset was reported at 82.7 MPa, being at 7.9 MPa above the bubble point pressure. At a similar total gas molar content for RC3 system (75.8 gas mol%, 250.2 gas m³/m³ gas fraction, 1.65 CH₄/CO₂ molar ratio), AOP was 59.6 MPa, at 6.4 MPa above bubble point pressure. Accordingly, CO₂ contribution allowed the reduction of asphaltene precipitation pressure and their existence region, along with solubilization of higher gas amount in crude oil.

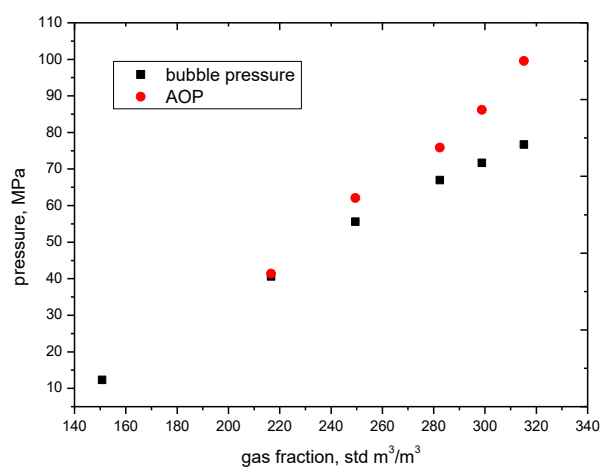


Figure 3.11. Bubble point pressure and AOP diagram as function of the GOR for crude oil and gas mixtures at reservoir conditions (343.15 K).

Table 3.2. Bubble point pressure P^{bubble} and AOP for studied systems at 343.15 K^a.

System	P^{bubble} / MPa	AOP / MPa
RC1	12.3	-
RC2	40.6	41.4
RC3	55.6	62.1
RC4	68.1	75.8
RC5	71.7	86.2
RC6	76.7	99.3

^a Combined uncertainty for transitions pressure determination $u_c(P) = 0.68$ MPa.

3.4. Conclusions

Non-conventional asphaltene insolubility was observed for Brazilian pre-salt crude oil mixtures with methane (CH₄) and carbon dioxide (CO₂), at different CH₄/CO₂ ratio. Non-typical fine dispersed phase has been the main characteristics of the samples studied, specially at high gas volumetric fraction. PVT measurements showed a transition from black-oil to near-critical fluid behavior as the gas volume fraction increases. Additionally, the system with higher gas volume fraction present phase transitions events at pressures above the bubble point pressure, determined by intermediate of NIR transmittance signal and HPM measurements, characterized by an atypical fine dispersion with no flocks or fractal aggregates formation. This low aggregation and high dispersity were maintained even at pressures far below the insolubility onset.

4 CHAPTER IV: PHASE BEHAVIOR EVALUATION FOR DIFFERENT PRE-SALT CRUDE OIL MIXTURED WITH METHANE AT HIGH GAS RATIO

Results published in: *Phase Behavior for Crude Oil and Methane Mixtures: Crude Oil Property Comparison*. Energy Fuels 2019. <https://doi.org/10.1021/acs.energyfuels.9b03560>.

4.1. Introduction

Results presented in the previous chapters have showed non-typical transitions for a Brazilian Pre-Salt crude oil when mixed with methane and CO₂, specially at high volumetric ratios. Even at large gas additions, morphological and redissolution characteristics for formed insolubilities are atypical for asphaltene precipitation process. Using these results as basis, it was selected the mixture of the used crude oil and 75.0 mol% of methane as a base case to compare different Brazilian Pre-Salt crude oil samples.

Asphaltene aggregation and phase morphology has been related to crude oil solvency for different reservoir fluids (ABUTAQIYA et al., 2019b; WANG et al., 2017; ZANGANEH et al., 2012; ZANGANEH; DASHTI; AYATOLLAHI, 2015, 2018). Mohammadi et al. has shown that aggregation and kinetics of asphaltene precipitation may depend on crude oil solvency for asphaltene, with smaller asphaltene aggregates for stable oils (MOHAMMADI et al., 2015). For this type of study, combination of high-pressure microscopy, and NIR light scattering are commonly used. Then, asphaltene properties as aggregation behavior, fractal morphology, particles size distribution, and growing rate are assessed, aiming to better understand asphaltene aggregation kinetics on crude oils (JOSHI et al., 2001; MOHAMMADI et al., 2016). However, the microscopic sample has limitation by only analyze a small fluid region and aliquot. Therefore, a combination of analytical techniques is necessary to evaluate the behavior of the overall bulk fluid, especially for small aggregation particles that could be not detected by optical or light scattering techniques.

To better understand complex phase transitions in Pre-Salt reservoir fluids, in this chapter an evaluation of different crude oils and methane mixtures was studied at high methane composition, and compared with the previous low asphaltene system from chapter II and III.

4.2. Material and Methods

A comparison of phase transitions for six Pre-Salt crude oils and methane mixtures were investigated. These mixtures were prepared based on previous results, where complex phase transitions were observed when crude oil was mixed with 75.0 mol% of methane. For comparison, crude oil used in chapter II and III will be named BRO in this chapter. Accordingly, mixtures of different crude oils and 75.0 mol% of methane were prepared, and their phase behavior was studied in a variable volume PVT cell. Two different tests were performed for each composition: a constant composition expansion (CCE) test, and an isothermal expansion for high pressure microscopy (HPM) analysis, detailed described in chapter II. Both tests were made at a referential temperature of 343.15 K.

4.2.1. Crude oils characterization

Six oil samples ranging from a condensate to heavy crude oil were supplied by Petrobras S. A. and Repsol-Sinopec Brasil S. A., here named P1 to P6, from the lighter to the heavier sample, respectively. All the samples were pretreated by heating for 4 hours at 65 °C to dissolve waxes. P1 crude oil was used as received because of their high volatility. Crude oils were characterized in terms of API gravity, SARA (saturates, aromatics, resins and asphaltene) content, wax appearance temperature (WAT), wax content and molar weight. Details of characterization is given elsewhere (ROMERO YANES et al., 2018). Asphaltenes were extracted by using *n*-pentane (nC5), *n*-hexane (nC6), and *n*-heptane (nC7). For P1 to P6 samples, average molecular weight was obtained by cryoscopic depression using benzene as solvent (ALGHANDURI et al., 2010). Stability of asphaltenes for all the crude samples were estimated from SARA composition, by Sepúlveda's Criteria, i.e., Qualitative-Quantitative Analysis (QQA), and Stability Cross Plot (SCP) test (GUZMÁN et al., 2017; KUMAR; VOOLAPALLI; UPADHYAYULA, 2018).

4.2.2. PVT sample preparation and CCE test

Same experimental setup from chapter II is used. However, mass measurement procedure for mixtures preparations was changed. Required mass for crude oil and methane was injected to the PVT cell by using pressurized blind cells, heated in the PVT

oven at 65 °C. The injected mass was measured by weighting the crude oil and gas cells in a Sartorius MSU5203P digital balance, with an accuracy of 0.005 g. Final molar composition was calculated by the estimated average molecular weight of crude oil, and the methane molecular weight, respectively.

After the desired amount of crude oil and gas were injected to the PVT, the cell content was continuously stirred and pressurized with a rate of 415 kPa/min (60 psi/min) until at least 14 MPa above the bubble point. It was kept under stirring, at least, 12 h before the CCE test. Same condition than BRO sample CCE and HPM test was adopted for each sample analysis, through depressurization ramps and equilibrium stages.

Formed phases were also evaluated in terms of dissolution by repressurizing the system from the AOP to the monophasic pressure. Pressurization was made by increasing PVT pressure with the HPM connected, at a rate of 208 kPa/min. NIR transmittance in the PVT cell was compared with the microscopy results during the repressurization.

4.3. Results and Discussion

4.3.1. Crude oils characterization and CCE test results

Crude oil characterization for all samples is presented in Table 4.1 organized by decreasing API gravity. Specifically, the lighter sample P1 consist of a condensate oil with no asphaltenes content. Then, P2 to P4 samples are medium crude oil type samples, asphaltene content does not exceed 1.0 wt%, and API gravity higher than 22°. One can note that BRO, case base used in previous chapter, has an intermediate API gravity between P2 and P3 and a similar asphaltene content than P3 sample. For the heavier crude oils, P5 and P6, asphaltenes content are higher than 2.0 wt% and P5 crude oil presented a notable high content of paraffins, higher than 7 wt%. From SARA composition, all crude oils are classified as stables by their high (resin+aromatic)/saturates ratio. Compositional analysis of crude oil is depicted in Table 4.2.

Table 4.1 Crude oil samples characterization by °API, SARA composition, average molecular weight, WAT and wax content.

crude oil properties	crude oil sample						
	P1	P2	BRO	P3	P4	P5	P6
API gravity, °API	44	31	28	26	25	20	19
average molar weight, kg/kmol	194	199	250	262	300	356	335
saturates ± 1 wt%	84 ^a	71	59	52	52	44	40
aromatic ± 1 wt%	12	15	22	27	25	31	20
resins ± 1 wt%	4	14	18	21	24	23	38
asphaltenes nC7 ± 0.05 wt%	0	0.09	0.68	0.54	0.12	2.69	2.09
asphaltenes nC6 ± 0.05 wt%	0	0.21	1.94	1.10	0.44	5.10	4.51
asphaltenes nC5 ± 0.05 wt%	0	0.67	3.33	1.91	0.90	7.28	6.68
asphaltenes nC7 stability, Sepúlveda criterions	-	stable	stable	stable	stable	stable	stable
WAT, ± 1 °C	18	27	27	25	23	36	29
wax content, wt%	-	3.08	6.2	2.1	7.0	> 7.0	0.42

^a SARA analysis for 65°C+ fraction.

Table 4.2 Compositional analysis of the dead crude oils.

CN	P2		BRO		P3		P4		P5		P6	
	wt %	mol %	wt %	mol %	wt %	mol %	wt %	mol %	wt %	wt %	mol %	mol %
C3	0.08	0.40	0.00	0.00	0.14	0.87	0.01	0.08	0.03	0.27	0.01	0.06
iC4	0.15	0.59	0.01	0.04	0.15	0.72	0.03	0.13	0.04	0.26	0.01	0.08
nC4	0.50	1.97	0.06	0.28	0.55	2.67	0.14	0.70	0.14	0.95	0.06	0.38
iC5	0.00	0.00	0.13	0.53	0.49	1.88	0.00	0.00	0.17	0.88	0.08	0.38
nC5	0.72	2.30	0.27	1.10	0.80	3.11	0.2	0.81	0.25	1.33	0.15	0.73
C6	2.78	7.58	0.95	3.31	1.59	5.30	1.53	5.23	0.64	2.92	0.37	1.57
C7	3.86	9.20	2.15	6.51	2.69	7.85	2.27	6.8	1.31	5.21	0.86	3.21
C8	4.86	10.38	3.09	8.43	3.33	8.70	3.09	8.3	1.78	6.35	1.31	4.41
C9	4.14	7.83	2.90	6.98	2.96	6.83	2.88	6.84	1.67	5.28	1.41	4.21
C10	3.60	6.14	2.58	5.61	2.59	5.40	2.60	5.57	1.52	4.35	1.40	3.76
C11	3.09	4.81	2.47	4.91	2.47	4.70	2.50	4.89	1.51	3.93	1.51	3.71
C12	2.79	3.96	2.35	4.26	2.36	4.09	2.41	4.30	1.46	3.46	1.70	3.81
C13	3.29	4.30	2.68	4.47	2.68	4.28	2.77	4.54	1.70	3.73	2.08	4.28
C14	2.89	3.47	2.41	3.70	2.41	3.55	2.51	3.80	1.61	3.25	2.04	3.87
C15	3.06	3.40	2.55	3.61	2.57	3.48	2.64	3.68	1.71	3.18	2.30	4.03
C16	2.49	2.57	2.09	2.74	2.09	2.64	2.14	2.77	1.47	2.54	2.08	3.39
C17	2.48	2.39	2.04	2.51	2.04	2.41	2.08	2.52	1.51	2.44	1.88	2.86
C18	2.65	2.42	2.23	2.59	2.25	2.51	2.27	2.6	1.68	2.56	2.06	2.95
C19	2.54	2.21	2.10	2.33	2.11	2.24	2.15	2.34	1.63	2.37	2.07	2.84
C20+	54.03	24.08	66.93	36.09	63.72	26.73	65.76	34.09	78.17	44.75	76.63	49.45
C20 MW		513		541		667		544		668		559

Pressure-volume (PV) curves of crude oil mixtures with methane at 75.0 mol% of methane, are presented in Figure 4.1. One can note that lower relative volumes were obtained for the lower density crudes, P1 and P2, as expected. For the medium crude oils, it was obtained similar bubble point pressure around 77.50 MPa, except for P2 crude oil that presented a lower bubble point pressure at 72.35 MPa. Also, lower methane solubility was observed for medium crude oil with higher asphaltenes content, as BRO and P3. Likewise, higher pressures for bubble point were obtained for the heaviest samples, P5 and P6, and higher relative volume due to its elevated density and heavier compounds presence.

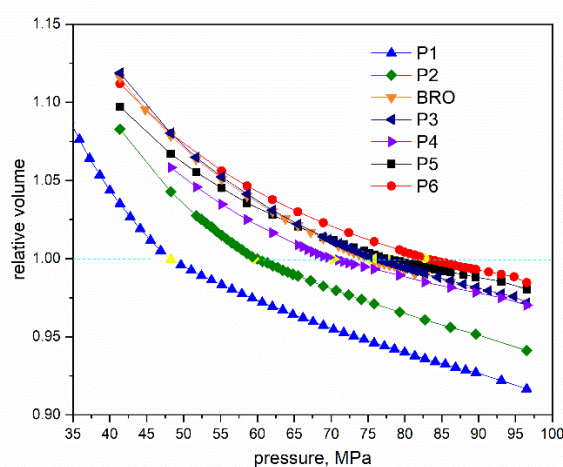


Figure 4.1. Relative volume and saturation pressures (yellow markers) for the different crude oils and methane mixtures during CCE depletions at 343.15 K.

Furthermore, from volumetric information it can be pointed that only the lighter crude oils, P1 and P2 present a markable inflection in the PV curves. The other crude oils presented near-critical behavior, with no PV slope change. Thus, saturation pressure was only detectable visually or by using the NIR transmittance detector. In Figure 4.2 it can be noted the liquid vapor transition observed in the frontal sapphire window of the PVT cell, confirming the bubble point pressures for the near-critical samples. As expected, higher bubble point pressure is observed for heavier crude oils. Among the medium crude oils, the higher

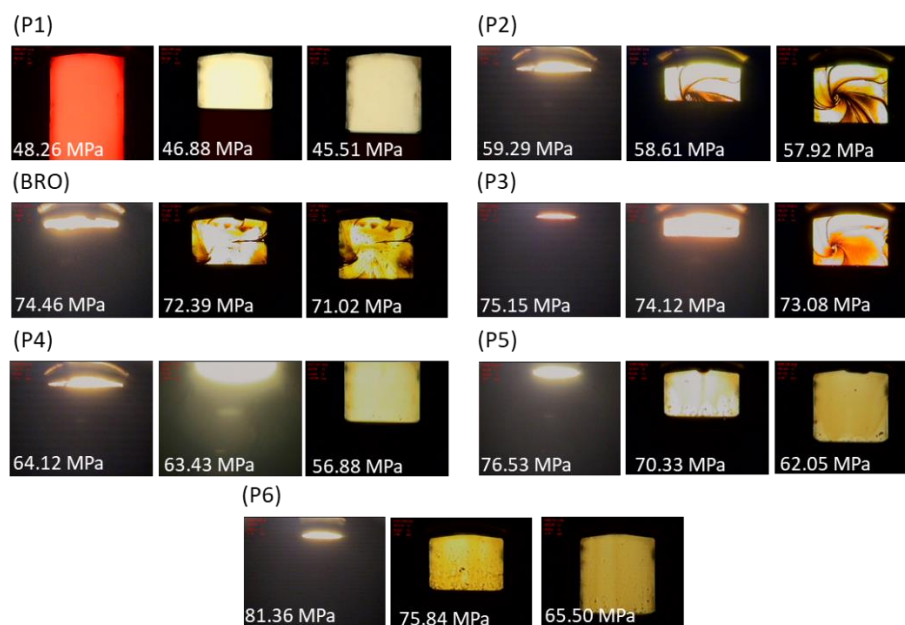


Figure 4.2. Bubble point identification on PVT head visor for the different crude oil and methane mixtures during CCE test.

In Figure 4.3 is presented the NIR transmittance results for crude oil and methane mixtures during CCE depletions. NIR signals were normalized using the initial samples transmittance for a better comparison. Correspondingly, bubble point pressure was identified by a sharp decrease in NIR transmittance. It can be noted that at higher pressures than bubble point, phase transitions, as AOP or other phase insolubility, were identified as a slight decrease in NIR signal. Specifically, BRO crude oil presented this behavior around 82.62 MPa, and similar results were obtained for P2 and P3 crude oil, with a phase transition at 75.84 MPa and 86.18 MPa respectively. Contrary, for P1 and P4 only a monotonical increase in NIR transmittance is observed, with no phase transitions detected above the bubble point pressure. For the heaviest samples, P5 and P6, NIR decreasing were also detected at pressures near the recombination condition, and their response during CCE is difficult to analyze.

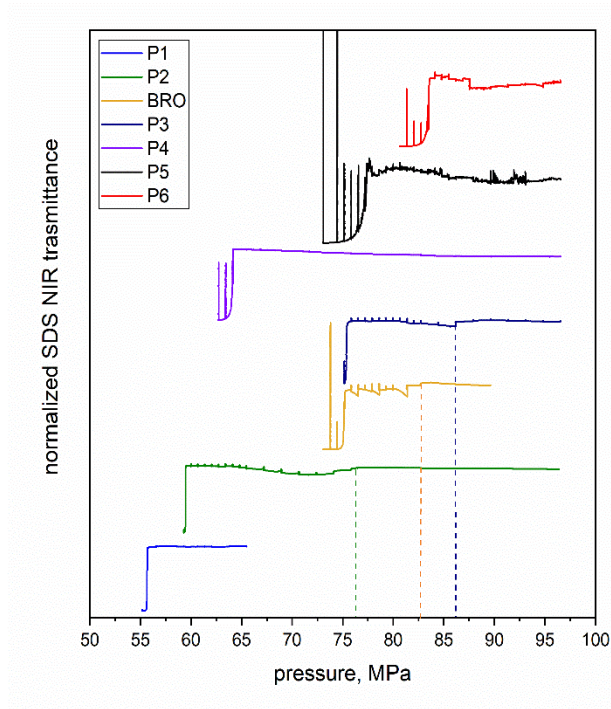


Figure 4.3 NIR transmittance signal during CCE test for the different crude oil and methane mixtures. (Evident phase transitions at pressures above the bubble point for medium oils was marked with dashed lines for better visualization).

4.3.2. Isothermal depressurization HPM results

While specific pressure condition for the phase transitions were established through volumetric and light scattering techniques, a complementary information of phase morphology and redissolution were studied by HPM for all samples.

Figure 4.4 depict the SDS and particles count during the isothermal depressurization HPM for all the crude oil + methane systems. It can be noted that in all the cases, the SDS NIR transmittance is similar during the HPM depletion than the obtained during the CCE test, previously discussed. Moreover, particles count confirms an evolving phase for P2 and P3, comparable with the obtained with BRO, previously identified in CCE by NIR transmittance. Correspondingly, there was not detected particles or phase heterogeneity for P1 and P4, with a constant particle count during all the test. Particularly, for P5 and P6, it was not possible determinate phase transitions by HPM above the bubble point pressure, due to the high samples' opacity. It can be noted also that for these heavy samples, NIR transmittance have a remarkable instability, and it could conduce to erroneous conclusions used by itself. Therefore, filtration or spectrometric analysis are recommended to better study this type of samples.

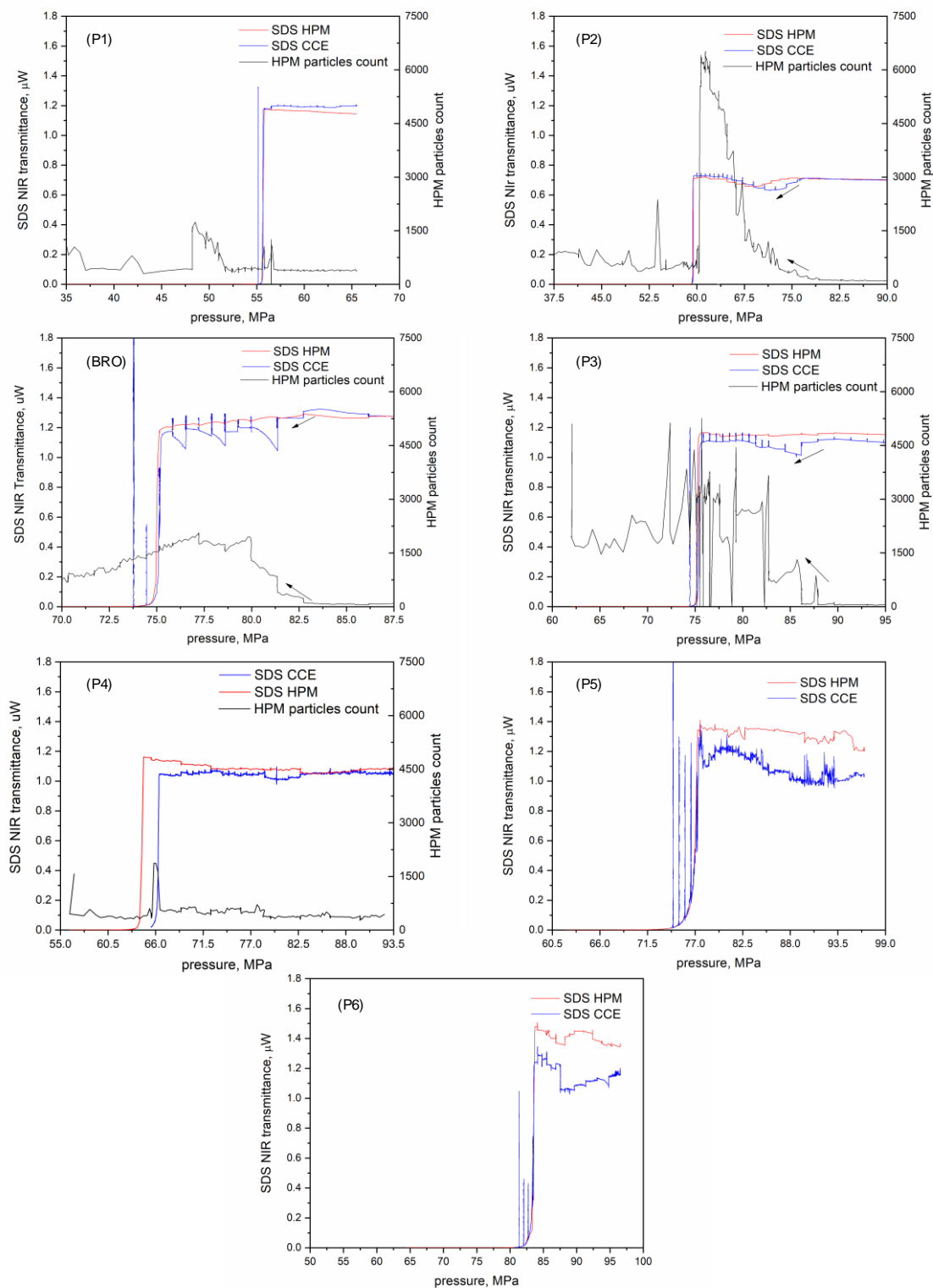


Figure 4.4. NIR transmittance, HPM particle count and micrographs for the different crude oil and methane mixtures during HPM test.

A series of micrographs obtained during the HPM test are present in Figure 4.5. As stated before, a monophasic fluid was observed for P1 and P4 samples during almost

all depletion, until bubble point pressure was observed. However, samples with P3 and BRO oils presented a fine dispersion formation, that occurs around 12 MPa up the vapor evolution. This phase is characterized by his low aggregation and no fractal geometry. For BRO, this behavior was related to the crude oil properties and high asphaltene stability. One can note from Table 4.1, that asphaltene stability is favored by the SARA composition, and the crude oils are classified as stable.

While a similar result in terms of onset pressure was observed for P2 sample, with a phase evolution at 12 MPa above the bubble point pressure, the behavior and characteristics are slightly different. One can note that at the phase appearing onset pressure, a similar dispersion with no major aggregates was observed. However, as the pressure is reduced during depletion, the particles start to grow and apparently the phase adhere to the microscope sapphire windows. This behavior could indicate some phase polarity that allows the interaction with the surface chemical species of the sapphire. Moreover, the most relevant characteristic is the phase stability even at pressures below the bubble point pressure. For P3 and BRO, the heterogeneous phase seems to completely dissolves when gas evolves in the bubble point pressure. Contrarily, the formed phase for P2 remains when gas evolves, possibly indicating some restraint in phase dissolution.

These results could indicate a heavy and stable phase formed during depletion for the mixture with P2 crude oil, despite the low asphaltene content in this sample. Additionally, the light absorbance of the crude oil sample varies while the phase evolves, with also a change in phase morphology from a fine dispersed particulate to a droplet-like material. Similar results have been reported by Abutaqiya et al. (ABUTAQIYA et al., 2019b) and according to the authors, were related with an increase in asphaltene mass deposition during depletion. It is important to mention that this oil has an elevated saturates to resin ratio, and then the heavy formed phase can present different characteristics than the other crude oils.

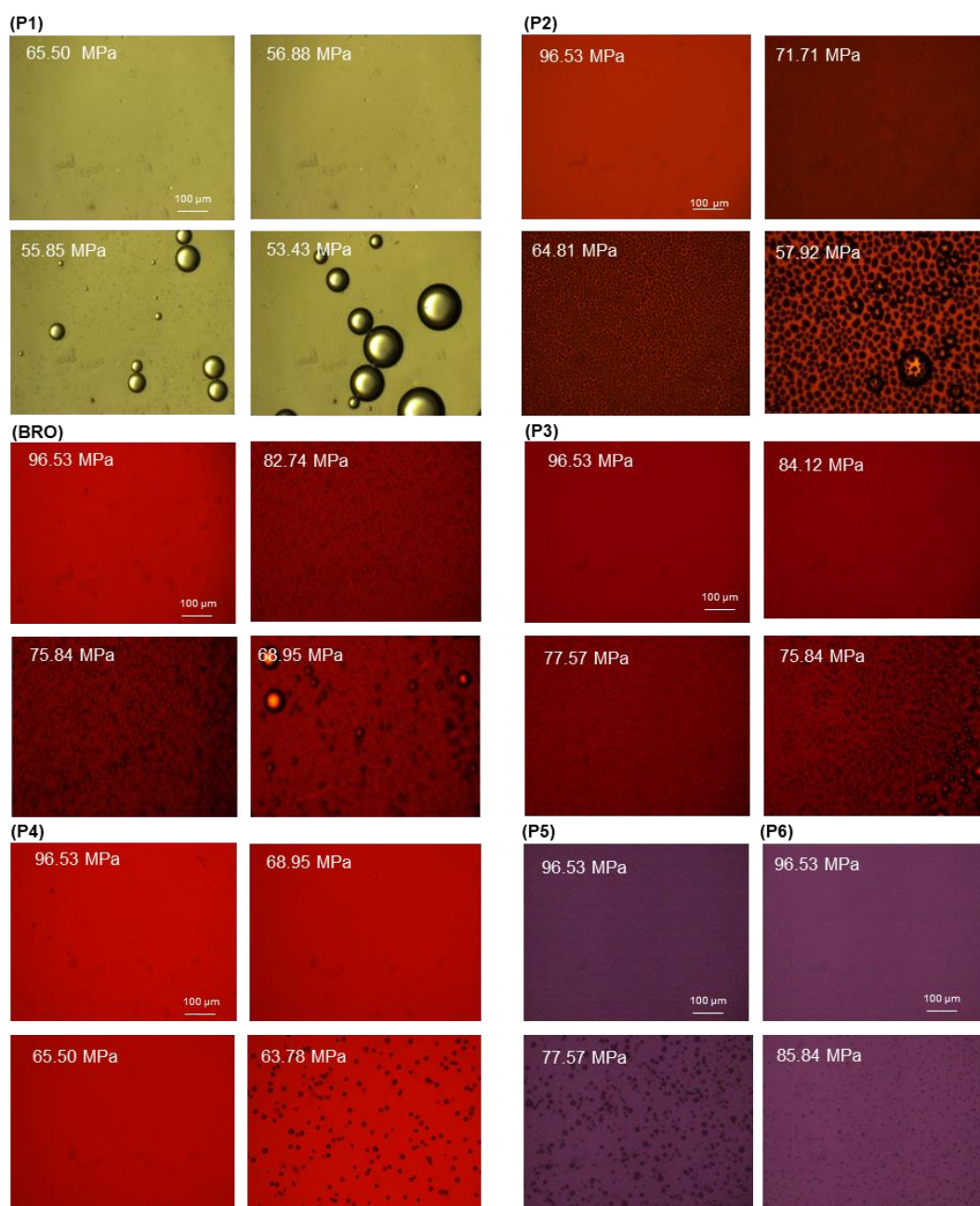


Figure 4.5 Micrographs for the different crude oil and methane systems during HPM depletion test.

Furthermore, one of the remarkable phase characteristics observed in BRO was de the instantaneous phase dissolving when pressurized at pressure near the appearance onset pressure. Similar behavior was observed for both P2 and P3 samples, presented in Figure 4.6 for P2, i.e., the heterogeneous phase totally dissolves when is pressurized above the AOP. Similar recovery of NIR transmittance was observed for both crude oils. Correspondently, a recovery of 99.7 % was obtained for P2 NIR transmittance after pressurization, and 99.5 % for P3 crude oil.

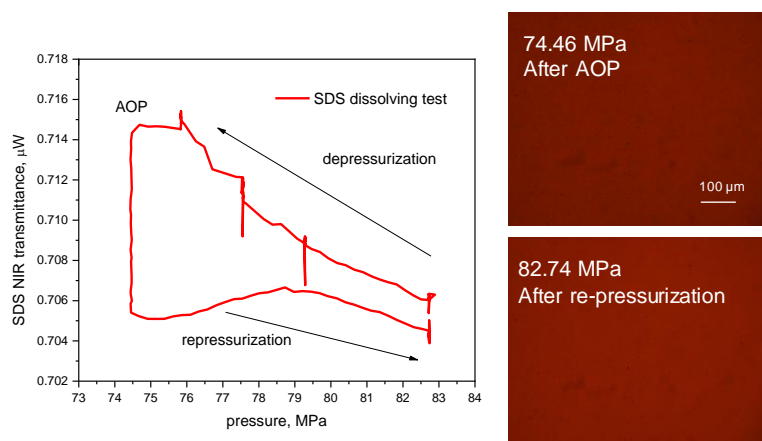


Figure 4.6 SDS variation during AOP-monophasic pressurization test and micrographs for from pressures above the AOP to monophasic condition, for 75.0 methane mol% mixture with P2 crude oil.

These results confirm a rapid redissolution P2 and BRO when the phase transition is evaluated near the AOP condition, with no temporal constraints for all the crude oil samples tested. However, the heterogeneous phase from P2 sample persists at pressures below bubble point pressure. Even if the asphaltenic phase dissolves rapidly at the AOP condition, it is well known that as the pressure is far below from AOP, the asphaltic phase is difficult to redissolve (JOSHI et al., 2001; MAQBOOL; BALGOA; FOGLER, 2009). These results could be associated to the nature of the heavy phase formation for the different crude oils and their relative response when mixed with low molecular gases as methane.

4.4. Conclusions

In this chapter, phase transitions of different Brazilian Pre-Salt crude oils were analyzed when mixed with methane 75.0 gas mol%. Crude oil composition varied from a light condensate fluid, to a heavy asphaltenic crudes. It was observed that even at minimal asphaltene content, heavy compounds could present phase transitions when mixed with methane at higher proportions. Crude stability has a fundamental influence in phase aggregation and morphology, reduced aggregation was observed for three of four medium crude oil analyzed. Moreover, regardless of the similar asphaltene content of crude oil samples, heavy phase transitions could present differences in terms of redissolution. For crude oils with high phase redissolution, a different phase transition

than typical asphaltene precipitation can be suggested. Their behavior could be more associated to a second liquid formed phase, than a solid asphaltenic phase. These differences could be associated to the nature and characteristics of the heavy compounds present in the crude oil mixtures.

5 CHAPTER V: EXPERIMENTAL PHASE BEHAVIOR AND SOLUBILITY PARAMETER FOR CRUDE OIL + METHANE (T = [311.15 – 373.15] K) AND CRUDE OIL + METHANE + CO₂ MIXTURES (T = [343.15 – 383.15] K)

Results published in: *Experimental phase behavior and solubility parameter for crude oil + methane [T = 311.15–373.15 K] and crude oil + methane + CO₂ mixtures [T = 343.15–383.15 K]*, *Fuel*. (2020) 119675. <https://doi.org/10.1016/j.fuel.2020.119675>

5.1. Introduction

In past chapters, phase behavior was studied for high gas content mixtures of Pre-Salt crude oils. For many of them, phase insolubilities were observed at high gas addition. The nature of the insolubility is still unclear, by classical NIR SDS techniques it is observed as typical asphaltene precipitation. However, HPM analysis present some unusual features for the phase heterogeneity.

To have an idea of the formed phase properties, solubility analysis can be made over the studied systems. The evaluation of solvency trends, at different gas additions, could reveal information of phase separation characteristics. In this chapter, experimental volumetric and compressibility data have been used to estimate crude oil solvency properties. This information can be used to better assess the nature of the observed phase transitions in Brazilian Pre-Salt fluids.

For instance, Verdier and coauthors have successfully used density and thermal expansivities measurements for live oil samples to calculate their solubility parameter at high pressure (VERDIER et al., 2006; VERDIER; DUONG; ANDERSEN, 2005). Because of the low volatility of crude oil, this parameter can be only determined indirectly by compressibility measurements. Then, solubility parameter relationship with pressure is usually related to phase behavior for live oils and crude + CO₂ mixtures (VERDIER et al., 2006).

Solubility parameter (δ) has been used widely in the description of asphaltene precipitation (ANDERSEN, 1999a; GONZALEZ et al., 2008a; ROGEL et al., 2016; THARANIVASAN; YARRANTON; TAYLOR, 2011). This parameter has been introduced by Hildebrand and Scott (HILDEBRAND; SCOTT, 1950), as follows:

$$\delta = \left(\frac{E(T,P)}{v(T,P)} \right)^{1/2} \quad \text{Eq. 5.1}$$

where E is the liquid cohesive energy, v is the molar volume, T is the temperature, and P is pressure. Cohesive energy can be expressed in terms of the negative residual internal energy, as:

$$E(T, P) = -\left(U_{liq}(T, P) - U_{vap}(T, P = 0)\right) \quad \text{Eq. 5.2}$$

where U_{liq} and U_{vap} are the internal energy of liquid and vapor phase, respectively. For practical purposes, cohesive energy is approximated to the energy of vaporization (BARTON, 1991). By using this approach, pressure effects on solubility parameter are represented by volumetric changes, while temperature effects are accounted by cohesive energy variations at saturation condition. Typically, solubility parameter estimation is calculated through the following Eq 5.3, at 278.15 K and atmospheric pressure.

$$\delta = \left(\frac{\Delta H_l^g - RT}{v_{liq}}\right)^{1/2} \quad \text{Eq. 5.3}$$

where ΔH_l^g is the vaporization enthalpy, R is the ideal gas constant, and v_{liq} is the liquid molar volume of the fluid.

When vaporization energies are not possible to measure, as occurs for crude oil samples, it is recommended the use of the internal pressure for solubility parameter estimation (BARTON, 1991; VERDIER; ANDERSEN, 2005). Internal pressure (π) is defined as the change of internal energy of a fluid, when it is isothermally expanded, as defined by Eq. 5.4

$$\pi = \left(\frac{\partial U}{\partial V}\right)_T = T \left(\frac{\partial P}{\partial T}\right)_V - P = T \frac{\alpha_P}{\kappa_T} - P \quad \text{Eq. 5.4}$$

where thermal expansivity (α_P) and isothermal compressibility (κ_T) are defined by Eqs. 5.5 and 5.6, given below.

$$\alpha_P = \frac{1}{v} \left(\frac{\partial v}{\partial T}\right)_P \quad \text{Eq. 5.5}$$

$$\kappa_T = -\frac{1}{v} \left(\frac{\partial v}{\partial P}\right)_T \quad \text{Eq. 5.6}$$

Bagley and coauthors (BAGLEY; NELSON; SCIGLIANO, 19710400) have established a relationship between solubility parameter and internal pressure by using two parameters, as follows: volume-dependent cohesion parameter (δ_v) and chemical interaction parameter (δ_R), as given by Eqs. 5.7 and 5.8. It is important to mention that for crude oil mixtures, the chemical interaction parameter presents a non-dominant effect. This parameter accounts for chemical interaction in solvents, as those observed in polar compounds, or those affected by hydrogen bonding (VERDIER; ANDERSEN, 2005). For this reason, solubility parameter for crude oil mixtures can be calculated using only internal pressure.

$$\delta_v^2 = \pi \quad \text{Eq. 5.7}$$

$$\delta_R^2 = \frac{-(U_{liq}(T,Psat) - U_{vap}(T,Psat)) - \pi v}{v} \quad \text{Eq. 5.8}$$

Using this approach, solubility parameter has been accurately estimated from internal pressure for non-polar solvents as a function of the pressure (error within 0.6 MPa^{1/2}) (VERDIER; ANDERSEN, 2005). For crude oil + gas systems, solubility parameter is estimated by intermediate of volumetric and compressibility experimental data and used as complementary information for their phase behavior interpretation (MOHAMMADI et al., 2016). However, few experimental data are reported in literature for different crude oil samples.

In this chapter, it was studied the phase behavior of two different Brazilian pre-salt crude oils mixed with gases, i.e. methane and carbon dioxide. Firstly, a highly stable crude oil, here named BR1 (P4 from chapter IV), was mixed with methane at 25.0 to 75.0 mol%, and PVT data used for study their solubility parameter behavior from 313.15 to 373.15 K. For the second sample, BR2 (BRO from chapter IV, with higher asphaltene content), the effect of CO₂ in gas composition were evaluated at a constant 75.0 % mol of gas. This experimental condition was selected by their interesting and non-typical asphaltene precipitation when gas is pure methane. Then, at the same molar gas content, phase behavior and solubility parameter were studied when varied the CO₂ content from 0 to 100 mol% (balance in methane), at temperatures from 343.15 to 383.15 K.

5.2. Materials and Methods

5.2.1. Crude oil samples

Two crude oils were selected from chapter IV for solubility parameter estimation. The first of them is P4, here named BR1. This crude oil did not present any insolubility when analyzed by conventional PVT techniques. The second oil used is the same than chapter II and III, here named BR2. Characterization results from both oils are presented in Table 4.1 and 4.2.

5.2.2. Phase behavior and PVT tests

Phase behavior and PVT data were obtained for the crude oil + gas mixtures (methane and CO₂, furnished by White Martins/Brazil, with a nominal purity of 99.9995 %, and 99.999 % purity, respectively). For BR1 crude oil, mixtures with pure methane were prepared for a gas composition ranging from 25.0 to 75.0 mol%, and temperatures of 313.15, 333.55, 353.15, and 373.15 K. Besides, for BR2 crude oil, a constant mol content of gas of 75.0 mol% was evaluated, varying composition of CO₂ from 0 to 100 mol%, for the 343.15, 363.15 and 383.15 K. Compositions and conditions for BR2 mixtures were specially selected based on previous results, at which an interesting and not typical asphaltene precipitation was observed.

5.2.2.1. Mixture preparation and equipment description

Crude oil + gas mixtures were prepared directly in the PVT-cell Vinci Fluid-Eval[®] described in chapter II. To remember, cell operational uncertainties (u) have been determined as: $u(P) = 0.1$ MPa for pressure; $u(T) = 0.1$ K for temperature; and, $u(V) = 1 \cdot 10^{-8}$ m³ (0.01 cm³) for volume. Maximum operational conditions are 100 MPa and 473.15 K. Before fluid injection, PVT cell was dried and vacuumed at 1 kPa.

Gas mass previously calculated for each mixture were gravimetrically injected in the PVT cell using pressurized blind cells, i.e., high-pressure floating piston vessels, at 65.0 °C, as described in chapter IV. Then, the injected mass of each fluid was measured by difference using a Sartorius MSU5203P digital balance, with a mass uncertainty of $u(m) = 0.005$ g. Final molar compositions of each mixture were calculated from the measured crude oil molar weight, and CO₂ and methane molar weight. Table 5.1 presents

the experimental composition of each evaluated system. Moreover, from the injected mass and the PVT volume measurements, densities were determined. Expanded uncertainties were $u(x) = 0.9$ mol% for compositions and $u(\rho) = 0.8$ kg/m³ for density, calculated according to the “Evaluation of Measurement Data – Guide to the Expression of Uncertainty in Measurement (GUM) (ISO/IEC GUIDE 98-3:2008). Experimental setup is presented in Figure 5.1.

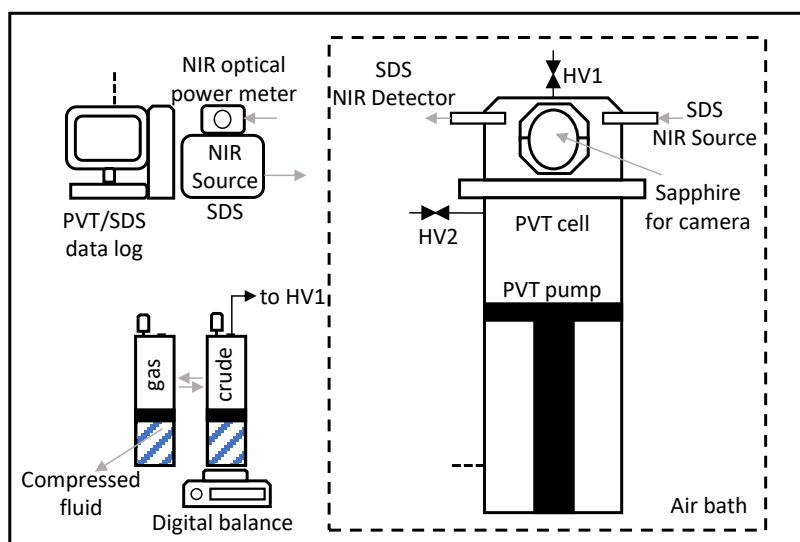


Figure 5.1. Schematic diagram of PVT, sample injection ensemble, and near-infrared (NIR) solid detection system (SDS).

Table 5.1 Experimental methane and CO₂ composition for crude oil + gas mixtures.

crude oil	methane content ± 0.9 mol %	CO ₂ content ± 0.9 mol % (CO ₂ content in gas, mol%)
BR1	26.5	-
	52.6	-
	74.7	-
BR2	75.2	0 (0)
	56.0	20.0 (26.3)
	47.5	28.5 (37.5)
	0	75.0 (100)

After crude oil and gas injection, systems were compressed at pressures, at least, 15 MPa above the bubble point pressure. Then, the whole system was homogenized for 12 h at the desired temperature. During this time, cell content was continuously stirred at 750 rpm, using a magnetic propel coupled in the top of the cell piston.

5.2.2.2. Phase transitions and volumetric measurements

After system homogenization, constant composition expansion (CCE) tests were performed, following experimental procedure described in chapter II. Additionally, density was estimated from volumetric data obtained from the PVT at different pressure and temperatures. Then, density was fitted to an interpolant Tamman-Tait modified equation (CIBULKA; HNĚDKOVSKÝ, 1996; DYMOND; MALHOTRA, 1988), by intermediate of the following expressions:

$$\rho(T, P) = \frac{\rho_o(T)}{1 - C \cdot \ln\left(\frac{B(T)+P}{B(T)+P_{ref}}\right)} \quad \text{Eq. 5.9}$$

$$\rho_o(T) = A_0 + A_1 \cdot T + A_2 \cdot T^2 \quad \text{Eq. 5.10}$$

$$B(T) = B_0 + B_1 \cdot T + B_2 \cdot T^2 \quad \text{Eq. 5.11}$$

where A_0 , A_1 , and A_2 are fitted parameters for density data at a reference pressure; P_{ref} as function of temperature. Additionally, B_0 , B_1 , B_2 , and C are fitting parameters for the entire density $P\rho T$ dataset. Fitting procedure was made following Levenberg-Marquardt algorithm (MOREÉ, 1978) for each mixture composition. Reference pressure (P_{ref}) was selected as the pressure where the sum of the squared errors is minimal ($SSE = \sum (\rho_{PVT} - \rho_{fit})^2 / \rho_{PVT}$, where ρ_{PVT} and ρ_{fit} are the experimental and fitted density, respectively).

By using the fitted Tamman-Tait equation, thermal expansivity and isothermal compressibility were calculated for each system using Eqs. (12) and (13). Finally, solubility parameter was estimated from the internal pressure approximation, using Eqs. (4) and (7). Additionally, cohesive energy E was calculated as the product of the molar volume and the square of the solubility parameter, using Eq. (1). Uncertainties have been estimated as follows: thermal expansivity: $u(\alpha_P) = 2.1 \cdot 10^{-7} \text{ K}^{-1}$; isothermal compressibility: $u(\kappa_T) = 5 \cdot 10^{-5} \text{ MPa}^{-1}$; solubility parameter: $u(\delta) = 0.6 \text{ MPa}^{1/2}$; molar volume: $u(v) = 7 \cdot 10^{-6} \text{ m}^3/\text{kmol}$; and, cohesive energy: $u(E) = 1.3 \text{ kJ/mol}$. All calculated

by error propagation, as recommended by GUM procedures (ISO/IEC GUIDE 98-3:2008(E)). Solubility parameter uncertainty is in the same order than reported in previous works (VERDIER; DUONG; ANDERSEN, 2005). Despite it could be quite large for process involving low solubility parameter span, it could be used for systems with wide variation of solubility parameter, as expected when different types of gases are mixed with crude oil.

$$k_T = \left(\frac{1}{\rho}\right) \cdot \left(\frac{\partial \rho}{\partial P}\right)_T = \frac{C}{\left(1 - C \cdot \ln\left(\frac{B(T)+P}{B(T)+P_{ref}}\right)\right) \cdot (B(T)+P)} \quad \text{Eq. 5.12}$$

$$\alpha_P = -\left(\frac{1}{\rho}\right) \cdot \left(\frac{\partial \rho}{\partial T}\right)_P = -\frac{A_1 + 2 \cdot A_2 \cdot T}{\rho(T, P_{ref})} - \frac{C \cdot (P_{ref} - P)}{(B(T)+P) \cdot (B(T)+P_{ref})} \cdot \frac{B_1 + 2 \cdot B_2 \cdot T}{[1 - C \cdot \ln\left(\frac{B(T)+P}{B(T)+P_{ref}}\right)]} \quad \text{Eq. 5.13}$$

This procedure was validated by using *n*-hexane and *n*-heptane using NIST density data (LEMMON; HUBER; MCLINDEN, 2007). Tammann-Tait equation was fitted, and solubility parameter estimated from compressibility and expansivity data, as shown in Table 5.2.

Table 5.2 Solubility parameters and internal pressures comparison from literature data and values obtained from NIST density, at 303.15 K and 0.1 MPa.

Compound	<i>n</i> -hexane	<i>n</i> -heptane
δ literature (BARTON, 1991), MPa ^{1/2}	14.7 ± 0.3	15.07 ± 0.3
$\pi^{1/2}$ from volumetric data (NIST), MPa ^{1/2}	15.5 ± 0.6	16.02 ± 0.6
δ Literature - $\pi^{1/2}$, MPa ^{1/2}	0.8	.95

5.2.3. Density measurements at high pressure using vibrating tube

To compare the feasibility of density data obtained by using the PVT cell, these data were measured in a U-tube DMA HPM Anton Paar densimeter. For that, two crude oil + gas mixtures have been selected, as follows: a medium gas content (BR1 + 50.0 methane mol%) and a higher gas content (BR1 + 75.0 methane %mol). Mixtures were prepared gravimetrically, follow the same procedure described above. However, fluids injection was made 50 cm³ high-pressure floating piston cylinders, furnished by Vinci Technologies. Cylinders were provided with an internal annular falling mixer, that

allowed the mixture homogenization after pressurization. Samples were mixed for 8 hours at 20 MPa above bubble point pressure, with constant tilting movements, while heated at 373.15 K. Special thermal cylinders thermal jackets provided by Vinci Technologies were used for heating. Pressure control was made continuously by Teledyne Isco 65D syringe pumps.

The high pressure densimeter equipment consists of a vibrating U-tube cell, with a nominal volume of 2 cm³. Unit thermal control was made with a circulating fluid bath Julabo FP50, and an internal PT-100 thermocouple allowed the fluid temperature measurements with an uncertainty of 0.01 K. The densimeter has been previously calibrated by using ultrapure Milli-Q® deionized water (conductivity of 18.2 ± 0.2 MΩcm, at 298.15 K) and nitrogen (White Martins, Brazil, nominal purity of 99.996 %), at the whole range of the apparatus (P=[1 – 100] MPa, and T = [298.15 to 423.15] K), as reported elsewhere (CHACON VALERO; et al., 2020; COMUÑAS et al., 2008).

After the mixture preparation, the cylinder sample were connected to a vacuumed Anton Paar DMA HPM density cell. A volume of 6 cm³ was gently purged to avoid flashing inside the measurement cell. Finally, density measurements were determined at the same temperature and pressure evaluated in the PVT cell. Cylinder cell sample pressurization has been controlled by intermediate of a Teledyne Isco 65D syringe pump, at a depressurization rate of 208 kPa/min. After each depressurization step, a 20 min stabilization time was accomplished to take density measurements ($\rho_{densimeter}$), with an uncertainty of $u(\rho_{densimeter}) = 0.47 \text{ kg/m}^3$. Difference between density experimental data obtained by using densimeter and data from PVT (ρ_{PVT}) was studied, taking the average absolute relative deviation (%AARD), defined as $1/N (|\rho_{densimeter} - \rho_{PVT}|/\rho_{PVT})$, were N is the number of evaluated points.

Additionally, high pressure density was determined for the dead oil samples BR1 and BR2, without gas addition. These measurements were used to calculate the dead oil solubility parameters and liquid cohesive energy, after fitting a Tammann-Tait density equation, following same procedures described above. Additionally, crude oil density measurements for BR1 and BR2 were determined. From these information, molar volume, solubility parameter, and cohesive energy, at the phase transitions PT_x -curve were determined crude oil + gas mixtures and dead oil samples.

5.3. Results and Discussion

5.3.1. BR1 crude oil + methane mixtures

Figure 5.2 shows a comparative trend between density data determined by using the PVT cell and the HPHT densimeter for mixtures of BR1 + methane. An %AARD below 1.1 % was obtained for the tested systems, as summarized in Table 5.3. Nevertheless, this small discrepancy could be associate to the experimental uncertainty measurements and the difference on the gas composition. Therefore, PVT density measurements could be appropriately used for derivative properties calculations, i.e. isothermal compressibility, and thermal expansion, and finally the solubility parameter.

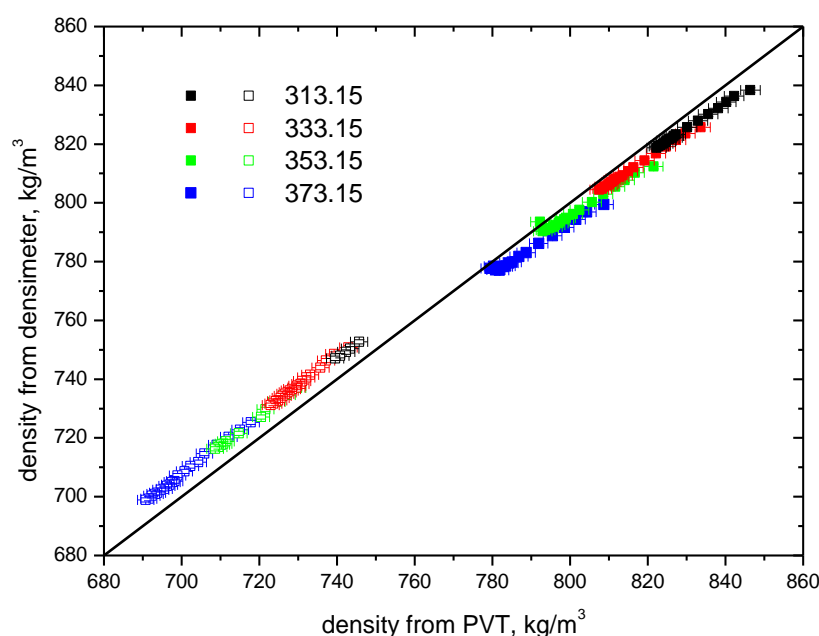


Figure 5.2 Density data crosschecking between PVT cell and HPHT densimeter for BR1 crude oil + methane for a medium methane content (around 50.0 mol%), solid marks; and, higher methane content (around 75.0 mol%), empty marks, for a temperature range of 313.15 to 373.15 K.

Table 5.3 Density data deviation (%AARD) between PVT cell and HPHT densimeter for a temperature domain of 313.15 K and 373.15 K.

		AARD %			
methane content for PVT mixture ± 0.9 mol%	methane content for densimeter mixture ± 0.9 mol%	temperature K			
		313.15	333.15	353.15	373.15
52.6	51.9	0.5	0.4	0.5	0.7
74.7	72.2	0.9	1.1	1.0	1.0

Figure 5.3 depicts BR1 crude oil + methane mixtures density data obtained in the PVT for mixtures from 26.5 to 74.7 methane mol%. As expected, density decreases by increasing gas content, as well by decreasing temperature. It is important to mention that the results these data corroborate the phase transition regions previously determined in chapter IV. It can be observed a sharp change in density values when bubble point pressure is reached, except for higher methane content. A typical behavior for a near-critical fluid is noted for mixtures with 74.7 methane mol%. In this case, SDS NIR transmittance was used to a proper bubble point pressure determination, summarized in Table 5.4.

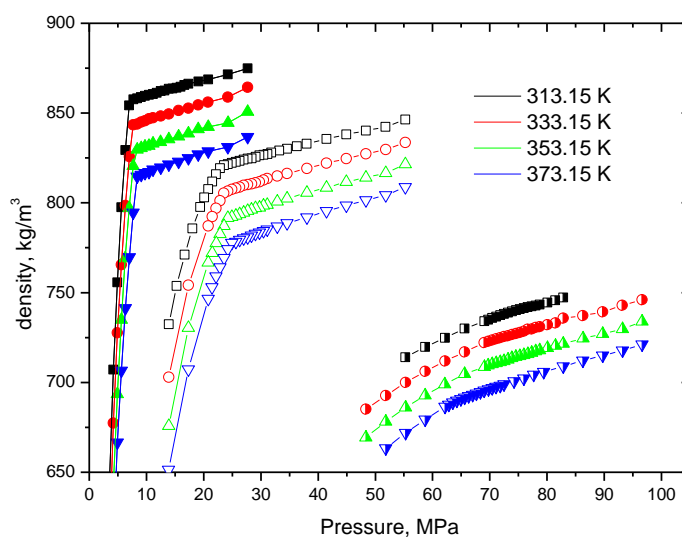


Figure 5.3 PVT density measurements for BR1 crude oil + methane mixtures for three different methane composition: (i) 26.5 mol% (solid marks), (ii) 52.6 mol% (empty marks), and (iii) 74.7 mol% (half-filled marks), at temperatures from 313.15 K to 373.15 K.

Table 5.4 Bubble point pressures for BR1 crude oil + methane mixtures at a temperature range of 313.15 K to 373.15 K.

bubble point pressure ± 0.6 MPa				
methane content ± 0.9 mol%	temperature ± 0.1 K			
	313.15	333.15	353.15	373.15
26.5	7.0	7.3	7.9	8.1
52.6	23.0	23.6	24.2	24.3
74.7	73.3	69.3	66.6	64.2

All experimental density data in the liquid region has been fitted to a Tammann-Tait equation, and it is in a good agreement with experimental data with an SSE below 3.8×10^{-5} , as reported in Table 5.5 (for detailed density data, please see Table S1 in the Appendix A). From this equation, isothermal compressibility, and thermal expansion were calculated (Table S2 to Table S3, in the Appendix A). It can be noted that as the methane content increases, the isothermal compressibility and thermal expansivity parameters increases, as expected. Finally, from these results the solubility parameter and cohesive energy can be calculated. These properties were reported as function of the pressure in the Table S4 to Table S6, in the Appendix A.

Table 5.5 Tammann–Tait equation fitting parameters, along with SSE values for BR1 crude oil + methane mixtures (x_1 is the methane mol percent)

x_1 mol%	A_0 $\text{Kg}\cdot\text{m}^{-3}$	A_1 $\text{Kg}\cdot\text{m}^{-3}\cdot\text{K}^{-1}$	A_2 $\text{Kg}\cdot\text{m}^{-3}\cdot\text{K}^{-2}$	B_0 MPa	B_1 MPa·K	B_2 MPa·K ²	C	P_{ref} MPa	SSE $\times 10^5$
26.5	1027.0	-0.382	-4.99E-04	291.2	-1.102	1.15E-03	0.7033	8.38	0.47
52.6	1055.0	-0.714	1.16E-04	337.9	-1.397	1.48E-03	0.0773	51.8	1.2
74.7	807.7	0.190	-1.23E-03	429.3	-2.667	3.78E-03	0.0424	82.8	3.8

Figure 5.4 illustrates the solubility parameter as a function of pressure for all BR1 crude oil + methane mixtures studied here. It can be noted that as the methane content increases, lower values of solubility parameter are obtained, as expected. Additionally, important variations against pressure are observed, because of the variation of samples thermal expansion coefficient. Especially, at the higher methane molar content studied, solubility parameter reaches values of $11.6 \text{ MPa}^{1/2}$. However, this value was not lower

enough to destabilize the asphaltenic fraction. It is important to emphasize that BR1 present a low content of asphaltenes with high stability, as reported in chapter IV.

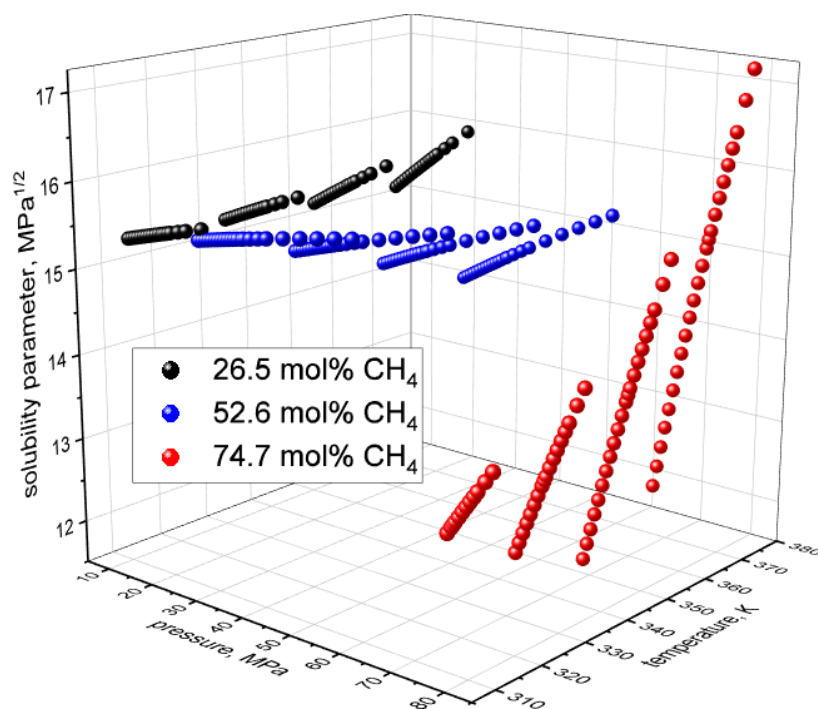


Figure 5.4. Solubility parameter as function of temperature and pressure for BR1 crude oil + methane mixtures (26.5 mol%, black points; 52.6 mol% blue points; and 74.7 mol%, red points).

Typically, crude oils have a solubility parameter around $18.0 \text{ MPa}^{1/2}$ (ROGEL, 1997), and their fractions, i.e. saturated, aromatic, resins, and asphaltenes have a solubility parameter from $15.9 \text{ MPa}^{1/2}$ (for saturates) to higher than $20.0 \text{ MPa}^{1/2}$ (for asphaltenes) (AKBARZADEH et al., 2005; ALVES et al., 2019; ROGEL, 1997; ROGEL et al., 2016; YARRANTON et al., 2018; YARRANTON; MASLIYAH, 1996). A comparison of the solubility parameter of the BR1 dead oil and pure methane is presented in Figure 5.5. Density measurements for BR1 dead oil are presented in Table S7, in the Appendix A, and their Tammann-Tait parameters in Table 5.6. From this fitting parameters, compressibility, solubility parameter, molar volume, and cohesive energy, were calculated and reported in Table S8 to Table S10, in the Appendix A. Methane solubility parameter has been calculated by using the Peng-Robinson equation of state, together with NIST database data for molar volume (Eq. 5.14).

$$\delta^2 = \frac{\sqrt{2}}{4b} \left(a - T \frac{da}{dT} \right) \left[\ln \left(\frac{v(T,P)+b(\sqrt{2}+1)}{v(T,P)-b(\sqrt{2}-1)} \right) \right] \frac{1}{v(T,P)} \quad \text{Eq. 5.14}$$

where v is the NIST molar volume obtained at P and T , b is the covolume, and a the attractive term of the equation of state.

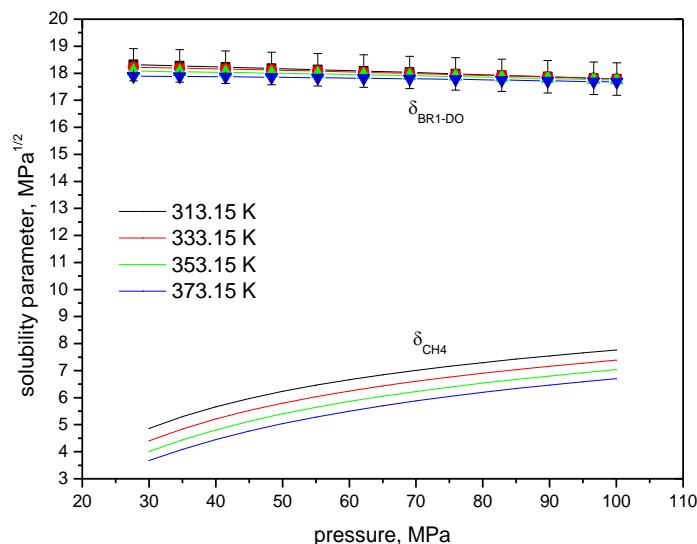


Figure 5.5 Solubility parameter for BR1 dead oil ($\delta_{\text{BR1-DO}}$) and methane (δ_{CH_4}) as function of pressure, for temperatures from 313.15 to 373.15 K.

Table 5.6 Tammann–Tait equation fitting parameters and SSE for BR1 dead oil.

A_0	A_1	A_2	B_0	B_1	B_2	C	P_{ref}	SSE
$\text{Kg}\cdot\text{m}^{-3}$	$\text{Kg}\cdot\text{m}^{-3}\cdot\text{K}^{-1}$	$\text{Kg}\cdot\text{m}^{-3}\cdot\text{K}^{-2}$	MPa	MPa $\cdot\text{K}$	MPa $\cdot\text{K}^2$		MPa	$\times 10^5$
1100.0	-0.620	-1.68E-04	445.9	-1.332	1.04E-03	0.0960	96.6	1.21

BR1 dead oil solubility parameter lies within the range of 17.7 and 18.5 $\text{MPa}^{1/2}$, with pressure neglected influence, as expected for regular liquids. On the contrary, for methane, it can be observed a huge variation with a minimum at low pressure and higher temperature. This behavior is also observed for the mixture of BR1 at higher methane content, as can be noted in Figure 5.4, with the broader change in their solubility parameter with pressure. Additionally, as the mixture methane content increases, the solubility parameter variation with pressure is more evident, with a span of 2.5 $\text{MPa}^{1/2}$, at the lower methane content tested, to 6.0 $\text{MPa}^{1/2}$ for high methane compositions.

Beside solubility parameter, another interesting observation could be done by calculating the cohesive energy. Vargas and coauthors have modelled the cohesive energy for mixtures (E_{mix}) of a model oil (toluene + asphaltene) and precipitants, ranging from methane to pentadecane (VARGAS et al., 2009b). Then, their ratio (E_{mix}/E_{DO}) with the cohesive energy of the model dead oil (E_{DO}) was calculated along a phase equilibrium curve, i.e., bubble point pressure, or AOP-composition curve. At this equilibrium curve, it was observed a linear relationship between cohesive energy ratio and precipitant molar content.

In this study, a different trend on E_{mix}/E_{DO} was observed, as illustrated in Figure 5.6 for BR1 crude oil + methane mixtures, at bubble point pressure condition. From this Figure it can be seen that cohesive energy ratio decreases tending toward 1 as the methane composition approaches zero, with a marked reduction even at low methane composition. This behavior is not observed for toluene + asphaltene + methane reported by Vargas and coauthors (2009). This difference could be associated to the BR1 crude oil compositional complexity, along with the repulsive effect between heavy molecules and gas when compared to toluene-based model oils.

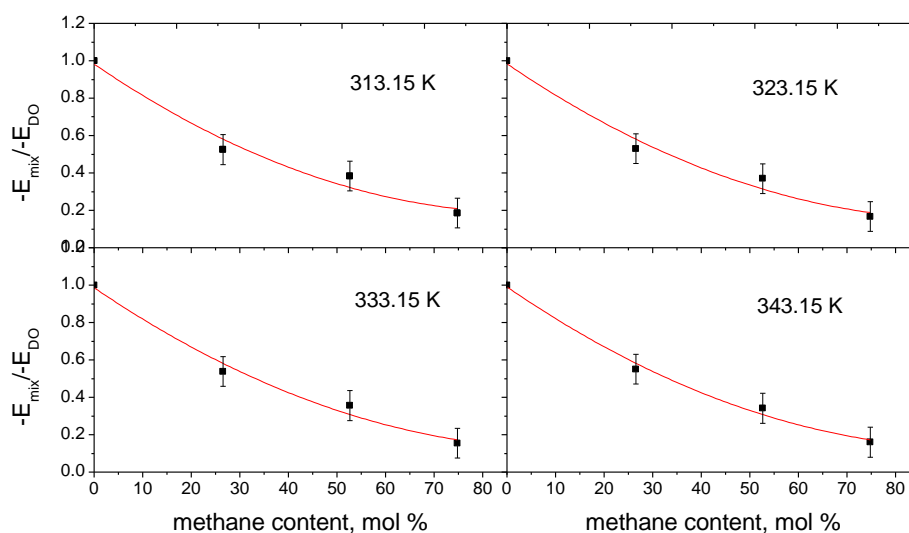


Figure 5.6 Cohesive energy ratio for BR1+methane mixtures (E_{mix}) and BR1 dead oil (E_{DO}) as a function of methane content, calculated at bubble point pressures for 313.15 K, 323.15 K, 333.15 K, and 314.15 K.

For the same P-x bubble point pressure curve, molar volume, and solubility parameter ratios have been calculated, as shown in Figures 5.7 and 5.8. Both relationships present a linear behavior with more pronounced methane effect for the molar volume

ratio. Moreover, apparent values, i.e., extrapolated values when methane composition tend to 0, reach the values of the dead oil, and their ratio tend to one. It is important to mention that cohesive energy is calculated as the product of the molar volume and the square of the solubility parameter. Despite the slight variation of the solubility parameter ratio with the methane composition, when estimated at the bubble point pressure, their squared value can contribute to the linearity lost when cohesive energy is calculated.

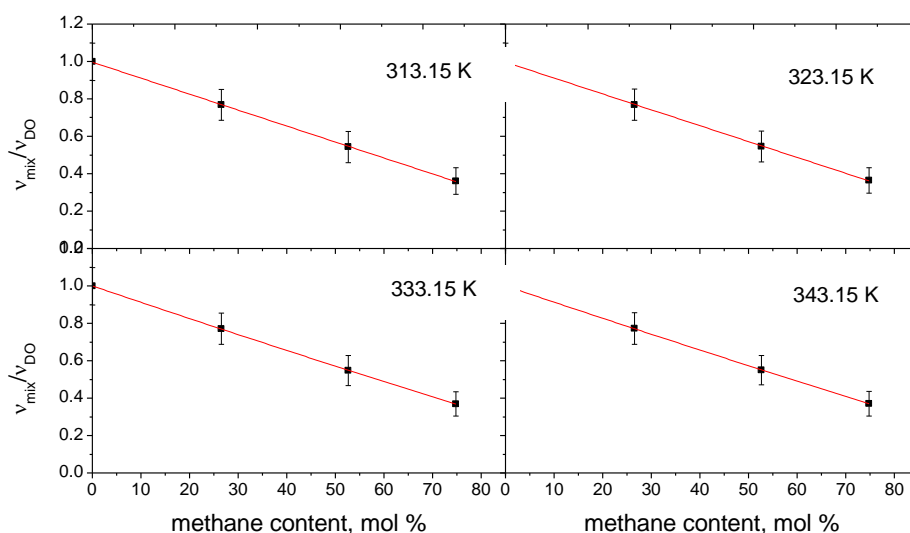


Figure 5.7 Molar volume ratios for BR1 + methane mixtures (v_{mix}) and BR1 dead oil (v_{DO}) as function of methane content, calculated at bubble point pressures for 313.15 K, 323.15 K, 333.15 K, and 314.15 K.

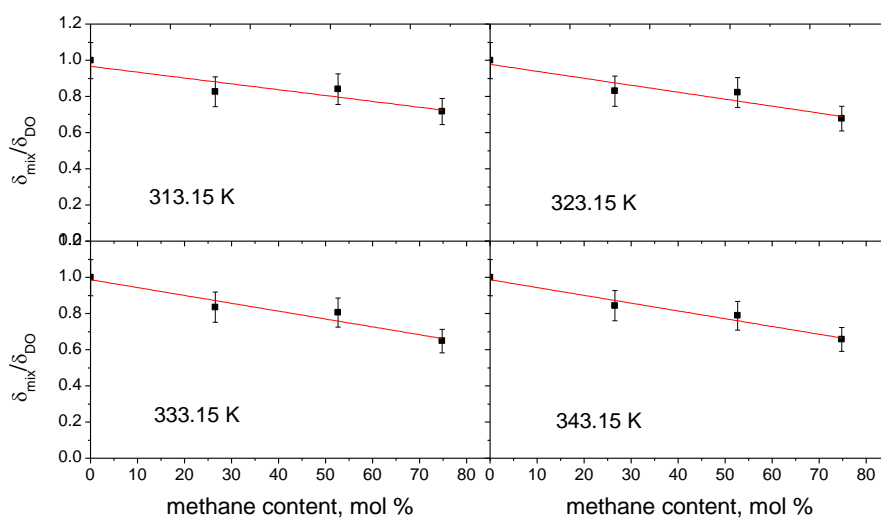


Figure 5.8 Solubility parameter ratio for BR1 + methane mixtures (δ_{mix}) and BR1 dead oil (δ_{DO}) as function of methane content, calculated at bubble point pressures for 313.15 K, 323.15 K, 333.15 K, and 314.15 K

5.3.2. *BR2 crude oil + methane mixtures + CO₂*

Phase transitions for BR2 mixtures were studied by intermediate of SDS NIR transmittance measurements, as presented in Figure 5.9. BR2 crude oil was previously studied in chapter II, and presented complex phase transitions when mixed with methane at 75.0 mol%. This phase transition was properly identified as a slight reduction in the SDS NIR transmittance during CCE tests, typically associated to asphaltenes. Additionally, phase heterogeneity from BR2 were characterized by their not typical high dispersion, low aggregation, and not fractal morphology when destabilized with methane, related to their high stability.

Despite these characteristics, same phase transitions were detected for all evaluated systems, i.e., SDS presented a slight decrease when AOP is reached. This observation is more evident at lower temperatures, where AOP are also detected at higher pressures. Table 5.7 gives the bubble point pressure and AOP for all evaluated conditions. Also, the difference between the AOP and the bubble point pressure was presented in this table, denominated as asphaltene existence region. This value indicates the pressure domain where a second asphaltic phase is observed.

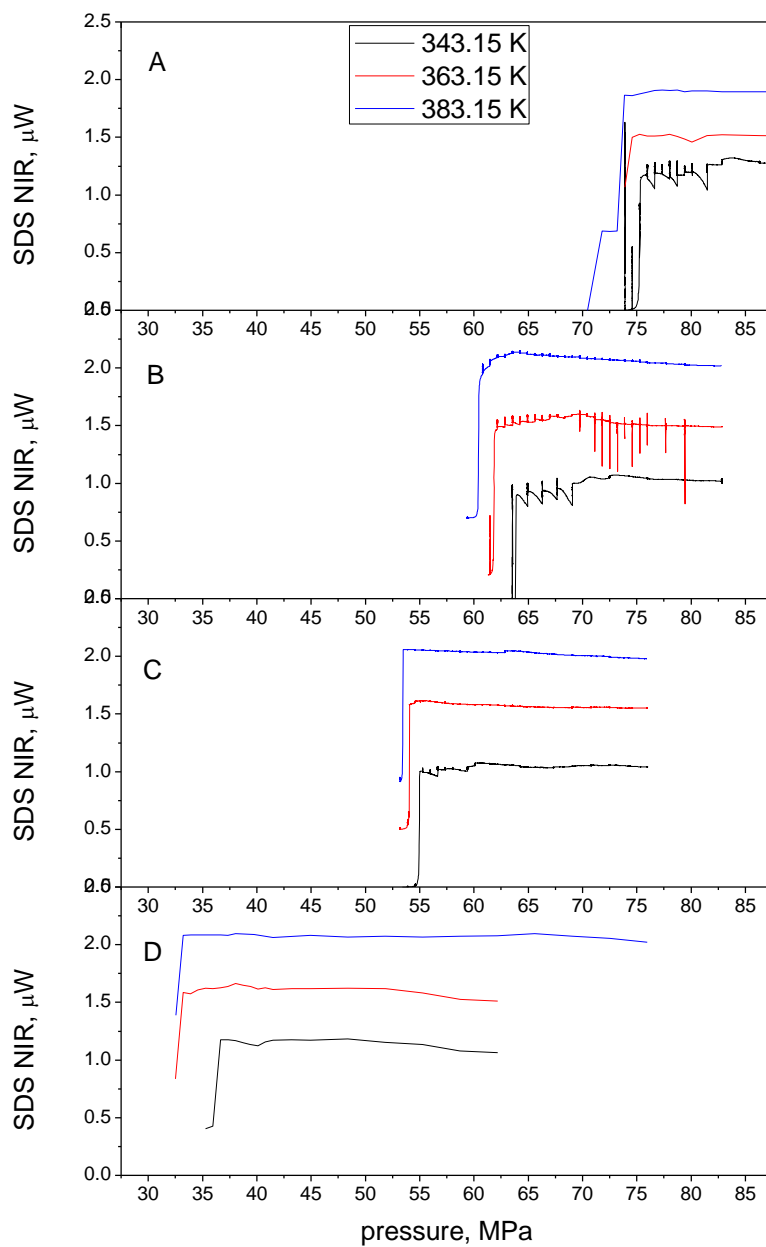


Figure 5.9 NIR transmittance measurements during CCE for BR2 + 75 % mol gas with (A) 0 % mol CO₂ (100 % methane); (B) 26.3 % mol CO₂; (C) 37.5 % mol CO₂; (D) 100 % mol CO₂ at temperatures of 343.15, 363.15 and 383.15 K.

Table 5.7 Bubble point pressures (P^b) for BR2 crude oil + methane + CO₂ mixtures, AOP, and asphaltene existence region (AOP- P^b) at a temperature range of 343.15 K to 383.15 K

CO ₂ content in gas ± 0.9 mol%	P^b	AOP	asphaltene existence
	± 0.6 Mpa	± 0.6 Mpa	region ± 1.2 MPa
T = 343.15 K			
0	74.5	82.7	8.2
26.3	63.8	72.5	8.7
37.5	55.3	60.1	4.8
100	36.3	41.5	5.2
T = 363.15 K			
0	73.0	80.7	7.7
26.3	60.5	69.0	8.5
37.5	53.1	56.6	3.5
100	32.9	38.0	5.1
T = 383.15 K			
0	71.8	75.9	4.1
26.3	59.8	64.9	5.1
37.5	53.3	-	-
100	32.9	-	-

From Table 5.7, it can be noted that as the CO₂ content increases, lower values of AOP and bubble point pressure are observed, as expected. These results can be related to the higher critical properties of CO₂ compared to methane. Additionally, it is noted a reduction in the asphaltene existence region for the systems with high CO₂ content, i.e. closer values of AOP to the bubble point. This observation can be related to solubility contributions of CO₂, characterized by their higher solubility parameter (GONZALEZ et al., 2008a). Moreover, it is important to mention that no precipitated asphaltene were detected at higher temperature for the 28.5 CO₂ mol% and 75.0 CO₂ mol% systems.

BR2 crude oil + methane + CO₂ solubility parameter was calculated trying to analyze the effect of the CO₂ addition in phase behavior. This parameter has been calculated by using the Tammann-Tait, as described previously. Table 5.8 depicts the Tammann-Tait equation fitting parameters for BR2 systems. Experimental density measurements, together with estimated molar volumes, compressibility factors, solubility

parameters, and cohesive energy, are presented in Table S11 to Table S16. These parameters were also calculated for BR2 dead oil, and presented in Table S17 to S20.

Table 5.8 Tammann–Tait equation fitting parameters, along with SSE values for BR2 crude oil + methane + CO₂ mixtures and BR2 dead oil (x_{CO_2} is the carbon dioxide mol percent).

x_{CO_2} mol%	A_0 Kg·m ⁻³	A_1 Kg·m ⁻³ ·K ⁻¹	A_2 Kg·m ⁻³ ·K ⁻²	B_0 MPa	B_1 MPa·K	B_2 MPa·K ²	C	P_{ref} MPa	SSE x10 ⁵
d.o.	1096.0	-0.609	1.59E-04	608.5	-2.295	2.38E-03	0.0898	96.6	0.35
0	1052.0	-1.138	7.09E-04	93.9	-0.327	6.33E-05	0.9522	89.7	0.38
26.3	1097.0	-0.994	2.68E-04	337.3	-1.981	2.39E-03	0.0676	69.0	0.52
37.5	1104.0	-0.984	2.69E-04	175.6	-0.812	7.76E-04	0.0748	72.5	0.42
100	1394.0	-1.679	9.90E-04	212.7	-0.7446	5.04E-05	0.0928	58.7	0.33

d.o.: BR2 dead oil

Figure 5.10 shows solubility parameter for BR2 crude oil + methane + CO₂ mixtures as a function of pressure. It can be noted that at higher CO₂ mol content in the mixture, higher solubility parameter is found, from around 14.7 MPa^{1/2} for BR2 crude oil + CO₂ mixture, to around 11.3 MPa^{1/2} for BR2 crude oil + methane. These results are associated to the increase of the ratio of the thermal expansivity and the isothermal compressibility parameters, as the CO₂ content increases. Additionally, for the pressure and temperature domain studied, CO₂ solubility parameter changes from 11.8 MPa^{1/2} (at 100 MPa and 343.15 K) to 7.11 MPa^{1/2} (at 30 MPa and 383.15 K), as shown in Figure 11. An interesting result is the solubility parameter similarity between pure CO₂ and BR2 crude oil + methane mixtures. Then, the increase of CO₂ in gas composition could cause higher values for mixture solubility parameter. This result could be related to the lower asphaltene region, as previously discussed for Table 5.7 data.

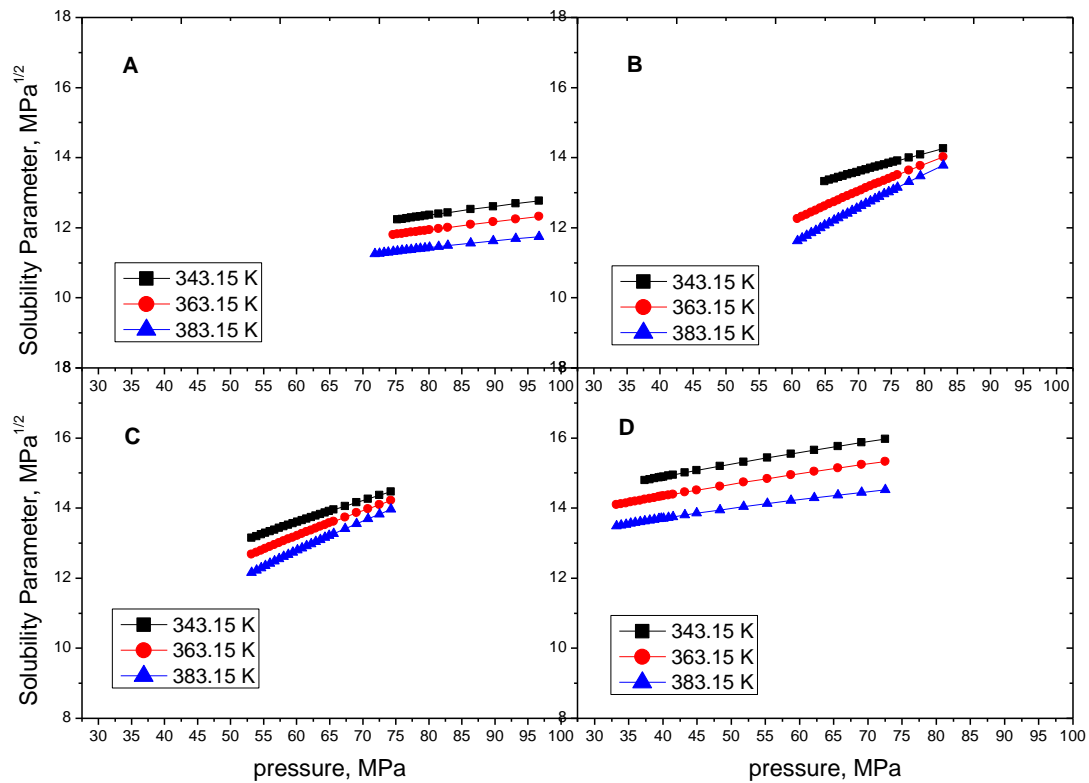


Figure 5.10 Solubility parameter as function of temperature and pressure for BR2 crude oil + methane + CO₂ mixtures. (A) 0.0 % mol CO₂ (100 % methane); (B) 26.3 % mol CO₂; (C) 37.5 % mol CO₂; (D) 100 % mol CO₂, at temperatures of 343.15 K, 363.15 K, and 373.15 K.

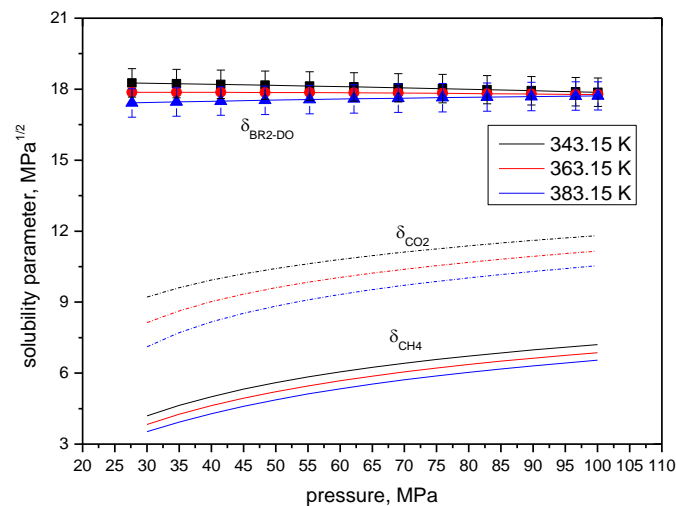


Figure 5.11. Solubility parameter for BR2 dead oil (δ_{BR2-DO}), methane (δ_{CH4}), and CO₂ (δ_{CO2}) as a function of pressure, for temperatures from 343.15 K to 383.15 K

Figure 5.12 relates the phase transitions points observed for BR2 mixtures to the mixture's solubility parameter and cohesive energy. Both parameters were calculated at the AOP and bubble point pressure (P^b) condition. It can be noted that at higher CO₂ content, the obtained solubility parameter increases over the P - x bubble point and AOP curves.

One can note that the mixtures solubility parameter, evaluated at AOP, increases from 12.4 MPa^{1/2} (343.15 K and 0 CO₂ %mol), to 14.9 MPa^{1/2} (343.15 K and 100 CO₂ mol%). This result can give some information on the type of phase that is formed. If the phase is promoted when lower solubility parameter is reached, or by the contrary, it is stabilized when solubility parameter increases, it could indicate that the formed phase could have a high solubility parameter. This observation is made using the basis that solubility increases for fluids with similar solubility parameter. Consequently, the formed phase heterogeneity can be associated to heavy compounds in crude oil, with high solubility parameter, as polyaromatics and asphaltenes.

It is well known that even small changes in solubility parameter can induce large changes in asphaltene stabilization. This increase in solubility parameter could be also associated to the reduction in the asphaltene existence region, and consequent BR2 asphaltene stabilization. As can be seen in Table 5.7, the asphaltene existence region is minimal at higher CO₂ content, reaching values of 4.8 MPa at 100 %mol CO₂ in gas, versus 8.2 MPa when mixed gas is pure methane.

Also, it can be stressed that the asphaltic immiscibility was obtained when mixture solubility parameter is reduced at least 3.1 MPa^{1/2} from dead oil values, found for mixtures with 100 %mol CO₂ in gas. This reduction is only achieved after adding 75.0 % mol gas to the crude oil. Moreover, as the methane content increase in the mixed gas, a higher difference on solubility parameter is observed. Specifically, a reduction on 5.6 MPa^{1/2} is reached for the higher methane content system. This solvency capacity decrease for crude oil systems could promote the separation of a heavy and asphaltenic phase. For that reason, higher AOP was obtained for methane rich systems.

In terms of cohesive energy, it can be noted in Figure 5.12 that BR2 mixtures presented a wide variation at the equilibrium P^b and AOP curves. Contrary to results obtained for BR1 mixtures, where the cohesive energy decreases as system is richer in methane, BR2 presented a marked increase on cohesive energy when CO₂ is added. This can be associated to the molar volume increase when CO₂ is included in the mixture. Those results, i.e., the increase of solubility parameter and cohesive energy, could

corroborate the stabilization effects of CO₂ for BR2 asphaltic fraction, despite their non-typical phase behavior.

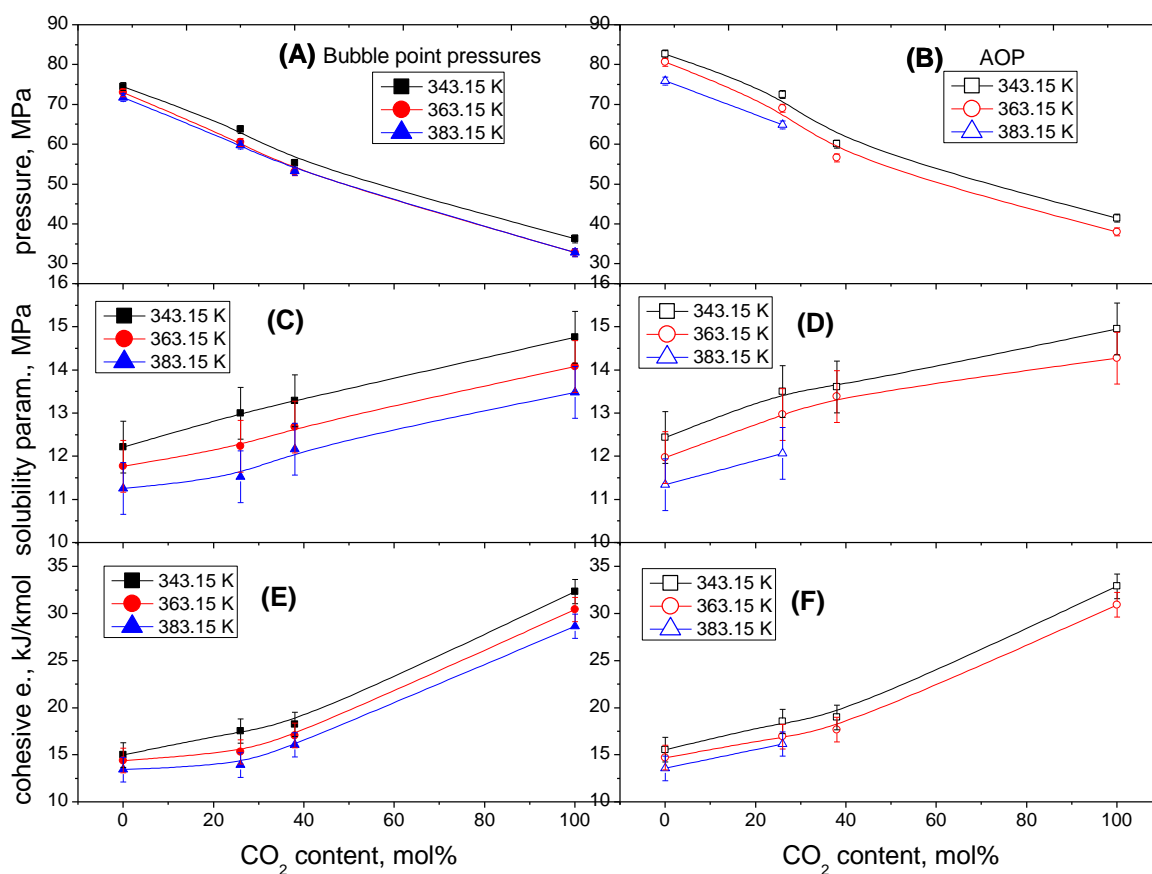


Figure 5.12. (A) Bubble point pressure; (B) AOP, (C) solubility parameter at bubble point pressure; (D) solubility parameter at AOP; (E) cohesive energy at bubble point pressure; and (F) cohesive energy at AOP, for BR2 + 75.0 mol% gas mixtures, as function of CO₂ composition, at 343.15 K, 363.15 K, 383.15 K.

5.4. Conclusions

Solubility parameter and cohesive energy were calculated from PVT data as a useful information to assess crude oil phase behavior. For stable and low asphaltenic crude oil, minimal solubility conditions can be reached without any phase separation when methane is added, despite the higher asphaltene destabilization capacity of methane. A marked reduction of cohesive energy is observed when methane was added to crude oil, and their non-linear decrease was associated to system compositional complexity. For the crude oil with higher asphaltene content, CO₂ addition contributed to heavy phase formation

stabilization. Solubility parameter and internal energy increase were properly identified for these systems and associated to the reduction on asphaltene existence region for mixtures with CO₂, also giving information of possible phase heterogeneity properties. Precisely, these results could suggest that the formed immiscibility could be associated to a heavy phase composed of the heavier fractions of crude oil.

6 CHAPTER VI: STUDY OF LIQUID–LIQUID AND LIQUID–LIQUID–VAPOR EQUILIBRIA FOR CRUDE OIL MIXTURES WITH CARBON DIOXIDE AND METHANE USING SHORT-WAVE INFRARED IMAGING: EXPERIMENTAL AND THERMODYNAMIC MODELING

Results published in: *Study of Liquid–Liquid and Liquid–Liquid–Vapor Equilibria for Crude Oil Mixtures with Carbon Dioxide and Methane Using Short-Wave Infrared Imaging: Experimental and Thermodynamic Modeling*, Energy Fuels. (2020).
<https://doi.org/10.1021/acs.energyfuels.0c03064>

6.1. Introduction

In past results, phase behavior of Pre-Salt crude oils was analyzed by conventional PVT techniques. These methods allowed to detect phase transitions in tested systems, but their characteristics are non-conventional. The study was based on NIR light scattering and HPM tests, two techniques that are limited for overall bulk fluid observation. Additionally, the high phase dispersity and no filtration retention difficult the individual study of the second formed phase.

Recently, a new visualization technique was developed in our laboratory to study opaque and complex mixtures of gases and crude oil (DARIDON et al., 2020). This methodology is based on the high transmittance of short-wave infrared (SWIR) wavelength through crude oil samples (DARIDON et al., 2020; HAMMAMI et al., 2000), allowing the complete visualization of crude oil bulk phase. Consequently, the method allows a direct observation of any phase dispersed in bulk fluid, as Liquid-Liquid phase transition, and the solid formation such as waxes or asphaltenes.

Therefore, the SWIR based technique was used in this chapter to identify the phase behavior of Brazilian pre-salt crude oil mixed with either methane or carbon dioxide. It was studied for a gas composition range from 20.0 to 86.0 mol%, under pressure up to 100 MPa, and temperature ranging from 293.15 to 378.15 K. This extended experimental temperature range, below the reservoir temperature of the crude oil, was chosen to understand the complex phase diagram of the systems and to study the equation of state capability to represent the phase behavior for such Pre-Salt oil systems.

6.2. Materials and Methods

6.2.1. Crude oil sample

The dead oil sample was supplied by Total and Petrobras S.A, the sample was collected during a well-test at stock tank conditions. This sample is taken from same reservoir than P4 crude oil from chapter IV, but differs on sampling time. The reservoir temperature is 85°C. The live oil under reservoir conditions is characterized by a GOR of 430 Std m³/Std m³. Compositional analysis of the crude oil is depicted in Table 6.1. The oil composition was based on standard analysis provided by Petrobras S.A. This standard analysis does not provide any information regarding C20+ composition except a molecular weight. Keeping the weight content of C20+ constant, this fraction was divided into two parts: a standard C20+ fraction and a CNA (heavy condensed) fraction. This splitting was necessary for modelling purposes, further details are presented in Section 6.2.3.

Phase behavior analyses were carried out by mixing a known mass of the crude oil sample with the target mass of methane, CO₂, or a mixture 1:1 methane:CO₂ (in mol) for a given calculated composition. Gas was supplied by Linde France, with a molar purity of 99.999, 99.9999 and 99.995 %, respectively. The following gas compositions were considered: 20.0, 40.0, 60.0, 70.0, 78.0, 84.0, and 86.0 gas mol%. Each mixture was prepared by successive additions of gas to the crude oil sample. After that, pressure was raised, and the system was strongly mixed at 1500 rpm to guarantee its thermodynamic equilibrium. As equilibrium criteria, it was considered no variations in pressure higher than 0.1 MPa at constant volume and temperature, during at least 20 min.

Table 6.1 Compositional analysis of the crude oil sample.

carbon number	wt %	mol %
C3	0.034	0.186
i-C4	0.027	0.115
n-C4	0.109	0.461
i-C5	0.125	0.424
n-C5	0.243	0.824
C6	0.720	2.096
Mcyclo-C5	0.292	0.850
Benzene	0.090	0.282
Cyclo-C6	0.210	0.610
C7	1.244	3.171
Mcyclo-C6	0.593	1.478
Toluene	0.212	0.564
C8	2.186	4.999
C2-Benzene	0.151	0.348
m&p-Xylene	0.352	0.811
o-Xylene	0.110	0.254
C9	2.513	5.082
C10	3.207	5.856
C11	2.915	4.852
C12	2.855	4.369
C13	3.278	4.645
C14	2.825	3.732
C15	3.026	3.747
C16	2.594	3.024
C17	2.443	2.694
C18	2.674	2.801
C19	2.513	2.509
C20+	54.703	35.770
CNA*	7.754	3.445
C20+ molar weight		374
CNA molar weight		551

*CNA = condensate naphthenic and aromatic compounds

6.2.2. Full visibility PVT tests

The full visibility PVT cell coupled with a SWIR imaging system was designed to carry out the same visual observations in dark crude oils than in transparent synthetic systems (DARIDON et al., 2020). In this apparatus, phase transitions are observed in a PVT cell composed of a high-pressure volumetric pump, adapted with a full visibility sapphire windows at the end of the pump thanks to infrared camera working in the SWIR range. The maximum volume, pressure, and temperature of the equipment are respectively 300 cm^3 , 100 MPa, and 383.15 K. Volume is controlled by the pump piston position with a precision of 0.001 cm^3 . Pressure was measured through a coupled transducer with 0.005 % precision. Cell temperature was measured with a Pt-100 directly in contact with the metallic cell body, and its control was achieved through a cell thermal jacket connected to a thermostatic bath. Moreover, the cell piston was equipped with a magnetic stirrer that allowed an efficient sample homogenization during the experiments. A diagram of the cell's assembly is depicted in Figure 6.1. PVT operational variables were registered continuously for data monitoring during Constant Composition Expansion experiments (CCE).

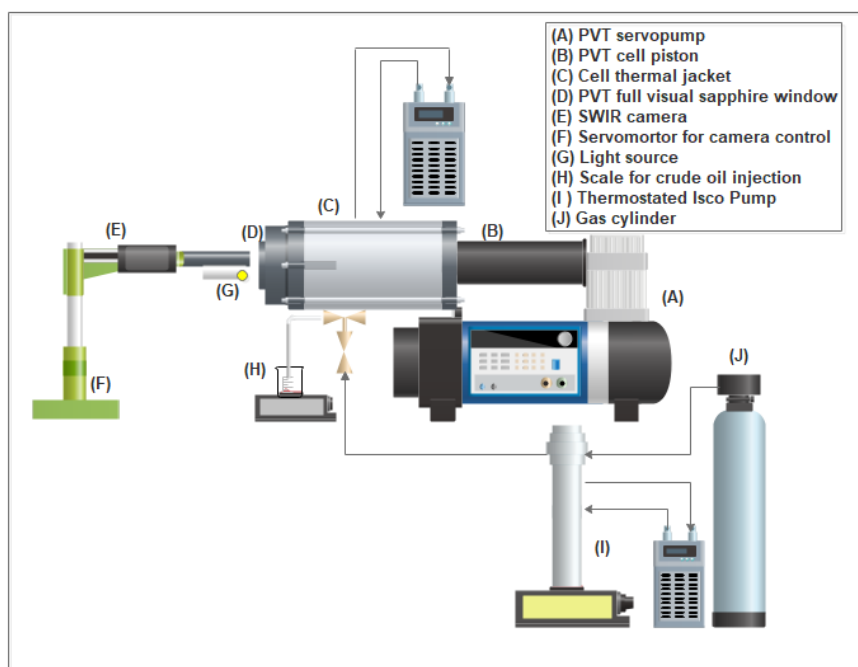


Figure 6.1 Schematic diagram of the PVT cell, SWIR camera, and sample injection ensemble.

PVT cell frontal sapphire window of large diameter (35.7 mm) allows a complete cell content visualization. Through this window, fluid inspections were made using a SWIR camera. This camera works in a spectral range from 900 to 1,900 nm, and the sample high transmittance could effectively be used for the determination of crude oil mixtures complex phase behavior (DARIDON et al., 2020; HAMMAMI et al., 2000). The camera is mounted either with a hyperspectral fixed focal 12.5 mm length lens or with a long working distance objective lens with magnification 4× and 8×. In Figure 6.2, the piston 3 cm away from the sapphire window is photographed using the imaging system when the cell is empty (Figure 6.2 A) and when the cell is filled with black crude oil sample (Figure 2 B). A xenon lamp with an optical fiber was used as light source, and the reflected light was recorded. Camera position, i.e., x, y, z coordinates movements, were controlled by three motorized stages.

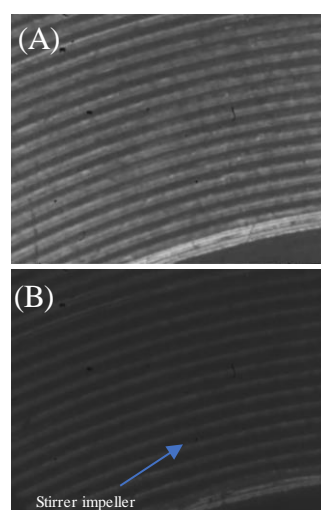


Figure 6.2 Cell inspection using SWIR camera. (A) stirrer impeller with empty cell; and (B) stirrer impeller with cell filled with black crude oil.

Before each experiment, the cell pressure was reduced using a vacuum pump. Also, crude oil sample was heated during 2 hours at 65 °C to prevent wax precipitation. Then, crude oil was introduced gravimetrically into the cell by suction, and the injected crude oil mass was determined by an analytical balance (0.001 g precision), as depicted in Figure 1. After that, the required amount of gas was injected by using a syringe pump, at 30 °C. The injected mass of gas was obtained by converting the volume change of the syringe pump into mass. The gas density data required for this conversion was taken from NIST REFPROP software (LEMMON; HUBER; MCLINDEN, 2007). Finally, the

mixture was homogenized under stirring at 378.15 K and, at least, 10 MPa above bubble point pressure for 20 minutes. The homogeneity of the system was controlled visually before starting pressure scanning experiments.

For each gas composition, an isothermal Constant Composition Expansion (CCE) test was performed, at five different temperatures, $T = (378.15, 358.15, 338.15, 323.15, 308.15, \text{ and } 293.15)$ K. From this data, PV curves were drawn to determine liquid vapor transitions ($L \rightarrow LV$ and $LL \rightarrow LLV$). Additionally, fluid visualization by intermediate of the SWIR camera was used for phase transitions involving several liquid phases such as $L \rightarrow LL$. This procedure was performed during pressures steps without any stirring. Then, when a new phase is detected, appearance pressure was registered for each mixture. From this experimental method, the expanded uncertainties with a conventional coverage factor $k_P = 2$ ($P = 95\%$) are 0.2 MPa for $L \rightarrow LV$ and $LL \rightarrow LLV$ phase transition pressures and 0.6 MPa for $L \rightarrow LL$ phase changes. These uncertainties were estimated using the quadratic sum of the uncertainties in pressure measurement and transition detection and by considering the effect of temperature uncertainty. The difference in pressure uncertainties between $L \rightarrow LV$ and $L \rightarrow LL$ transitions is mainly caused by the difficulty to detect the onset of liquid–liquid phase splitting in comparison to the observation of bubble formation. Furthermore, the steep slopes of liquid–liquid transition curves in p, T diagram significantly heighten the uncertainty of such phase transition pressures.

6.2.3. QCR Asphaltene flocculation test

Samples with asphaltene destabilization observed in the full visibility cell SWIR were analyzed using an PVT QCR assemble. Same compositions were reproduced and prepared in a variable-volume PVT cell adapted with a QCR sensor. This cell operates in pressures up to 100 MPa and in a temperature range of 283.15 K to 398.15 K. A piezoelectric quartz (intrinsic frequency of 3 MHz) is placed inside cell to scan acoustic properties of the fluid during CCE, as depicted in Figure 6.3. PVT cell pressure transducer was calibrated using an external pressure transducer at each temperature testing, resulting on 0.025% relative uncertainty. Crude oil and gas were injected using same procedure than used for SWIR assemble. System homogenization was achieved by intermediate of a magnetic agitator with a rotating velocity of 500 rpm^{-1} . Temperature measurements was achieved with a PT-100 thermometer located in the cell body, placed in a minimum distance relative to the fluid. Thermal control was made through a heating jacket and a

recirculating silicon thermal bath. Thermal regulation was achieved within ± 0.1 K. Variation of QCR frequency Δf and dissipation $\Delta \Gamma$ was determined between QCR vacuum signal and loaded QCR signal during CCE experiments. Harmonics 1 to 7 were recorded simultaneously during expansion of the oil. Same CCE depressurization rate than SWIR tests was implemented.

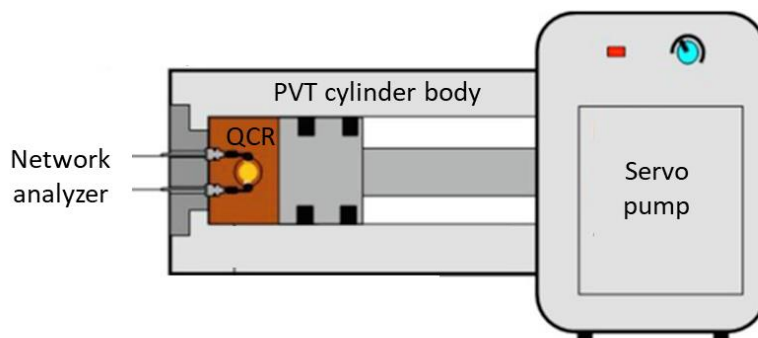


Figure 6.3 PVT with QCR assemble diagram (adapted from DARIDON; ORLANDI; CARRIER, 2016).

6.2.4. Thermodynamic Modelling

Liquid-vapor, liquid-liquid, and liquid-liquid-vapor equilibria for crude oil and gas mixtures were modelled by using Peng-Robinson equation of state (PR EOS) (PENG; ROBINSON, 1976), presented in Eq. 1. The use of PR EOS aims to show that the experimental behavior could be qualitatively reproduced with the thermodynamic model used in the oil and gas industry. At thermodynamic equilibrium, isofugacity was considered between the phases, and the fugacity coefficients for each component in each phase were calculated coupling the PR EOS with its classical mixing rules (Eqs. 6.2 and 6.3).

$$P = \frac{RT}{V_m - b} - \frac{a}{(V_m + b)(V_m - b)} \quad \text{Eq. 6.1}$$

$$a = \sum_i \sum_j x_i x_j \sqrt{a_i a_j} (1 - k_{ij}) \quad \text{Eq. 6.2}$$

$$b = \sum_i x_i b_i \quad \text{Eq. 6.3}$$

where p is the pressure, T is the temperature, R the universal gas constant, V_m the mixture molar volume, x_i is the molar fraction of the component i , a_i and b_i are their attraction

parameters and co-volume, and k_{ij} is the binary interaction parameter between component i and j , respectively.

For each component, the attraction parameters (a_i) and co-volume (b_i) for the PR EOS are calculated according to Eq. 6.4 and Eq. 6.5.

$$a_i = 0.45724 \cdot \frac{(RTc_i)^2}{Pc_i} \cdot \alpha_i(T) \quad \text{Eq. 6.4}$$

$$b_i = 0.0778 \cdot \frac{RTc_i}{Pc_i} \quad \text{Eq. 6.5}$$

Temperature dependence of the attraction parameter is calculated as follows:

$$\alpha_i(T) = \left(1 + m_i \left(1 - \sqrt{\frac{T}{Tc_i}} \right) \right)^2 \quad \text{Eq. 6.6}$$

The form factor (m_i) for PR EOS is derived from the acentric factor (ω_i), as presented in Eqs. 7 and 8:

$$m_i = 0.37464 + 1.54226\omega_i - 0.26992\omega_i^2 \quad \text{for } \omega_i < 0.49 \quad \text{Eq. 6.7}$$

$$m_i = 0.379642 + 1.48503\omega_i - 0.164423\omega_i^2 + 0.016666\omega_i^3 \quad \text{for } \omega_i \geq 0.49 \quad \text{Eq. 6.8}$$

For the equations presented above, Pc_i and Tc_i represent the critical pressure and critical temperature of the components in the mixtures, respectively. These properties are listed in Table 6.2 for pure components, as methane, carbon dioxide, and the pure hydrocarbons. Nevertheless, there are some difficulties to determine these properties for heavy crude oil fractions. For this purpose, several approaches were proposed in the literature (KESLER; LEE, 1976; KATZ; FIROOZABADI, 1978; TWU, 1984; PEDERSEN; THOMASSEN; FREDENSLUND, 1988; PEDERSEN; FREDENSLUND; THOMASSEN, 1989; ZHANG; PEDROSA; MOORWOOD, 2012; KUMAR; OKUNO, 2012). In this work, Total S.A. in-house correlations were used. They were designed to use the minimum number of parameters in order to rely on the two relatively well studied quantities: the density and the boiling point (based on the alkane retention times and the ASTM table) (“ASTM D 5307 (1992) Determination of Boiling Range Distribution of Crude Petroleum by Gas Chromatography. American Society for Testing and Materials”;

UNGERER; BATUT, 1997). To get the LL behavior, a heavy condensed CNA fraction was split from the C20+ cut. Compared to a standard fraction with the same molecular weight, the CNA fraction has a high critical pressure, in line with the aromatic components trend.

Table 6.2 Molecular weight, critical temperature, critical pressure, and acentric factor for gases and crude oil cuts for condensed model

Compound	<i>MW</i>	<i>T_c</i> , K	<i>P_c</i> , MPa	<i>ω</i>
CO ₂	44.01	304.20	7.380	0.2250
C1	16.04	190.60	4.600	0.0115
C3	44.10	369.80	4.246	0.1454
iC4	58.12	408.10	3.650	0.1760
nC4	58.12	425.20	3.800	0.1928
iC5	71.89	465.83	3.496	0.2226
nC5	72.15	469.60	3.370	0.2273
C6	84.00	512.55	3.350	0.2504
Mcyclo-C5	84.16	532.70	3.790	0.2395
Benzene	78.11	562.00	4.890	0.2120
Cyclo-C6	84.16	553.40	4.070	0.2144
C7	96.00	548.15	3.140	0.2848
Mcyclo-C6	98.19	572.10	3.480	0.2333
Toluene	92.14	591.70	4.110	0.2566
C8	107.00	576.35	2.970	0.3155
C2-Benzene	106.16	617.10	3.610	0.3011
m&p-Xylene	106.16	616.20	3.520	0.3243
o-Xylene	106.16	630.20	3.730	0.3136
C9	121.00	606.04	2.837	0.3735
C10	134.00	632.48	2.684	0.4096
C11	147.03	656.30	2.551	0.4171
C12	159.90	677.96	2.434	0.4458
C13	172.64	697.83	2.331	0.4736
C14	185.22	716.18	2.239	0.5004
C15	197.62	733.22	2.157	0.5264
C16	209.83	749.14	2.084	0.5516
C17	221.82	764.06	2.018	0.5761
C18	233.59	778.11	1.958	0.5998
C19	245.11	791.38	1.904	0.6230
C20+	374.19	900.63	1.464	0.8327
CNA	550.78	1240.00	1.550	1.2000

Phase boundaries were calculated using a multiphasic flash software developed by Total S.A. (BEST v12.5, from Total, France), based on Michelsen tangent plan distance method (MICHELSEN, 1982a, 1982b). Binary interactions parameters between crude oil fractions and gases, i.e., methane and carbon dioxide, were fitted to correlate experimental phase transition data, by minimizing the relative absolute deviation (*RAD*) objective function:.

$$RAD = \sum_{i=1}^{N^{exp}} |(P_i^{calc} - P_i^{exp}) / P_i^{exp}| \quad \text{Eq. 6.9}$$

where P_i^{calc} and P_i^{exp} are the calculated and experimental phase transition pressures, respectively.

After fitting, the model was used predictively to describe the phase behavior of crude oil + methane + CO₂, the only interaction parameter fitted for that system was between the methane and CO₂.

6.3. Results and Discussion

6.3.1. Mixtures of crude oil and CO₂

Phase diagrams for the crude oil + CO₂ mixtures (up to 70 mol% of CO₂) are depicted in Figure 6.4 and the experimental data are presented in Table 6.3. From these data, it could be observed that for carbon dioxide content below 60 mol%, only LV transitions occur, over the covered temperature domain. For these systems, the bubble point pressures were properly identified by changes in compressibility during depletion, which indicates the formation of a gaseous phase.

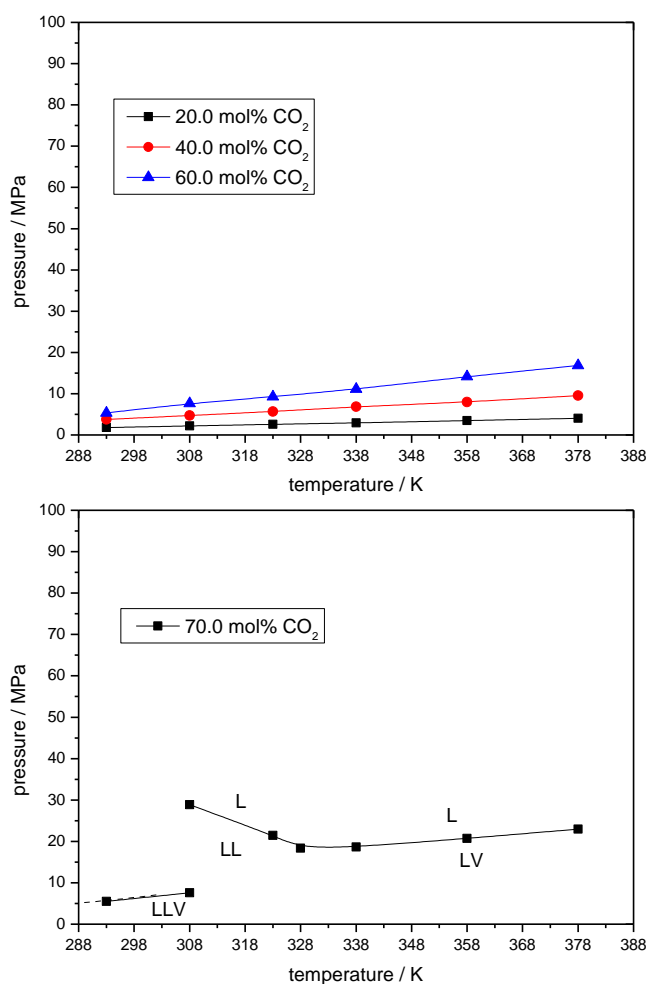


Figure 6.4 Crude oil + CO₂ phase diagrams obtained for carbon dioxide composition of 20.0, 40.0, 60.0, and 70.0 mol%, at T = (293.15 to 378.15). Adjusted lines for eye-guide.

Table 6.3 Experimental phase transition data for crude oil + CO₂ systems^a.

T / K	p / MPa	Transition	T / K	p / MPa	Transition
$x_{\text{CO}_2} = 20.0 \text{ mol\%}$			$x_{\text{CO}_2} = 78.1 \text{ mol\%}$		
293.15	1.8	L→LV	293.15	5.6	LL→LLV
308.15	2.2	L→LV	308.15	7.6	LL→LLV
323.15	2.6	L→LV	329.15	67.8	L→LL
338.15	2.9	L→LV	331.15	52.3	L→LL
358.15	3.5	L→LV	338.15	41.8	L→LL
378.15	4.1	L→LV	358.15	34.3	L→LV
			378.15	33.9	L→LV
$x_{\text{CO}_2} = 39.7 \text{ mol\%}$			$x_{\text{CO}_2} = 84.0 \text{ mol\%}$		
293.15	3.7	L→LV	293.15	5.4	LL→LLV
308.15	4.7	L→LV	308.15	7.6	LL→LLV
323.15	5.7	L→LV	349.15	78.3	L→LL
338.15	6.8	L→LV	353.15	68.7	L→LL
358.15	8.0	L→LV	356.15	65.0	L→LL
378.15	9.5	L→LV	358.15	62.7	L→LL
			361.15	59.0	L→LL
293.15	5.3	L→LV	365.35	55.8	L+Asph→L+Asph+V
308.15	7.6	L→LV	367.15	54.0	L+Asph→L+Asph+V
323.15	9.3	L→LV	378.15	51.7	L+Asph→L+Asph+V
338.15	11.1	L→LV	368.15	73.0	L→L+Asph (AOP)
358.15	14.1	L→LV	378.15	74.4	L→L+Asph (AOP)
378.15	16.8	L→LV			
$x_{\text{CO}_2} = 60.2 \text{ mol\%}$			$x_{\text{CO}_2} = 86.1 \text{ mol\%}$		
293.15	5.5	LL→LLV	293.15	5.5	LL→LLV
308.15	7.6	LL→LLV	308.15	7.6	LL→LLV
308.15	28.9	L→LL	358.15	91.8	LL+Asph→LL
323.15	21.5	L→LL	378.15	69.8	LL+Asph→LL
328.15	18.4	L→LV			
338.15	18.6	L→LV			
358.15	20.7	L→LV			
378.15	23.0	L→LV			

^a Standard uncertainties u are $u(T) = 0.05 \text{ K}$ and the expanded uncertainties U_c (level of confidence = 0.95) is $U_c(p \text{ L→LV}) = 0.2 \text{ MPa}$, $U_c(p \text{ LL→LLV}) = 0.2 \text{ MPa}$, $U_c(p \text{ L→LL}) = 0.6 \text{ MPa}$.

As the CO₂ content increases up to 70.0 mol%, the phase behavior exhibits a Liquid-Liquid immiscibility. The behavior observed with this pseudo-binary seems like a Type III diagram, according the van Konynenburg and Scott classification for binary mixtures. The L→LV transition switches into a LL immiscibility region at low

temperatures, with LL→LLV transitions near to the carbon dioxide critical point. For this composition, a LL equilibrium domain is observed for temperature below 328.15 K. For higher temperatures, liquid immiscibility was not observed and only L→LV transitions were found. It is important to mention that the L→LL transition cannot be identified by changes in system compressibility, indicating similar density for the different liquid phases.

Figure 6.5 depicts crude oil + CO₂ volumetric behavior obtained from constant composition expansion (CCE) tests carried out in mixtures with a carbon dioxide molar fraction ranging from 20.0 to 70.0 mol%, at two different temperatures (293.15 K and 323.15 K). From this figure, it can be clearly observed a L→LV transition at 323.15 K, for a gas composition below 60.0 mol%. When CO₂ content reaches 70.0 %mol, no sharp changes in compressibility are observed at 323.15 K. Additionally, for the same composition and at 293.15 K, a clear LL→LLV transition is observed with a sharp change in system compressibility. Same volumetric behavior was observed at 308.15 K, not reported in this figure.

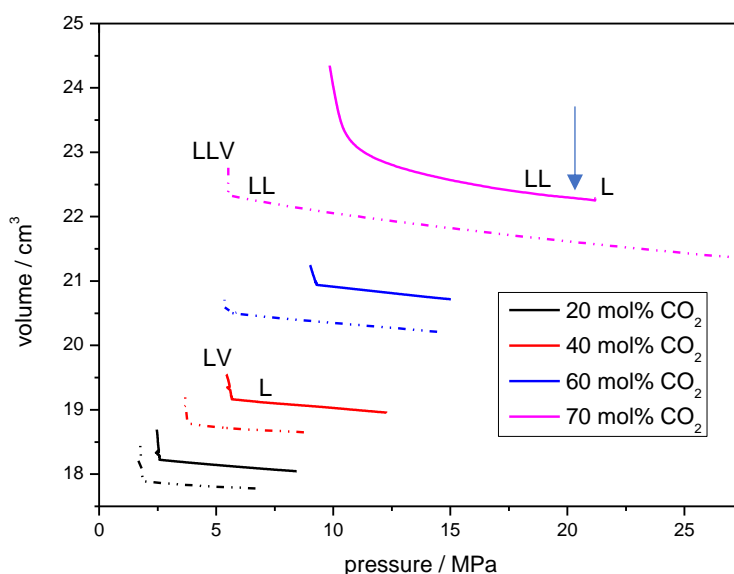


Figure 6.5 pV curves of crude oil + CO₂ systems for four CO₂ different composition (20.0, 40.0, 60.0, and 70.0 mol%), at 293.15 K (dashed lines) and 323.15 K (continuous lines).

Fluid inspection using the SWIR camera was necessary to properly identify some of the fluid-fluid transitions detected in high CO₂ content systems. Figure 6.6 shows

L→LV, L→LL and LL→LLV phase equilibria found in crude oil + CO₂ systems with different carbon dioxide contents up to 70.0 mol%. Typical L→LV transitions are like those presented in Figure 6.6-(A); gas bubbles arise from the bulk fluid when pressure decreases below the bubble point pressure. As the bubbles interface disperses the light, the fluid inspection below this point was only possible in a limited part of the cell, near the sapphire window.

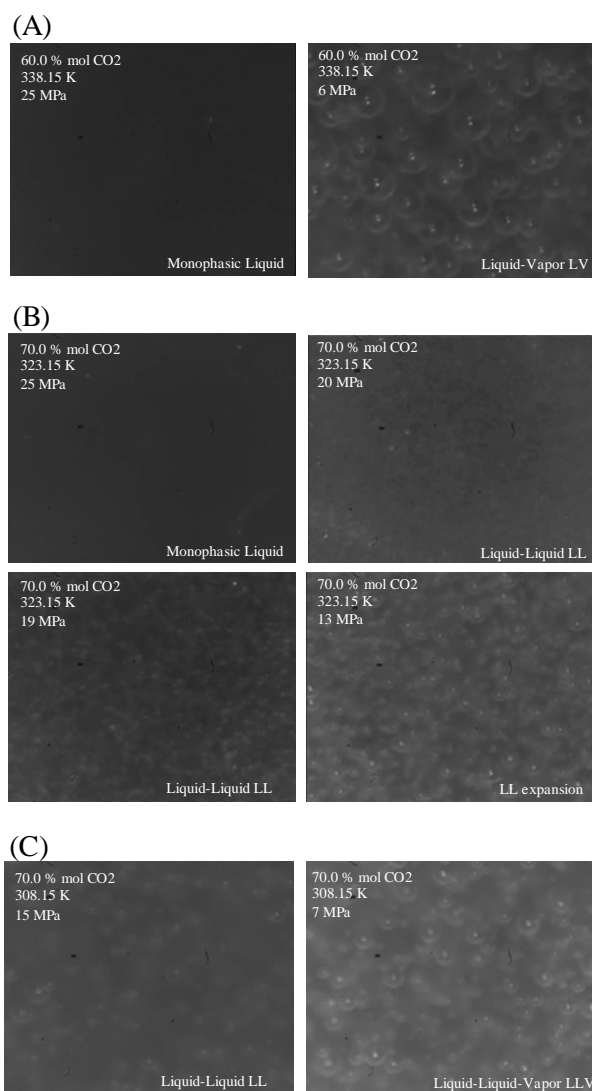


Figure 6.6 Different phase transitions detected by SWIR camera, as follows: (A) Liquid-vapor transition, for crude oil + 60.0 CO₂ mol% at 338.15 K; (B) Liquid-liquid transition, for crude oil + 70.0 CO₂ mol% at 323.15 K; and (C) liquid-liquid-vapor transition, for crude oil + 70.0 CO₂ mol% at 308.15 K.

For crude oil + CO₂ mixtures with a high CO₂ content, L→LL transitions were detected when the pressure decreases from monophasic liquid condition to two liquid phases equilibrium by the appearance of turbidity in the system as presented for the 70.0 mol% of CO₂, at 323.15 K in Figure 6.6 B), . Fine dispersed liquid phase evolves from the bulk fluid, with negligible compressibility changes. When pressure continues decreasing, LL equilibrium is more evident and droplets start to grow until they resemble to the LV equilibrium with big bubbles dispersed in the oily phase. This liquid dispersed phase was associated in the literature with a dense and CO₂-rich phase that also solubilizes some crude oil compounds (EGHBALI; DEGHANPOUR, 2019; LINDELOFF; MOGENSEN; OKUNO; XU, 2014; ORR; YU; LIEN, 1981). It is important to mention that no phase segregation was observed during depletion, indicating that the high dispersity is related to density similarities between the two liquid phases (AL GHAFRI; MAITLAND; TRUSLER, 2014; OKUNO; XU, 2014a; ORR; YU; LIEN, 1981; WANG et al., 2003). At lower temperatures and pressures conditions, close to critical conditions of pure CO₂, a LLV equilibrium is detected, as presented in Figure 6.6-(C). Visually, this phase transition is not evident but the compressibility change in the system reveals the vapor phase evolution, as previously presented in Figure 6.5.

Crude oil + CO₂ phase behavior for higher CO₂ content (above 70 mol%) is presented in Figure 6.7. LL region shifts to higher temperatures, with the increase of carbon dioxide content. The mixture containing 78.0 mol% of CO₂ displayed a LL region at 338.15 K, which is 15 K above the mixture with 70.0 mol% of CO₂. This LL region change was associated to heavy compounds in the C₇₊ crude oil fraction (HUANG; TRACHT, 1974; ORR; YU; LIEN, 1981), along with the asymmetry between CO₂ and crude oil, by increasing carbon dioxide content. It was described in the literature (AL GHAFRI; MAITLAND; TRUSLER, 2014; HUANG; TRACHT, 1974; ORR; YU; LIEN, 1981) a LL region located 6 K from the LLV UCEP, typically reported as 317.15 K for CO₂ + crude oil systems. However, heavier compounds present in the studied crude oil could be the responsible for this LL region expansion. It can be noted in Table 2.1 that most of the existing literature for LLV in crude oil systems, used lighter crude oil samples for analysis, especially with lighter MW C₂₀₊ fraction.

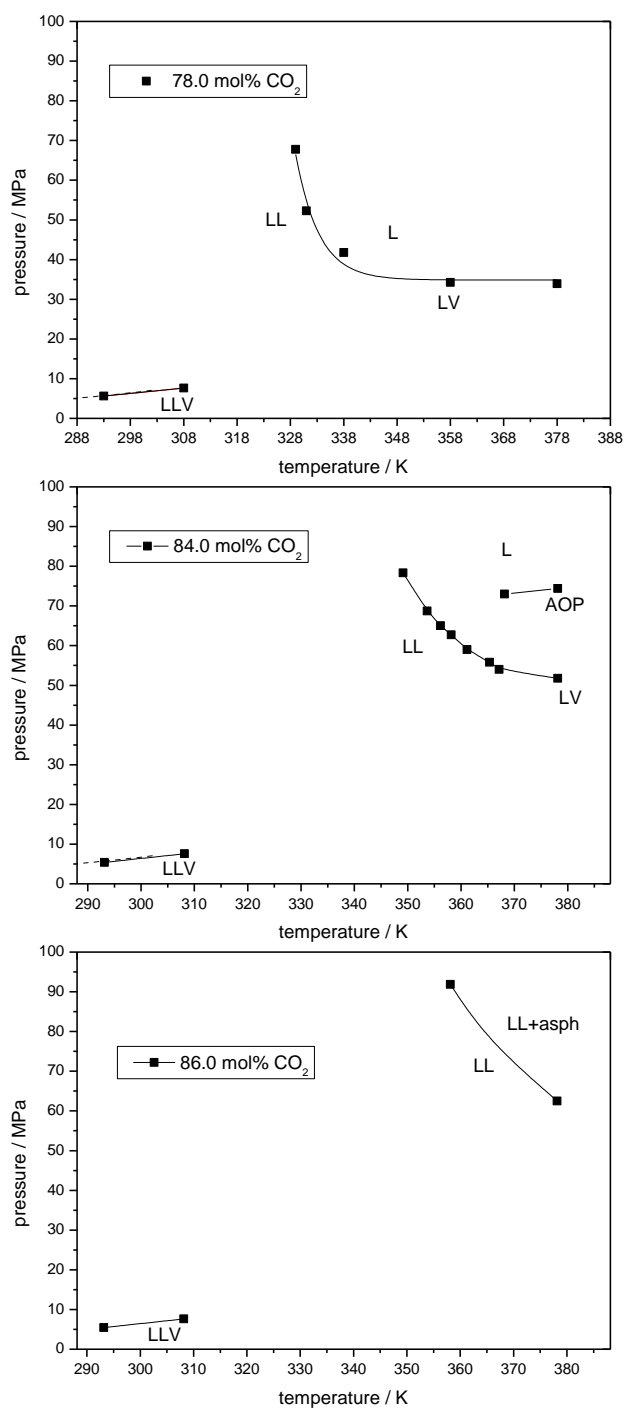


Figure 6.7 Crude oil + CO₂ systems phase diagrams obtained for a CO₂ composition of 78.0, 84.0, and 86.0 mol%, at a temperature range of $T = (293.15 \text{ to } 378.15) \text{ K}$. Adjusted lines for eye-guide.

Moreover, the LL equilibrium presented different characteristics when compared to those at 70.0 mol% of CO₂. For mixtures containing 78.0 and 84.0 mol% of CO₂, SWIR camera results are depicted in Figure 6.8-(A) and (B). For these compositions, an extremely dispersed phase heterogeneity was observed in the fluid. It must be the reason why it can only be detected using the visualization of the stirrer at the end point of the cell as a reference. When the LL pressure point is reached, the visibility of the stirrer is lost due to the fluid turbidity. Therefore, the formed phase is observed as a fine dispersed fluid, that only grows to form big droplets at lower pressures.

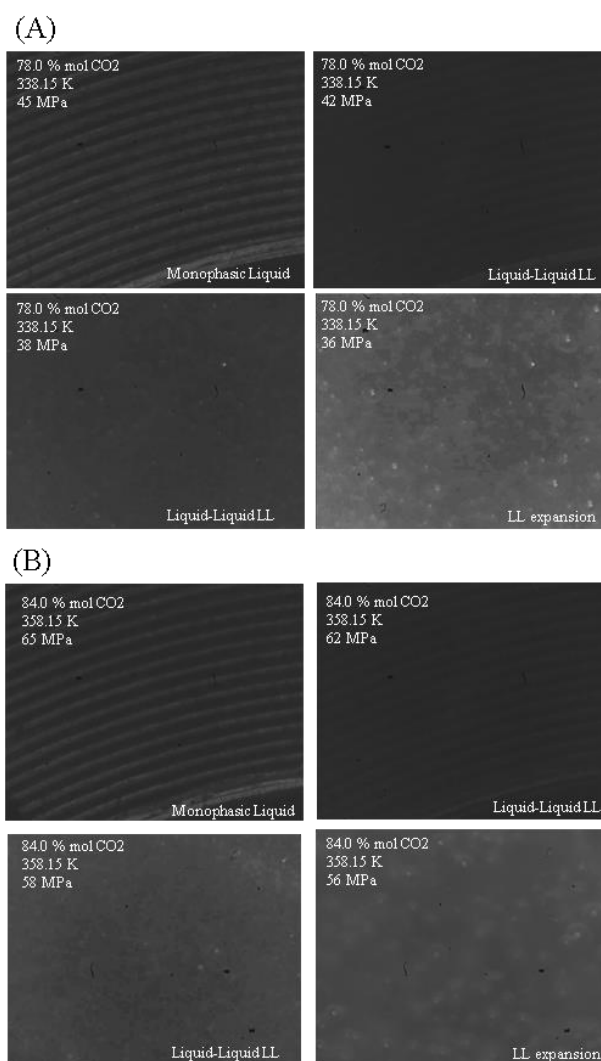


Figure 6.8 Crude oil + CO₂ liquid-liquid phase transition for 78.0 mol% CO₂ at 338.15 K (A) and 84.0 mol% CO₂ at 358.15 K (B), during constant composition expansion.

Also, it is important to mention that no droplets segregation by gravity was observed, what could indicate similar densities for the different phases (AL GHAFRI; MAITLAND; TRUSLER, 2014; OKUNO; XU, 2014a; ORR; YU; LIEN, 1981; WANG et al., 2003). Additionally, the second liquid phase (CO₂-rich dispersed phase) instantaneously redissolves when the pressure is increased above the L→LL transition pressure. This rapid redissolution behavior was reported for a similar crude oil when mixed with high composition of methane in previous chapters.

For the mixture containing 84.0 mol% of CO₂, it was observed the formation of an asphaltenic phase by using the SWIR fluid inspection. This phase was detected at 358.15 and 378.15 K, at higher pressures than the LL locus. However, the asphaltene onset pressure (AOP) was difficult to determinate trough SWIR imaging. For that reason, complementary tests were made at 368.15 and 378.15 K using a quartz crystal resonator (QCR) technique. The AOP obtained by using the QCR technique for the 84.0 mol% CO₂ mixture is presented in Figure 6.7. It is interesting to mention that no asphaltenes precipitation were detected at the below the LL locus.

For the highest CO₂ content studied (86.0 mol%), no monophasic condition was found in the temperature pressure ranges investigated (up to 90 MPa). Specifically, an asphaltic phase was observed, generated by the high gas content in the system. This phase was observed as an opaque phase that adhered to the sapphire window of the PVT cell (CARDOSO et al., 2015). Similar observations were recently reported for asphalt phase formation using the same SWIR visualization technique (DARIDON et al., 2020). SWIR camera results for this system are presented in Figure 6.9 for T = 378.15 K. From these experiments at 86.0 mol % gas, the adhered phase starts to dissolve forming brightener spots in the sapphire window, as shown in the Figure 6.9-(A). When pressure reaches 68 MPa at 378.15 K, only LL equilibrium remains present in the form of small droplets. At lower temperatures, Figure 6.9-(B), the behavior is similar, but the liquid droplets are bigger, which could be related to the high gas content of the mixture.

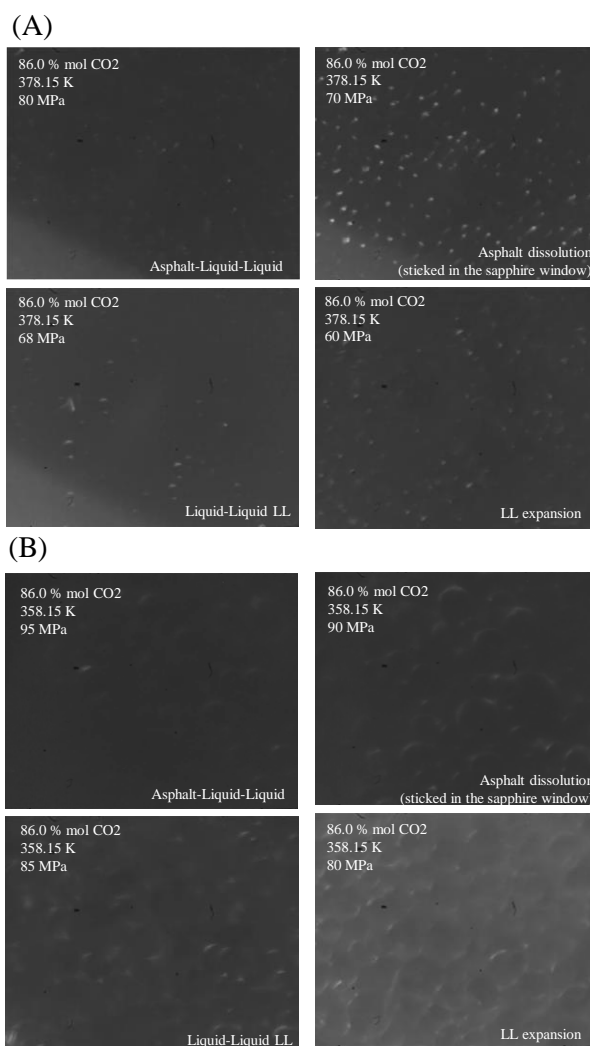


Figure 6.9 Crude oil + CO₂ liquid-liquid phase transition for 86.0 mol% CO₂ at T = 378.15 K (A) and at T = 358.15 K (B), during constant composition expansion.

It is important to mention that even for high gas content, LL→LLV transition was detected at low temperatures. Accordingly, a sharp change in system compressibility was observed near the pure CO₂ critical pressure, similarly to the PV curves for the crude oil + CO₂ systems at 293.15 K given in the Figure 6.5. Additionally, LL→LLV transition pressure is independent to the CO₂ content, even at the higher carbon dioxide composition. This behavior was previously described by Orr et al., classified as a Type II LLV locus, and it was shown to be related to the lack of light-ends in the crude oil sample (COUTINHO; JØRGENSEN; STENBY, 1995; ORR; YU; LIEN, 1981).

6.3.1.1. QCR analysis for mixtures of crude oil and CO₂

Phase transitions type L→LV, L→LL and LL→LLV (low temperature) were evaluated for 78.0 mol% CO₂ by intermediate of QCR, results are presented in Figure 6.10 to Figure 6.12. It can be noted that QCR dissipation response is sensible to transition involving a vapor phase formation, i.e., LV and LLV. The transition is identified as a sharp V-shape correlated to an increase in the quartz dissipation Γ as pressure decrease associated to sample's gas release effect on fluid density and viscosity product. No significant changes were detected in QCR frequency during L→LV transitions. Additionally, variation on frequency or dissipation were not able to detect L→LL transitions during isobaric cooling. This result could indicate neglectable changes on the product of the viscosity and density between the monophasic and LL region.

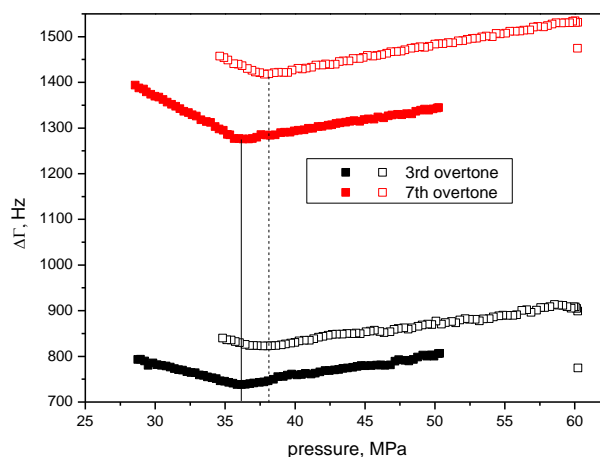


Figure 6.10 QCR dissipation during CCE for crude oil + 78.0 mol% CO₂ systems at 105 °C (solid symbols) and 85 °C (unfilled symbols).

Higher CO₂ content were tested to study crude oil asphaltene destabilization. Results for 78.0, 82.0, 84.0 and 84.7 CO₂ mol% are presented in Figure 6.11. Only 7th overtone response is showed as reference because of their better resolution, same behavior is observed for other overtones. It can be noted that above 84.0 CO₂ mol% content, a change in QCR frequency and dissipation behavior is observed during CCE. This change is associated to the increase of system viscosity by asphaltenes flocculation, together with deposition in QCR surfaces. This effect is more evident at higher gas content and coincides to the dispersed solid phase observed using the SWIR camera, however QCR results allow a better the determination of AOP.

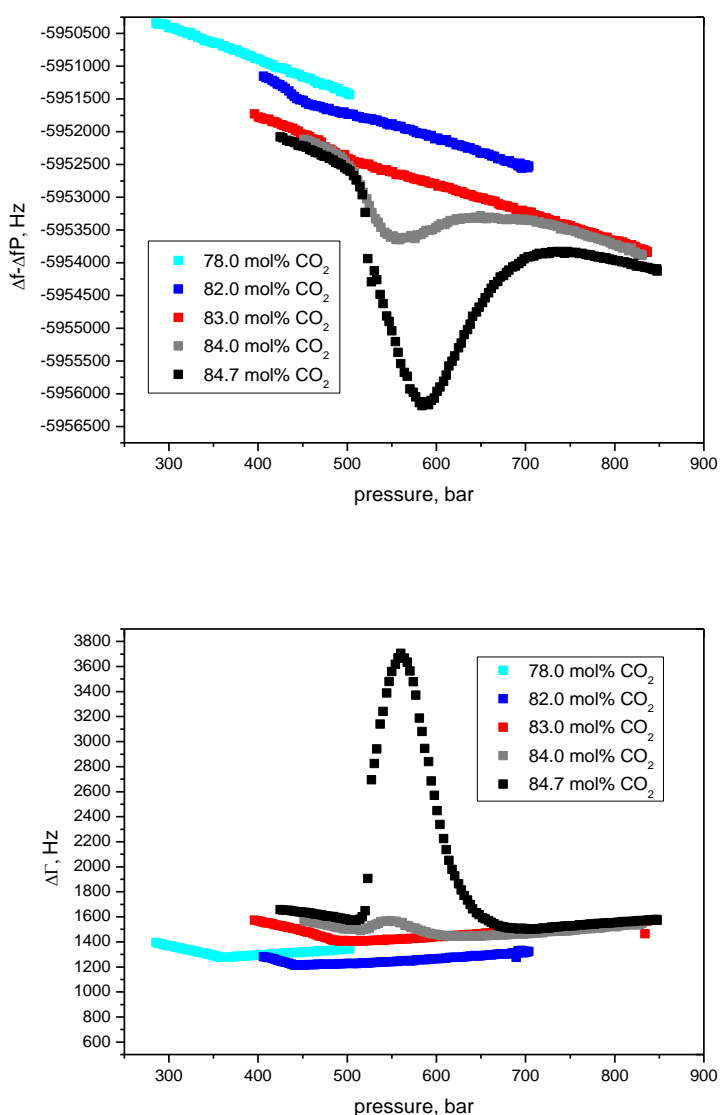


Figure 6.11 7th overtone QCR frequency and dissipation during CCE for crude oil and CO₂ systems at 378.15 K.

A comparison between the full phase diagrams determined by either full SWIR visibility cell and indirect QCR results are shown in Figure 6.12. One can note that minimal variation on L→LV and LL→LLV detections between techniques is achieved. Differences in the transition region can be attributed to the marked increase on steep slopes pressures, and experimental composition differences. However, it is important to stress that this type of diagrams can be only achieved by the conjunction of the two used techniques. As previously mentioned, the LL phase equilibria correspond to a fine dispersed liquid phase that only was detected by SWIR inspection. For AOP, QCR gives

the quantitative data for the final construction of the phase diagram whereas visual observation in SWIR light provides qualitative visual information on the nature and morphology of the asphaltene rich phase (small aggregates, big flock flocks, or heavy phase and bitumen) whereas the combination of both techniques allows to know if its remain dispersed or on the other hand it deposit on equipment surfaces.

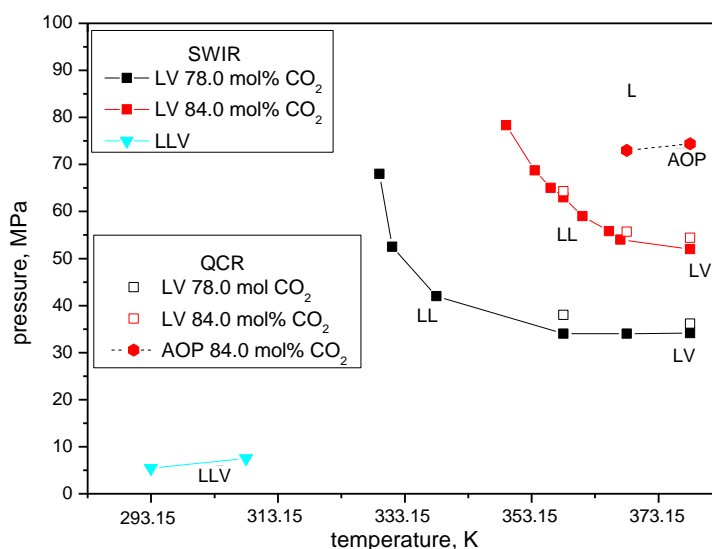


Figure 6.12. Phase diagram obtained using SWIR imaging and QCR analysis for crude oil and CO₂ mixtures.

6.3.2. Mixtures of crude oil and methane

Figure 6.13 depicts crude oil + methane phase diagrams for methane composition of 30.0, 45.0, 60.0, 70.0, 78.0, and 80.0 mol%, at $T = (293.15 \text{ to } 378.15 \text{ K})$. Moreover, experimental data is presented in Table 6.4. For methane composition below 45.0 mol%, only LV transitions are observed, with an increase in bubble point pressure with temperature. As the methane content increases, the bubble point pressure variation with temperature is almost negligible, until a methane content above 78.0 mol% for which the bubble point pressure decreases with temperature. This behavior is expected for near-critical fluids, due to the high methane content in the mixture. Figure 6.14 depicts the pressure-composition ($P-x_{CH_4}$) diagram for two reference temperatures ($T = 323.15$ and 378.15 K). From these results, there is no evidence of dew point at higher methane content evaluated.

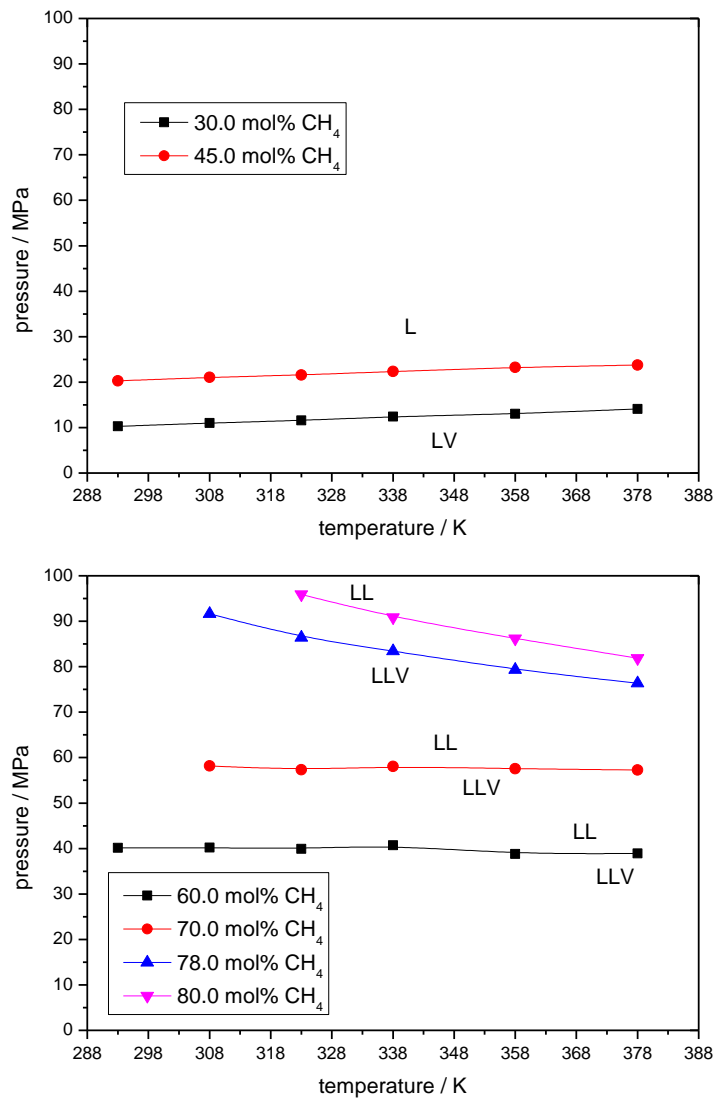


Figure 6.13. Crude oil + methane phase diagrams obtained for methane composition of 30.0, 45.0, 60.0, 70.0, 78.0 and 80.0 mol%, at $T = (293.15 \text{ to } 378.15)$. Adjusted lines for eye-guide.

Table 6.4 Experimental phase transition data for crude oil + methane systems ^a.

T / K	p / MPa	Transition	T / K	p / Mpa	Transition
$x_{\text{CH}_4} = 31.0 \text{ mol\%}$			$x_{\text{CH}_4} = 70.2 \text{ mol\%}$		
293.15	10.3	L→LV	308.15	58.4	LL→LLV
308.15	11.1	L→LV	323.15	57.6	LL→LLV
323.15	11.7	L→LV	338.15	58.3	LL→LLV
338.15	12.5	L→LV	358.15	57.8	LL→LLV
358.15	13.2	L→LV	378.15	57.5	LL→LLV
378.15	14.2	L→LV			
$x_{\text{CH}_4} = 45.3 \text{ mol\%}$			$x_{\text{CH}_4} = 78.2 \text{ mol\%}$		
293.15	20.3	L→LV	308.15	91.7	LL→LLV
308.15	21.1	L→LV	323.15	86.6	LL→LLV
323.15	21.7	L→LV	338.15	83.6	LL→LLV
338.15	22.6	L→LV	358.15	79.6	LL→LLV
358.15	23.4	L→LV	378.15	76.6	LL→LLV
378.15	23.9	L→LV			
$x_{\text{CH}_4} = 60.2 \text{ mol\%}$			$x_{\text{CH}_4} = 80.2 \text{ mol\%}$		
293.15	40.2	LL→LLV	323.15	96.0	LL→LLV
308.15	40.4	LL→LLV	338.15	91.0	LL→LLV
323.15	40.1	LL→LLV	358.15	86.4	LL→LLV
338.15	40.9	LL→LLV	378.15	82.1	LL→LLV
358.15	39.0	LL→LLV			
378.15	39.1	LL→LLV			

^a Standard uncertainties u are $u(T) = 0.05 \text{ K}$ and the expanded uncertainties U_c (level of confidence = 0.95) is $U_c(p \text{ L→LV}) = 0.2 \text{ MPa}$, $U_c(p \text{ LL→LLV}) = 0.2 \text{ MPa}$.

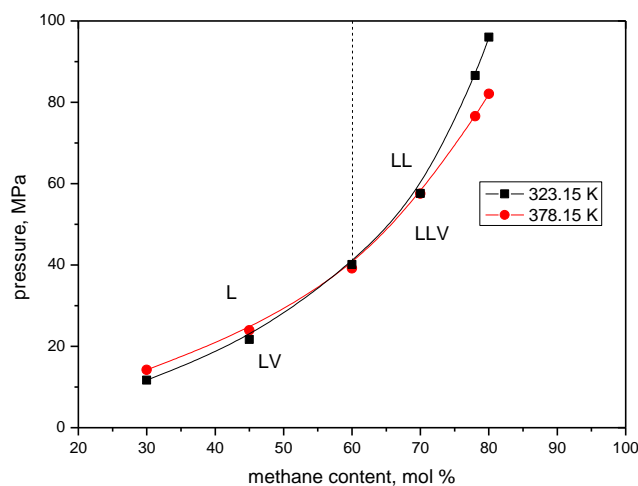


Figure 6.14. Crude oil + methane mixtures pressure-composition diagram for $T = (323.15$ and $378.15)$ K. Adjusted continuous lines for eye-guide. Dashed line indicates experimental LL region.

Additionally, a phase immiscibility was detected for the mixtures with methane content above 60.0 mol%. This phase was observed when the fluid was inspected with the SWIR camera, with no changes in fluid compressibility during expansion. In Figure 6.15, a typical PV results during CCE is reported. From these results, LV transitions can be identified by a sharp change in system volume, especially for methane content below 78.0 mol%. For higher methane content, the vapor phase formation was confirmed by using the SWIR camera inspection.

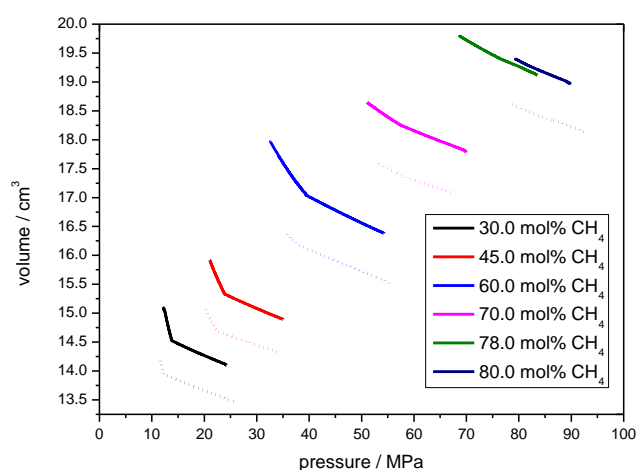


Figure 6.15 PV curves for the crude oil + methane systems for four methane different composition (30.0, 45.0, 60.0, 70.0, 78.0, and 80.0 mol%), at 338.15 K (dashed lines) and 378.15 K (continuous lines).

Figure 6.16 reports typical results for fluid behavior observed with the SWIR camera for different methane contents. $T = 358.15$ K was selected as an example, but similar observations were detected for all tested temperatures. For methane content below 45.0 mol%, under high pressure conditions, a monophasic fluid is obtained, as shown in Figure 12-(A) and (B). No dispersed phase is observed, and the gas totally dissolves in the crude oil. Then, LV is detected at lower pressure, concordant with the system compressibility increase.

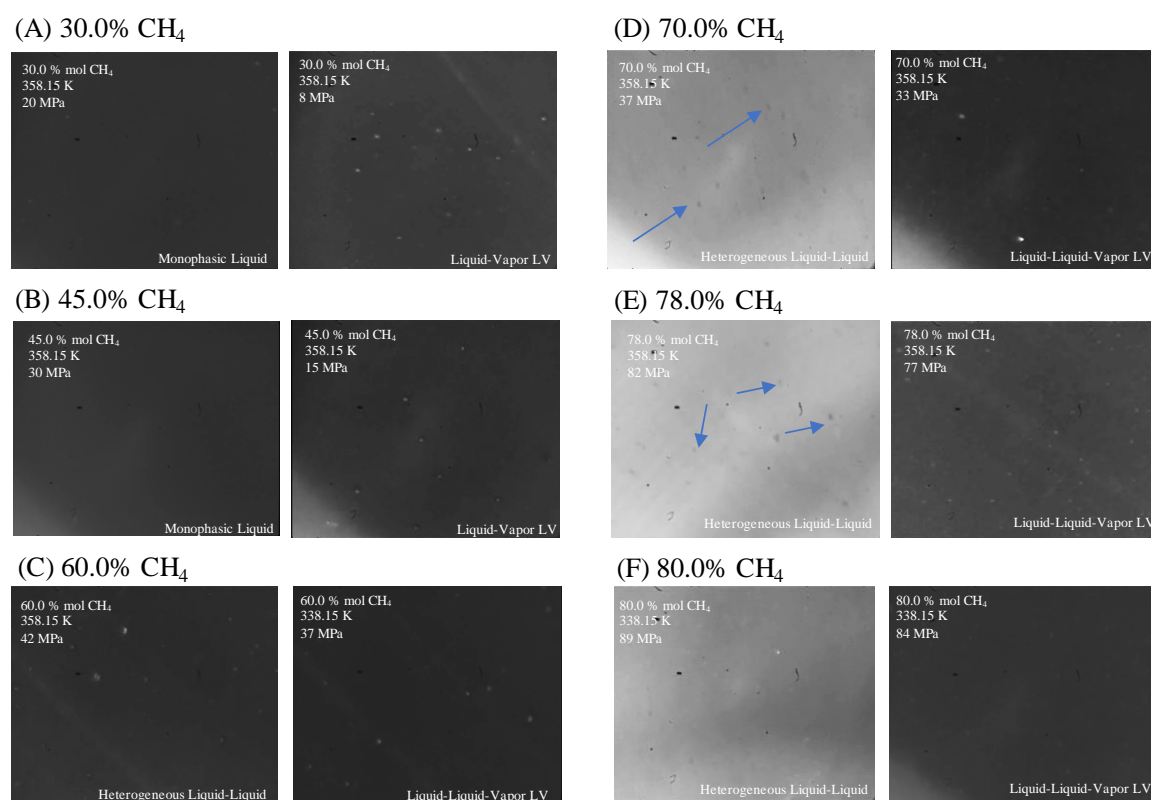


Figure 6.16. Crude oil + methane phase transition detected by SWIR camera for different methane content, as follows: (A) 30.0 mol%; (B) 45.0 mol%, (C), 60.0 mol%, (D) 70.0 mol%, (E) 78.0 mol%, and (F) and 80.0 mol%, at a referential $T = 358.15$ K, during constant composition expansion.

On the other hand, when the methane content increases up to 60.0 mol%, a different behavior is observed. No monophasic system is obtained at high pressure, even at 70 MPa. This phase immiscibility is associated with a liquid-liquid equilibrium, characterized by small droplets remaining dispersed in the oily phase (Figure 6.16-(C)). In contrast of vapor phase bubbles ascending and accumulating at the top of the cell due

to their lower density, the liquid phase constantly moves around, which should indicate a similar density to the one of the oil phase.

For a methane content above 60 mol%, fluid density reaches a minimum and a brighter fluid is observed with the SWIR camera, as presented in Figure 6.16 (D) to (F). For the mixtures with methane content above 70 mol%, the liquid-liquid heterogeneity is also observed. Specifically, the oleic phase bulk showed a more and more important droplets dispersion. When the whole fluid is examined – i.e., SWIR camera displaced throughout the entire volume of the sample – the LL dispersion appeared to affect the entire fluid, without segregation or decantation by gravity. Moreover, when the pressure is reduced, a vapor phase is observed leading to the fluid opacification which could be explained by the light diffraction at the bubbles interface.

Results on previous chapters showed atypical phase behavior when crude oil is mixed with methane at high gas proportion. Classical techniques did not allow to properly determine the properties and characteristics of the dispersed phase. Until this point, the information from past chapter could indicate that formed phase is constituted by heavy compounds. However, it is impossible to address if the formed phase is related to LL type equilibria. There are some common features for both studies – i.e., SWIR and conventional PVT, as follows: (i) the phase heterogeneity is observed as a fine dispersion that easily dissolves when vapor evolves; and, also, (ii) the formation of a heavy asphaltic phase formation seems to create a sticking material, less disperse, that agglomerates in the cell and interact to polar surfaces, as the sapphire windows of the HPM and cell windows.

6.3.3. *Mixtures of crude oil + methane + CO₂*

Results of phase behavior for mixtures of crude oil and methane + CO₂ is presented in Figure 6.17. Similar than results using pure methane as gas, liquid-liquid immiscibility region is also observed from 60.0 mol% of gas for this system. LV and LLV transitions were observed at lower pressures than pure methane systems because of CO₂ contribution. This reduction in systems vapor transitions allowed the recombination of 4.0 mol% more gas, the maximum gas composition reached with pure methane was 80.0 mol% because of PVT operational limits. At this higher gas composition, asphaltene immiscibility was observed at 84.0 mol% of gas. It is important to stress that it is achieved 2.0 gas mol% below the observed flocculation point using pure CO₂. This reduction on

asphaltene flocculation gas composition can be related to the higher precipitant effect of methane than pure CO₂.

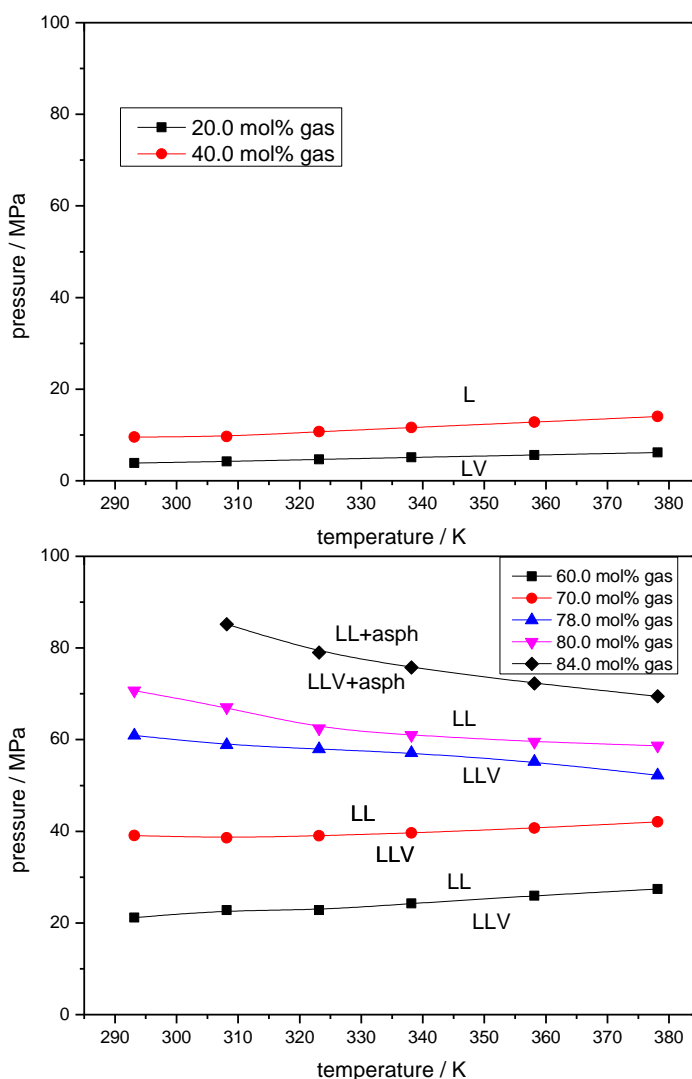


Figure 6.17. Phase diagrams obtained for crude oil + methane + CO₂ systems, with 20.0, 40.0, 60.0, 70.0, 78.0, 80.0 and 84.0 gas mol% from 293.15 to 378.15 K (adjusted lines for eye-guide).

The different types of phase transitions detected by SWIR imaging are presented in Figure 6.18. At lower gas content, only L→LV transition is observed. At 60.0 mol%, a fine dispersed heterogeneity is noted and does not dissolve with pressure until 85.0 MPa. This behavior remains until 80.0 mol% of gas. At the higher gas content of 84.0 mol%, an asphaltenic phase is noted as a material that sticks in the sapphire windows.

This phase is more evidently detected during high stirring velocities, as depicted in Figure 6.19.

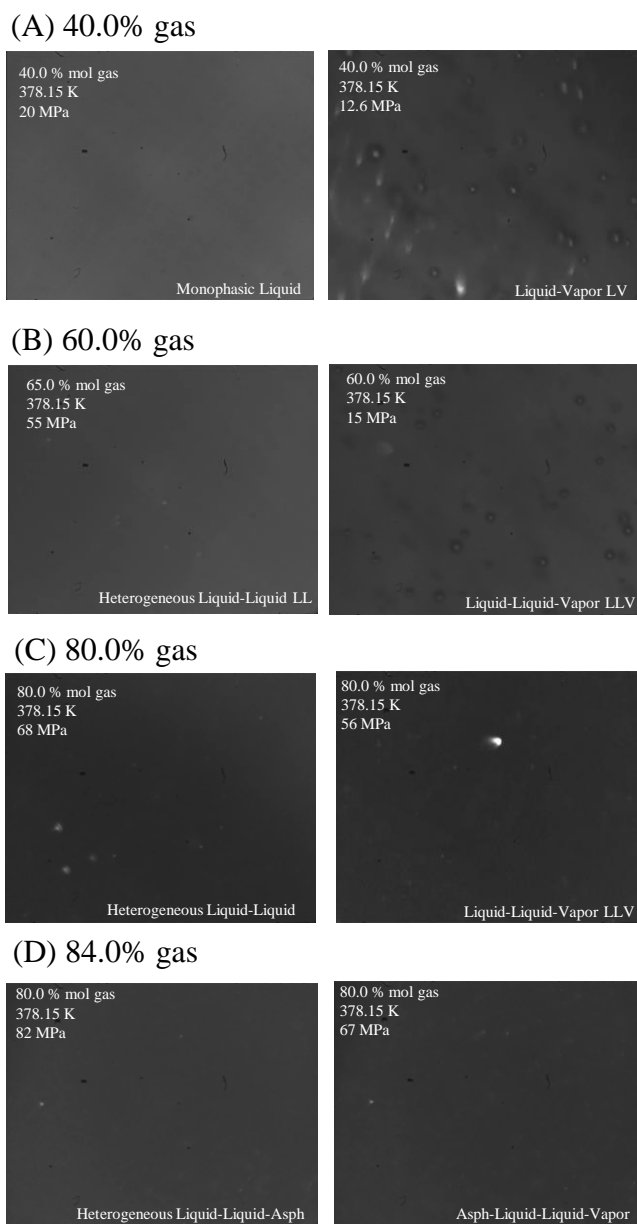


Figure 6.18. Different phase transitions detected by SWIR camera for crude oil + methane + CO₂, as follows: (A) L→LV transition at 40.0 gas mol%; (B) LL→LLV transition at 40.0 gas mol%, and (C) LL→LLV transition at 80.0 gas mol%; and (D) AsphL→AsphLLV transition at 84.0 gas mol%.

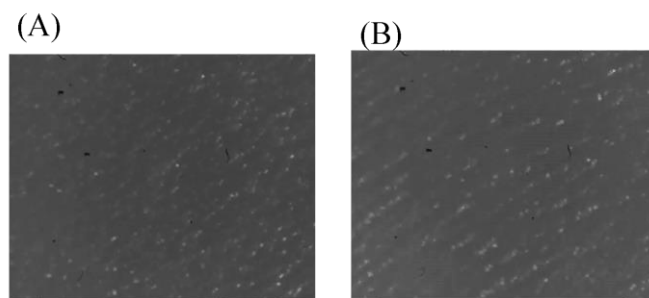


Figure 6.19 Asphalt phase in sapphire windows at 358.15 K (A), and 338.15 K (B) detected by SWIR camera for crude oil + methane + CO₂.

These results show that even reducing the methane content in the recombination gas, the LL immiscibility is formed at almost same composition of 60 gas mol%. Also, by the first time it was detected the HPHT LL in equilibrium with an asphaltic phase. It confirms that two different forms of heavy phase can be obtained, one fine and dispersed, associated in this work to a LL immiscibility. And a heavy sticking phase, named in this work as asphalt. The features of this asphalt phase are not observed in the conventional PVT techniques, as discussed in previous chapters. On the contrary, the observed phase heterogeneity present similar characteristics than LL detected by SWIR: high dispersed, no fractal, no aggregative, and no does not deposit in polar surfaces. These features could help to differentiate the asphalt formation from LLE in conventional PVT analysis.

To better identify the AOP for CO₂ + methane + crude oil mixtures, QCR tests were made from 78.0 to 84.0 gas mol %, by successive increasing of 2.0 gas mol % in the mixture. Asphaltene flocculation was detected at 82.0 gas mol %, and temperature effect on AOP is depicted in Figure 6.20. Despite temperature effects on asphaltene precipitation is still controversial in literature, it can be noted that asphaltenes flocculation follows the most reported trend, i.e., a decrease on AOP while high temperature is reached. This system presenting LL and LL + asphaltene equilibria was studied by SWIR HPM test. Results are presented in Figure 6.21. It can be noted that a high disperse phase is observed at pressures above the AOP that correspond to two liquid phases in equilibrium. When pressure is reduced, asphaltene precipitates and a well-defined solid phase is also identified in equilibrium with the LL. This asphaltenic phase is different from the other two, and is detected as aggregative particles in the crude oil.

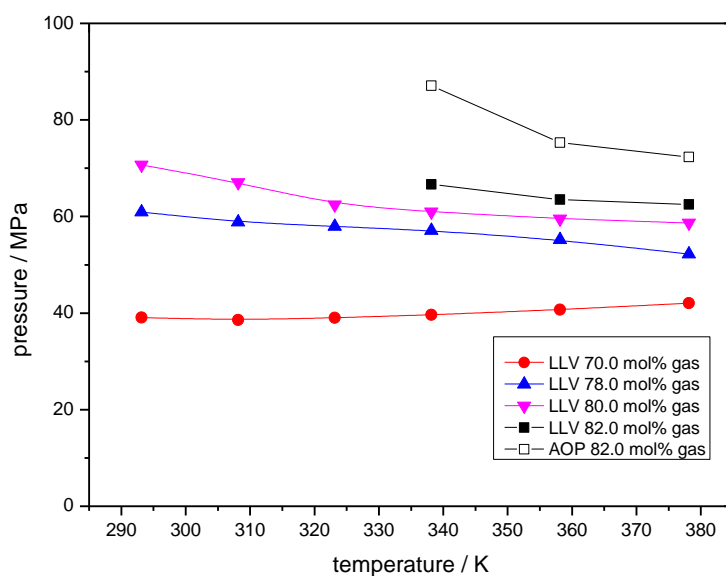


Figure 6.20. Phase diagram obtained using SWIR imaging and QCR analysis for crude oil + CO₂ + methane mixtures.

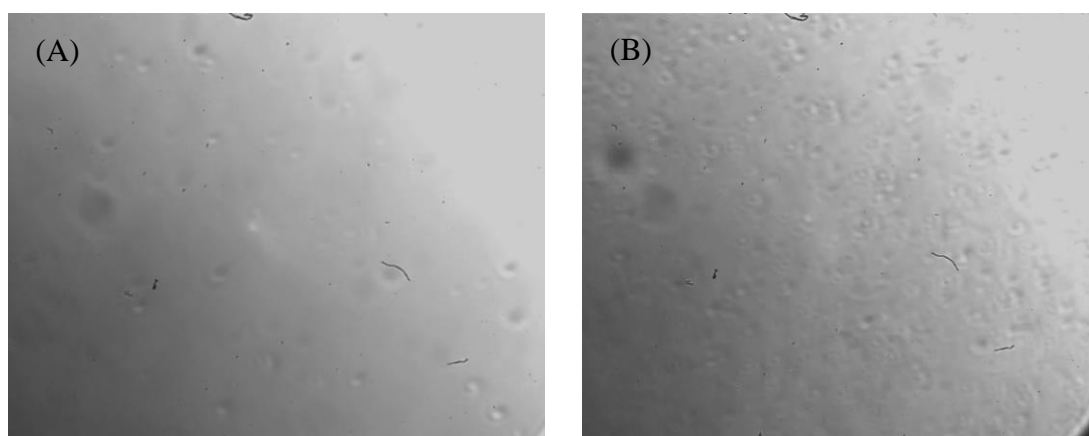


Figure 6.21. SWIR microscopy (50x) for (A) LL and (B) LL + asphaltene equilibria for 82.0 gas mol % mixture at 358.15 K.

Summarizing, SWIR camera made possible the detection of such opaque unconventional phase behavior for crude oil + gas (methane and/or carbon dioxide) systems. For these types of mixtures under the studied pressure, temperature, and gas composition ranges, LL equilibria presented the following characteristics: (i) high dispersity. (ii) low aggregation, and (iii) no significant differences in density. These characteristics, together with crude oil low light transmittance prevent LL detection by

classical PVT techniques – i.e., fluid visual inspection, volumetric measurements, laser scattering, high pressure microscopy, for instance. Therefore, SWIR camera imaging is recommended to study LL phase transition, due to its visual inspection capability to analyze opaque systems.

6.3.4. Thermodynamic modelling

Phase envelopes for the different experimental mixtures were calculated using PR EOS after binary interaction parameters fitting. The obtained k_{ij} are presented in Table 6.5. In general, similar good fitting was achieved for all tested system. For all of them, as expected, k_{ij} between crude oil fraction and CO₂ were higher than those between crude oil and methane. However, even a higher interaction parameter was obtained between the heaviest fraction of crude oil (CNA) and methane. This condition was necessary to properly describe the experimental phase behavior of methane systems.

This heavy fraction was treated in several forms aiming to elucidate the causes and properties of the phase insolubility. The first approach, was define a heavy CNA lump with critical properties like heavy aromatic hydrocarbons, as commented in the methodology section. However, a more detailed CNA splitting was also tested to differentiate a heavy saturate fraction, and a heavy aromatic fraction. From both approaches, a similar good description of experimental results was reached. Additionally, the interaction parameter of heavy CNA aromatic fraction was crucial for fitting procedures.

Calculated phase envelopes are depicted in Figure 6.22 for the systems crude + CO₂, and in Figure 6.23 for the systems crude oil + methane. For both cases, the thermodynamic modelling has an appropriate qualitative description of the experimental phase behavior.

Table 6.5 Fitted binary interaction parameter between crude oil fractions/carbon dioxide (k_{CO_2-i}), and crude oil fraction/methane (k_{CH_4-i}) for condensed model.

Compound	k_{CO_2-i}	k_{C1-i}
C3	0.130	0.000
i-C4	0.130	0.000
n-C4	0.125	0.000
i-C5	0.125	0.000
n-C5	0.100	0.000
C6	0.100	0.000
Mcyclo-C5	0.100	0.000
Benzene	0.100	0.000
Cyclo-C6	0.100	0.000
C7	0.100	0.005
Mcyclo-C6	0.100	0.005
Toluene	0.100	0.005
C8	0.100	0.005
C2-Benzene	0.100	0.005
m&p-Xylene	0.100	0.005
o-Xylene	0.090	0.015
C9	0.090	0.017
C10	0.090	0.019
C11	0.090	0.021
C12	0.090	0.023
C13	0.090	0.025
C14	0.090	0.027
C15	0.090	0.028
C16	0.090	0.030
C17	0.090	0.032
C18	0.090	0.034
C19	0.090	0.036
C20+	0.089	0.060
CNA	0.100	0.150

In the case of crude oil + CO₂ systems (Figure 6.22), the model describes the classical LL and LLV regions for CO₂ compositions above 70.0 mol%, with a LLV region near the critical condition of pure CO₂ (COUTINHO; JØRGENSEN; STENBY, 1995; KHAN; POPE; SEPEHRNOORI, 1992; ORR; YU; LIEN, 1981). However, a non-typical LLV region was also described by the model at pressures near the LL-LV locus. Focusing on phase compositions, two different LL regimes are highlighted:

- The first one is formed at temperatures below the classical LL locus, e.g., at 300 K for 84.0 %mol CO₂ mixture, as described in Figure 6.25. In this region, two liquid phases are formed in a molar ratio $L_2/(L_1+L_2)$ ranging from 30/70 to 50/50 mol. Where L₂ is the CO₂ rich phase, composed by more than 95 mol% of CO₂, with a minor quantity of crude oil fractions.
- A second one is observed at temperatures above the classical LL locus and under lower pressure, e.g., at 400 K and 55 MPa for 84.0 % mol CO₂ mixture (see Figure 13). The molar proportion between the liquid phases, $L_2/(L_1+L_2)$, changes to 0.08 to 1.20 mol% when pressure is decreased, along with a change in phase composition. A liquid phase, L₁ has a molar composition close to the global mixture composition, and a minor liquid phase L₂, contains around 30 to 38 mol% of all heavy compounds of the crude oil (CNA fraction). Experimentally, as given in Section 6.3.1 (Figure 6.8), there is also a significant change in phase transition characteristics when CO₂ content is higher than 78.0 mol%. This LL immiscibility could be then associated with heavy crude oil fraction separation at high CO₂ content systems.

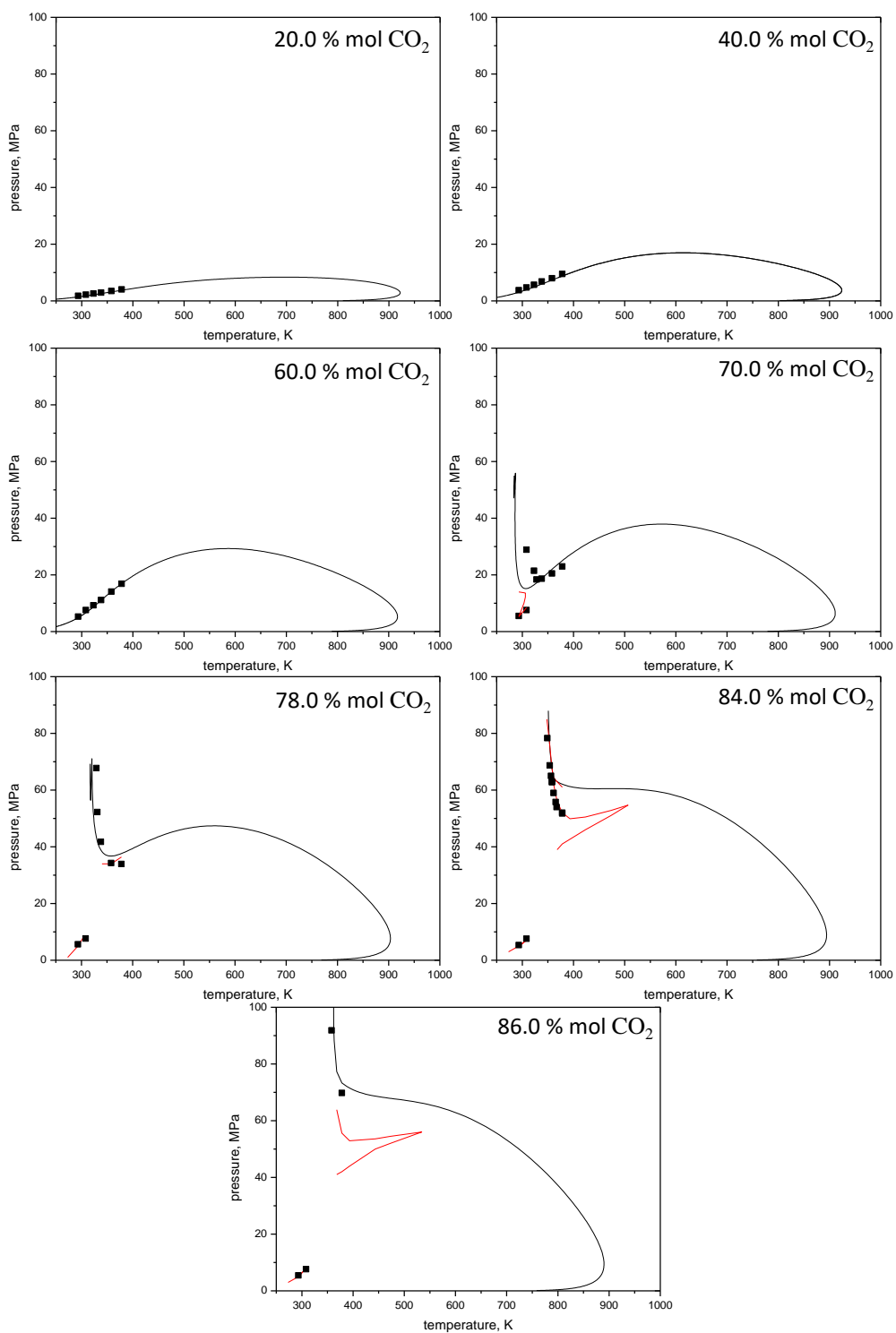


Figure 6.22 P-T diagrams for the crude oil + CO₂ systems, at 20.0, 40.0, 60.0, 78.0, 84.0, and 86.0 CO₂ mol%. Experimental data in black squares, and PR EOS in continuous line.

Similar results are obtained for methane systems, as shown in Figure 6.23. Specifically, a wide LLV region was described for systems with methane content above 60.0 mol%. This LLV region was obtained under pressures lower than the one of LL locus. It can be noted that monophasic region is only reached at pressures above 100 MPa for the systems with higher methane content, at the experimental temperatures. The molar ratio between the LL phases is like the one obtained for the CO₂ systems at high CO₂ content, with a molar content of the L2 phase around 0.08 to 1.2 mol%. This low proportion coincides with the fine dispersion observed experimentally. Additionally, L2 molar composition is predominately composed of the CNA heavy oil fraction, as depicted in Figure 6.24 for L2 phase composition at a referential temperature of 338.15 K and 100 MPa. It is interesting to note that at the higher methane content system, the CNA content in the L2 phase represents almost 92.0 mol% of the overall heavy fraction of the crude oil. This observation could be correlated to the changes in light absorbance detected for the system with methane content above 70.0 mol%. Also, it is important to stress that CNA extracted in L2 phase is almost 3-fold larger than the obtained for CO₂ systems. This result can be related to the solubility differences among the gases and the crude oil fractions.

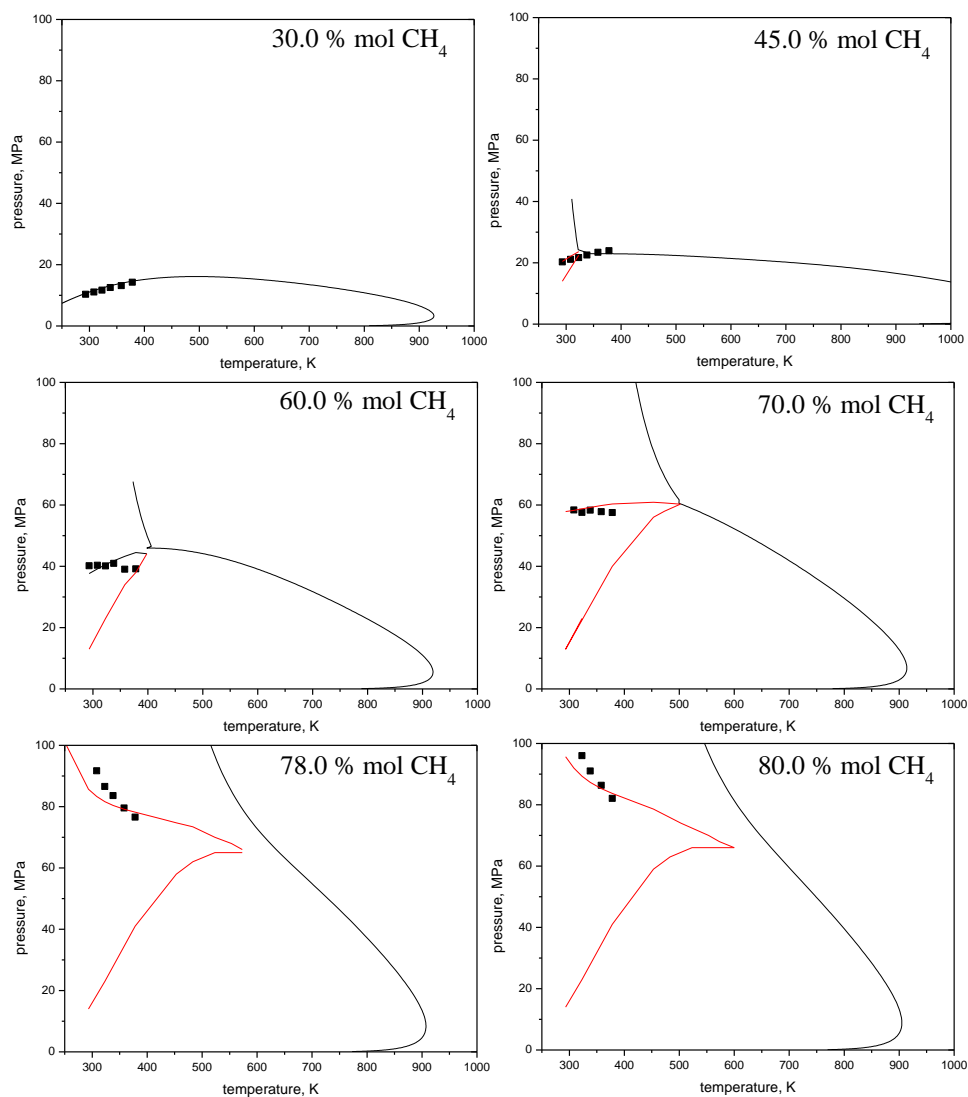


Figure 6.23 P-T diagrams for the crude oil + methane systems, at 30.0, 45.0, 60.0, 78.0, and 80.0, methane mol%. Experimental data in black squares, and PR EOS in continuous line.

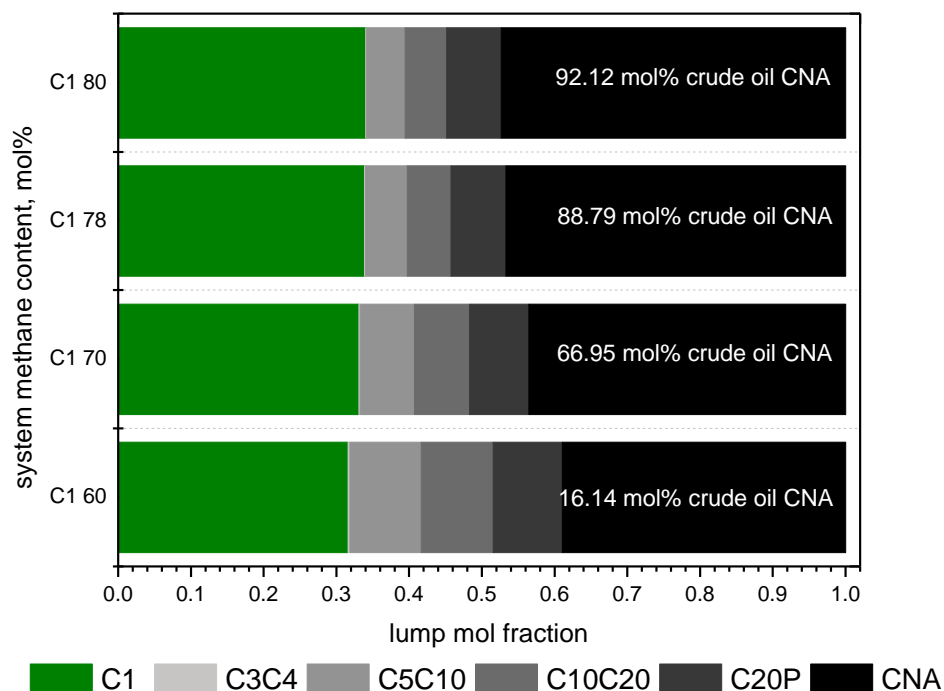


Figure 6.24 Modeled composition of the L2 phase for the systems crude oil + methane, with methane content of 60.0, 70.0, 78.0, and 80.0 methane mol%, together with the CNA extraction percent, at a referential condition of 100 MPa and 338.15 K.

As described in the Methodology section, fitted model was used predictively to describe the crude + methane + CO₂ mixtures phase behavior. For these systems, the only interaction parameter fitted was $k_{CH_4-CO_2} = -0.01$, and modeling results are presented in Figure 6.25. It can be noted that the model qualitatively describes the experimental phase behavior observed, with an internal HPHT LLE. The second liquid phase has similar characteristics than described for methane, with a molar content of the L2 phase around 0.08 to 1.0 mol%. The molar composition of L2 phase is presented in Figure 6.26. It can be noted a reduction in CNA extraction compared to pure methane systems; when CO₂ is included, the CNA extraction only reaches 66.0 mol% of the total crude CNA. This can be related to the solubility contribution of CO₂.

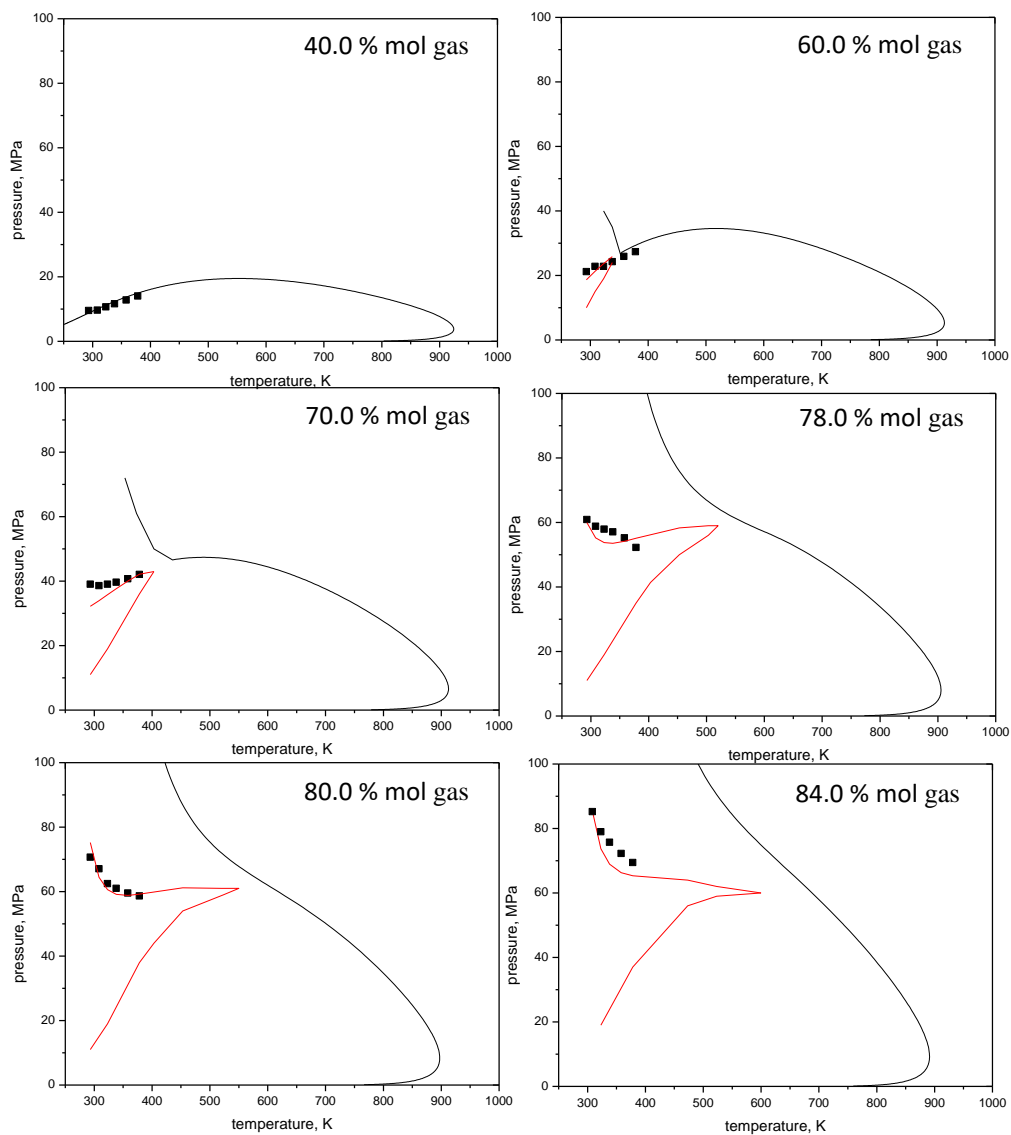


Figure 6.25 P-T diagrams for the crude oil + methane + CO₂ systems, at 40.0, 60.0, 70.0, 78.0, 80.0, and 84.0, gas mol%. Experimental data in black squares, and PR EOS in continuous line.

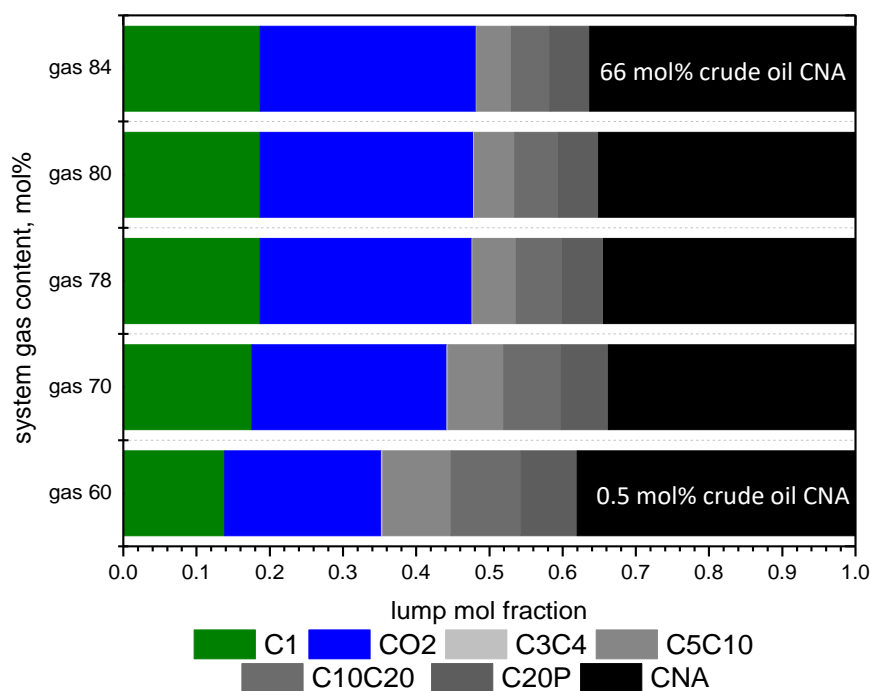


Figure 6.26 Modeled composition of the L2 phase for the systems crude oil + methane + CO₂, with gas content of 60.0, 70.0, 78.0, 80.0 and 84.0 gas mol%, together with the CNA extraction percent, at a referential condition of 100 MPa and 338.15 K.

From these results, non-typical phase transitions can be properly determined by using classical equation of states, as PR EOS. This model can be readily applied to live oil evaluation after fitting of light-end interaction parameters. The proper description of heavy fractions of crude oil has a significant influence on the correct representation of the fluid phase behavior. Also, the adequate experimental assemblage is fundamental for the identification of phase insolubilities in heavy and opaque crude oils.

6.4. Conclusions

Crude oil + carbon dioxide and/or methane phase behaviors were determined using a SWIR imaging in a full visual PVT cell. This technique allowed to detect non-typical liquid-liquid and liquid-liquid-vapor phase transitions, even in highly opaque systems that cannot be detected by classical direct or indirect PVT methods. Liquid-liquid equilibria were characterized by high dispersity, along with a poor segregation, making difficult to detect by classical PVT techniques. These liquid-liquid and liquid-liquid-vapor equilibria

were properly modelled with classical Peng-Robinson cubic equation of state. From this model, phases immiscibility was related to the heaviest compounds in the crude oil, and their interaction with the added gases at high gas concentration.

Addition of CO₂ in the mixture allowed the inclusion of more gas in the systems, promoting asphaltene precipitation. This phase can coexist with the liquid – liquid, and their AOP determination can be successfully made by QCR measurements.

7 CHAPTER VII: STUDY OF HIGH-PRESSURE PHASE EQUILIBRIA (LVE, LLE, LSE, AND LLVE) FOR MODEL SYSTEMS INCLUDING HIGH CARBON NUMBER BRANCHED PARAFINS, POLYAROMATICS, METHANE AND CARBON DIOXIDE.

7.1. Introduction

In chapter VI, non-conventional phase behavior of crude oil and gas mixtures (methane and carbon dioxide) was detected by intermediate of SWIR inspection technique. Specifically, a LLVE was observed for mixtures of methane and crude oil, and methane + carbon dioxide and crude oil. This LLVE is located in the internal region of a wider biphasic envelope in the p,T phase diagram, at higher pressures and temperatures. The system in liquid-liquid phase equilibrium was found in the form of a dispersed phase in the continuous oil phase characterized by a high turbidity. For opaque crude oils systems, this formation of a cloudy droplet dispersion is challenger to detect under high pressure. The dispersed phase formation makes high-pressure sampling particularly tricky, limiting analytical methods. On the other hand, the cloudiness of the system makes the synthetic method by direct visual observation problematic. For that reason, similar reports of LLV at high pressure and temperature are scarce in open literature. Only a continuous biphasic locus, with a low pressure-low temperature triphasic LLV locus, are described for some petroleum fluids.

Through the combination of experimental and modeling techniques carried out and presented in previous chapters it was found that the observed LL immiscibility in pre-salt oils is generated from the demixing of heavy hydrocarbon compounds from crude oils. From modeling exercise, a heavy and aromatic fraction with maximum critical pressure, minimal critical temperature, and large acentric factor, was indispensable to achieve a proper representation of the LL phase separation observed during experiments performed in pseudo-binary mixtures of a Pre-Salt dead oil and a light gas in significant content. Considering this finding, we sought to build simple model systems formed by a synthetic heavy fraction and a pure gas or a gas mixture able to reproduce the particular phase behavior observed in pre-salt reservoir fluid with the occurrence of LLE and LLVE at elevated temperature and pressure.

Phase behavior of organic compounds and gases systems are widely reported in literature (CHRISTOV; DOHRN, 2002; DOHRN; BRUNNER, 1995; DOHRN; PEPPER;

FONSECA, 2010; FONSECA; DOHRN; PEPER, 2011). In terms of petroleum derived compounds, the most studied systems are binary mixtures of light gas with a paraffinic, naphthenic, or aromatic component of moderate molecular weight. As the molecular weight of the heavy compound in the mixture increases, complex phase diagrams are expected. However, the fluid region of these systems is restrained by the elevated fusion temperature of hydrocarbon molecules with a high carbon number. Among petroleum compounds, branched paraffins have the lower melting temperature in comparison to linear paraffins alky, allowing a wider fluid phase behavior evaluation. Nevertheless, their fluid phase behavior, in binary or multicomponent systems, has been not widely studied in the literature (AL GHAFRI; MAITLAND; TRUSLER, 2014; VITU et al., 2007).

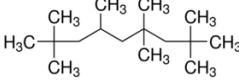
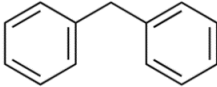
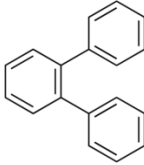
In this last chapter, the phase behavior pseudo-binary synthetic mixture composed of a light gas (either methane or CO₂ or a mixture of both in a ratio of 1/1) and a heavy fraction formed by an aromatic and a branched paraffin in a ratio of 2/1 was studied. Particularly, 2,2,4,4,6,8,8-heptamethylnonane was chosen for the saturated compound, whereas diphenylmethane or *o*-terphenyl were considered to represent the aromatic part. The compounds were selected based on (i) their fusion temperature; (ii) their suitable critical properties to mimic heavy fractions of Pre-salt fluids (trying to minimize the critical pressure and to maximize the critical temperature and the acentric factor); and (iii) the practical availability and cost. The measurements were carried out in order to find a simple system capable of reproducing LLE and LLVE in HT-HP condition. The obtained phase behaviors for different investigated systems were also modelled using predictive cubic equations of state.

7.2. Material and Methods

7.2.1. Chemicals

The compounds used for systems formulation are listed in Table 7.1, together with their purity and supplier. Their molecular weight, fusion and boiling normal temperature were listed in Table 7.2. All chemicals were used without any further purification. The same gases from chapter VI were used, including methane, CO₂, and the mixture 1:1 molar methane/CO₂.

Table 7.1 CAS registry number, molecular structure, mass fraction purity, and suppliers of the chemicals.

Compound	CAS Reg. No.	molecular structure	mass purity, %	supplier
2,2,4,4,6,8,8-heptamethylnonane	4390-04-9		99.6 ^a	Sigma-Aldrich
Diphenylmethane	101-81-5		99	Sigma-Aldrich
<i>o</i> -terphenyl	84-15-1		99	Sigma-Aldrich

^a certificated gas chromatography analysis informed by supplier.

Table 7.2 Chemicals molecular weight, fusion temperature (T_f), and normal boiling temperature (T_b)^a.

Compound	MW	T_f , K	T_b , K
2,2,4,4,6,8,8-heptamethylnonane	226.44	203.15	513.0
Diphenylmethane	168.23	299.0	537.5
<i>o</i> -terphenyl	230.30	331.0	610.2

^a from NIST webbook (LINSTROM; MALLARD, 2001).

7.2.2. Systems preparation and phase behavior study

The same full visual PVT cell from chapter VI was used for phase behavior study and systems preparation. For all tested systems, a constant molar proportion aromatic/saturate 2/1 was selected. This high aromatic condition was established from crude oil modeling results, in which aromatic fractions were crucial for LLE description. At this molar proportion, the 2,2,4,4,6,8,8-heptamethylnonane and the aromatics were totally soluble at temperatures above their fusion point. Mixtures were prepared by directly mixing the chemicals, and their mass was determined by using an analytical balance with 0.001 g precision. Then, the mixtures were heated at 80.0 °C, to guarantee solids melting, and manually stirred.

After the mixture's preparation, injection procedure to the PVT cell was achieved following same procedures as the ones used in chapter VI. Precisely, the hot liquid binary mixture sample was introduced to the previously vacuumed PVT by suction. All valves and connections were heated by a thermal tape during injection, while Teflon tubing was preheated in an oven. Finally, the total mass of liquid introduced in the PVT was gravimetrically determined by using an analytical balance with 0.001 g precision.

Table 7.3 System molar composition for different aromatics and gases used.

aromatic type	aromatic/saturate molar ratio	gas mol %	gas type
diphenylmethane	2.002	20.62	CH ₄
diphenylmethane	2.002	40.33	CH ₄
diphenylmethane	1.999	60.38	CH ₄
diphenylmethane	2.002	70.81	CH ₄
diphenylmethane	1.998	20.12	CH ₄ +CO ₂
diphenylmethane	1.998	36.83	CH ₄ + CO ₂
diphenylmethane	1.998	59.97	CH ₄ + CO ₂
diphenylmethane	1.998	69.96	CH ₄ + CO ₂
diphenylmethane	1.998	80.02	CH ₄ + CO ₂
diphenylmethane	1.998	14.90	CO ₂
diphenylmethane	1.988	50.40	CO ₂
diphenylmethane	1.988	73.17	CO ₂
diphenylmethane	1.988	78.21	CO ₂
diphenylmethane	1.988	85.99	CO ₂
diphenylmethane	1.996	89.92	CO ₂
diphenylmethane	1.996	92.57	CO ₂
<i>o</i> -terphenyl	1.994	20.38	CH ₄
<i>o</i> -terphenyl	1.994	40.40	CH ₄
<i>o</i> -terphenyl	1.994	60.90	CH ₄
<i>o</i> -terphenyl	1.994	70.46	CH ₄
<i>o</i> -terphenyl	1.996	20.70	CH ₄ + CO ₂
<i>o</i> -terphenyl	1.994	39.32	CH ₄ + CO ₂
<i>o</i> -terphenyl	1.994	59.41	CH ₄ + CO ₂
<i>o</i> -terphenyl	2.000	70.04	CH ₄ + CO ₂
<i>o</i> -terphenyl	2.000	79.99	CH ₄ + CO ₂
<i>o</i> -terphenyl	1.994	84.00	CH ₄ + CO ₂
<i>o</i> -terphenyl	1.994	14.70	CO ₂
<i>o</i> -terphenyl	1.996	31.41	CO ₂
<i>o</i> -terphenyl	1.997	50.40	CO ₂
<i>o</i> -terphenyl	2.001	61.41	CO ₂
<i>o</i> -terphenyl	2.001	73.17	CO ₂
<i>o</i> -terphenyl	1.997	78.17	CO ₂
<i>o</i> -terphenyl	1.997	83.37	CO ₂
<i>o</i> -terphenyl	1.997	88.65	CO ₂

Gas injection was made volumetrically by intermediate of a Teledyne Isco 100D syringe pump, with volume measurement precision of 0.01 cm^3 . The gas density data required for gas mass determination was taken from NIST REFPROP software (LEMMON; HUBER; MCLINDEN, 2007). Systems compositions were listed in Table 7.3. Finally, the mixture was homogenized under stirring at 378.15 K and, at least, 10 MPa above bubble point pressure for 20 minutes.

7.2.2.1. Liquid-Vapor transitions determination

For each gas composition, CCE tests were performed at five different temperatures $T = (378.15, 358.15, 338.15, 323.15, 308.15, \text{ and } 293.15) \text{ K}$. As commented in chapter IV, PV curves from CCE were used to determine liquid – vapor transitions (L→LV and LL→LLV). Liquid–liquid phase transitions (L→LL) were determined by visual fluid inspection, using a typical digital microscope camera, EO USB 2.0 CMOS Machine Vision Camera, from Edmund Optics. This camera was coupled to an optical objective with 8x magnification to better detect any dispersed phase in the fluid. Fluid inspection was performed during pressure steps without any stirring. Then, when a new phase was detected, appearance pressure was registered for each mixture.

7.2.2.2. Liquid-Solid transitions determination

For mixtures involving *o*-terphenyl, the aromatic with higher fusion temperature, liquid-solid transitions (L→LS) were also observed and the transition temperature was measured. For L-S locus determination under high pressure, isobaric cooling visual tests are commonly performed at different pressures above the L-V locus. However, in such cooling experiments, large errors can be obtained because of subcooling effects. involving an underestimation of the L→LS measured temperatures. This effect is particularly noteworthy with heavy aromatics as it can lead to the formation of metastable solid phases that biases results (MILHET et al., 2008). Furthermore, it is very significant when system temperature is reduced too fast. To avoid error due to subcooling effects, the liquid solid transition should be performed with heating rather than with cooling. However, during such type of heating experiments in PVT cells under high pressure, overheating can also seriously influence the measuring results.

To melt a totally solidified system in the cell, a large amount of energy is necessary and supplied by heating, then temperature can increase away from the LS transition point. For that reason, system thermal regulation was made when only few crystals were observed (2 – 5 crystals) at temperature below melting temperature and pressure above the LV transition pressure. At this temperature, the system was equilibrated during almost 1 hour. Then, variations of 0.1 °C were made stepwise until the crystals were totally dissolved. Finally, an increase in pressure was made to confirm the dissolution and to generate new solid crystals by LS locus interception, as depicted in Figure 7.1. When this specific pressure and temperature were detected, LS point was registered. Then, system temperature was increased in 2 – 5 °C while changing the pressure so as to keep the system with few solid crystals in equilibrium with the fluid phase just below the melting line so as to reach a desired pressure to carry out a new measurement. The procedure is repeated up to higher pressure of measurement.

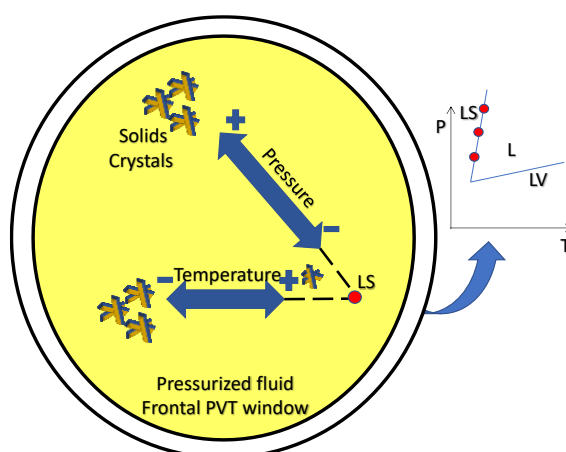


Figure 7.1 Schematic figure of Liquid-Solid determination test.

7.2.3. Thermodynamic Modelling

Liquid-vapor, liquid-liquid, and liquid-liquid-vapor equilibria for each system were modelled using Peng-Robinson equation of state (PR EOS) (PENG; ROBINSON, 1976), as described in chapter VI. As previously commented, this EOS was used aiming to show that the experimental behavior could be qualitatively obtained with the thermodynamic model used in the oil and gas industry. Total BEST software was used for phase equilibria calculations. All equations are presented in Section 6.2.5 from Eq.

6.1 to Eq. 6.9. Critical properties for chemical compounds are presented in Table 7.4, obtained from NIST webbook.

Table 7.4 Critical temperature, critical pressure, and acentric factor for chemical compounds

compound	P_c , MPa	T_c , K	ω
CH ₄	4.600	190.60	0.0115
CO ₂	7.380	304.20	0.2250
2,2,4,4,6,8,8-heptamethylnonane	1.57	692.0	0.4825
diphenylmethane	2.9789	767.0	0.4750
<i>o</i> -terphenyl	3.0	857.0	0.5707

Acentric factor for hydrocarbon compounds was calculated using the relation defined by Pitzer between the normal boiling point temperature and the critical temperature of each compound, presented in equation Eq. 7.1 (BYCHINSKY et al., 2013; LEE; KESLER, 1975).

$$\omega = \frac{-\ln(P_c) - 5.92714 + 6.09648 \cdot \theta^{-1} + 1.28862 \cdot \ln(\theta) - 0.169347 \cdot \theta^6}{15.2518 - 15.6875 \cdot \theta^{-1} - 13.4721 \cdot \ln(\theta) + 0.43577 \cdot \theta^6} \quad \text{Eq. 7.1}$$

where $\theta = T_b/T_c$, both temperatures in K, and P_c in bar.

As presented in chapter VI, phase equilibria calculation was performed using a multiphase flash software developed by Total S.A. (BEST v12.5, from Total, France), based on Michelsen tangent plan distance method (MICHELSEN, 1982a, 1982b). However, no fitting was made for binary interaction parameters between systems compounds. Instead, interaction parameter was estimated using a predictive PR EOS (PPR78), based on a group contribution method developed by Jaubert and collaborators (JAUBERT et al., 2005, 2013; JAUBERT; MUTELET, 2004; JAUBERT; PRIVAT, 2010; VITU et al., 2007; VITU; JAUBERT; MUTELET, 2006). In this method, the interaction parameter is given by:

$$k_{ij}(T) = \left\{ \left[-\frac{1}{2} \sum_{k=1}^{N_g} \sum_{l=1}^{N_g} (\alpha_{ik} - \alpha_{jk})(\alpha_{il} - \alpha_{jl}) A_{kl} (T_0/T)^{\left(\frac{B_{kl}}{A_{kl}} - 1\right)} \right] - \left[\frac{\sqrt{a_i(T)}}{b_i} - \frac{\sqrt{a_j(T)}}{b_j} \right]^2 \right\} \cdot \left(2 \cdot \frac{\sqrt{a_i(T)a_j(T)}}{b_i b_j} \right)^{-1} \quad \text{Eq.7.2}$$

where, N_g represents the total number of functional groups present in the molecule, α_{ik} is the occurrence of group k in component i divided by N_g , and A_{kl} and B_{kl} are group parameters. It has been defined until now 21 functional groups for PR78, group parameters A_{kl} and B_{kl} were obtained by fitting experimental binary VLE data using the PR78 EoS with the Soave alpha (α) function (JAUBERT et al., 2005, 2013; JAUBERT; MUTELET, 2004; JAUBERT; PRIVAT, 2010; VITU et al., 2007; VITU; JAUBERT; MUTELET, 2006). For this work, a constant k_{ij} was considered for PT phase envelope construction. Specifically, mean values from 293.15 to 373.15 K were used for k_{ij} , the obtained values were listed in Table 7.5.

Table 7.5 Binary interaction parameter matrix for systems compounds.

compound i\j	CO ₂	CH ₄	heptamethylnonane	diphenylmethane	<i>o</i> -terphenyl
CO ₂		0.1175	0.0767	0.0943	0.0943
CH ₄	0.1175		0.0544	0.0875	0.0655
heptamethylnonane	0.0767	0.0544		0.0043	0
diphenylmethane	0.0943	0.0875	0.0043		-0.0274
<i>o</i> -terphenyl	0.0943	0.0566	-0.0274		

7.3. Results

7.3.1. *Experimental phase behavior results*

Experimental phase transition results for the mixture of 2,2,4,4,6,8,8-heptamethylnonane, diphenylmethane, and gases are listed in Table 7.6 to Table 7.8. In these Tables, it is presented the phase change pressure, temperature, and the type of phase transition for each system. When gas content reaches 86.0 mol %, a low temperature LLVE was identified from both visual and volumetric measurements. A picture of LLVE that was observed from the PVT inspection window is presented in Figure 7.2. It can be noted that for this type of LLVE, a clear three phase separation is observed, as follows: (i) a heavy liquid phase, probably rich in hydrocarbon compounds, (ii) a lighter liquid phase, probably rich in carbon dioxide; and (iii) a gaseous phase. This result is expected for hydrocarbon mixtures with carbon dioxide at high gas content and temperatures below CO₂ critical point.

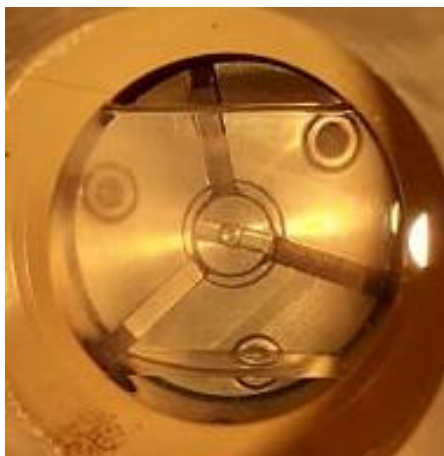


Figure 7.2 LLVE for the mixture of CO₂, diphenylmethane and 2,2,4,4,6,8,8-heptamethylnonane at 89.93 mol% gas, 293.42 K, and pressures below 5.23 MPa.

Table 7.6 Experimental phase transition data for mixtures of carbon dioxide (1), diphenylmethane (2) and 2,2,4,4,6,8,8-heptamethylnonane.

T / K	P / MPa	transition	T / K	P / MPa	Transition
$x_1=14.90, x_2=56.72$			$x_1=81.98, x_2=12.01$		
293.36	1.06	L → LV	293.10	5.16	L → LLV
307.60	1.34	L → LV	308.43	7.23	L → LV
322.80	1.68	L → LV	323.16	10.39	L → LV
337.96	1.99	L → LV	338.36	14.06	L → LV
357.77	2.48	L → LV	357.65	17.99	L → LV
378.42	2.89	L → LV	377.60	21.33	L → LV
$x_1=50.40, x_2=33.00$			$x_1=85.99, x_2=9.32$		
293.81	4.04	L → LV	293.24	5.20	L → LLV
307.57	5.11	L → LV	308.06	8.30	L → LL
323.10	6.66	L → LV	308.06	7.33	LL → LLV
338.75	8.33	L → LV	322.58	12.55	L → LV
357.97	10.19	L → LV	338.33	16.46	L → LV
377.67	12.01	L → LV	358.05	19.70	L → LV
			378.77	22.84	L → LV
$x_1=73.17, x_2=17.85$			$x_1=89.93, x_2=6.71$		
294.03	5.17	L → LV	293.42	6.15	L → LL
308.38	7.05	L → LV	293.42	5.20	LL → LLV
323.58	9.74	L → LV	308.34	9.37	L → LL
338.60	12.91	L → LV	308.34	7.31	LL → LLV
358.64	16.65	L → LV	323.45	13.09	V → LV
378.20	19.89	L → LV	338.73	16.55	V → LV
			358.19	20.37	V → LV
			378.70	23.69	V → LV
$x_1=78.21, x_2=14.50$			$x_1=92.58, x_2=4.95$		
293.22	5.12	L → LLV	293.32	5.23	L → LL
308.47	7.30	L → LV	293.32	6.63	LL → LLV
323.07	11.31	L → LV	307.79	9.71	L → LL
338.53	14.98	L → LV	307.79	7.22	LL → LLV
358.58	19.11	L → LV	323.67	13.31	V → LV
378.84	22.41	L → LV	338.33	16.53	V → LV
			358.17	20.40	V → LV
			378.67	23.56	V → LV

Differently, for systems including methane, the monophasic fluid condition was difficult to confirm for all tested temperatures. Specifically, at temperatures below 323.15 K, some phase heterogeneity was detected. This fluid immiscibility was very difficult to define, and it was observed that microscopical dispersion remains spread in the fluid even after 2 h of vigorous stirring. Without any optical magnification, the fluid seems similar to a homogeneous mixture by direct observation. However, when the camera is coupled with an 8X objective, the same objective used for SWIR oil inspection, a very disperse phase is observed in the PVT cell, as depicted in Figure 7.3. For that reason, Table 7.7 and Table 7.8 include LL to LLV transition points for systems in which the insolubility was detected.

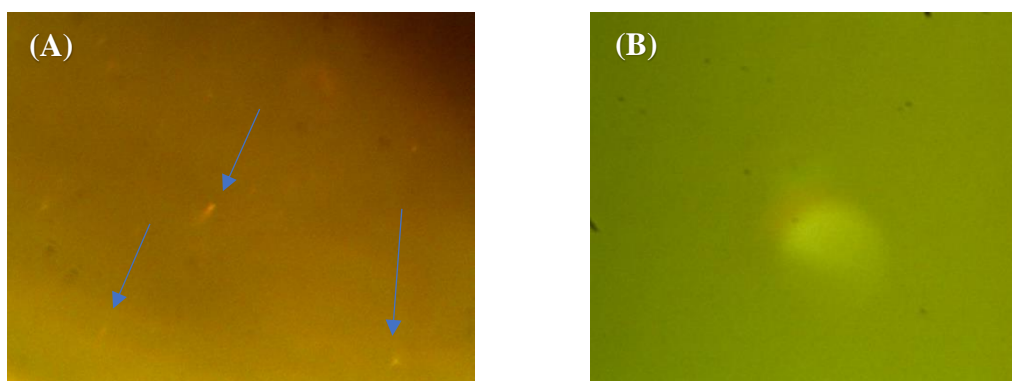


Figure 7.3 Fluid inspection using a magnification lens for the mixture of methane, diphenylmethane and 2,2,4,4,6,8,8-heptamethylnonane at 40.33 mol% gas, at (A) 308.15 K (immiscibility as bright droplets), and (B) 328.15 K (totally homogeneous) at 40.0 MPa.

Table 7.7 Experimental phase transition data for mixtures of methane (1), diphenylmethane (2) and 2,2,4,4,6,8,8-heptamethylnonane.

T / K	P / MPa	transition	T / K	P / MPa	Transition
$x_1=20.62, x_2=52.94$			$x_1=60.38, x_2=26.41$		
292.54	8.53	LL → LLV	293.5	53.06	LL → LLV
309.80	8.87	LL → LLV	308.01	50.81	LL → LLV
323.14	9.00	L → LV	323.57	47.30	L → LV
339.19	9.26	L → LV	338.91	45.85	L → LV
358.15	9.52	L → LV	357.90	43.24	L → LV
378.48	9.76	L → LV	378.41	41.74	L → LV
$x_1 = 40.33, x_2 = 39.80$			$x_1=70.81, x_2=19.47$		
293.41	21.92	LL → LLV	298.67	72.54	LL → LLV
308.12	22.21	LL → LLV	307.91	70.15	LL → LLV
323.36	22.64	L → LV	323.37	65.00	L → LV
338.11	22.91	L → LV	338.00	61.42	L → LV
357.33	23.44	L → LV	358.50	57.93	L → LV
378.74	23.80	L → LV	378.08	55.38	L → LV

Table 7.8 Experimental phase transition data for mixtures of methane/CO₂ (1:1 molar) (1), diphenylmethane (2) and 2,2,4,4,6,8,8-heptamethylnonane.

T / K	P / MPa	transition	T / K	P / MPa	Transition
$x_1=20.13, x_2=53.23$			$x_1=69.96, x_2=20.02$		
293.73	4.53	L → LV	292.66	33.80	LL → LLV
307.93	5.03	L → LV	308.37	34.52	LL → LLV
323.44	5.32	L → LV	323.27	34.92	L → LV
338.04	5.63	L → LV	338.27	35.48	L → LV
357.79	6.04	L → LV	357.76	36.14	L → LV
377.88	6.39	L → LV	378.17	36.61	L → LV
$x_1=36.83, x_2=42.10$			$x_1=80.02, x_2=13.32$		
293.80	9.86	LL → LLV	293.68	45.15	LL → LLV
308.29	10.81	LL → LLV	307.80	44.30	LL → LLV
322.79	11.84	L → LV	322.77	44.09	L → LV
338.28	12.74	L → LV	338.36	43.74	L → LV
357.28	13.60	L → LV	357.84	43.72	L → LV
377.95	14.57	L → LV	377.83	43.50	L → LV
$x_1=59.97, x_2=26.68$					
293.57	23.95	LL → LLV			
307.99	25.05	LL → LLV			
322.90	26.06	L → LV			
338.51	27.08	L → LV			
358.17	28.13	L → LV			
377.90	28.90	L → LV			

Because of the extreme dispersion of the second phase, together with minimal differences on refraction index relative to bulk fluid, it is difficult to determine with precision the liquid – liquid appearance locus. For systems with pure methane and the CO₂/methane mixtures, this phase heterogeneity is lost when temperature increases above 323.15 K. When the system is heated, the phase seems to dissolve instantaneously at temperatures near 323.15 K. However, their formation while the system is cooled is not always detected, and in some cases a large equilibration time is required to detect the dispersed phase once more.

For crude oil mixtures, a similar phase insolubility was observed. However, their detection was more evident because of differences on SWIR light absorbance between the bulk fluid and the dispersed phase. This difference could be attributed to compositional changes between phases, since the dispersed phase seems to extract some heavy compounds of the crude oil. Also, interfacial effects can promote their detection: as larger the interfacial tension is, a highly defined interphase is formed and detected. However, for the studied model systems, the difficulty on phase separation and their high dispersion could indicate some similitude on density, composition, and a reduced interfacial tension. To better assess and confirm this phase behavior, it is recommended to use a method that allows the detection of micrometric or submicrometric dispersions. Some tests can be primarily made using an HPM cell, aiming to confirm the phase dispersity existence.

HPM evaluation of LL condition for diphenylmethane systems containing methane was made using a 50x objective and an HPM cell. An example of the obtained micrography is depicted in Figure 7.4. No bigger insolubility was observed at pressures above the vapor evolution. However, small droplets were detected and that could indicate a high dispersed phase, with minimal size.

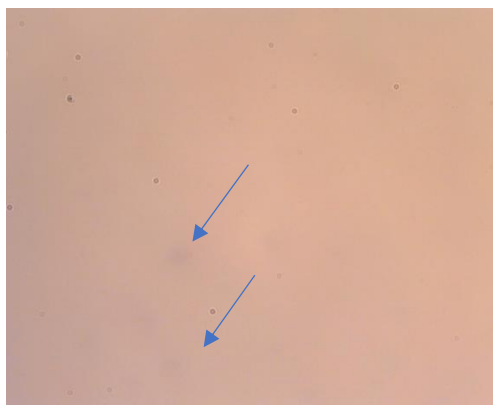


Figure 7.4 Micrography for LL condition of 60.3 methane mol % mixture with diphenylmethane and 2,2,4,4,6,8,8-heptamethylnonane at 308.15 K and 70 MPa.

Similar results were obtained when *o*-terphenyl was used. The results of phase behavior are listed from Table 7.9 to Table 7.14. For CO₂ mixtures (Table 7.9), LLVE was observed at low temperatures when gas content is higher than 73.16 mol %. At this condition, the LS boundary is lower than the critical temperature of pure CO₂, and a low temperature triphasic LLV region is observed. LS data for CO₂ mixtures with *o*-terphenyl systems are presented in Table 7.10. It is important to mention that at gas composition above 73.16 mol %, the system presents a turbidity that does not disappear even at pressure higher than 70 MPa and temperature of 338.15 K. Also, it becomes more evident as the gas content increases, and coincides with an increase on LS locus. This turbidity was analyzed by microscopy and depicted in Figure 7.5. It can be noted a more defined phase heterogeneity, greater than the observed for methane mixtures and diphenylmethane. This result could suggest an immiscibility region of CO₂ at higher temperature and pressure, as observed for Pre-Salt fluids.

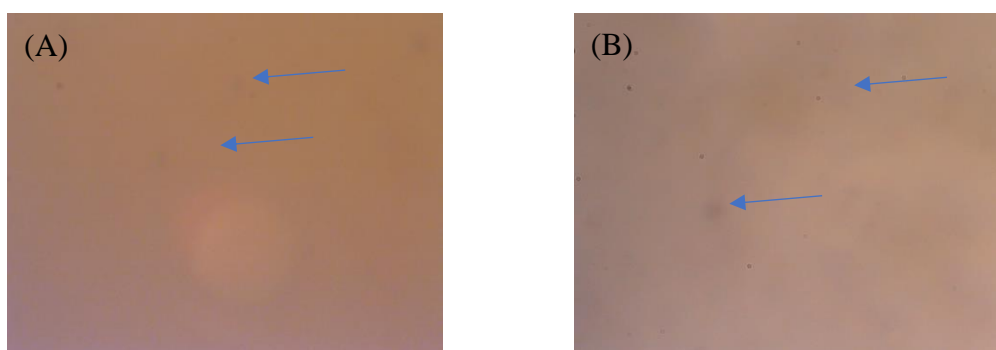


Figure 7.5 Pictures from PVT frontal camera (A) and micrography (B) for LL condition of 83.37 CO₂ mol % mixture with *o*-terphenyl and 2,2,4,4,6,8,8-heptamethylnonane at 325.15 K and 70 MPa.

Table 7.9 Experimental LV and LLV phase transition data for mixtures of carbon dioxide (1), *o*-terphenyl (2), and 2,2,4,4,6,8,8-heptamethylnonane.

T / K	P / MPa	Transition	T / K	P / MPa	transition
$x_1=14.70, x_2=56.81$			$x_1=73.17, x_2=17.89$		
322.80	1.44	L → LV	308.61	21.19	L → LL
338.35	1.76	L → LV	308.61	7.37	LL → LLV
358.28	2.18	L → LV	323.54	17.92	L → LV
378.20	2.48	L → LV	338.59	19.52	L → LV
			358.60	22.38	L → LV
			378.70	25.14	L → LV
$x_1=31.41, x_2=45.70$			$x_1=78.17, x_2=14.54$		
323.73	3.57	L → LV	307.74	35.22	L → LL
338.62	4.13	L → LV	307.74	7.43	LL → LLV
358.72	4.99	L → LV	323.70	26.81	L → LV
378.55	5.80	L → LV	338.50	25.31	L → LV
			358.35	26.38	L → LV
			378.42	28.34	L → LV
$x_1=50.40, x_2=33.05$			$x_1=83.38, x_2=11.08$		
323.58	6.97	L → LV	310.25	59.31	L → LL
338.50	8.56	L → LV	311.65	7.57	LL → LLV
358.42	10.70	L → LV	323.45	45.19	L → LV
378.49	12.64	L → LV	338.58	34.69	L → LV
			358.14	31.72	L → LV
			378.34	32.48	L → LV
$x_1=61.41, x_2=25.73$			$x_1=88.65, x_2=7.56$		
323.07	9.04	L → LV	323.67	66.19	L → LV
338.59	11.28	L → LV	338.33	46.27	L → LV
358.54	14.23	L → LV	358.17	39.49	L → LV
378.84	16.92	L → LV	378.04	37.55	L → LV

Table 7.10 Experimental LS phase transition data for mixtures of carbon dioxide (1), *o*-terphenyl (2), and 2,2,4,4,6,8,8-heptamethylnonane.

T / K	P / MPa	transition
$x_1=31.41, x_2=45.70$		
319.06	28.47	L → LS
314.65	13.05	L → LS
$x_1=61.41, x_2=25.73$		
311.42	49.50	L → LS
313.27	55.09	L → LS
308.40	35.33	L → LS
$x_1=73.17, x_2=17.89$		
306.65	30.70	L → LS
308.58	42.80	L → LS
310.27	50.70	L → LS
$x_1=78.17, x_2=14.54$		
308.69	43.13	L → LS
309.79	47.83	L → LS
310.86	54.55	L → LS
$x_1=83.38, x_2=11.08$		
312.06	57.50	L → LS
314.38	67.60	L → LS

For systems with methane and methane/CO₂, a fluid heterogeneity was detected at highest temperatures than LSE. The results are presented in Table 7.11 and Table 7.13. Differently than systems with diphenylmethane, the phase heterogeneity was stable even at the higher temperature tested. However, the same complexities on phase detection were faced, the phase was extremely dispersed and finely divided, as depicted in Figure 7.6 (C). Even if the phase dispersion resembles the observed in crude oil systems, it is difficult to define this behavior, especially because there are no similar precedents within the literature of this field.

Liquid solid phase equilibria were also studied for mixtures including methane, presented in Table 7.12 and Table 7.14. As expected, the LSE temperature is reduced as the gas content increases. Additionally, the inclusion of CO₂ in the mixed gas shifted the LSE locus to lower temperatures.

Table 7.11 Experimental phase transition data for mixtures of methane (1), *o*-terphenyl (2), and 2,2,4,4,6,8,8-heptamethylnonane.

T / K	P / MPa	Transition	T / K	P / MPa	transition
$x_1=20.38, x_2=53.03$			$x_1=60.90, x_2=26.04$		
323.26	8.62	LL → LLV	323.30	59.53	LL → LLV
338.70	9.11	LL → LLV	337.63	57.79	LL → LLV
358.04	9.50	LL → LLV	357.91	53.34	LL → LLV
377.95	9.91	LL → LLV	378.50	50.58	LL → LLV
$x_1=40.40, x_2=39.70$			$x_1=70.46, x_2=19.67$		
328.31	23.78	LL → LLV	338.00	89.80	LL → LLV
338.71	24.05	LL → LLV	358.13	76.52	LL → LLV
358.21	24.35	LL → LLV	378.07	69.58	LL → LLV
377.67	24.54	LL → LLV			

Table 7.12 Experimental LS phase transition data for mixtures of methane (1), *o*-terphenyl (2), and 2,2,4,4,6,8,8-heptamethylnonane.

T / K	P / MPa	transition
$x_1=20.38, x_2=53.03$		
324.45	25.11	LL → LLS
326.25	32.20	LL → LLS
327.97	39.26	LL → LLS
$x_1=40.40, x_2=39.70$		
322.93	41.76	LL → LLS
324.65	49.85	LL → LLS
326.43	55.94	LL → LLS
$x_1=60.90, x_2=26.04$		
324.18	73.24	LL → LLS
325.34	79.81	LL → LLS

Table 7.13 Experimental phase transition data for mixtures of methane/CO₂ (1:1 molar) (1), *o*-terphenyl (2), and 2,2,4,4,6,8,8-heptamethylnonane.

T / K	P / Mpa	transition	T / K	P / MPa	transition
$x_1=20.70, x_2=52.83$			$x_1=70.04, x_2=20.00$		
323.55	5.66	LL → LLV	323.12	49.69	LL → LLV
338.52	6.13	LL → LLV	338.23	48.12	LL → LLV
357.95	6.67	LL → LLV	357.76	47.34	LL → LLV
378.46	7.12	LL → LLV	378.06	46.88	LL → LLV
$x_1=39.32, x_2=40.42$			$x_1=79.99, x_2=13.34$		
322.87	13.98	LL → LLV	322.87	81.39	LL → LLV
338.24	15.18	LL → LLV	338.24	70.45	LL → LLV
357.95	16.34	LL → LLV	358.93	63.74	LL → LLV
378.23	17.25	LL → LLV	378.53	60.55	LL → LLV
$x_1=59.41, x_2=27.03$			$x_1=84.00, x_2=10.65$		
323.36	30.82	LL → LLV	338.17	83.15	LL → LLV
338.17	31.66	LL → LLV	358.6	72.59	LL → LLV
358.355	32.79	LL → LLV	377.96	66.32	LL → LLV
378.535	34.25	LL → LLV			LL → LLV

Table 7.14 Experimental LS phase transition data for mixtures of methane/CO₂ (1:1 molar) (1), *o*-terphenyl (2), and 2,2,4,4,6,8,8-heptamethylnonane.

T / K	P / MPa	transition
$x_1=20.70, x_2=52.83$		
323.85	25.88	LL → LLS
$x_1=39.32, x_2=40.42$		
318.84	37.05	LL → LLS
320.26	43.21	LL → LLS
322.15	51.73	LL → LLS
$x_1=59.41, x_2=27.03$		
314.58	50.78	LL → LLS
312.4	39.99	LL → LLS
311.7	37.89	LL → LLS
$x_1=70.04, x_2=20.00$		
312.15	77.79	LL → LLS
310.35	71.75	LL → LLS
309.3	64.76	LL → LLS

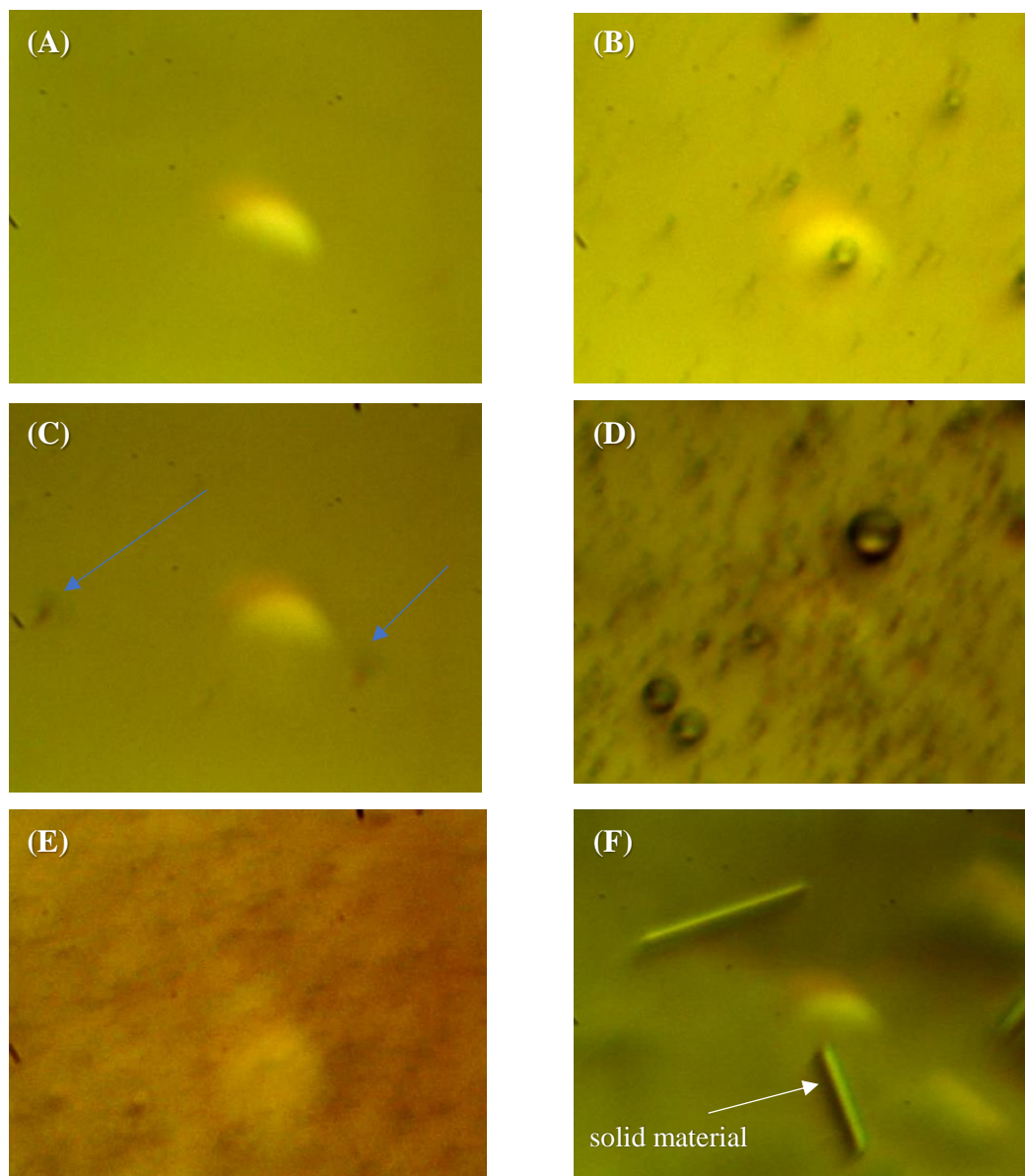


Figure 7.6 Images of different fluid condition obtained by full visual PVT for systems including heptamethylnonane, *o*-terphenyl and gases: (A) monophasic condition for mixture with 50.0 mol% CO₂ at 358.15 K and 12.0 MPa, (B) LV condition for mixture with 50.0 mol% CO₂ at 358.15 K and 9.7 MPa, (C) LL condition for mixture with 60.0 mol% methane at 358.15 K and 60.0 MPa, (D) LLV condition for mixture with 60.0 mol% methane at 358.15 K and 50.0 MPa, (E) LL condition for mixture with 83.30 mol % CO₂ at 338.15 K and 32.5 MPa, and (F) LS condition for mixture with 60.90 mol % methane at 324.19 K and 73.0 MPa.

7.3.2. *Thermodynamic modeling results*

Phase envelopes for systems with diphenylmethane are presented on Figure 7.7 to Figure 7.9. For mixtures with CO₂, the model provides a good description of the experimental phase behavior observed as shown in Figure 7.7. The largest differences are observed at high gas content, especially for L→LV and L→LL transitions. Punctually, the model overestimates the biphasic envelope at high gas content; however, it could be improved by fine fitting on interaction parameter. On the contrary, LLV loci nearby CO₂ critical region are well described by the EOS without having to tune the model.

For systems including methane, Figure (7.8 and 7.9), it can be noted that the predicted LV envelope is in accordance with experimental results. Additionally, the model identifies a biphasic region at low temperatures, even for low gas content systems. This biphasic region goes from temperatures of 293.15 to 310.15 K. Experimentally, a phase insolubility was also detected in this region, and their appearance was shifted to higher gas composition when the mixed gas included CO₂. This behavior was also observed by modelling, in which a LL biphasic region only appears at high gas content for systems with the gas mixture 1:1 CO₂/methane. However, the modeled LLVE locus does not follows the experimental tendency, i.e., it does not decrease with temperature. Contrarily, the modeled LLVE has a sharp increase with temperature until it intercepts the biphasic envelope. This behavior could be easily modified by tuning the interaction parameters.

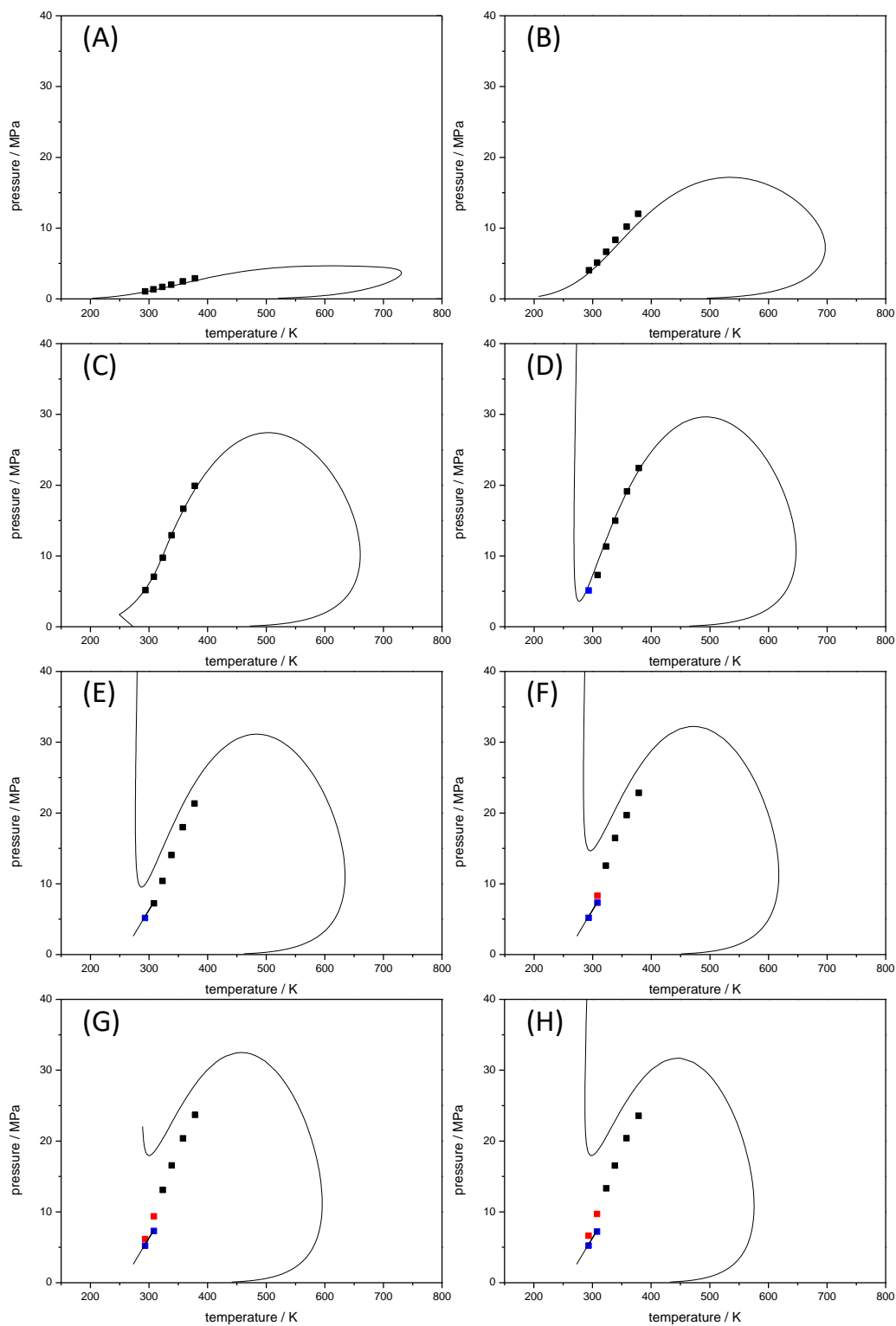


Figure 7.7 P-T diagrams for 2,2,4,4,6,8,8-heptamethylnonane + diphenylmethane + CO₂ systems, at (A) 14.90, (B) 50.40, (C) 73.17, (D) 78.21, (E) 81.98, (F) 85.99, (G) 89.93, and (H) 92.58, gas mol%. Experimental LVE data in black squares, LLE in red squares, LLVE data in blue squares, and PPR EOS in continuous line.

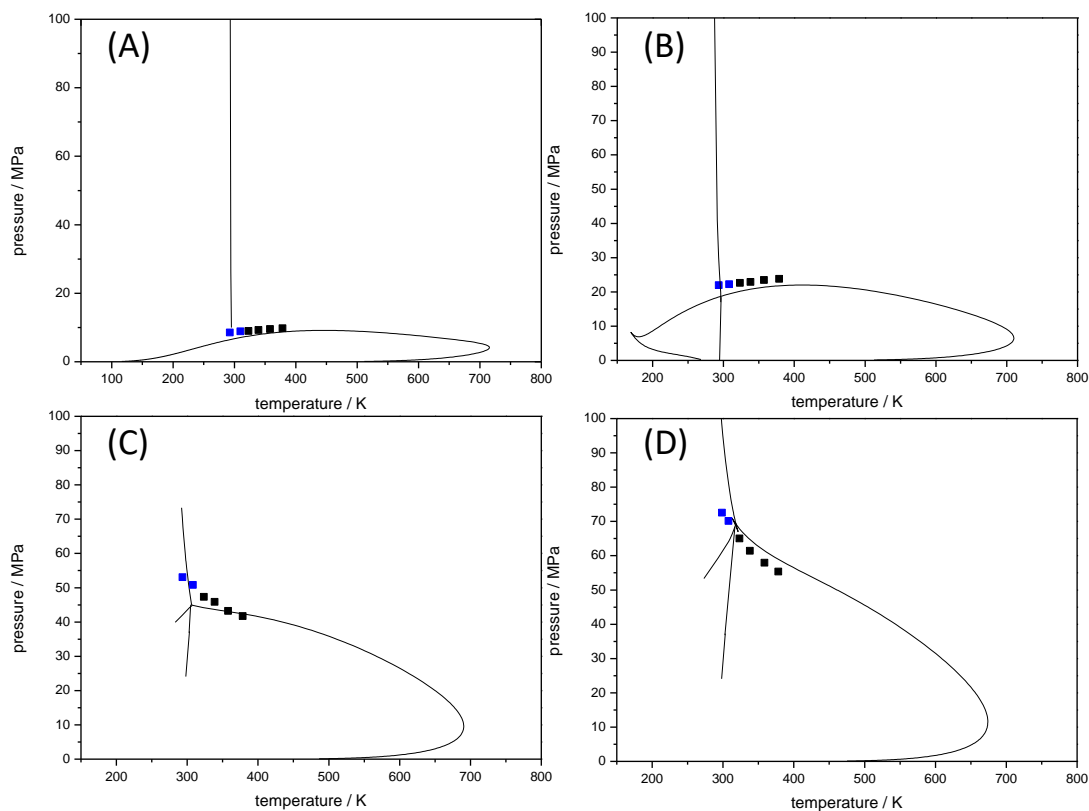


Figure 7.8 P-T diagrams for 2,2,4,4,6,8,8-heptamethylnonane + diphenylmethane + methane systems, at (A) 20.62, (B) 40.33, (C) 60.38, and (D) 70.81 gas mol%. Experimental LVE data in black squares, LLVE data in blue squares, and PPR EOS in continuous line.

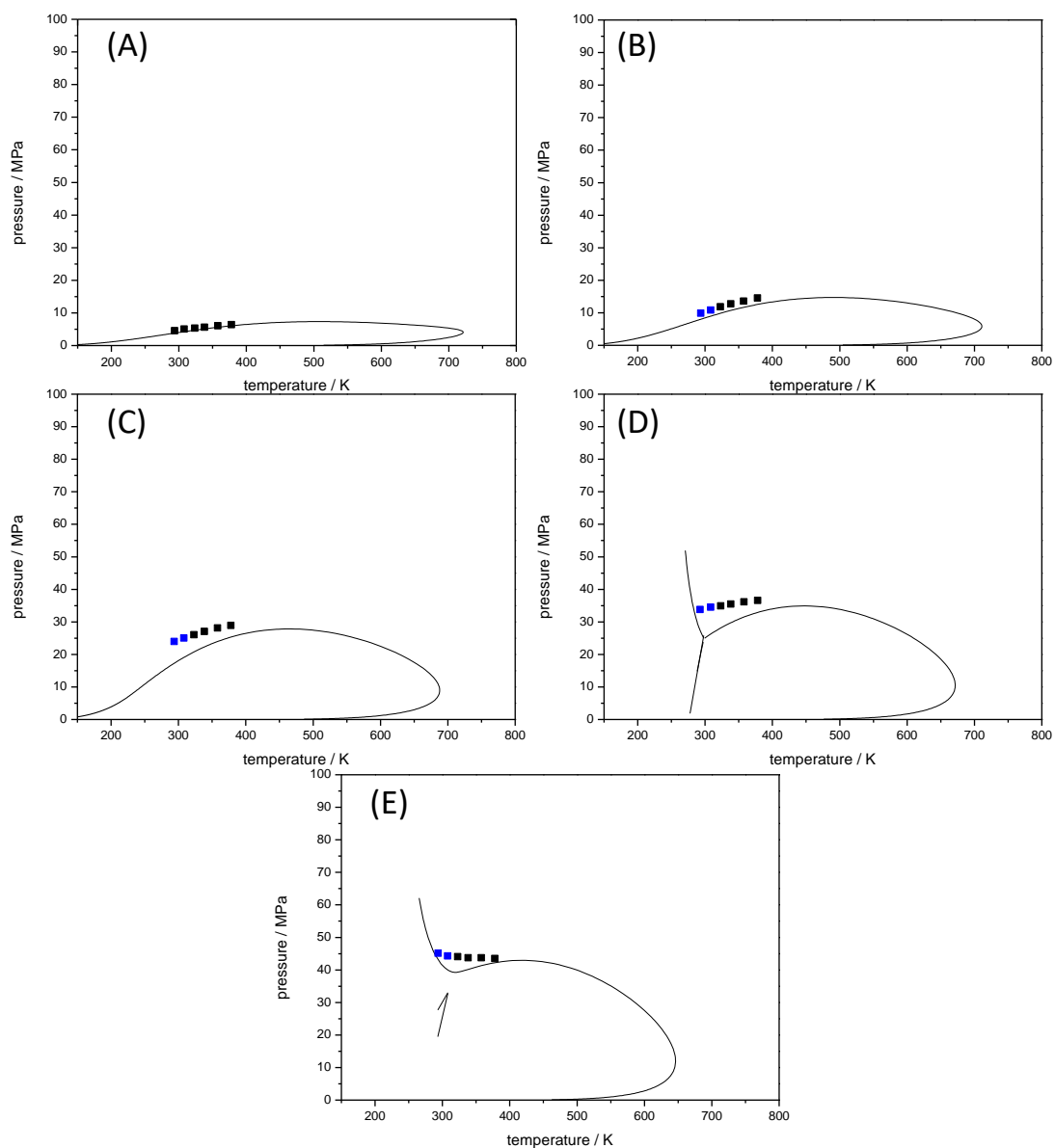


Figure 7.9 P-T diagrams for 2,2,4,4,6,8,8-heptamethylnonane + diphenylmethane + methane + CO₂ systems, at (A) 20.125, (B) 36.86, (C) 59.97, (D) 69.96, and (E) 80.02 gas mol% (gas 1:1 molar CO₂/methane). Experimental LVE data in black squares, LLVE data in blue squares, and PPR EOS in continuous line.

Modelled phase envelopes for systems with *o*-terphenyl are depicted in Figures 7.10 to Figure 7.12. Results for mixtures with CO₂, Figure 7.10, are in good accordance with the experimental LV data, especially when gas content is lower than 61.41 mol %. At higher gas content, LLE region deforms the LV phase envelope to higher pressures, and modelling results overestimate the transitions pressures. It is important to remember that the model is purely predictive, and no experimental data fitting was made. Considering this, the model has a good qualitative description of the experimental phase behavior.

Results for system including pure methane are presented in Figure 7.11. Similarly to what was obtained for diphenylmethane systems, a LL biphasic region is described by the model at low temperatures. However, with the increase of the aromatic compound molecular weight, the LL region becomes wider in the temperature region. Specifically, the LL domain can reach almost 350.K at high gas content when the aromatic is *o*-terphenyl. This behavior was also detected experimentally, and model results may help to validate the phase heterogeneity observed during experiments. When CO₂ is included in the mixing gas, Figure 7.12, the LL region is obtained at lower temperatures, and more gas is needed for its formation.

It is important to mention that, after a sensibility study, it was observed that LL region is widely affected by the k_{ij} between the aromatic and the saturate compound. For the mixture of *o*-terphenyl and heptamethylnonane, the k_{ij} estimated by PPR78 was -0.0274. However, if this interaction parameter is considered to be zero, a wider LLE region is obtained, as presented in Figure 7.13. Punctually, the LLE region goes to temperatures that exceeds 308.15 K. Also, the LLV locus shape can be modified by changing the interaction parameter between the hydrocarbon compounds and gases, but the larger incidence on the LLE region is affected by the interaction parameter between the aromatic and saturate components. Despite these fitting uncertainties, it is worth to stress that increasing the molecular weight of the aromatic compounds results could conduct to a possible wider LLE region, as observed in the crude oil mixtures.

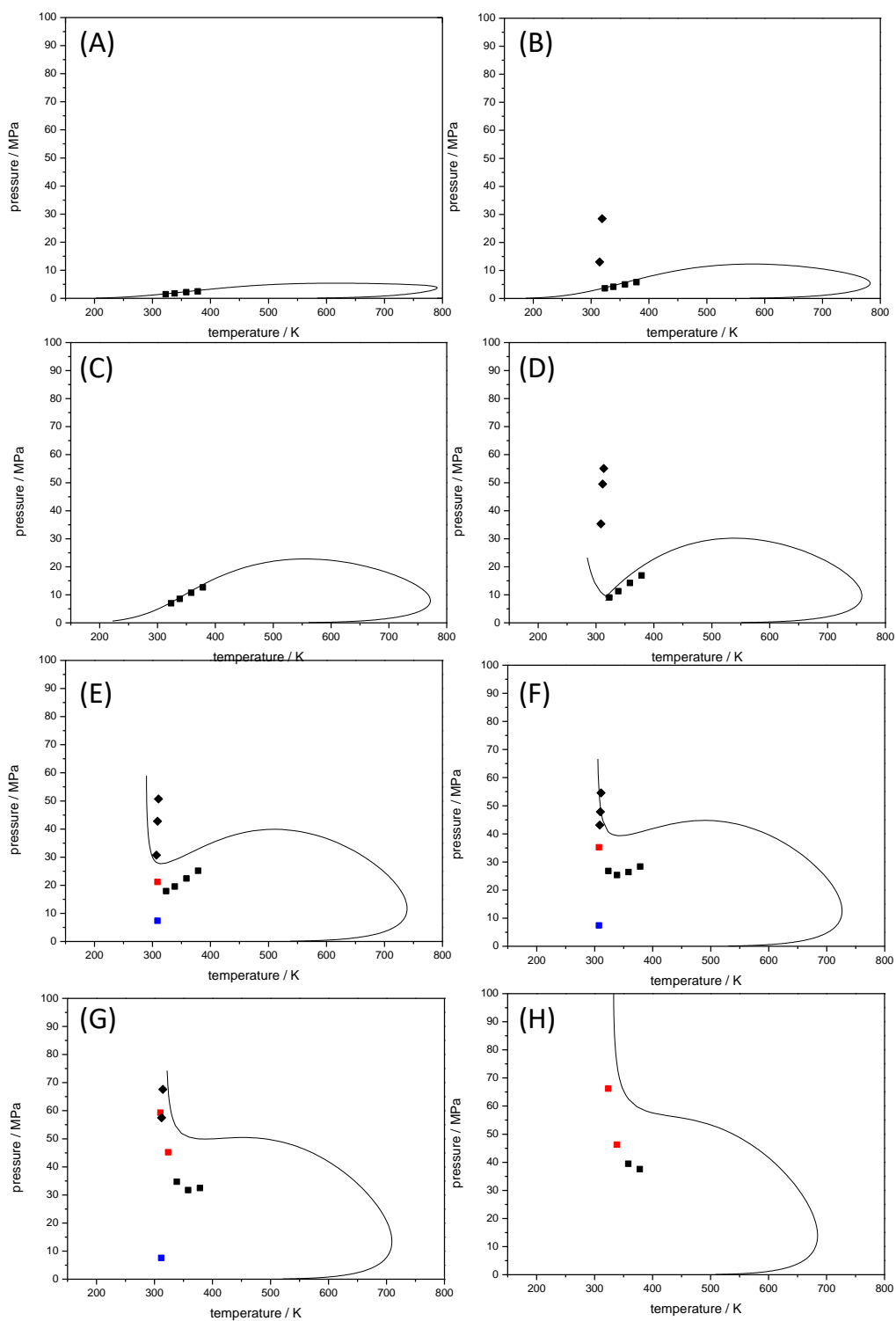


Figure 7.10 P-T diagrams for 2,2,4,4,6,8,8-heptamethylnonane + *o*-terphenyl + CO₂ systems, at (A) 14.70, (B) 31.41, (C) 50.42, (D) 61.50, (E) 73.17, (F) 78.17, (G) 83.38, and (H) 88.65, gas mol%. Experimental LVE data in black squares, LLE in red squares, LLVE data in blue squares, LSE data in black diamonds, and PPR EOS in continuous line.

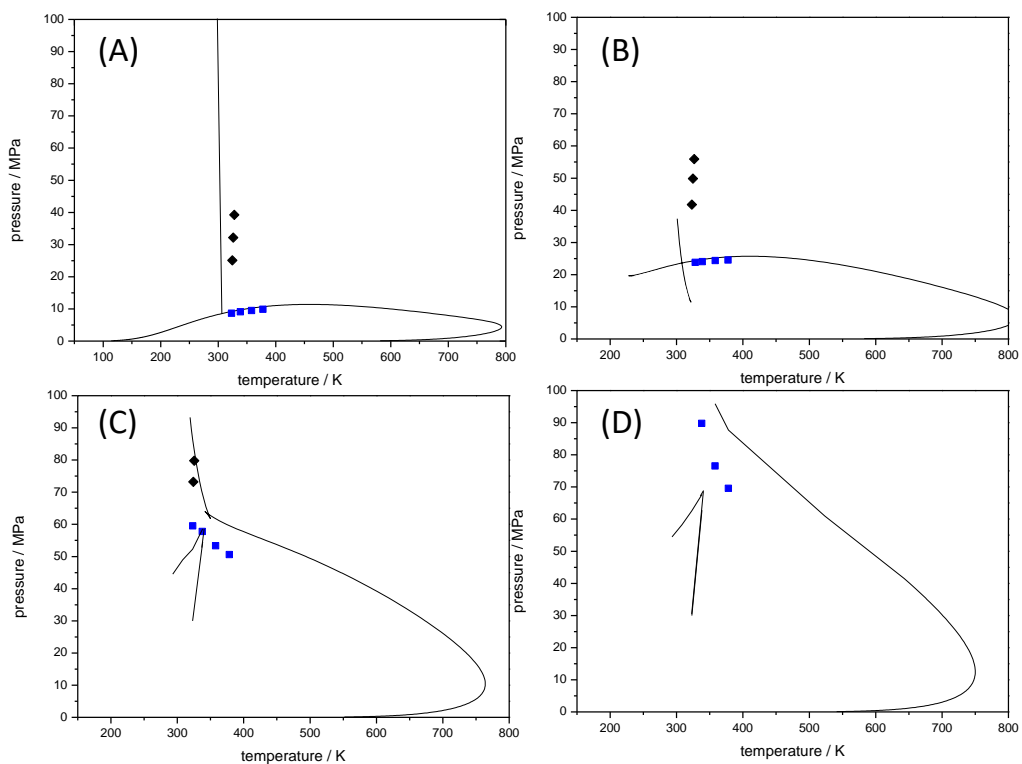


Figure 7.11 P-T diagrams for 2,2,4,4,6,8,8-heptamethylnonane + *o*-terphenyl + methane systems, at (A) 20.38, (B) 40.40, (C) 60.90, and (D) 70.46 gas mol%. Experimental LSE data in black diamonds, LLVE data in blue squares, and PPR EOS in continuous line.

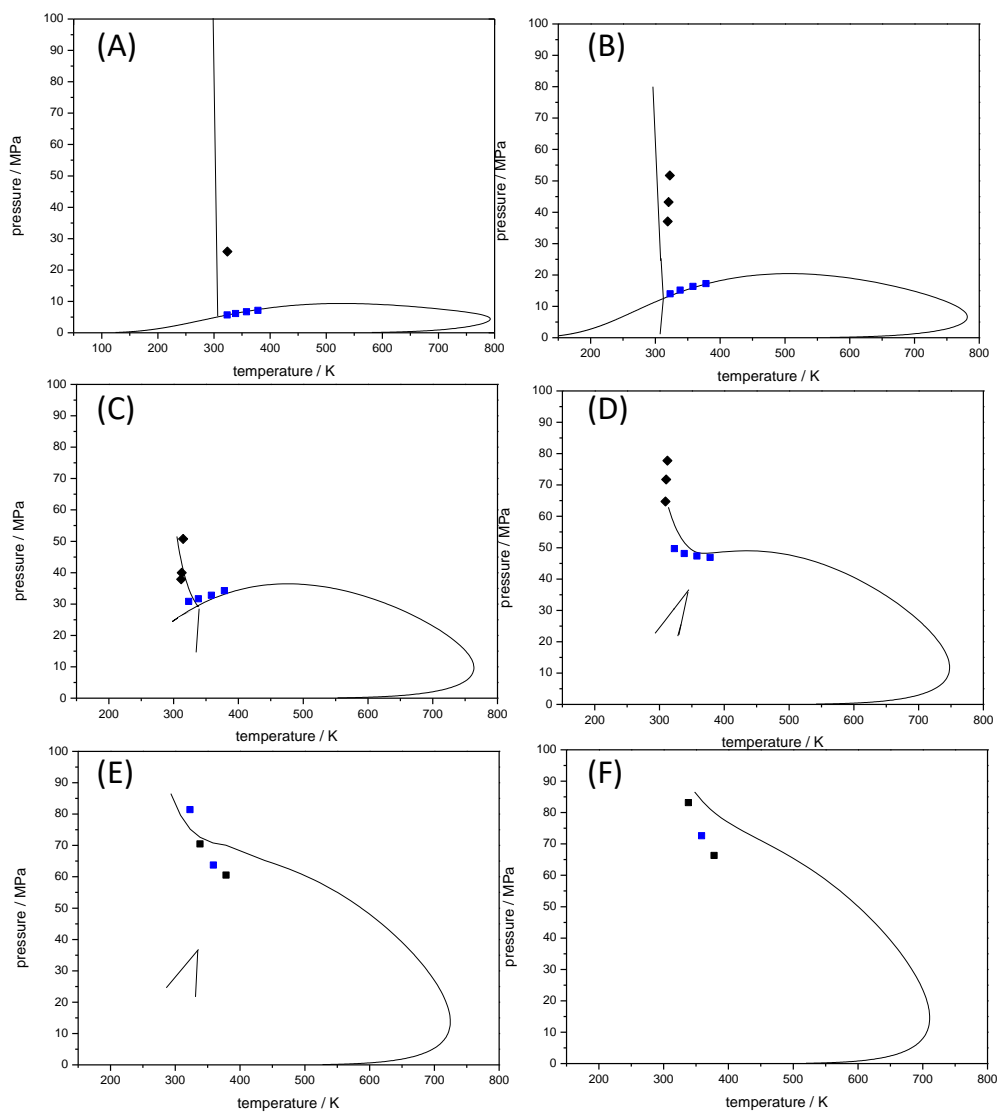


Figure 7.12 P-T diagrams for 2,2,4,4,6,8,8-heptamethylnonane + *o*-terphenyl + methane + CO₂ systems, at (A) 20.70, (B) 39.32, (C) 59.41, (D) 70.04, (E) 79.99, and (G) 84.00 gas mol% (gas 1:1 molar CO₂/methane). Experimental LSE data in black diamonds, LLVE data in blue squares, and PPR EOS in continuous line.

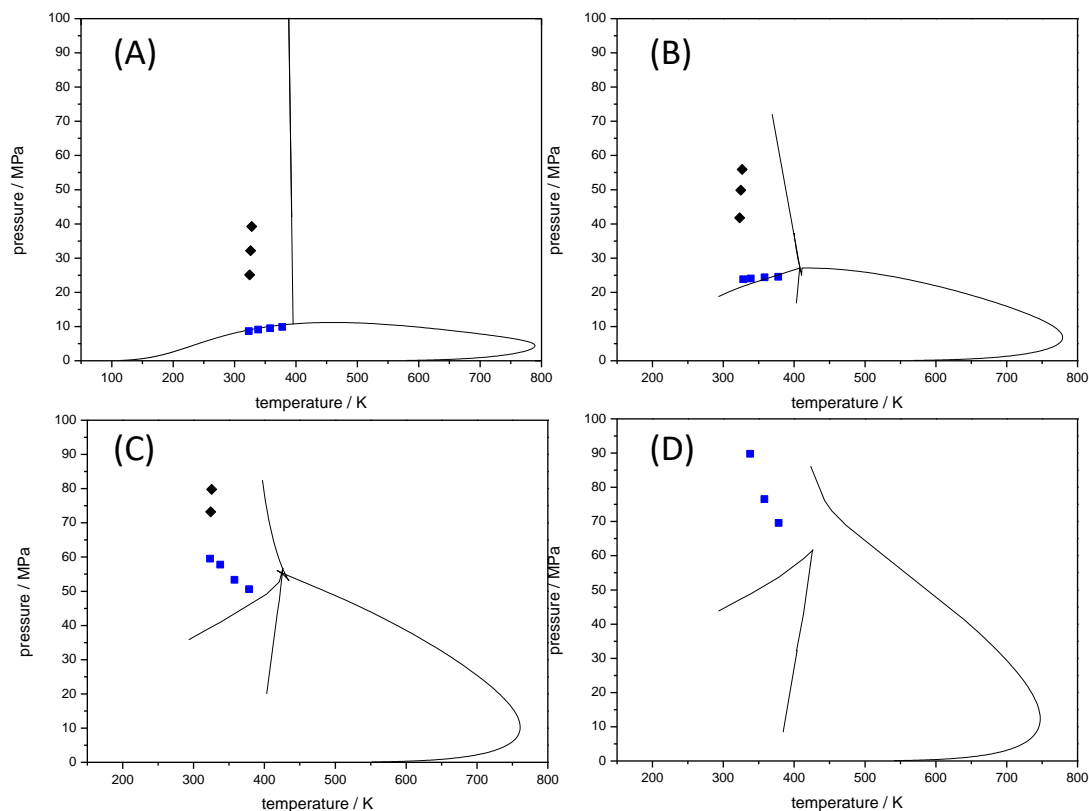


Figure 7.13 Sensibility study of P-T diagrams for 2,2,4,4,6,8,8-heptamethylnonane + *o*-terphenyl + methane systems, at (A) 20.38, (B) 40.40, (C) 60.90, and (D) 70.46 gas mol%. Experimental LSE data in black diamonds, LLVE data in blue squares, and PPR EOS in continuous line considering $k_{\text{heptamethylnonane}, o\text{-terphenyl}} = 0$.

7.4. Conclusions

Phase behavior was investigated for asymmetric mixtures including high molecular weight branched paraffins (heptamethylnonane), polyaromatics (diphenylmethane or *o*-terphenyl), methane and/or CO₂. For system mixed with CO₂, a classical Type III phase diagram is observed for the studied systems mixed with methane, it was observed a high dispersed phase immiscibility during PVT measurements at HPHT conditions. This immiscibility was detected in a wider temperature range as the molecular weight of the aromatic compound increases. This behavior was also represented by totally predictive thermodynamic models. Finally, the addition of CO₂ in the mixed gas results in a reduction of the LL immiscible region, and the LS region.

8 GENERAL CONCLUSIONS

This work has been motivated by the complex phase behavior observed in Brazilian Pre-Salt crude oil, detected during live oil fluid evaluations. Precisely, a type of liquid – liquid equilibria has been identified in medium crude oil associated with high gas content. For that reason, systematic PVT analyses were made using dead crude oils and gas mixtures, aiming to reproduce the observed phase transitions of Brazilian Pre-Salt reservoir fluids.

In this work, a similar phase immiscibility was observed for dead oil samples mixed with light gases with a high gas content. The second formed liquid phase was characterized by its high dispersity, with neglectable separation even using mechanical methods. Also, it presented low aggregation or flocculation in all the liquid – liquid pressure domain, with minimal growing, even at pressures far below their incipient formation onset.

This liquid – liquid immiscibility can be confused with solid asphaltenes if used conventional PVT techniques, specially by its response in near-infrared light scattering test. However, its morphological, aggregative, and dissolution features differ from conventional asphaltene precipitation. For its assessment and study, a combination of PVT techniques and protocols was necessary, especially for opaque crude oils.

From this work, it was noted that the formation of liquid – liquid equilibria in crude oil pre-salt is mainly promoted by inclusion of methane at high Gas-to-Oil ratio. The addition of carbon dioxide in these systems can also cause the destabilization of an asphaltenic phase, that remains in equilibria with the two other liquid phases. Accordingly, it was demonstrated that different types of phase equilibria can be obtained for Brazilian Pre-Salt crude oils, ranging from typical liquid – vapor transitions, to multiphase scenarios, as liquid – liquid equilibria, liquid – liquid – vapor equilibria, asphaltene – liquid – vapor equilibria, and asphaltene – liquid – liquid – vapor equilibria.

For a proper detection of the liquid – liquid biphasic domain, a full visual fluid study was required. Conventional PVT techniques are limited in the observation of this type of equilibria, especially during routine analysis. Therefore, SWIR fluid visualization has been successfully tested and validated for liquid – liquid equilibria detection in opaque pre-salt oils. This technique is not altered by liquid – liquid equilibria, and asphaltenes precipitation can be properly detected.

Thermodynamic simulation and solubility analysis carried out in this work for crude oil and gas mixtures could show that the liquid – liquid immiscibility observed in Pre-Salt crude oil could be related to heavy and aromatic compounds in crude oil. Additionally, modeling results have suggested that carbon dioxide can increase the system solvency towards heavy compounds, also reducing the liquid – liquid region.

The study of highly asymmetric systems including pure hydrocarbon and gases shows that a liquid – liquid immiscibility region could be formed at high pressure and temperature. Results indicate that this type of equilibria is wider in temperature domain as heavier aromatic hydrocarbon compounds are evaluated. The inclusion of CO₂ promoted a reduction of the LS region, and classical low pressure – low temperature LLV was also observed for the tested systems. However, the phase dispersity formed at HPHT conditions is still challenging in detection and study, even for simple and clear fluids.

9 RECOMMENDATIONS FOR FUTURE RESEARCH

It is proposed that the following recommendations be explored in future research:

1. Extension of liquid – liquid equilibria evaluation for different types of crude oils. In this thesis, this phenomenon was studied for Brazilian Pre-Salt crude oils, after initial research from the Brazilian state oil company and Pre-Salt operators. This thesis describes how the liquid – liquid equilibrium is detected by using complementary PVT techniques, and this study can be expanded to diverse type of crude oils with different chemical characteristics and from different geographical location.
2. Evaluation of separation methods for the detected liquid – liquid immiscibility on petroleum fluids. The second liquid formed phase was detected as a fine dispersion in the continuous oil phase. The high dispersity limited the phase separation and sampling, future efforts are required for evaluation of separation methods for this second phase. Mechanical methods have been unable for this task, for that reason it is suggested to evaluate surfactants effects on the dispersed phase coalescence.
3. Confirmation of second liquid phase composition and yield. After the second liquid sampling, chemical composition is recommended. Also, the density or yield of the second liquid phase is necessary for better description of the observed phase equilibrium and their modelling.
4. Comparison of liquid – liquid immiscibility with the asphaltene precipitation on unstable crude oils. It is recommended to compare and contrast the detection of both phase transitions using conventional and unconventional PVT techniques. From the results of this work, a wide multiphasic region at high pressure conditions was detected by SWIR full visibility PVT. This phase equilibrium is normally neglected by indirect PVT methods as NIR-SDS or QCR. The comparison of liquid – liquid detection protocols with those made for unstable asphaltenic crude oils, could contribute to better assessment of reservoir fluids phase equilibria.
5. Inclusion of wax and asphaltene precipitation on the thermodynamic modelling used for Pre-Salt crude oil and gas mixtures, together with the improvement of physicochemical properties description for the obtained second liquid phase.

10 REFERENCES

- ABEDI, S. J. et al. Simultaneous phase behaviour, elemental composition and density measurement using X-ray imaging. **Fluid Phase Equilibria**, v. 158–160, p. 775–781, 1999.
- ABUDU, A.; GOUAL, L. Adsorption of Crude Oil on Surfaces Using Quartz Crystal Microbalance with Dissipation (QCM-D) under Flow Conditions. **Energy & Fuels**, v. 23, n. 3, p. 1237–1248, 2009.
- ABUTAQIYA, M. I. L. et al. Systematic Investigation of Asphaltene Deposition in the Wellbore and Near-Wellbore Region of a Deepwater Oil Reservoir Under Gas Injection. Part 1: Thermodynamic Modeling of the Phase Behavior of Polydisperse Asphaltenes. **Energy & Fuels**, 2019.
- AGRAWAL, P. et al. Measurement and modeling of the phase behavior of solvent diluted bitumens. **Fluid Phase Equilibria**, v. 334, p. 51–64, 2012.
- AKBARZADEH, K. et al. A generalized regular solution model for asphaltene precipitation from n-alkane diluted heavy oils and bitumens. **Fluid Phase Equilibria**, v. 232, n. 1–2, p. 159–170, 2005.
- AL GHAFRI, S. Z.; MAITLAND, G. C.; TRUSLER, J. P. M. Experimental and modeling study of the phase behavior of synthetic crude oil+CO₂. **Fluid Phase Equilibria**, v. 365, p. 20–40, 2014.
- ALBOUDWAREJ, H. et al. Sensitivity of Asphaltene Properties to Separation Techniques. **Energy & Fuels**, v. 16, n. 2, p. 462–469, 2002.
- ALGHANDURI, L. M. et al. Characterization of Libyan Waxy Crude Oils. **Energy & Fuels**, v. 24, n. 5, p. 3101–3107, 2010.
- ALHAMMADI, A. A.; VARGAS, F. M.; CHAPMAN, W. G. Comparison of Cubic-Plus-Association and Perturbed-Chain Statistical Associating Fluid Theory Methods for Modeling Asphaltene Phase Behavior and Pressure–Volume–Temperature Properties. **Energy & Fuels**, v. 29, n. 5, p. 2864–2875, 2015.
- ALVES, C. A. et al. Effect of Temperature on Asphaltenes Precipitation: Direct and Indirect Analyses and Phase Equilibrium Study. **Energy & Fuels**, v. 33, n. 8, p. 6921–6928, 2019.
- AMJAD, K. et al. **Reservoir Fluid Identification – A Case Study of a Near Critical Fluid From Low Permeability Exploratory Reservoir**. Abu Dhabi International Petroleum Exhibition & Conference. **Anais...** In: Abu Dhabi International Petroleum Exhibition & Conference. Abu Dhabi, UAE: Society of Petroleum Engineers, 2016.
- ANDERSEN, S. I. Flocculation Onset Titration of Petroleum Asphaltenes. **Energy & Fuels**, v. 13, n. 2, p. 315–322, 1999.

ANDERSEN, S. I.; BIRDI, K. S. Aggregation of asphaltenes as determined by calorimetry. **Journal of Colloid and Interface Science**, v. 142, n. 2, p. 497–502, 1991.

ANDERSEN, S. I.; LINDELOFF, N.; STENBY, E. H. Investigation of Asphaltene Precipitation at Elevated Temperature. **Petroleum Science and Technology**, v. 16, n. 3–4, p. 323–334, 1998.

ARTOLA, P.-A. et al. Understanding the fluid phase behaviour of crude oil: Asphaltene precipitation. **Fluid Phase Equilibria**, v. 306, n. 1, p. 129–136, 2011.

ASKE, N. et al. Asphaltene Aggregation from Crude Oils and Model Systems Studied by High-Pressure NIR Spectroscopy. **Energy & Fuels**, v. 16, n. 5, p. 1287–1295, 2002.

ASTM D 5307 (1992) Determination of Boiling Range Distribution of Crude Petroleum by Gas Chromatography. American Society for Testing and Materials.

BAGLEY, E. B.; NELSON, T. P.; SCIGLIANO, J. M. Three-dimensional solubility parameters and their relationship to internal pressure measurements in polar and hydrogen bonding solvents. **Journal of paint technology**, v. 43, n. 555, p. 35–42.

BARTON, A. F. M. **CRC Handbook of Solubility Parameters and Other Cohesion Parameters, Second Edition**. CRC Press, 1991.

BELTRAO, R. L. C. et al. **SS: Pre-salt Santos basin - Challenges and New Technologies for the Development of the Pre-salt Cluster, Santos Basin, Brazil**. . In: Offshore Technology Conference. Offshore Technology Conference, 1 jan. 2009

BUCKLEY, J. S. Microscopic Investigation Of The Onset Of Asphaltene Precipitation. **Fuel Science and Technology International**, 25 2007.

BYCHINSKY, V. A. et al. Methods for Calculating the Critical Constants of Hydrocarbons (Using the n-Alkane Series as an Example). **Journal of Chemical & Engineering Data**, v. 58, n. 11, p. 3102–3109, 2013.

CALLES, J. A. et al. Properties of Asphaltenes Precipitated with Different n-Alkanes. A Study To Assess the Most Representative Species for Modeling. **Energy & Fuels**, v. 22, n. 2, p. 763–769, 2008.

CAO, M.; GU, Y. Oil recovery mechanisms and asphaltene precipitation phenomenon in immiscible and miscible CO₂ flooding processes. **Fuel**, v. 109, p. 157–166. 2013.

CARDOSO, F. M. R. et al. CO₂ and Temperature Effects on the Asphaltene Phase Envelope As Determined by a Quartz Crystal Resonator. **Energy & Fuels**, v. 28, n. 11, p. 6780–6787, 2014.

CARDOSO, F. M. R. et al. **Phase Behavior of CO₂-Rich Live Oil Samples From High Pressure Reservoirs**. . In: OTC BRASIL. Offshore Technology Conference, 27 oct. 2015

CARRIER, H. et al. Acoustic method for measuring asphaltene flocculation in crude oils. **Journal of Petroleum Science and Engineering**, v. 27, n. 3, p. 111–117, 2000.

- CASAS, Y. A. et al. Settling of Asphaltene Aggregates in n-Alkane Diluted Bitumen. **Energy & Fuels**, v. 33, n. 11, p. 10687–10703, 2019.
- CASTILLO, J. et al. Optical fiber extrinsic refractometer to measure RI of samples in a high pressure and temperature systems: Application to wax and asphaltene precipitation measurements. **Fuel**, v. 85, n. 14, p. 2220–2228, 2006.
- CHACON VALERO, A. M.; FEITOSA, F. X.; BATISTA DE SANT'ANA, H. Density and Volumetric Behavior of Binary CO₂ + n-Decane and Ternary CO₂ + n-Decane + Naphthalene Systems at High Pressure and High Temperature. **Journal of Chemical & Engineering Data**, v. 65, n. 7, p. 3499–3509, 2020.
- CHAISSONTORNYOTIN, W.; BINGHAM, A. W.; HOEPFNER, M. P. Reversibility of Asphaltene Precipitation Using Temperature-Induced Aggregation. **Energy & Fuels**, v. 31, n. 4, p. 3392–3398, 2017.
- CHEN, R. J. J.; CHAPPELEAR, P. S.; KOBAYASHI, R. Dew-point loci for methane-n-hexane and methane-n-heptane binary systems. **Journal of Chemical & Engineering Data**, v. 21, n. 2, p. 213–219, 1976.
- CHRISTOV, M.; DOHRN, R. High-pressure fluid phase equilibria: Experimental methods and systems investigated (1994–1999). **Fluid Phase Equilibria**, v. 202, n. 1, p. 153–218, 2002.
- CIBULKA, I.; HNĚDKOVSKÝ, L. Liquid Densities at Elevated Pressures of n-Alkanes from C₅ to C₁₆: A Critical Evaluation of Experimental Data. **Journal of Chemical & Engineering Data**, v. 41, n. 4, p. 657–668, 1996.
- COMUÑAS, M. J. P. et al. Density of Diethyl Adipate using a New Vibrating Tube Densimeter from (293.15 to 403.15) K and up to 140 MPa. Calibration and Measurements. **Journal of Chemical & Engineering Data**, v. 53, n. 4, p. 986–994, 2008.
- COUTINHO, J. A. P. et al. Reliable Wax Predictions for Flow Assurance. **Energy & Fuels**, v. 20, n. 3, p. 1081–1088, 2006.
- COUTINHO, J. A. P.; DARIDON, J.-L. Low-Pressure Modeling of Wax Formation in Crude Oils. **Energy & Fuels**, v. 15, n. 6, p. 1454–1460, 2001.
- COUTINHO, J. A. P.; JØRGENSEN, M.; STENBY, E. H. Predictions of three-phase regions in CO₂-oil mixtures. **Journal of Petroleum Science and Engineering**, v. 12, n. 3, p. 201–208, 1995.
- DA COSTA FRAGA, C. T. et al. **Brazilian Pre-Salt: An Impressive Journey from Plans and Challenges to Concrete Results**. . In: Offshore Technology Conference. Offshore Technology Conference, 4 may 2015
- DARIDON, J. L. et al. Probing Asphaltene Flocculation by a Quartz Crystal Resonator. **Energy & Fuels**, v. 27, n. 8, p. 4639–4647, 2013.

DARIDON, J. L.; ORLANDI, E.; CARRIER, H. Measurement of bubble point pressure in crude oils using an acoustic wave sensor. **Fluid Phase Equilibria**, v. 427, p. 152–160, 2016.

DARIDON, J. L.; PAULY, J.; MILHET, M. High pressure solid–liquid phase equilibria in synthetic waxes. **Physical Chemistry Chemical Physics**, v. 4, n. 18, p. 4458–4461, 2002.

DARIDON, J.-L. et al. Combined Investigations of Fluid Phase Equilibria and Fluid–Solid Phase Equilibria in Complex CO₂–Crude Oil Systems under High Pressure. **Journal of Chemical & Engineering Data**, v. 65, n. 7, p. 3357–3372, 2020.

DARIDON, J.-L.; CARRIER, H. Measurement of Phase Changes in Live Crude Oil Using an Acoustic Wave Sensor: Asphaltene Instability Envelope. **Energy & Fuels**, v. 31, n. 9, p. 9255–9267, 2017.

DERUITER, R. A.; NASH, L. J.; SINGLETARY, M. S. Solubility and Displacement Behavior of a Viscous Crude With CO₂ and Hydrocarbon Gases. **SPE Reservoir Engineering**, v. 9, n. 02, p. 101–106, 1994.

DÍAZ, O. C. et al. Modeling the phase behavior of heavy oil and solvent mixtures. **Fluid Phase Equilibria**, v. 304, n. 1, p. 74–85, 2011.

DINI, Y.; BECERRA, M.; SHAW, J. M. Phase Behavior and Thermophysical Properties of Peace River Bitumen + Propane Mixtures from 303 K to 393 K. **Journal of Chemical & Engineering Data**, v. 61, n. 8, p. 2659–2668, 2016.

DOHRN, R.; BRUNNER, G. High-pressure fluid-phase equilibria: Experimental methods and systems investigated (1988–1993). **Fluid Phase Equilibria**, v. 106, n. 1, p. 213–282, 1995.

DOHRN, R.; PEPPER, S.; FONSECA, J. M. S. High-pressure fluid-phase equilibria: Experimental methods and systems investigated (2000–2004). **Fluid Phase Equilibria**, v. 288, n. 1, p. 1–54, 2010.

DURAN, J. A.; SCHOEGGL, F. F.; YARRANTON, H. W. Kinetics of asphaltene precipitation/aggregation from diluted crude oil. **Fuel**, v. 255, p. 115859, 2019.

DYMOND, J. H.; MALHOTRA, R. The Tait equation: 100 years on. **International Journal of Thermophysics**, v. 9, n. 6, p. 941–951, 1988.

EGHBALI, S.; DEGHANPOUR, H. An Experimental and Modeling Study on Interactions of Cold Lake Bitumen with CO₂, C₃, and C₄ at High Temperatures. **Energy & Fuels**, v. 33, n. 5, p. 3957–3969, 2019.

ENICK, R.; HOLDER, G. D.; MORSI, B. I. Critical and three phase behavior in the carbon dioxide/tridecane system. **Fluid Phase Equilibria**, v. 22, n. 2, p. 209–224, 1985.

ESCOBEDO, J.; MANSOORI, G. A. Viscometric Determination of the Onset of Asphaltene Flocculation: A Novel Method. **SPE Production & Facilities**, v. 10, n. 02, p. 115–118, 1995.

ESTRERA, S. S.; ARBUCKLE, M. M.; LUKS, K. D. Solubility and partial miscibility of ethane in certain hydrocarbon liquids. **Fluid Phase Equilibria**, v. 35, n. 1, p. 291–307, 1987.

ESTRERA, S. S.; LUKS, K. D. Liquid-liquid-vapor equilibria behavior of certain ethane + n-paraffin mixtures. **Journal of Chemical & Engineering Data**, v. 32, n. 2, p. 201–204, 1987.

FALL, D. J.; FALL, J. L.; LUKS, K. D. Liquid-liquid-vapor immiscibility limits in carbon dioxide + n-paraffin mixtures. **Journal of Chemical & Engineering Data**, v. 30, n. 1, p. 82–88, 1985.

FALL, D. J.; LUKS, K. D. Phase equilibria behavior of the systems carbon dioxide + n-dotriacontane and carbon dioxide + n-docosane. **Journal of Chemical & Engineering Data**, v. 29, n. 4, p. 413–417, 1984.

FALL, D. J.; LUKS, K. D. Liquid-liquid-vapor equilibria of the binary mixtures carbon dioxide + n-pentadecylbenzene and carbon dioxide + n-nonylbenzene. **Fluid Phase Equilibria**, v. 23, n. 2, p. 259–267, 1985a.

FALL, D. J.; LUKS, K. D. Liquid-liquid-vapor phase equilibria of the binary system carbon dioxide + n-tridecane. **Journal of Chemical & Engineering Data**, v. 30, n. 3, p. 276–279, 1985b.

FIROOZINIA, H.; FOULADI HOSSEIN ABAD, K.; VARAMESE, A. A comprehensive experimental evaluation of asphaltene dispersants for injection under reservoir conditions. **Petroleum Science**, v. 13, n. 2, p. 280–291, 2016.

FONSECA, J. M. S.; DOHRN, R.; PEPPER, S. High-pressure fluid-phase equilibria: Experimental methods and systems investigated (2005–2008). **Fluid Phase Equilibria**, v. 300, n. 1, p. 1–69, 2011.

FORNARI, R. E.; ALESSI, P.; KIKIC, I. High pressure fluid phase equilibria: experimental methods and systems investigated (1978–1987). **Fluid Phase Equilibria**, v. 57, n. 1, p. 1–33, 1990.

FOTLAND, P.; ANFINDSEN, H.; FADNES, F. H. Detection of asphaltene precipitation and amounts precipitated by measurement of electrical conductivity. **Fluid Phase Equilibria**, v. 82, p. 157–164, 1993.

FRANÇA, D. et al. Speciation and quantification of high molecular weight paraffins in Brazilian whole crude oils using high-temperature comprehensive two-dimensional gas chromatography. **Fuel**, v. 234, p. 1154–1164, 2018.

FUHR, B. J. et al. Properties of asphaltenes from a waxy crude. **Fuel**, Eastern oil shale symposium. v. 70, n. 11, p. 1293–1297, 1991.

FUHR, B. J.; KLEIN, L. L.; REICHERT, C. Measurement Of Asphaltene Flocculation In Bitumen Solutions. **Journal of Canadian Petroleum Technology**, v. 25, n. 05, 1986.

- GARCÍA, J.; LUGO, L.; FERNÁNDEZ, J. Phase Equilibria, P VT Behavior, and Critical Phenomena in Carbon Dioxide + n -Alkane Mixtures Using the Perturbed-Chain Statistical Associating Fluid Theory Approach. **Industrial & Engineering Chemistry Research**, v. 43, n. 26, p. 8345–8353, 2004.
- GARCÍA, M. DEL C.; CARBOGNANI, L. Asphaltene–Paraffin Structural Interactions. Effect on Crude Oil Stability. **Energy & Fuels**, v. 15, n. 5, p. 1021–1027, 2001.
- GODBOLE, S. P.; THELE, K. J.; REINBOLD, E. W. EOS Modeling and Experimental Observations of Three-Hydrocarbon-Phase Equilibria. **SPE Reservoir Engineering**, v. 10, n. 02, p. 101–108, 1995.
- GONCALVES, M. A. et al. **Lessons Learned on Wax Issues From Deep Offshore Brazil**. . In: OTC BRASIL. Offshore Technology Conference, 29 oct. 2013
- GONZALEZ, D. L. et al. Prediction of Asphaltene Instability under Gas Injection with the PC-SAFT Equation of State. **Energy & Fuels**, v. 19, n. 4, p. 1230–1234, 2005.
- GONZALEZ, D. L. et al. Modeling Study of CO₂-Induced Asphaltene Precipitation †. **Energy & Fuels**, v. 22, n. 2, p. 757–762, 2008.
- GOUAL, L. et al. Adsorption of Bituminous Components at Oil/Water Interfaces Investigated by Quartz Crystal Microbalance: Implications to the Stability of Water-in-Oil Emulsions. **Langmuir**, v. 21, n. 18, p. 8278–8289, 2005.
- GOUAL, L. et al. Asphaltene Aggregation and Impact of Alkylphenols. **Langmuir**, v. 30, n. 19, p. 5394–5403, 2014.
- GUI, X. et al. Measurement and Correlation of High Pressure Phase Equilibria for CO₂ + Alkanes and CO₂ + Crude Oil Systems. **Journal of Chemical & Engineering Data**, v. 62, n. 11, p. 3807–3822, 2017.
- GUZMÁN, R. et al. Methods for determining asphaltene stability in crude oils. **Fuel**, v. 188, p. 530–543, 2017.
- HAMMAMI, A. et al. Asphaltene Precipitation from Live Oils: An Experimental Investigation of Onset Conditions and Reversibility. **Energy & Fuels**, v. 14, n. 1, p. 14–18, jan. 2000.
- HILDEBRAND, J. H.; SCOTT, R. L., **Reinhold Publishing Corporation**, 1950.
- HIRSCHBERG, A. et al. Influence of Temperature and Pressure on Asphaltene Flocculation. **Society of Petroleum Engineers Journal**, v. 24, n. 03, p. 283–293, 1984.
- HOSEIN, R. .; MAYRHOO, R. .; MCCAIN, W. D. **Determination of Bubble-Point and Dew-Point Pressure Without a Visual Cell**. 2014
- HOTIER, G.; ROBIN, M. Action de divers diluants sur les produits pétroliers lourds : mesure, interprétation et prévision de la floculation des asphaltènes. **Revue de l'Institut Français du Pétrole**, v. 38, n. 1, p. 101–120, 1983.

HOTTOVY, J. D.; KOHN, J. P.; LUKS, K. D. Partial miscibility behavior of the methane-ethane-n-octane system. **Journal of Chemical & Engineering Data**, v. 26, n. 2, p. 135–137, 1981.

HOTTOVY, J. D.; KOHN, J. P.; LUKS, K. D. Partial miscibility behavior of the ternary systems methane-propane-n-octane, methane-n-butane-n-octane, and methane-carbon dioxide-n-octane. **Journal of Chemical & Engineering Data**, v. 27, n. 3, p. 298–302, 1982.

HOTTOVY, J. D.; LUKS, K. D.; KOHN, J. P. Three-phase liquid-liquid-vapor equilibriums behavior of certain binary carbon dioxide-n-paraffin systems. **Journal of Chemical & Engineering Data**, v. 26, n. 3, p. 256–258, 1981.

HUANG, E. T. S.; TRACHT, J. H. **The Displacement of Residual Oil By Carbon Dioxide**. . In: SPE Improved Oil Recovery Symposium. Society of Petroleum Engineers, 1 jan. 1974

IMAI, M. et al. Reduced variables method for four-phase equilibrium calculations of hydrocarbon-water-CO₂ mixtures at a low temperature. **Fluid Phase Equilibria**, v. 497, p. 151–163, 2019.

ISO/IEC GUIDE 98-3:2008(E) Guide to the expression of uncertainty in measurement (GUM:1995). First Edition. 2008.

JANGKAMOLKULCHAI, A.; ARBUCKLE, M. M.; LUKS, K. D. Liquid—liquid—vapor phase equilibria behavior of certain binary ethane + n-alkylbenzene mixtures. **Fluid Phase Equilibria**, v. 40, n. 3, p. 235–245, 1988.

JAUBERT, J.-N. et al. Extension of the PPR78 model (predictive 1978, Peng–Robinson EOS with temperature dependent k_{ij} calculated through a group contribution method) to systems containing aromatic compounds. **Fluid Phase Equilibria**, v. 237, n. 1, p. 193–211, 2005.

JAUBERT, J.-N. et al. Reliability of the correlation allowing the k_{ij} to switch from an alpha function to another one in hydrogen-containing systems. **Fluid Phase Equilibria**, v. 338, p. 23–29, 2013.

JAUBERT, J.-N.; MUTELET, F. VLE predictions with the Peng–Robinson equation of state and temperature dependent k_{ij} calculated through a group contribution method. **Fluid Phase Equilibria**, v. 224, n. 2, p. 285–304, 2004.

JAUBERT, J.-N.; PRIVAT, R. Relationship between the binary interaction parameters (k_{ij}) of the Peng–Robinson and those of the Soave–Redlich–Kwong equations of state: Application to the definition of the PR2SRK model. **Fluid Phase Equilibria**, v. 295, n. 1, p. 26–37, 2010.

JOHNSTON, K. A. et al. Phase behavior of bitumen and n-pentane. **Fluid Phase Equilibria**, v. 442, p. 1–19, 2017.

JOSHI, N. B. et al. Asphaltene Precipitation from Live Crude Oil. **Energy & Fuels**, v. 15, n. 4, p. 979–986, 2001.

- JUYAL, P. et al. Study of Live Oil Wax Precipitation with High-Pressure Micro-Differential Scanning Calorimetry. **Energy & Fuels**, v. 25, n. 2, p. 568–572, 2011.
- KARAN, K. et al. Evaluation of Asphaltene Instability and a Chemical Control During Production of Live Oils. **Petroleum Science and Technology**, v. 21, n. 3–4, p. 629–645, 2003.
- KATZ, D. L.; FIROOZABADI, A. Predicting Phase Behavior of Condensate/Crude-Oil Systems Using Methane Interaction Coefficients. **Journal of Petroleum Technology**, v. 30, n. 11, p. 1.649-1.655, 1978.
- KEIJI KANAZAWA, K.; GORDON, J. G. The oscillation frequency of a quartz resonator in contact with liquid. **Analytica Chimica Acta**, v. 175, p. 99–105, 1985.
- KESLER, M. G.; LEE, B. I. Improve prediction of enthalpy of fractions. **Hydrocarbon processing**, p. 153–158, 1976.
- KHAN, S. A.; POPE, G. A.; SEPEHRNOORI, K. **Fluid Characterization of Three-Phase CO₂/Oil Mixtures**. . In: SPE/DOE Enhanced Oil Recovery Symposium. Society of Petroleum Engineers, 1 jan. 1992
- KHARRAT, A. M. et al. Issues with Comparing SARA Methodologies. **Energy & Fuels**, v. 21, n. 6, p. 3618–3621, 2007.
- KHATANIAR, S. et al. **CO₂ and Miscible Gas Injection for Enhanced Recovery of Schrader Bluff Heavy Oil**. . In: International Thermal Operations/Heavy Oil Symposium. Society of Petroleum Engineers, 1999
- KOHN, J. P.; BRADISH, W. F. Multiphase and Volumetric Equilibria of the Methane-n-Octane System at Temperatures between -110 and 150 C. **Journal of Chemical & Engineering Data**, v. 9, n. 1, p. 5–8, 1964.
- KOHN, J. P.; KIM, Y. J.; PAN, Y. C. Partial Miscibility Phenomena in Binary Hydrocarbon Systems Involving Ethane. **Journal of Chemical & Engineering Data**, v. 11, n. 3, p. 333–335, 1966.
- KUMAR, A.; OKUNO, R. **Fluid Characterization Using an EOS for Compositional Simulation of Enhanced Heavy-Oil Recovery**. SPE Annual Technical Conference and Exhibition. San Antonio, Texas, USA: Society of Petroleum Engineers, 2012
- KUMAR, R.; VOOLAPALLI, R. K.; UPADHYAYULA, S. Prediction of crude oil blends compatibility and blend optimization for increasing heavy oil processing. **Fuel Processing Technology**, v. 177, p. 309–327, 2018.
- LAM, D. H.; JANGKAMOLKULCHAI, A.; LUKS, K. D. Liquid-liquid-vapor phase equilibrium behavior of certain binary ethane + n-alkanol mixtures. **Fluid Phase Equilibria**, v. 59, n. 3, p. 263–277, 1990.
- LANSANGAN, R. M.; JANGKAMOLKULCHAI, A.; LUKS, K. D. Binary vapor liquid equilibria behavior in the vicinity of liquid liquid vapor loci. **Fluid Phase Equilibria**, v. 36, p. 49–66, 1987.

- LEE, B. I.; KESLER, M. G. A generalized thermodynamic correlation based on three-parameter corresponding states. **AIChE Journal**, v. 21, n. 3, p. 510–527, 1975.
- LEI, H. et al. Experimental Investigation and Application of the Asphaltene Precipitation Envelope. **Energy & Fuels**, v. 29, n. 11, p. 6920–6927, 2015.
- LEMMON, E. W.; HUBER, M. L.; MCLINDEN, M. O. **NIST Standard Reference Database 23: Reference Fluid Thermodynamic and Transport Properties-REFPROP**. MD: NIST: Gaithersburg, 2007.
- LINDELOFF, N. et al. **Investigation of Miscibility Behavior of CO₂-rich Hydrocarbon Systems - With Implications for Gas Injection EOR**. . In: SPE Annual Technical Conference And Exhibition. Society of Petroleum Engineers, 30 sept. 2013
- LINDELOFF, N.; MOGENSEN, K. Investigation of Miscibility Behavior of CO₂ rich Hydrocarbon Systems – With Application for Gas Injection EOR. p. 14.
- LINSTROM, P. J.; MALLARD, W. G. **NIST Chemistry WebBook, NIST Standard Reference Database Number 69**, 2011. Gaithersburg MD: National Institute of Standards and Technology.
- MANCILLA-POLANCO, A. . et al. **The Phase Behavior of Heavy Oil and Propane Mixtures**. 15 fev. 2017
- MAQBOOL, T.; BALGOA, A. T.; FOGLER, H. S. Revisiting Asphaltene Precipitation from Crude Oils: A Case of Neglected Kinetic Effects. **Energy & Fuels**, v. 23, n. 7, p. 3681–3686, 2009.
- MAQBOOL, T.; SRIKIRATIWONG, P.; FOGLER, H. S. Effect of Temperature on the Precipitation Kinetics of Asphaltenes. **Energy & Fuels**, v. 25, n. 2, p. 694–700, 2011.
- MCKEAN, T. A. M. et al. **Schrader Bluff CO₂ EOR Evaluation**. In: Spe Western Regional Meeting. Society of Petroleum Engineers, 1 jan. 1999
- MEHROTRA, A. Viscosity, density and gas solubility data for oil sand bitumens. Part III : Wabasca bitumen saturated with N₂, CO, CH₄ and CO₂ and C₂H₆. v. 2, n. 2, p. 83–93, 1985.
- MICHELSEN, M. L. The isothermal flash problem. Part I. Stability. **Fluid Phase Equilibria**, v. 9, n. 1, p. 1–19, 1982a.
- MICHELSEN, M. L. The isothermal flash problem. Part II. Phase-split calculation. **Fluid Phase Equilibria**, v. 9, n. 1, p. 21–40, 1982b.
- MILHET, M. et al. Solid–Liquid Equilibria under High Pressure of Nine Pure n-Alkylbenzenes. **Journal of Chemical & Engineering Data**, v. 53, n. 1, p. 233–237, 2008.
- MOHAMMADI, S. et al. Reversibility of Asphaltene Aggregation in Live Oils: Qualitative and Quantitative Evaluation. **Journal of Chemical & Engineering Data**, v. 60, n. 9, p. 2646–2654, 2015.

- MOHAMMADI, S. et al. Kinetics of asphaltene aggregation phenomena in live oils. **Journal of Molecular Liquids**, v. 222, p. 359–369, 2016.
- MOHEBBINIA, S.; SEPEHRNOORI, K.; JOHNS, R. T. Four-Phase Equilibrium Calculations of Carbon Dioxide/Hydrocarbon/Water Systems With a Reduced Method. **SPE Journal**, v. 18, n. 05, p. 943–951, 2013.
- MORÉ, J. J. **The Levenberg-Marquardt algorithm: Implementation and theory.** (G. A. Watson, Ed.) Numerical Analysis: Lecture Notes in Mathematics. Berlin, Heidelberg: Springer, 1978
- NEGAHBAN, S. et al. “Digital Fluid Physics”: Prediction of phase equilibria for several mixtures of CO₂ with petroleum fluid systems. **Journal of Petroleum Science and Engineering**, v. 187, p. 106752, 2020.
- OKUNO, R.; XU, Z. Efficient Displacement of Heavy Oil by Use of Three Hydrocarbon Phases. **SPE Journal**, v. 19, n. 05, p. 956–973, 2014a.
- OKUNO, R.; XU, Z. Mass Transfer on Multiphase Transitions in Low-Temperature Carbon Dioxide Floods. **SPE Journal**, v. 19, n. 06, p. 1005–1023, 2014b.
- ORR, F. M.; YU, A. D.; LIEN, C. L. Phase Behavior of CO₂ and Crude Oil in Low-Temperature Reservoirs. **Society of Petroleum Engineers Journal**, v. 21, n. 04, p. 480–492, 1981.
- PAN, H. et al. Phase-Behavior Modeling and Flow Simulation for Low-Temperature CO₂ Injection. **SPE Reservoir Evaluation & Engineering**, v. 18, n. 02, p. 250–263, 2015.
- PEDERSEN, K. S.; FREDENSLUND, A.; THOMASSEN, P. **Properties of Oils and Natural Gases.** [s.l.] Gulf Publishing Company, Book Division, 1989.
- PEDERSEN, K. S.; THOMASSEN, P.; FREDENSLUND, A. **Characterization of gas condensate mixtures.** . In: Conference: American Institute Of Chemical Engineers Spring National Meeting. New York, NY; American Institute of Chemical Engineers, 1988
- PENG, D.-Y.; ROBINSON, D. B. A New Two-Constant Equation of State. **Industrial & Engineering Chemistry Fundamentals**, v. 15, n. 1, p. 59–64, 1976.
- PETERS, C. J.; DE ROO, J. L.; LICHTENTHALER, R. N. Measurements and calculations of phase equilibria in binary mixtures of ethane + eicosane. **Fluid Phase Equilibria**, v. 69, p. 51–66, 1991.
- PETERS, C. J.; SPIEGELAAR, J.; DE SWAAN ARONS, J. Phase equilibria in binary mixtures of ethane + docosane and molar volumes of liquid docosane. **Fluid Phase Equilibria**, v. 41, n. 3, p. 245–256, 1988.
- QUINTEROS-LAMA, H.; LLOVELL, F. Global phase behaviour in methane plus n-alkanes binary mixtures. **The Journal of Supercritical Fluids**, v. 111, p. 151–161, 2016.

- QUINTEROS-LAMA, H.; LLOVELL, F. Global phase behaviour in carbon dioxide plus n-alkanes binary mixtures. **The Journal of Supercritical Fluids**, v. 140, p. 147–158, 2018.
- RAMOS, A. C. DA S. et al. Determination of solubility parameters of oils and prediction of oil compatibility. **Journal of Petroleum Science and Engineering**, v. 102, p. 36–40, 2013.
- ROGEL, E. Theoretical Estimation of the Solubility Parameter Distributions of Asphaltenes, Resins, and Oils from Crude Oils and Related Materials. **Energy & Fuels**, v. 11, n. 4, p. 920–925, 1997.
- ROGEL, E. et al. Asphaltene Densities and Solubility Parameter Distributions: Impact on Asphaltene Gradients. **Energy & Fuels**, v. 30, n. 11, p. 9132–9140, 2016.
- ROGEL, E.; MOIR, M. Effect of precipitation time and solvent power on asphaltene characteristics. **Fuel**, v. 208, p. 271–280, 2017.
- ROMERO YANES, J. F. et al. Paraffin effects on the stability and precipitation of crude oil asphaltenes: Experimental onset determination and phase behavior approach. **Fluid Phase Equilibria**, v. 474, p. 116–125, 2018a.
- ROWLINSON, J. S.; SWINTON, F. L. **Liquids and Liquid Mixtures**. Elsevier, 1982.
- SAIDOUN, M. et al. Revisiting asphaltenes instability predictions by probing destabilization using a fully immersed quartz crystal resonator. **Fuel**, v. 251, p. 523–533, 2019.
- SHADMAN, M. M. et al. The Effect of Inhibitors on Asphaltene Precipitation in Crude Oil Using the Viscometric Method. **Energy Sources, Part A: Recovery, Utilization, and Environmental Effects**, v. 34, n. 9, p. 827–838, 2012.
- SHARMA, A. K. et al. **Miscible Displacement of Heavy West Sak Crude by Solvents in Slim Tube**. . In: SPE California Regional Meeting. Society of Petroleum Engineers, 1 jan. 1989
- SHAW, J. M.; BÉHAR, E. SLLV phase behavior and phase diagram transitions in asymmetric hydrocarbon fluids. **Fluid Phase Equilibria**, v. 209, n. 2, p. 185–206, 2003.
- SHAW, J. M.; DELOOS, T. W.; ARONS, J. DE S. An explanation for solid-liquid-liquid-vapour phase behaviour in reservoir fluids. **Petroleum Science and Technology**, v. 15, n. 5–6, p. 503–521, 1997.
- SHAW, J. M.; ZOU, X. Phase Behavior of Heavy Oils. In: MULLINS, O. C. et al. (Eds.). . **Asphaltenes, Heavy Oils, and Petroleomics**. New York, NY: Springer, 2007. p. 489–510.
- SHELTON, J. L.; YARBOROUGH, L. Multiple Phase Behavior in Porous Media During CO₂ or Rich-Gas Flooding. **Journal of Petroleum Technology**, v. 29, n. 09, p. 1171–1178, 1 set. 1977.

SPEIGHT, J. G. Petroleum Asphaltene - Part 1: Asphaltene, Resins and the Structure of Petroleum. **Oil & Gas Science and Technology**, v. 59, n. 5, p. 467–477, 2004.

TAVAKKOLI, M. et al. Precipitated Asphaltene Amount at High-Pressure and High-Temperature Conditions. **Energy & Fuels**, v. 28, n. 3, p. 1596–1610, 2014a.

TAVAKKOLI, M. et al. Asphaltene Deposition in Different Depositing Environments: Part 1. Model Oil. **Energy & Fuels**, v. 28, n. 3, p. 1617–1628, 2014b.

THARANIVASAN, A. K.; YARRANTON, H. W.; TAYLOR, S. D. Application of a Regular Solution-Based Model to Asphaltene Precipitation from Live Oils. **Energy & Fuels**, v. 25, n. 2, p. 528–538, 2011.

THARANIVASAN, A. K.; YARRANTON, H. W.; TAYLOR, S. D. Asphaltene Precipitation from Crude Oils in the Presence of Emulsified Water. **Energy & Fuels**, v. 26, n. 11, p. 6869–6875, 2012.

TING, P. D.; HIRASAKI, G. J.; CHAPMAN, P. W. G. Modeling of Asphaltene Phase Behavior with the SAFT Equation of State. **Petroleum Science and Technology**, v. 21, n. 3–4, p. 647–661, 2003.

TUREK, E. A.; METCALFE, R. S.; FISHBACK, R. E. Phase Behavior of Several CO₂/ West Texas-Reservoir-Oil Systems. **SPE Reservoir Engineering**, v. 3, n. 02, p. 505–516, 1988.

TWU, C. H. An internally consistent correlation for predicting the critical properties and molecular weights of petroleum and coal-tar liquids. **Fluid Phase Equilibria**, v. 16, n. 2, p. 137–150, 1984.

UNGERER, P.; BATUT, C. Prédiction des propriétés volumétriques des hydrocarbures par une translation de volume améliorée. **Revue de l'Institut Français du Pétrole**, v. 52, n. 6, p. 609–623, 1997.

VAN KONYNENBURG, P. H.; SCOTT, R. L.; ROWLINSON, J. S. Critical lines and phase equilibria in binary van der Waals mixtures. **Philosophical Transactions of the Royal Society of London. Series A, Mathematical and Physical Sciences**, v. 298, n. 1442, p. 495–540, 1980.

VANINI, G. et al. Analytical advanced techniques in the molecular-level characterization of Brazilian crude oils. **Microchemical Journal**, v. 137, p. 111–118, 2018.

VARGAS, F. M. et al. Modeling Asphaltene Phase Behavior in Crude Oil Systems Using the Perturbed Chain Form of the Statistical Associating Fluid Theory (PC-SAFT) Equation of State. **Energy & Fuels**, v. 23, n. 3, p. 1140–1146, 2009a.

VARGAS, F. M. et al. Development of a General Method for Modeling Asphaltene Stability †. **Energy & Fuels**, v. 23, n. 3, p. 1147–1154, 2009b.

VENKATARAMANAN, L. et al. Uncertainty Analysis of Visible and Near-Infrared Data of Hydrocarbons. **Applied Spectroscopy**, v. 60, n. 6, p. 653–662, 2006.

VERDIER, S. et al. Study of Pressure and Temperature Effects on Asphaltene Stability in Presence of CO₂. **Energy & Fuels**, v. 20, n. 4, p. 1584–1590, 2006.

VERDIER, S.; ANDERSEN, S. I. Internal pressure and solubility parameter as a function of pressure. **Fluid Phase Equilibria**, v. 231, n. 2, p. 125–137, 2005.

VERDIER, S.; DUONG, D.; ANDERSEN, S. I. Experimental Determination of Solubility Parameters of Oils as a Function of Pressure †. **Energy & Fuels**, v. 19, n. 4, p. 1225–1229, 2005.

VILAS BÔAS FÁVERO, C. et al. Revisiting the flocculation kinetics of destabilized asphaltenes. **Advances in Colloid and Interface Science**, Special Issue in Honor of the 90th Birthday of Prof. Eli Ruckenstein. v. 244, p. 267–280, 2017.

VITU, S. et al. Bubble and Dew Points of Carbon Dioxide + a Five-Component Synthetic Mixture: Experimental Data and Modeling with the PPR78 Model. **Journal of Chemical & Engineering Data**, v. 52, n. 5, p. 1851–1855, 1 set. 2007.

VITU, S.; JAUBERT, J.-N.; MUTELET, F. Extension of the PPR78 model (Predictive 1978, Peng–Robinson EOS with temperature dependent kij calculated through a group contribution method) to systems containing naphtenic compounds. **Fluid Phase Equilibria**, v. 243, n. 1, p. 9–28, 2006.

WANG, Y. et al. **Compositional Modeling of Gas Injection With Three Hydrocarbon Phases for Schrader Bluff EOR**. . In: SPE Annual Technical Conference And Exhibition. Society of Petroleum Engineers, 1 jan. 2003

WANG, Z. et al. Effect of pressure, temperature, and mass fraction of CO₂ on the stability of the asphaltene constituents in crude oil. **Petroleum Science and Technology**, v. 35, n. 22, p. 2109–2114, 2017.

WILKEN, M.; FISCHER, K.; GMEHLING, J. Transitiometry: PVT – Scanning Calorimetry for the Simultaneous Determination of Thermal and Mechanical Properties. **Chemical Engineering & Technology**, v. 25, n. 8, p. 779–784, 2002.

YARRANTON, H. W. Asphaltene Self-Association. **Journal of Dispersion Science and Technology**, v. 26, n. 1, p. 5–8, 2005.

YARRANTON, H. W. et al. Regular solution based approach to modeling asphaltene precipitation from native and reacted oils: Part 2, molecular weight, density, and solubility parameter of saturates, aromatics, and resins. **Fuel**, v. 215, p. 766–777, 2018.

YARRANTON, H. W.; CHEN, T.; THOMAS, F. B. **Detection of Phase Transitions with Acoustic Resonance Technology**. 4 jun. 2000

YARRANTON, H. W.; MASLIYAH, J. H. Molar mass distribution and solubility modeling of asphaltenes. **AIChE Journal**, v. 42, n. 12, p. 3533–3543, 1996.

YEN, A.; YIN, Y. R.; ASOMANING, S. **Evaluating Asphaltene Inhibitors: Laboratory Tests and Field Studies**. . In: SPE International Symposium On Oilfield Chemistry. Society of Petroleum Engineers, 1 jan. 2001

YONEBAYASHI, H. et al. Determination of Asphaltene-Onset Pressure Using Multiple Techniques in Parallel. **SPE Production & Operations**, v. 33, n. 03, p. 486–497, 13 2018.

ZANGANEH, P. et al. **Asphaltene Deposition during CO₂ Injection and Pressure Depletion: A Visual Study**. research-article.
<<https://pubs.acs.org/doi/abs/10.1021/ef2012744>>.

ZANGANEH, P.; DASHTI, H.; AYATOLLAHI, S. Visual investigation and modeling of asphaltene precipitation and deposition during CO₂ miscible injection into oil reservoirs. **Fuel**, v. 160, p. 132–139, 2015.

ZANGANEH, P.; DASHTI, H.; AYATOLLAHI, S. Comparing the effects of CH₄, CO₂, and N₂ injection on asphaltene precipitation and deposition at reservoir condition: A visual and modeling study. **Fuel**, v. 217, p. 633–641, 2018.

ZHANG, X.; PEDROSA, N.; MOORWOOD, T. Modeling Asphaltene Phase Behavior: Comparison of Methods for Flow Assurance Studies. **Energy & Fuels**, v. 26, n. 5, p. 2611–2620, 2012.

ZHOU, X. et al. Experimental study on foamy oil behavior using a heavy oil–methane system in the bulk phase. **Journal of Petroleum Science and Engineering**, v. 158, p. 309–321, 2017.

ZOU, X.-Y.; SHAW, J. M. Dispersed Phases and Dispersed Phase Deposition Issues Arising in Asphaltene Rich Hydrocarbon Fluids. **Petroleum Science and Technology**, v. 22, n. 7–8, p. 759–771, 2004.

APPENDIX A: Uncertainty, repeatability, and validation analysis

A.1 PVT uncertainty analysis

Uncertainties of molar fractions

Different injection techniques were used during synthetic method for mixtures preparation. For chapter II and III, volumetric measurements were made during fluid injection in the PVT. Then, the combined uncertainty of the molar fractions $u_c(x_j)$ was determined according to equation S1.

$$u_c(x_j) = \sqrt{\sum_{i=1}^n \left[\frac{\partial x_1}{\partial v_i} * u(v_i) \right]^2 + \left[\frac{\partial x_1}{\partial \rho_{oil}} * u(\rho_{oil}) \right]^2 + \left[\frac{\partial x_1}{\partial PM_{oil}} * u(MW_{oil}) \right]^2} \quad (S1)$$

where v_i is the volume of the “i” component, $u(v_i)$ is the volume-measuring uncertainty n is the total number of components in the mixture, and x_j is defined by:

$$x_j = \frac{v_i * \rho_i / MW_i}{\sum_{i=1}^n v_i * \rho_i / MW_i} \quad (S2)$$

where ρ_i is the compound i density. Uncertainty of crude oil density $u(\rho_{oil}) = 0.0001 \text{ g/cm}^3$; and its molar weight $u(MW_{oil}) = 5 \text{ g/mol}$ were also considered as uncertainty sources during calculation. The volume-measuring uncertainty $u(v_i)$ was calculated as twice the standard uncertainty of 0.01 cm^3 from the syringe pump.

For chapter IV and V, compositions were estimated by gravimetric measurements. Then, the combined uncertainty of the molar fractions $u_c(x_j)$ was determined as follows:

$$u_c(x_j) = \sqrt{\sum_{i=1}^n \left[\frac{\partial x_1}{\partial m_i} * u(m_i) \right]^2 + \left[\frac{\partial x_1}{\partial PM_{oil}} * u(MW_{oil}) \right]^2} \quad (S3)$$

where m_i is the mass of the “i” component, $u(m_i) = 0.01 \text{ g}$ is the mass-measuring uncertainty, and x_i is defined by:

$$x_j = \frac{m_i / MW_i}{\sum_{i=1}^n m_i / MW_i} \quad (S4)$$

Finally, for chapter VI and VII, compositions were estimated by a combination of volumetric and gravimetric measurements. Then, the combined uncertainty of the molar fractions $u_c(x_j)$ of solvent j was determined as follows:

$$u_c(x_j) = \sqrt{\sum_{i=1}^2 \left[\frac{\partial x_1}{\partial v_i} * u(v_i) \right]^2 + \left[\frac{\partial x_1}{\partial m_{oil}} * u(m_{oil}) \right]^2 + \left[\frac{\partial x_1}{\partial PM_{oil}} * u(MW_{oil}) \right]^2} \quad (S5)$$

where v_i is the volume of the methane, CO₂, or their mixture, $u(m_{oil}) = 0.001$ g is the analytical balance uncertainty, and x_i is defined by:

$$x_j = \frac{v_j * \rho_j / MW_j}{\sum_{i=1}^n v_j * \rho_j / MW_j + m_{oil} / MW_{oil}} \quad (S6)$$

Finally, expanded uncertainty for composition $U(x_j)$ was calculated with a conventional coverage factor $kp = 2$, at 95 % of confidence, as follows:

$$U(x_j) = kp \cdot u_c(x_j) \quad (S7)$$

Validation and repeatability of phase transitions pressure measurements

To validate the phase measurements on the PVT equipment, a simple binary mixture of methane and docosane at 89.80 methane mol % was prepared and analyzed. Its phase behavior was compared to the data reported by Flöter et al. (1998) [Flöter, E.; Hollanders, B.; De Loos, T. W.; Swaan Arons, J. The effect of the addition of water, propane, or docosane on the vapour-liquid and solid-fluid equilibria in asymmetric binary n -alkane mixtures. Fluid Phase Equilib., 1998, 143, 185-203].

This system was selected to verify LV and LS boundaries, and results are presented in Figure S1 to Figure S4. It can be noted that bubble point pressure coincides with reported data with a relative deviation of 1.04 %. Additionally, the deviation at LS locus increases to 2.2 %. This divergence could be related to differences in experimental procedures. In the study of Flöter et al., they intercept the LS locus by changes in pressure at isothermal condition, while we use an isobaric cooling method in this case. Also, it is important to mention that visual, NIR light scattering, and HPM techniques were

coincident in LS detection within the instruments uncertainty. This can help to confirm that HPM sampling and analysis are in concordance with bulk fluid behavior.

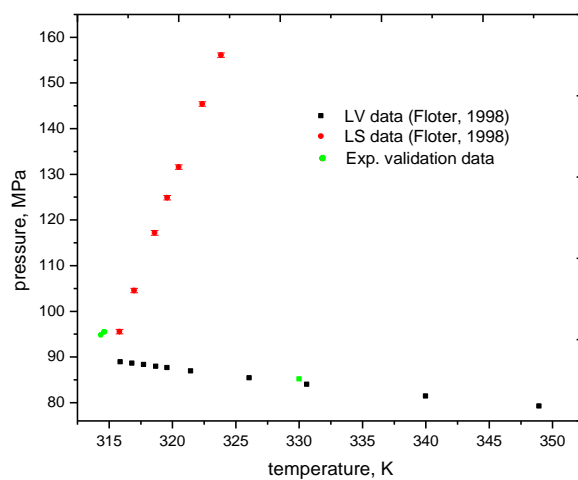


Figure S1. Validation of L→LV and L→LS phase transitions for the binary mixture of docosane and methane at 89.80 methane mol %.

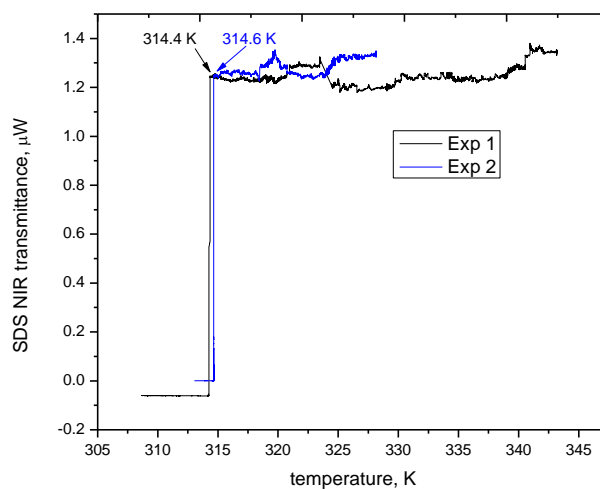


Figure S2. Repeatability of L→LS phase transition for the binary mixture of docosane and methane at 89.80 methane mol % analyzed by NIR-SDS at 95.66 MPa.

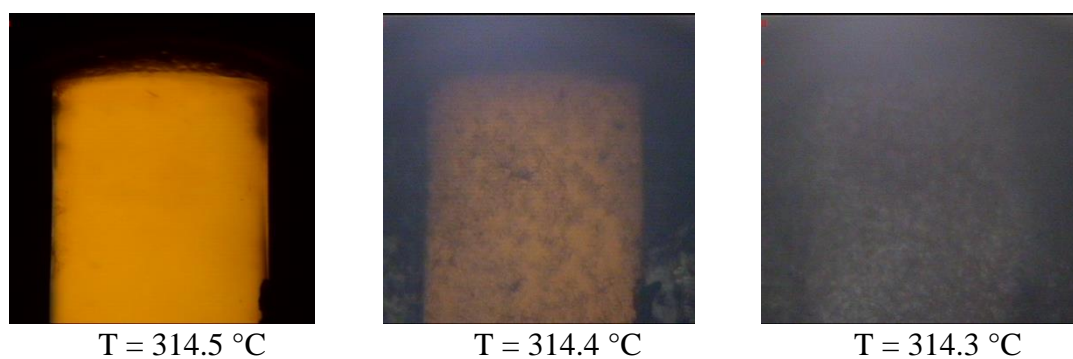


Figure S3. L→LS phase transition for the binary mixture of docosane and methane at 89.80 methane mol % detected by fluid visual inspection through PVT windows at 95.66 MPa.

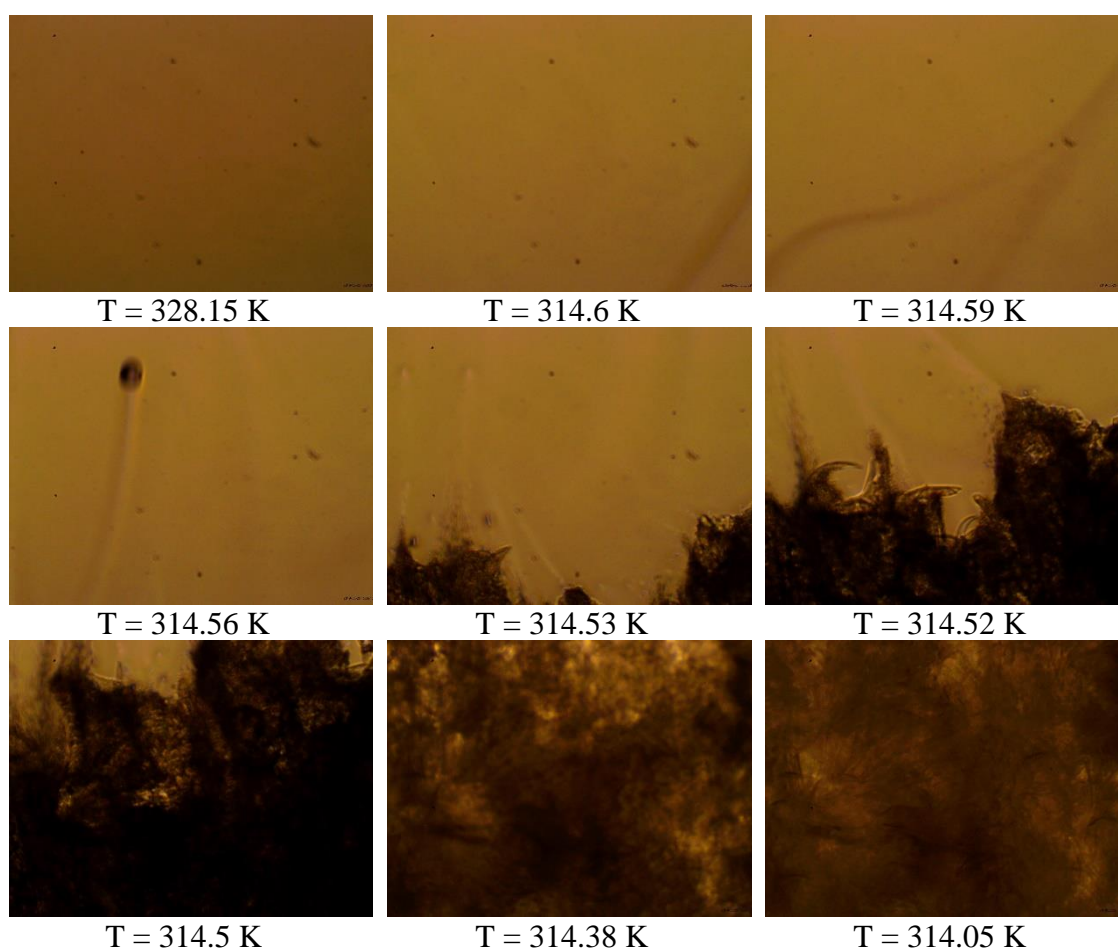


Figure S4. L→LS phase transition for the binary mixture of docosane and methane at 89.80 methane mol % detected by HPM test at 95.66 MPa.

Verification between volumetric, NIR-SDS, and HPM procedures for phase transition evaluation was also made for crude oil mixtures, results are presented in Figure

S5 to S8. In these Figures, it is presented the repeatability analysis for phase transition identification of medium and high methane content systems. From these results, it was observed that deviation and repeatability between techniques for bubble point determination and AOP were below 0.63 MPa.

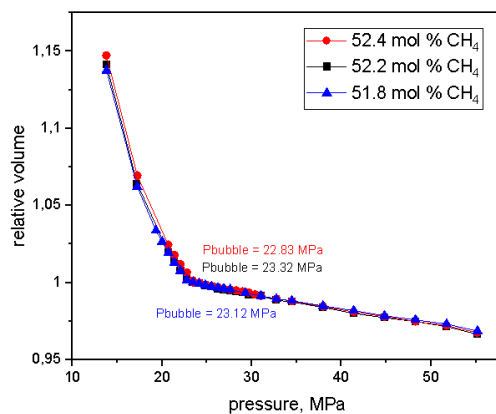


Figure S5. Repeatability of bubble point pressure determination for crude oil and methane mixtures obtained by volumetric measurements at 333.15 K.

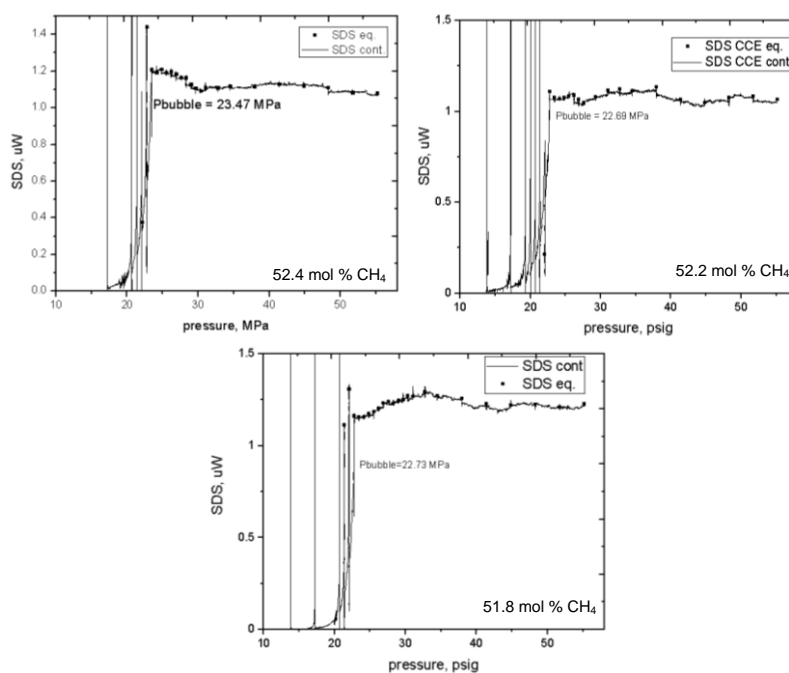


Figure S6. Repeatability of bubble point pressure determination for crude oil and methane mixtures obtained by NIR-SDS at 333.15 K.

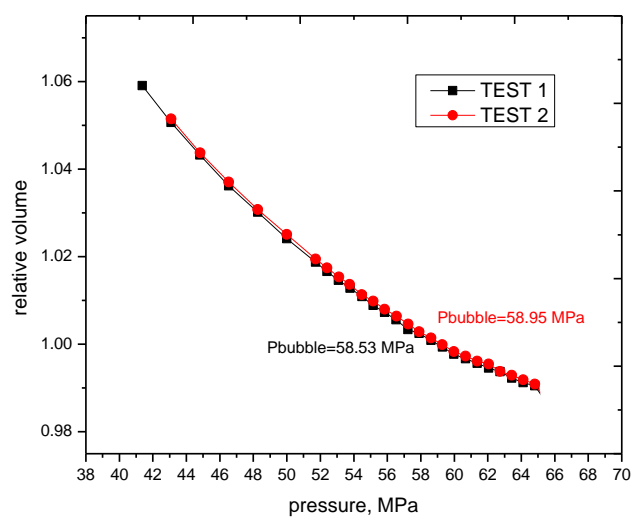


Figure S7. Repeatability of bubble point pressure determination for crude oil and gas mixtures at 75.0 gas wt % obtained by volumetric measurements at 343.15 K.

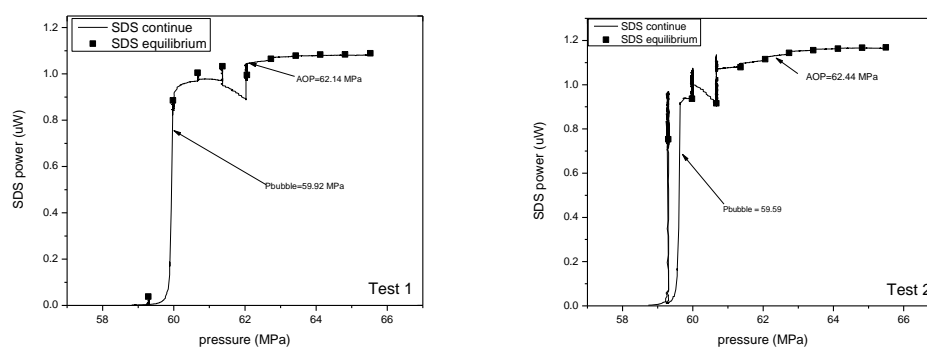


Figure S8. Repeatability of bubble point pressure and AOP determination for crude oil and gas mixtures at 75.0 gas wt % obtained by volumetric measurements at 343.15 K.

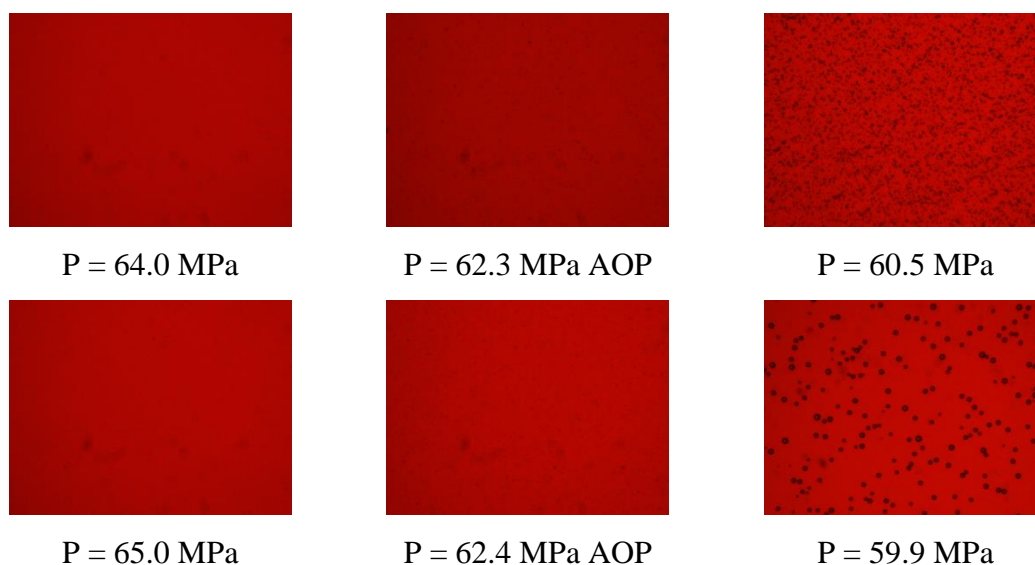


Figure S9. Repeatability of bubble point pressure and AOP determination for crude oil and gas mixtures at 75.0 wt % obtained by HPM test at 343.15 K.

Considering all data collected to date (not all shown here) the standard uncertainty for the phase transition determination $u(P_f)$ was calculated. For the different procedures used for phase transition identification, the standard uncertainties are listed in Table A1.

Table A1. Average standard uncertainty for phase transition determination for the different experimental procedures.

methodology	type of phase transition	$u_c(P_f)$, MPa
volumetric	bubble point pressure	0.14
NIR SDS	bubble point pressure	0.16
HPM	bubble point pressure	0.22
NIR SDS	AOP	0.18
HPM	AOP	0.22

Combined standard uncertainty of phase transitions determination $u_c(P_f)$ was determined including four uncertainty sources: the volume uncertainty $u(v)$ of 0.01 cm^3 , the temperature uncertainty $u(T)$ of 0.1 K, the pressure uncertainty $u(p)$ of 0.1 MPa, and the standard error for the phase transition determination $u(P_f)$, as follows:

$$u_c(P_f) = \sqrt{u(P_f)^2 + u(p)^2 + \left[\frac{\partial P_f}{\partial T} * u(T)\right]^2 + \left[\frac{\partial P_f}{\partial v} * u(v)\right]^2}$$

Numerical differentiation was made for partial derivatives evaluation. Finally, expanded uncertainty for phase transitions determination $U(P_f)$ was calculated for each technique using a conventional coverage factor $kp = 2$, at 95 % of confidence, averages values are presented in Table A2.

Table A2. Average expanded uncertainty for phase transition determination for the different experimental procedures.

methodology	type of phase transition	$U(P_f)$, MPa
volumetric	bubble point pressure	0.624
NIR SDS	bubble point pressure	0.629
HPM	bubble point pressure	0.647
NIR SDS	AOP	0.634
HPM	AOP	0.647

APPENDIX B: Derivative PVT properties for crude oil and gas mixtures

Table S1. Experimental density (ρ_{PVT}) and Tammann-Tait estimated density (ρ_{fitted}) as function of temperature and pressure for BR1 crude oil + methane mixtures (x_1 is the methane mol percent).

T / K	313.15	333.15	353.25	373.15	313.15	333.15	353.25	373.15
P / MPa	$\rho_{PVT} / \text{kg/m}^3$ $x_1 = 26.5$				$\rho_{fitted} / \text{kg/m}^3$ $x_1 = 26.5$			
24.2	871.6	858.9	844.5	831.1	871.5	858.6	845.3	831.6
20.8	868.7	856.1	842.3	828.7	868.8	855.7	842.2	828.3
19.1	867.5	854.5	841.1	826.9	867.5	854.3	840.6	826.6
13.9	863.4	849.5	835.4	821.4	863.3	849.7	835.7	821.3
12.5	862.2	848.3	833.9	819.7	862.1	848.4	834.3	819.8
11.1	860.6	847.3	833.0	818.6	860.9	847.1	832.9	818.2
10.4	860.1	846.8	831.8	817.2	860.3	846.4	832.1	817.4
9.7	859.6	845.7	831.4	816.6	859.7	845.7	831.4	816.6
9.1	858.8	844.9	830.5	815.6	859.1	845.1	830.6	815.8
8.4	858.1	843.9	829.6	814.6	858.5	844.4	829.9	815.0
7.7	857.6	843.4			857.9	843.7		
P / MPa	$\rho_{PVT} / \text{kg/m}^3$ $x_1 = 52.6$				$\rho_{fitted} / \text{kg/m}^3$ $x_1 = 52.6$			
55.3	846.4	833.6	821.5	808.7	845.0	832.4	819.8	807.5
51.8	842.2	829.7	816.7	804.3	842.7	829.9	817.2	804.6
48.4	840.2	827.3	814.1	801.5	840.4	827.4	814.4	801.7
44.9	838.1	824.7	811.6	798.6	838.0	824.8	811.6	798.7
41.5	835.5	822.1	808.5	795.5	835.5	822.0	808.6	795.5
38.0	832.9	819.2	805.6	791.9	832.9	819.2	805.5	792.1
34.6	830.1	816.3	802.4	788.7	830.2	816.3	802.3	788.6
32.9		815.0	800.8	786.8	828.6	814.8	800.7	786.8
31.1	827.2	813.5	798.9	785.1	827.5	813.2	799.0	784.9
30.4	826.7	812.7	798.5	784.3	826.9	812.6	798.3	784.2
29.8	826.4	811.7	797.4	783.5	826.3	812.0	797.6	783.4
29.1	825.5	811.2	797.1	782.9	825.7	811.3	796.9	782.6
28.4	824.8	810.6	796.3	781.8	825.2	810.7	796.1	781.8
27.7	824.6	810.2	795.6	780.9	824.6	810.0	795.4	781.0
27.0	824.0	809.7	794.6	780.3	824.0	809.4	794.7	780.2
26.3	823.3	808.8	793.7	779.4	823.4	808.7	793.9	779.4
25.6	822.8	808.3	793.0	778.3	822.8	808.0	793.2	778.6
24.9	822.2	807.5	792.2	777.7	822.2	807.4	792.4	777.7
24.2	821.5	806.5			821.6	806.7		
23.5	821.0				821.0			

Table S1. Experimental density (ρ_{PVT}) and Tammann-Tait estimated density (ρ_{fitted}) as function of temperature and pressure for BR1 crude oil + methane mixtures (x_1 is the methane mol percent). *Cont.*

T / K	313.15	333.15	353.25	373.15	313.15	333.15	353.25	373.15
P / MPa	$\rho_{PVT} / \text{kg/m}^3$ $x_1 = 74.7$				$\rho_{fitted} / \text{kg/m}^3$ $x_1 = 74.7$			
96.6		742.9	729.7	717.8	752.7	741.3	729.1	715.6
93.2		739.3	727.1	715.0	751.2	739.6	727.3	713.9
89.7		737.2	724.5	712.1	749.5	737.7	725.3	712.0
86.3		735.7	721.6	709.0	747.7	735.7	723.2	709.9
82.8	745.7	733.1	720.4	705.9	745.8	733.5	720.8	707.6
81.5	744.5	732.1	719.2		744.9	732.5	719.8	706.6
80.1	743.4	731.0	718.0		744.1	731.6	718.7	705.6
78.7	742.8	730.6	717.4		743.2	730.5	717.6	704.5
78.0	742.4	729.8	716.6		742.8	730.0	717.0	703.9
77.3	742.0	729.5	715.9	702.2	742.3	729.4	716.4	703.4
76.6	741.4	728.4	715.2		741.8	728.9	715.8	702.8
75.9	740.9	727.8	714.7	700.7	741.4	728.3	715.2	702.2
75.3	740.3	727.3	714.2		740.9	727.7	714.6	701.5
74.6	739.5	726.7	713.6	698.9	740.4	727.1	713.9	700.9
73.9	738.8	726.0	712.7		739.9	726.5	713.2	700.2
73.2		725.5	711.9		739.3	725.9	712.5	699.6
72.5		724.9	711.4	698.2	738.8	725.2	711.8	698.9
71.8		724.3	710.8	697.6	738.3	724.6	711.0	698.1
71.1		723.6	710.2	696.9	737.7	723.8	710.2	697.3
70.4		722.9	709.5	696.2	737.1	723.1	709.4	696.6
69.7		722.2	708.6	695.5	736.5	722.4	708.6	695.8
69.0				694.6	735.9	721.6	707.7	694.9
68.4				693.8	735.3	720.8	706.8	694.1
67.7				693.2	734.7	720.0	705.9	693.2
67.0				692.3	734.0	719.2	704.9	692.2
66.3				691.6	733.3	718.3	703.9	691.2
65.6				690.7	732.7	717.4	702.8	690.2
64.9				689.9	732.0	716.4	701.7	689.1

Table S2. Isothermal compressibility as function of temperature and pressure for BR1 crude oil + methane mixtures (x_1 is the methane mol percent).

T / K	313.15	333.15	353.25	373.15	313.15	333.15	353.25	373.15	
P / MPa	$\kappa_T \cdot 10^4 / \text{MPa}^{-1}$				P / MPa	$\kappa_T \cdot 10^4 / \text{MPa}^{-1}$			
	x = 26.5					x = 74.7			
26.0	8.4	9.2	10.1	10.9	100.0	6.7	7.2	7.4	7.2
24.0	8.6	9.5	10.3	11.2	98.0	6.9	7.4	7.6	7.4
22.0	8.8	9.7	10.6	11.5	96.0	7.1	7.7	7.9	7.7
20.0	9.0	9.9	10.9	11.9	94.0	7.3	7.9	8.2	7.9
18.0	9.2	10.2	11.2	12.3	92.0	7.6	8.2	8.5	8.2
16.0	9.5	10.5	11.6	12.7	90.0	7.8	8.6	8.8	8.6
14.0	9.7	10.8	11.9	13.1	88.0	8.1	8.9	9.2	8.9
12.0	10.0	11.1	12.3	13.6	86.0	8.4	9.3	9.6	9.3
10.0	10.2	11.4	12.7	14.1	84.0	8.8	9.7	10.0	9.7
8.0	10.5	11.8	13.2	14.7	82.0	9.1	10.1	10.5	10.1
7.0	10.7				80.0	9.5	10.6	11.0	10.6
P / MPa	$\kappa_T \cdot 10^4 / \text{MPa}^{-1}$				78.0	9.9	11.1	11.6	11.1
	x = 52.6				76.0	10.4	11.7	12.2	11.7
55.0	7.7	8.4	9.2	10.0	75.0	10.7	12.0	12.6	12.0
50.0	8.1	8.9	9.7	10.6	74.0	10.9	12.4	13.0	12.4
45.0	8.5	9.4	10.4	11.3	73.0	11.2	12.7	13.4	12.7
40.0	8.9	10.0	11.0	12.2	72.0	11.5	13.1	13.8	13.1
38.0	9.1	10.2	11.3	12.5	71.0	11.8	13.5	14.2	13.5
36.0	9.3	10.5	11.7	12.9	70.0	12.2	14.0	14.7	14.0
34.0	9.6	10.7	12.0	13.3	69.0		14.4	15.2	14.4
32.0	9.8	11.0	12.4	13.8	68.5		14.7	15.5	14.7
31.0	9.9	11.2	12.6	14.0	68.0		14.9	15.8	14.9
30.0	10.0	11.3	12.8	14.3	67.5		15.2	16.1	15.2
29.0	10.2	11.5	13.0	14.5	67.0		15.5	16.4	15.5
28.0	10.3	11.7	13.2	14.8	66.5			16.7	15.7
27.0	10.4	11.8	13.4	15.1	66.0			17.0	16.0
26.0	10.5	12.0	13.6	15.4	65.5			17.4	16.3
25.0	10.7	12.2	13.8	15.7	65.0			17.7	16.7
24.0	10.8	12.4			64.5			18.1	17.0
23.0	11.0				64.0				17.3

Table S3. Thermal expansion as function of temperature and pressure for BR1 crude oil + methane mixtures (x_1 is the methane mol percent).

T / K	313.15	333.15	353.25	373.15		313.15	333.15	353.25	373.15
P / MPa	$\alpha_P \cdot 10^4 / K^{-1}$				P / MPa	$\alpha_P \cdot 10^4 / K^{-1}$			
	x = 26.5					x = 74.7			
26.0	7.245	7.552	7.892	8.288	100.0	7.130	8.237	9.512	10.846
24.0	7.325	7.636	7.978	8.373	98.0	7.195	8.275	9.512	10.808
22.0	7.407	7.724	8.069	8.463	96.0	7.265	8.316	9.512	10.768
20.0	7.494	7.816	8.164	8.559	94.0	7.339	8.359	9.512	10.724
18.0	7.585	7.913	8.266	8.661	92.0	7.418	8.406	9.512	10.678
16.0	7.680	8.016	8.373	8.770	90.0	7.503	8.456	9.512	10.627
14.0	7.781	8.124	8.488	8.886	88.0	7.593	8.510	9.512	10.573
12.0	7.886	8.239	8.609	9.010	86.0	7.691	8.569	9.512	10.514
10.0	7.997	8.360	8.739	9.143	84.0	7.796	8.633	9.512	10.451
8.0	8.114	8.489	8.878	9.287	82.0	7.910	8.702	9.512	10.381
7.0	8.175				80.0	8.034	8.779	9.512	10.304
P / MPa	$\alpha_P \cdot 10^4 / K^{-1}$					$\alpha_P \cdot 10^4 / K^{-1}$			
	x = 52.6								
					78.0	8.169	8.863	9.512	10.220
					76.0	8.317	8.956	9.512	10.127
55.0	7.499	7.552	7.615	7.680	75.0	8.396	9.006	9.512	10.077
50.0	7.688	7.752	7.819	7.880	74.0	8.479	9.060	9.512	10.024
45.0	7.897	7.974	8.049	8.107	73.0	8.567	9.116	9.512	9.967
40.0	8.127	8.223	8.310	8.369	72.0	8.659	9.176	9.512	9.908
38.0	8.227	8.331	8.424	8.484	71.0	8.756	9.239	9.512	9.844
36.0	8.331	8.445	8.544	8.607	70.0	8.859	9.307	9.512	9.777
34.0	8.440	8.564	8.672	8.738	69.0		9.379	9.512	9.705
32.0	8.554	8.690	8.808	8.878	68.5		9.417	9.512	9.667
31.0	8.613	8.756	8.879	8.951	68.0		9.456	9.512	9.628
30.0	8.674	8.824	8.952	9.028	67.5		9.496	9.512	9.587
29.0	8.736	8.893	9.027	9.107	67.0		9.538	9.512	9.545
28.0	8.799	8.964	9.105	9.188	66.5			9.512	9.502
27.0	8.865	9.038	9.186	9.273	66.0			9.512	9.456
26.0	8.932	9.114	9.269	9.362	65.5			9.512	9.410
25.0	9.001	9.191	9.356	9.453	65.0			9.512	9.361
24.0	9.071	9.272			64.5			9.512	9.310
23.0	9.144				64.0				9.257

Table S4. Solubility parameter as function of temperature and pressure for BR1 crude oil + methane mixtures (x_1 is the methane mol percent).

T / K	313.15	333.15	353.25	373.15		313.15	333.15	353.25	373.15
P / Mpa	$\delta / \text{MPa}^{1/2}$ x = 26.5				P / MPa	$\delta / \text{MPa}^{1/2}$ x = 74.7			
26.0	15.6	15.7	15.8	16.1	100.0	15.3	16.8	18.9	21.5
24.0	15.6	15.7	15.8	16.0	98.0	15.2	16.5	18.5	21.1
22.0	15.5	15.6	15.7	15.9	96.0	15.0	16.3	18.2	20.7
20.0	15.5	15.5	15.6	15.8	94.0	14.8	16.0	17.8	20.2
18.0	15.5	15.5	15.5	15.7	92.0	14.7	15.7	17.4	19.8
16.0	15.4	15.4	15.5	15.5	90.0	14.5	15.5	17.1	19.3
14.0	15.4	15.4	15.4	15.4	88.0	14.3	15.2	16.7	18.9
12.0	15.3	15.3	15.3	15.3	86.0	14.1	14.9	16.3	18.4
10.0	15.3	15.3	15.2	15.2	84.0	14.0	14.6	15.9	17.9
8.0	15.3	15.2	15.2	15.1	82.0	13.8	14.3	15.4	17.4
7.0	15.3				80.0	13.6	14.0	15.0	16.8
P / MPa	$\delta / \text{MPa}^{1/2}$ x = 52.6				78.0	13.4	13.7	14.6	16.3
					76.0	13.2	13.4	14.1	15.7
55.0	15.8	15.6	15.4	15.2	75.0	13.1	13.2	13.9	15.4
50.0	15.8	15.5	15.3	15.1	74.0	13.0	13.0	13.6	15.1
45.0	15.7	15.4	15.2	14.9	73.0	12.9	12.9	13.4	14.8
40.0	15.6	15.3	15.0	14.7	72.0	12.8	12.7	13.1	14.5
38.0	15.6	15.3	15.0	14.6	71.0	12.7	12.5	12.9	14.2
36.0	15.6	15.3	14.9	14.6	70.0	12.6	12.3	12.6	13.8
34.0	15.6	15.2	14.9	14.5	69.0		12.1	12.3	13.5
32.0	15.5	15.2	14.8	14.4	68.5		12.1	12.2	13.3
31.0	15.5	15.2	14.8	14.4	68.0		12.0	12.0	13.1
30.0	15.5	15.1	14.8	14.3	67.5		11.9	11.9	13.0
29.0	15.5	15.1	14.7	14.3	67.0		11.8	11.8	12.8
28.0	15.5	15.1	14.7	14.3	66.5		11.7	11.6	12.6
27.0	15.5	15.1	14.7	14.2	66.0			11.5	12.4
26.0	15.5	15.1	14.6	14.2	65.5			11.3	12.2
25.0	15.5	15.1	14.6	14.1	65.0			11.2	12.0
24.0	15.4	15.0			64.5			11.0	11.8
23.0	15.4				64.0				11.6

Table S5. Molar volume as function of temperature and pressure for BR1 crude oil + methane mixtures (x_1 is the methane mol percent).

T / K	313.15	333.15	353.25	373.15		313.15	333.15	353.25	373.15
P / MPa	$v \cdot 10^4 / \text{m}^3/\text{mol}$				P / MPa	$v \cdot 10^4 / \text{m}^3/\text{mol}$			
	x = 26.5					x = 74.7			
26.0	2.57	2.61	2.65	2.70	100.0	1.16	1.18	1.20	1.22
24.0	2.58	2.62	2.66	2.70	98.0	1.16	1.18	1.20	1.22
22.0	2.58	2.62	2.66	2.71	96.0	1.17	1.18	1.20	1.23
20.0	2.59	2.63	2.67	2.71	94.0	1.17	1.19	1.21	1.23
18.0	2.59	2.63	2.68	2.72	92.0	1.17	1.19	1.21	1.23
16.0	2.60	2.64	2.68	2.73	90.0	1.17	1.19	1.21	1.23
14.0	2.60	2.64	2.69	2.73	88.0	1.17	1.19	1.21	1.23
12.0	2.61	2.65	2.69	2.74	86.0	1.17	1.19	1.21	1.24
10.0	2.61	2.66	2.70	2.75	84.0	1.18	1.19	1.22	1.24
8.0	2.62	2.66	2.71	2.76	82.0	1.18	1.20	1.22	1.24
7.0	2.62				80.0	1.18	1.20	1.22	1.24
P / MPa	$v \cdot 10^4 / \text{m}^3/\text{mol}$				78.0	1.18	1.20	1.22	1.25
	x = 52.6				76.0	1.18	1.20	1.23	1.25
55.0	1.78	1.81	1.84	1.87	75.0	1.18	1.21	1.23	1.25
50.0	1.79	1.82	1.85	1.88	74.0	1.19	1.21	1.23	1.25
45.0	1.80	1.83	1.86	1.89	73.0	1.19	1.21	1.23	1.25
40.0	1.80	1.83	1.87	1.90	72.0	1.19	1.21	1.23	1.26
38.0	1.81	1.84	1.87	1.90	71.0	1.19	1.21	1.24	1.26
36.0	1.81	1.84	1.87	1.91	70.0	1.19	1.21	1.24	1.26
34.0	1.82	1.85	1.88	1.91	69.0	1.19	1.22	1.24	1.26
32.0	1.82	1.85	1.88	1.92	68.5		1.22	1.24	1.26
31.0	1.82	1.85	1.89	1.92	68.0		1.22	1.24	1.26
30.0	1.82	1.85	1.89	1.92	67.5		1.22	1.24	1.27
29.0	1.82	1.86	1.89	1.92	67.0		1.22	1.24	1.27
28.0	1.83	1.86	1.89	1.93	66.5		1.22	1.25	1.27
27.0	1.83	1.86	1.90	1.93	66.0			1.25	1.27
26.0	1.83	1.86	1.90	1.93	65.5			1.25	1.27
25.0	1.83	1.87	1.90	1.94	65.0			1.25	1.27
24.0	1.83	1.87			64.5			1.25	1.27
23.0	1.84				64.0				1.28

Table S7. Experimental density ($\rho_{densimeter}$) and Tammann-Tait estimated density (ρ_{fitted}) as function of temperature and pressure for BR1 dead oil

T / K	313.15	323.15	333.15	343.15	353.15	363.15	373.15	383.15
P / MPa	$\rho_{densimeter} / \text{kg/m}^3$							
3.5	877.8	870.9	864.5	857.9	851.3	844.5	837.5	830.9
7.0	879.9	873.0	866.8	860.0	853.8	847.0	840.2	833.6
13.9	883.9	877.2	871.1	864.5	858.5	851.9	845.4	839.1
20.8	887.7	881.1	875.4	868.8	863.0	856.6	850.2	844.1
27.7	891.3	884.9	879.2	872.9	867.2	861.1	855.0	849.0
34.6	894.9	888.7	883.0	876.9	871.2	865.3	859.4	853.4
41.5	898.3	892.1	886.7	880.6	875.4	869.2	863.4	857.7
48.4	901.6	895.4	890.2	884.3	879.0	873.1	867.4	862.0
55.3	904.9	898.7	893.6	887.7	882.8	876.9	871.3	865.8
62.2	907.9	901.9	896.9	891.1	886.0	880.3	874.9	869.6
69.0	910.9	904.9	900.0	894.3	889.4	883.9	878.4	873.2
75.9	913.9	907.9	903.0	897.4	892.5	887.1	881.9	876.6
82.8	916.7	910.7	906.0	900.5	895.7	890.3	885.1	880.0
89.7	919.3	913.5	908.8	903.2	898.6	893.4	888.3	883.3
96.6	922.0	916.2	911.7	906.2	901.7	896.5	891.4	886.5
100.1	923.2	917.5	912.9	907.6	903.1	897.9	893.0	888.1
	$\rho_{fitted} / \text{kg/m}^3$							
3.5	877.7	871.1	864.5	857.9	851.2	844.4	837.7	830.8
7.0	879.8	873.3	866.7	860.2	853.6	847.0	840.3	833.6
13.9	883.7	877.4	871.0	864.6	858.3	851.8	845.4	838.9
20.8	887.5	881.3	875.1	868.9	862.7	856.5	850.2	844.0
27.7	891.2	885.2	879.1	873.0	867.0	860.9	854.8	848.8
34.6	894.8	888.8	882.9	877.0	871.0	865.1	859.2	853.3
41.5	898.2	892.4	886.6	880.8	875.0	869.2	863.4	857.7
48.4	901.5	895.8	890.1	884.4	878.7	873.1	867.4	861.8
55.3	904.7	899.1	893.5	887.9	882.4	876.8	871.3	865.8
62.2	907.8	902.3	896.8	891.3	885.9	880.4	875.0	869.7
69.0	910.9	905.4	900.0	894.6	889.3	883.9	878.6	873.4
75.9	913.8	908.5	903.1	897.8	892.6	887.3	882.1	876.9
82.8	916.7	911.4	906.1	900.9	895.7	890.6	885.5	880.4
89.7	919.5	914.3	909.1	903.9	898.8	893.8	888.7	883.7
96.6	922.2	917.1	911.9	906.9	901.8	896.8	891.9	886.9
100.1	923.5	918.4	913.4	908.3	903.3	898.4	893.4	888.5

Table S8. Isothermal compressibility and thermal expansion as function of temperature and pressure for BR1 dead oil

T / K	313.15	323.15	333.15	343.15	353.15	363.15	373.15	383.15
P / MPa	$\kappa_T \cdot 10^4 / \text{MPa}^{-1}$							
3.5	6.8	7.2	7.5	7.9	8.4	8.8	9.3	9.9
7.0	6.7	7.0	7.3	7.7	8.1	8.6	9.0	9.5
13.9	6.4	6.7	7.0	7.3	7.7	8.1	8.5	8.9
20.8	6.1	6.4	6.7	7.0	7.3	7.7	8.0	8.4
27.7	5.9	6.1	6.4	6.7	7.0	7.3	7.6	8.0
34.6	5.6	5.9	6.1	6.4	6.7	6.9	7.2	7.6
41.5	5.4	5.7	5.9	6.1	6.4	6.6	6.9	7.2
48.4	5.2	5.5	5.7	5.9	6.1	6.3	6.6	6.9
55.3	5.1	5.3	5.5	5.7	5.9	6.1	6.3	6.6
62.2	4.9	5.1	5.3	5.5	5.7	5.9	6.1	6.3
69.0	4.8	4.9	5.1	5.3	5.4	5.6	5.8	6.0
75.9	4.6	4.8	4.9	5.1	5.3	5.4	5.6	5.8
82.8	4.5	4.6	4.8	4.9	5.1	5.2	5.4	5.6
89.7	4.3	4.5	4.6	4.8	4.9	5.1	5.2	5.4
96.6	4.2	4.4	4.5	4.6	4.8	4.9	5.1	5.2
100.1	4.2	4.3	4.4	4.6	4.7	4.8	5.0	5.1
	$\alpha_P \cdot 10^4 / \text{K}^{-1}$							
3.5	7.499	7.593	7.685	7.787	7.887	7.997	8.111	8.228
7.0	7.386	7.473	7.556	7.648	7.738	7.837	7.939	8.043
13.9	7.176	7.248	7.316	7.392	7.465	7.545	7.626	7.708
20.8	6.983	7.044	7.099	7.161	7.219	7.284	7.348	7.413
27.7	6.806	6.856	6.901	6.952	6.998	7.050	7.101	7.151
34.6	6.643	6.684	6.719	6.761	6.796	6.838	6.878	6.917
41.5	6.491	6.525	6.552	6.585	6.613	6.645	6.676	6.705
48.4	6.351	6.378	6.398	6.424	6.444	6.469	6.492	6.514
55.3	6.220	6.241	6.256	6.275	6.289	6.307	6.324	6.339
62.2	6.097	6.114	6.123	6.138	6.146	6.159	6.170	6.180
69.0	5.983	5.995	5.999	6.009	6.013	6.021	6.028	6.033
75.9	5.875	5.883	5.884	5.890	5.889	5.894	5.896	5.898
82.8	5.774	5.779	5.775	5.778	5.774	5.775	5.774	5.772
89.7	5.679	5.680	5.674	5.673	5.666	5.664	5.660	5.656
96.6	5.588	5.587	5.578	5.575	5.565	5.560	5.554	5.547
100.1	5.545	5.543	5.532	5.528	5.517	5.511	5.504	5.496

Table S9. Solubility parameter and molar volume as function of temperature and pressure for BR1 dead oil

T / K	313.15	323.15	333.15	343.15	353.15	363.15	373.15	383.15
P / MPa	$\delta / \text{MPa}^{1/2}$							
3.5	18.5	18.4	18.3	18.2	18.1	18.0	17.9	17.8
7.0	18.4	18.4	18.3	18.2	18.1	18.0	17.9	17.8
13.9	18.4	18.4	18.3	18.2	18.1	18.0	17.9	17.8
20.8	18.4	18.3	18.3	18.2	18.1	18.0	17.9	17.8
27.7	18.3	18.3	18.2	18.2	18.1	18.0	17.9	17.8
34.6	18.3	18.2	18.2	18.1	18.1	18.0	17.9	17.8
41.5	18.2	18.2	18.2	18.1	18.0	18.0	17.9	17.8
48.4	18.2	18.2	18.1	18.1	18.0	17.9	17.9	17.8
55.3	18.1	18.1	18.1	18.0	18.0	17.9	17.8	17.8
62.2	18.1	18.1	18.0	18.0	17.9	17.9	17.8	17.7
69.0	18.0	18.0	18.0	18.0	17.9	17.9	17.8	17.7
75.9	18.0	18.0	18.0	17.9	17.9	17.8	17.8	17.7
82.8	17.9	17.9	17.9	17.9	17.8	17.8	17.7	17.7
89.7	17.9	17.9	17.9	17.8	17.8	17.8	17.7	17.7
96.6	17.8	17.8	17.8	17.8	17.8	17.7	17.7	17.6
100.1	17.8	17.8	17.8	17.8	17.7	17.7	17.7	17.6
	$v \cdot 10^4 / \text{m}^3/\text{mol}$							
3.5	3.42	3.44	3.47	3.50	3.52	3.55	3.58	3.61
7.0	3.41	3.44	3.46	3.49	3.51	3.54	3.57	3.60
13.9	3.39	3.42	3.44	3.47	3.49	3.52	3.55	3.58
20.8	3.38	3.40	3.43	3.45	3.48	3.50	3.53	3.55
27.7	3.37	3.39	3.41	3.44	3.46	3.48	3.51	3.53
34.6	3.35	3.38	3.40	3.42	3.44	3.47	3.49	3.52
41.5	3.34	3.36	3.38	3.41	3.43	3.45	3.47	3.50
48.4	3.33	3.35	3.37	3.39	3.41	3.44	3.46	3.48
55.3	3.32	3.34	3.36	3.38	3.40	3.42	3.44	3.47
62.2	3.30	3.33	3.35	3.37	3.39	3.41	3.43	3.45
69.0	3.29	3.32	3.33	3.35	3.37	3.39	3.42	3.44
75.9	3.28	3.30	3.32	3.34	3.36	3.38	3.40	3.42
82.8	3.27	3.29	3.31	3.33	3.35	3.37	3.39	3.41
89.7	3.26	3.28	3.30	3.32	3.34	3.36	3.38	3.40
96.6	3.25	3.27	3.29	3.31	3.33	3.35	3.37	3.38
100.1	3.25	3.27	3.29	3.31	3.32	3.34	3.36	3.38

Table S10. Cohesive energy as function of temperature and pressure for BR1 dead oil

T / K	313.15	323.15	333.15	343.15	353.15	363.15	373.15	383.15
P / MPa	<i>E</i> / kJ/mol							
3.5	116.4	116.7	116.6	116.5	116.1	115.6	115.0	114.2
7.0	115.9	116.2	116.1	116.0	115.6	115.2	114.6	113.8
13.9	114.9	115.2	115.2	115.1	114.8	114.4	113.8	113.1
20.8	113.9	114.3	114.2	114.3	113.9	113.6	113.1	112.4
27.7	112.9	113.3	113.3	113.4	113.1	112.8	112.4	111.8
34.6	111.9	112.4	112.4	112.5	112.3	112.0	111.7	111.1
41.5	110.9	111.4	111.5	111.6	111.4	111.3	111.0	110.5
48.4	110.0	110.5	110.6	110.8	110.6	110.5	110.3	109.8
55.3	109.0	109.6	109.7	109.9	109.8	109.8	109.5	109.2
62.2	108.0	108.6	108.8	109.1	109.0	109.0	108.9	108.6
69.0	107.1	107.7	107.9	108.2	108.2	108.3	108.2	107.9
75.9	106.1	106.8	107.0	107.4	107.4	107.5	107.5	107.3
82.8	105.1	105.9	106.2	106.6	106.6	106.8	106.8	106.7
89.7	104.2	105.0	105.3	105.7	105.8	106.0	106.1	106.0
96.6	103.2	104.0	104.4	104.9	105.0	105.3	105.4	105.4
100.1	102.8	103.6	104.0	104.5	104.6	104.9	105.0	105.1

Table S11. Experimental density (ρ_{PVT}) and Tammann-Tait estimated density (ρ_{fitted}) as function of temperature and pressure for BR2 crude oil + methane + CO₂ mixtures (x_{CO_2} is the carbon dioxide mol percent in mixed gas).

T / K	343.15	363.15	383.25	343.15	363.15	383.25
P / MPa	$\rho_{PVT} / \text{kg/m}^3$			$\rho_{fitted} / \text{kg/m}^3$		
	$x_{CO_2}=0.0$ (100.0 CH ₄ mol%)			$x_{CO_2}=0.0$ (100.0 CH ₄ mol%)		
96.6		738.3	726.3	751.0	738.6	726.8
93.2		735.0	723.1	748.0	735.5	723.4
89.7	744.5	731.9	719.7	745.0	732.3	720.0
86.3	741.5	729.1	716.0	741.9	729.0	716.5
82.8	738.5	725.5	712.4	738.6	725.4	712.7
81.5	737.3	723.8	711.1	737.2	724.0	711.2
80.1	735.9	722.4	709.5	735.9	722.5	709.6
79.4	735.1	722.1	708.8	735.2	721.8	708.8
78.7	734.6	721.2	707.7	734.5	721.1	708.0
78.0	733.8	720.4	707.1	733.8	720.3	707.2
77.3	733.6	719.2	706.3	733.1	719.5	706.4
76.6	732.5	718.6	705.5	732.4	718.8	705.6
75.9	731.7	718.1	704.7	731.6	718.0	704.7
75.2	731.0	717.5	704.0	730.9	717.2	703.9
74.6		716.3	703.1	730.2	716.4	703.0
73.9		715.5	702.4	729.4	715.6	702.2
73.2			701.5	728.7	714.8	701.3
72.5			700.7	727.9	714.0	700.4
71.8			699.8	727.2	713.2	699.5

Table S11. Experimental density (ρ_{PVT}) and Tammann-Tait estimated density (ρ_{fitted}) as function of temperature and pressure for BR2 crude oil + methane + CO₂ mixtures (x_{CO_2} is the carbon dioxide mol percent in mixed gas). *Cont.*

P / MPa	$\rho_{PVT} / \text{kg/m}^3$			$\rho_{fitted} / \text{kg/m}^3$		
	$x_{CO_2}=26.3$			$x_{CO_2}=26.3$		
82.8	804.7	790.1	776.2	803.2	789.3	774.7
79.4	799.6	785.4	770.6	799.6	785.4	770.5
77.7		782.9	768.4	797.7	783.4	768.4
75.9	795.7	780.9	766.0	795.8	781.3	766.2
75.3		780.3	765.4	795.1	780.5	765.3
74.6		779.9	764.6	794.3	779.6	764.4
73.9		779.0	763.6	793.5	778.8	763.5
73.2		778.0	762.7	792.7	777.9	762.6
72.5	791.8	776.8	761.7	791.9	777.1	761.7
71.8		776.1	760.9	791.1	776.2	760.7
71.1		775.0	759.8	790.4	775.4	759.8
70.4		774.6	758.9	789.6	774.5	758.9
69.7		773.8	758.0	788.7	773.6	757.9
69.0	788.0	772.5	756.8	787.9	772.7	756.9
68.4		771.9	756.0	787.1	771.8	756.0
67.7	786.3	770.9	755.1	786.3	770.9	755.0
67.0		770.0	754.1	785.4	770.0	754.0
66.3	784.6	768.9	753.0	784.6	769.1	753.0
65.6		768.2	752.0	783.8	768.1	752.0
64.9	782.8	767.2	750.9	782.9	767.2	751.0
64.2		766.0	750.0	782.0	766.3	749.9
63.5		765.2	749.1	781.2	765.3	748.9
62.8		764.5	747.8	780.3	764.3	747.8
62.2		763.5	746.7	779.4	763.4	746.8
61.5		762.2	745.7	778.5	762.4	745.7
60.8		760.9	744.6	777.6	761.4	744.6

Table S11. Experimental density (ρ_{PVT}) and Tammann-Tait estimated density (ρ_{fitted}) as function of temperature and pressure for BR2 crude oil + methane + CO₂ mixtures (x_{CO_2} is the carbon dioxide mol percent in mixed gas). *Cont.*

T / K	343.15	363.15	383.25	343.15	363.15	383.25
P / MPa	$\rho_{PVT} / \text{kg/m}^3$ $x_{CO_2}=37.5$			$\rho_{fitted} / \text{kg/m}^3$ $x_{CO_2}=37.5$		
74.2		784.2	768.6	799.7	783.9	768.4
72.5	798.4	782.4	766.8	798.0	782.1	766.5
70.8	797.0	780.8	764.8	796.3	780.3	764.5
69.0	794.7	778.5	762.7	794.5	778.4	762.4
67.3	793.1	776.5	760.5	792.7	776.4	760.4
65.6	791.3	774.6	758.3	790.9	774.4	758.2
64.9	790.7	773.8	757.4	790.1	773.6	757.3
64.2	789.5	772.9	756.6	789.4	772.7	756.4
63.5	788.6	771.9	755.6	788.6	772.0	755.5
62.8	788.1	771.2	754.7	787.8	771.1	754.5
62.1	787.0	770.5	753.7	787.0	770.2	753.6
61.5	786.3	769.6	752.8	786.2	769.3	752.7
60.8	785.3	768.5	751.7	785.4	768.4	751.7
60.1	784.6	767.6	750.7	784.6	767.6	750.7
59.4	783.8	766.4	749.8	783.7	766.7	749.7
58.7	782.8	765.8	748.6	782.9	765.7	748.7
58.0	782.1	764.7	747.6	782.1	764.8	747.7
57.3	781.1	763.9	746.6	781.2	763.9	746.6
56.6	780.1	762.8	745.6	780.3	762.9	745.6
56.0	779.4	762.0	744.5	779.5	761.9	744.5
55.3		761.0	743.3		760.9	743.4
54.6		759.9	742.1		759.9	742.3
53.9		758.5	741.2		758.9	741.1

Table S11. Experimental density (ρ_{PVT}) and Tammann-Tait estimated density (ρ_{fitted}) as function of temperature and pressure for BR2 crude oil + methane + CO₂ mixtures (x_{CO_2} is the carbon dioxide mol percent in mixed gas). *Cont.*

P / MPa	$\rho_{PVT} / \text{kg/m}^3$			$\rho_{fitted} / \text{kg/m}^3$		
	$x_{CO_2} = 100.0$			$x_{CO_2} = 100.0$		
72.5			913.5	949.2	930.9	913.4
69.0			909.5	945.7	927.0	909.3
65.6			905.1	942.1	923.2	905.0
62.1			901.4	938.3	919.0	900.5
58.7	934.1	914.5	895.6	934.4	914.8	895.9
55.3	930.3	910.3	891.8	930.4	910.4	891.1
51.8	926.5	905.9	885.5	926.1	905.7	885.9
48.4	921.6	900.8	880.4	921.8	901.0	880.5
44.9	917.1	895.9	874.7	917.2	895.8	874.7
43.2	914.7	893.2		914.8	893.2	871.8
41.5	912.6	890.6	868.6	912.4	890.5	868.7
40.8	911.6	889.6		911.4	889.4	867.4
40.1	910.1	888.3		910.4	888.2	866.1
39.7	909.1	887.2		909.8	887.6	865.4
39.4			865.8	909.4	887.1	864.8
38.7	908.3	885.9		908.4	885.9	863.5
38.0	907.4	884.6	862.1	907.3	884.7	862.1
37.3	906.3	883.6	860.5	906.3	883.5	860.7
36.6	905.1	882.1	859.4	905.2	882.3	859.3
36.0		881.0	858.1	904.3	881.3	858.1
35.3		880.0	857.4	903.2	880.0	856.7
34.6		878.8	855.4	902.1	878.8	855.2
33.9		877.3	853.6	901.0	877.5	853.7
33.2		875.9	852.1	899.8	876.2	852.2

Table S12. Isothermal compressibility as function of temperature and pressure for BR2 crude oil + methane + CO₂ mixtures (x_{CO_2} is the carbon dioxide mol percent in mixed gas).

T / K	343.15	363.15	383.25		343.15	363.15	383.25
P / MPa	$\kappa_T \cdot 10^4 / \text{MPa}^{-1}$			P / MPa	$\kappa_T \cdot 10^4 / \text{MPa}^{-1}$		
	$x_{\text{CO}_2} = 0.0$ (100% mol CH ₄)				$x_{\text{CO}_2} = 26.3$		
95.0	11.4	12.2	13.1	84.0	12.7	14.0	15.1
92.5	11.7	12.6	13.6	82.0	13.0	14.3	15.5
90.0	12.0	13.0	14.0	80.0	13.3	14.6	15.9
87.5	12.4	13.4	14.5	78.0	13.6	15.0	16.3
85.0	12.8	13.8	15.0	76.0	13.9	15.3	16.8
82.5	13.2	14.3	15.6	74.0	14.2	15.7	17.2
80.0	13.6	14.8	16.2	72.0	14.5	16.1	17.7
78.0	14.0	15.2	16.7	70.0	14.9	16.6	18.3
77.0	14.1	15.4	17.0	68.0	15.3	17.0	18.8
76.0	14.3	15.7	17.3	66.0	15.7	17.5	19.4
75.0	14.5	15.9	17.6	65.0	15.9	17.8	19.8
74.0	14.8	16.2	17.9	64.0	16.1	18.1	20.1
73.0	15.0	16.4	18.2	63.0	16.3	18.3	20.4
72.0	15.2	16.7	18.5	62.0	16.5	18.6	20.8
71.0	15.4	17.0	18.9	61.0	16.8	18.9	21.2
P / MPa	$\kappa_T \cdot 10^4 / \text{MPa}^{-1}$			P / MPa	$\kappa_T \cdot 10^4 / \text{MPa}^{-1}$		
	$x_{\text{CO}_2} = 27.5$				$x_{\text{CO}_2} = 100$		
74.0	12.0	13.2	14.3	70.0	10.8	11.8	13.0
72.0	12.4	13.6	14.9	65.0	11.4	12.5	13.9
70.0	12.8	14.1	15.4	60.0	12.1	13.4	15.0
68.0	13.2	14.6	16.1	55.0	12.8	14.3	16.2
66.0	13.7	15.1	16.7	50.0	13.7	15.5	17.6
64.0	14.2	15.7	17.5	45.0	14.8	16.8	19.4
62.0	14.7	16.4	18.3	40.0	16.0	18.4	21.6
61.0	15.0	16.7	18.7	39.0	16.3	18.8	22.1
60.0	15.2	17.1	19.1	38.0	16.6	19.1	22.6
59.0	15.5	17.5	19.6	37.0	16.8	19.5	23.2
58.0	15.9	17.9	20.1	36.0	17.1	19.9	23.8
57.0	16.2	18.3	20.6	35.0		20.4	24.4
56.0	16.5	18.7	21.2	34.0		20.8	25.0
55.0	16.9	19.2	21.8	33.0		21.3	25.7
54.0		19.6	22.4	32.0		21.8	26.4

Table S13. Thermal expansion as function of temperature and pressure for BR2 crude oil + methane + CO₂ mixtures (x_{CO_2} is the carbon dioxide mol percent in mixed gas).

T / K	343.15	363.15	383.25		343.15	363.15	383.25
P / MPa	$\alpha_{\text{P}} \cdot 10^4 / \text{K}^{-1}$			P / MPa	$\alpha_{\text{P}} \cdot 10^4 / \text{K}^{-1}$		
	$x_{\text{CO}_2} = 0.0$ (100% mol CH ₄)				$x_{\text{CO}_2} = 26.3$		
95.0	8.532	8.265	7.976	84.0	8.427	8.924	9.465
92.5	8.631	8.378	8.106	82.0	8.550	9.047	9.580
90.0	8.736	8.498	8.245	80.0	8.678	9.176	9.702
87.5	8.846	8.625	8.394	78.0	8.811	9.311	9.831
85.0	8.964	8.762	8.553	76.0	8.951	9.453	9.966
82.5	9.089	8.907	8.725	74.0	9.097	9.602	10.109
80.0	9.222	9.063	8.909	72.0	9.251	9.759	10.260
78.0	9.336	9.196	9.068	70.0	9.411	9.924	10.420
77.0	9.394	9.265	9.151	68.0	9.580	10.099	10.591
76.0	9.455	9.337	9.237	66.0	9.758	10.284	10.772
75.0	9.517	9.411	9.326	65.0	9.850	10.381	10.867
74.0		9.487	9.418	64.0	9.945	10.480	10.966
73.0		9.566	9.514	63.0	10.042	10.583	11.068
72.0			9.613	62.0	10.142	10.689	11.173
71.0			9.715	61.0	10.245	10.798	11.282
P / MPa	$\alpha_{\text{P}} \cdot 10^4 / \text{K}^{-1}$			P / MPa	$\alpha_{\text{P}} \cdot 10^4 / \text{K}^{-1}$		
	$x_{\text{CO}_2} = 37.5$				$x_{\text{CO}_2} = 100$		
74.0	9.930	9.992	10.053	70.0	10.120	9.835	9.494
72.0	10.041	10.111	10.177	65.0	10.369	10.132	9.856
70.0	10.160	10.238	10.310	60.0	10.647	10.469	10.271
68.0	10.287	10.375	10.455	55.0	10.962	10.855	10.754
66.0	10.423	10.522	10.611	50.0	11.320	11.301	11.324
64.0	10.568	10.681	10.781	45.0	11.733	11.824	12.009
62.0	10.723	10.852	10.967	40.0	12.215	12.448	12.849
61.0	10.806	10.944	11.066	39.0	12.321	12.587	13.040
60.0	10.891	11.039	11.171	38.0	12.431	12.733	13.241
59.0	10.980	11.138	11.280	37.0	12.545	12.884	13.452
58.0	11.072	11.243	11.396	36.0	12.663	13.042	13.673
57.0	11.169	11.351	11.517	35.0		13.206	13.906
56.0	11.269	11.466	11.645	34.0		13.378	14.152
55.0	11.374	11.585	11.780	33.0		13.558	14.412
54.0	11.483	11.711	11.923	32.0		13.746	14.686

Table S14. Solubility parameter as function of temperature and pressure for BR2 crude oil + methane + CO₂ mixtures (x_{CO_2} is the carbon dioxide mol percent in mixed gas).

T / K	343.15	363.15	383.25		343.15	363.15	383.25
P / MPa	$\delta / \text{MPa}^{1/2}$			P / MPa	$\delta / \text{MPa}^{1/2}$		
	$x_{\text{CO}_2} = 0.0$ (100% mol CH ₄)				$x_{\text{CO}_2} = 26.3$		
95.0	12.7	12.3	11.7	84.0	12.0	12.2	12.5
92.5	12.7	12.2	11.7	82.0	12.0	12.2	12.4
90.0	12.6	12.2	11.6	80.0	12.0	12.2	12.4
87.5	12.6	12.1	11.6	78.0	12.0	12.2	12.4
85.0	12.5	12.1	11.5	76.0	12.0	12.2	12.3
82.5	12.4	12.0	11.5	74.0	12.1	12.2	12.3
80.0	12.4	11.9	11.4	72.0	12.1	12.1	12.2
78.0	12.3	11.9	11.4	70.0	12.1	12.1	12.2
77.0	12.3	11.9	11.4	68.0	12.1	12.1	12.1
76.0	12.3	11.8	11.4	66.0	12.2	12.1	12.1
75.0	12.2	11.8	11.3	65.0	12.2	12.1	12.1
74.0		11.8	11.3	64.0	12.2	12.1	12.0
73.0		11.8	11.3	63.0	12.2	12.1	12.0
72.0			11.3	62.0	12.2	12.1	12.0
71.0			11.2	61.0	12.2	12.1	12.0
P / MPa	$\delta / \text{MPa}^{1/2}$			P / MPa	$\delta / \text{MPa}^{1/2}$		
	$x_{\text{CO}_2} = 37.5$				$x_{\text{CO}_2} = 100$		
74.0	14.5	14.2	13.9	70.0	15.9	15.3	14.5
72.0	14.3	14.1	13.8	65.0	15.7	15.1	14.4
70.0	14.2	13.9	13.6	60.0	15.6	15.0	14.2
68.0	14.1	13.8	13.5	55.0	15.4	14.8	14.1
66.0	14.0	13.7	13.3	50.0	15.3	14.7	14.0
64.0	13.9	13.5	13.1	45.0	15.1	14.5	13.9
62.0	13.7	13.4	13.0	40.0	14.9	14.3	13.7
61.0	13.7	13.3	12.9	39.0	14.9	14.3	13.7
60.0	13.6	13.2	12.8	38.0	14.8	14.3	13.6
59.0	13.5	13.1	12.7	37.0	14.8	14.2	13.6
58.0	13.5	13.1	12.6	36.0	14.7	14.2	13.6
57.0	13.4	13.0	12.5	35.0		14.2	13.6
56.0	13.3	12.9	12.4	34.0		14.1	13.5
55.0	13.3	12.8	12.3	33.0		14.1	13.5
54.0		12.7	12.2	32.0		14.1	13.5

Table S15. Molar volume as function of temperature and pressure for BR2 crude oil + methane + CO₂ mixtures (x_{CO_2} is the carbon dioxide mol percent in mixed gas).

T / K	343.15	363.15	383.25		343.15	363.15	383.25
P / MPa	$v \cdot 10^4 / \text{m}^3/\text{mol}$			P / MPa	$v \cdot 10^4 / \text{m}^3/\text{mol}$		
	$x_{\text{CO}_2} = 0.0$ (100% mol CH ₄)				$x_{\text{CO}_2} = 26.3$		
95.0	0.99	1.01	1.02	84.0	0.97	0.99	1.00
92.5	0.99	1.01	1.03	82.0	0.97	0.99	1.01
90.0	1.00	1.01	1.03	80.0	0.97	0.99	1.01
87.5	1.00	1.02	1.04	78.0	0.98	0.99	1.01
85.0	1.01	1.02	1.04	76.0	0.98	1.00	1.02
82.5	1.01	1.03	1.04	74.0	0.98	1.00	1.02
80.0	1.01	1.03	1.05	72.0	0.98	1.00	1.02
78.0	1.01	1.03	1.05	70.0	0.99	1.01	1.03
77.0	1.01	1.03	1.05	68.0	0.99	1.01	1.03
76.0	1.01	1.03	1.05	66.0	0.99	1.01	1.03
75.0	1.01	1.03	1.05	65.0	0.99	1.01	1.04
74.0		1.03	1.05	64.0	1.00	1.02	1.04
73.0		1.03	1.05	63.0	1.00	1.02	1.04
72.0			1.06	62.0	1.00	1.02	1.04
71.0			1.06	61.0	1.00	1.02	1.05
P / MPa	$v \cdot 10^4 / \text{m}^3/\text{mol}$			P / MPa	$v \cdot 10^4 / \text{m}^3/\text{mol}$		
	$x_{\text{CO}_2} = 37.5$				$x_{\text{CO}_2} = 100$		
74.0	1.01	1.03	1.05	70.0	1.42	1.45	1.48
72.0	1.01	1.03	1.05	65.0	1.43	1.46	1.49
70.0	1.01	1.03	1.05	60.0	1.44	1.47	1.50
68.0	1.01	1.03	1.06	55.0	1.44	1.48	1.51
66.0	1.02	1.04	1.06	50.0	1.45	1.49	1.52
64.0	1.02	1.04	1.06	45.0	1.46	1.50	1.54
62.0	1.02	1.04	1.07	40.0	1.48	1.51	1.55
61.0	1.02	1.05	1.07	39.0	1.48	1.52	1.56
60.0	1.02	1.05	1.07	38.0	1.48	1.52	1.56
59.0	1.03	1.05	1.07	37.0	1.48	1.52	1.56
58.0	1.03	1.05	1.08	36.0	1.49	1.52	1.57
57.0	1.03	1.05	1.08	35.0		1.53	1.57
56.0	1.03	1.06	1.08	34.0		1.53	1.57
55.0	1.03	1.06	1.08	33.0		1.53	1.58
54.0		1.06	1.08	32.0		1.54	1.58

Table S16. Cohesive energy as function of temperature and pressure for BR2 crude oil + methane + CO₂ mixtures (x_{CO_2} is the carbon dioxide mol percent in mixed gas).

T / K	343.15	363.15	383.25		343.15	363.15	383.25
P / MPa	$E / \text{kJ/mol}$ $x_{\text{CO}_2} = 0.0$ (100% mol CH ₄)			P / MPa	$E / \text{kJ/mol}$ $x_{\text{CO}_2} = 26.3$		
95.0	16.0	15.2	14.0	84.0	13.8	14.6	15.6
92.5	16.0	15.1	14.0	82.0	13.9	14.6	15.6
90.0	15.9	15.0	14.0	80.0	14.0	14.7	15.5
87.5	15.8	15.0	13.9	78.0	14.1	14.7	15.5
85.0	15.7	14.9	13.9	76.0	14.2	14.7	15.4
82.5	15.6	14.8	13.8	74.0	14.3	14.8	15.4
80.0	15.4	14.7	13.7	72.0	14.4	14.8	15.3
78.0	15.3	14.6	13.6	70.0	14.5	14.8	15.3
77.0	15.3	14.5	13.6	68.0	14.6	14.9	15.2
76.0	15.2	14.5	13.5	66.0	14.7	14.9	15.1
75.0	15.1	14.4	13.5	65.0	14.7	14.9	15.1
74.0		14.4	13.5	64.0	14.8	14.9	15.1
73.0		14.3	13.4	63.0	14.8	14.9	15.0
72.0			13.4	62.0	14.8	14.9	15.0
71.0			13.3	61.0	14.9	14.9	15.0
P / MPa	$E / \text{kJ/mol}$ $x_{\text{CO}_2} = 37.5$			P / MPa	$E / \text{kJ/mol}$ $x_{\text{CO}_2} = 100$		
74.0	21.0	20.7	20.4	70.0	35.9	33.8	30.9
72.0	20.7	20.4	20.0	65.0	35.4	33.3	30.7
70.0	20.4	20.0	19.6	60.0	34.9	32.9	30.4
68.0	20.2	19.7	19.2	55.0	34.4	32.5	30.1
66.0	19.9	19.3	18.8	50.0	33.9	32.1	29.8
64.0	19.6	19.0	18.4	45.0	33.3	31.6	29.5
62.0	19.3	18.6	17.9	40.0	32.8	31.1	29.2
61.0	19.1	18.5	17.7	39.0	32.6	31.0	29.1
60.0	19.0	18.3	17.5	38.0	32.5	30.9	29.0
59.0	18.8	18.1	17.3	37.0	32.4	30.8	29.0
58.0	18.7	17.9	17.1	36.0	32.3	30.7	28.9
57.0	18.5	17.8	16.9	35.0		30.6	28.8
56.0	18.4	17.6	16.7	34.0		30.5	28.8
55.0	18.2	17.4	16.5	33.0		30.4	28.7
54.0		17.2	16.2	32.0		30.3	28.6

Table S17. Experimental density ($\rho_{densimeter}$) and Tammann-Tait estimated density (ρ_{fitted}) as function of temperature and pressure for BR2 dead oil

T / K	333.15	343.15	353.15	363.15	373.15	383.15	393.15
P / MPa	$\rho_{densimeter} / \text{kg/m}^3$						
3.5	862.9	856.5	849.3	842.8	836.0	829.2	822.5
7.0	865.1	858.9	851.9	845.4	838.7	832.0	825.5
13.9	869.5	863.5	856.8	850.4	843.9	837.7	831.3
20.8	873.6	867.9	861.4	855.3	848.9	842.7	836.6
27.7	877.7	872.1	865.7	859.9	853.6	847.7	841.7
34.6	881.5	876.1	869.9	864.1	858.1	852.3	846.5
41.5	885.3	879.9	873.9	868.2	862.4	856.6	851.0
48.4	888.8	883.5	877.7	872.1	866.4	860.9	855.3
55.3	892.3	886.9	881.1	875.8	870.4	864.8	859.4
62.2	895.7	890.4	884.9	879.5	874.0	868.6	863.3
69.0	898.9	893.7	888.1	882.9	877.6	872.3	867.2
75.9	901.9	896.8	891.3	886.2	881.1	875.8	870.7
82.8	904.8	899.9	894.5	889.5	884.4	879.2	874.3
89.7	907.7	902.8	897.6	892.6	887.6	882.6	877.7
96.6	910.5	905.6	900.5	895.6	890.8	885.7	881.0
100.1	912.1	907.0	902.0	897.1	892.3	887.3	882.5
	$\rho_{fitted} / \text{kg/m}^3$						
3.5	877.7	871.1	864.5	857.9	851.2	844.4	837.7
7.0	879.8	873.3	866.7	860.2	853.6	847.0	840.3
13.9	883.7	877.4	871.0	864.6	858.3	851.8	845.4
20.8	887.5	881.3	875.1	868.9	862.7	856.5	850.2
27.7	891.2	885.2	879.1	873.0	867.0	860.9	854.8
34.6	894.8	888.8	882.9	877.0	871.0	865.1	859.2
41.5	898.2	892.4	886.6	880.8	875.0	869.2	863.4
48.4	901.5	895.8	890.1	884.4	878.7	873.1	867.4
55.3	904.7	899.1	893.5	887.9	882.4	876.8	871.3
62.2	907.8	902.3	896.8	891.3	885.9	880.4	875.0
69.0	910.9	905.4	900.0	894.6	889.3	883.9	878.6
75.9	913.8	908.5	903.1	897.8	892.6	887.3	882.1
82.8	916.7	911.4	906.1	900.9	895.7	890.6	885.5
89.7	919.5	914.3	909.1	903.9	898.8	893.8	888.7
96.6	922.2	917.1	911.9	906.9	901.8	896.8	891.9
100.1	923.5	918.4	913.4	908.3	903.3	898.4	893.4

Table S18. Isothermal compressibility and thermal expansion as function of temperature and pressure for BR2 dead oil

T / K	333.15	343.15	353.15	363.15	373.15	383.15	393.15
P / MPa	$\kappa_T \cdot 10^4 / \text{MPa}^{-1}$						
3.5	7.7	8.1	8.7	9.2	9.7	10.3	10.9
7.0	7.4	7.9	8.4	8.9	9.4	9.9	10.5
13.9	7.1	7.5	7.9	8.3	8.8	9.2	9.7
20.8	6.7	7.1	7.5	7.9	8.2	8.6	9.0
27.7	6.4	6.7	7.1	7.4	7.8	8.1	8.5
34.6	6.1	6.4	6.7	7.0	7.4	7.7	8.0
41.5	5.9	6.1	6.4	6.7	7.0	7.3	7.5
48.4	5.6	5.9	6.1	6.4	6.6	6.9	7.2
55.3	5.4	5.6	5.9	6.1	6.3	6.6	6.8
62.2	5.2	5.4	5.6	5.9	6.1	6.3	6.5
69.0	5.0	5.2	5.4	5.6	5.8	6.0	6.2
75.9	4.8	5.0	5.2	5.4	5.6	5.8	5.9
82.8	4.7	4.9	5.0	5.2	5.4	5.5	5.7
89.7	4.5	4.7	4.9	5.0	5.2	5.3	5.5
96.6	4.4	4.5	4.7	4.9	5.0	5.1	5.3
100.1	4.3	4.5	4.6	4.8	4.9	5.1	5.2
	$\alpha_P \cdot 10^4 / \text{K}^{-1}$						
3.5	8.013	8.075	8.121	8.145	8.143	8.110	8.039
7.0	7.855	7.908	7.947	7.964	7.956	7.920	7.849
13.9	7.565	7.604	7.629	7.636	7.620	7.581	7.511
20.8	7.303	7.331	7.347	7.346	7.326	7.286	7.219
27.7	7.067	7.086	7.095	7.089	7.067	7.027	6.965
34.6	6.852	6.864	6.868	6.859	6.836	6.798	6.741
41.5	6.655	6.663	6.663	6.652	6.628	6.593	6.542
48.4	6.474	6.478	6.476	6.464	6.441	6.410	6.364
55.3	6.308	6.309	6.305	6.292	6.272	6.244	6.204
62.2	6.154	6.153	6.147	6.136	6.117	6.093	6.059
69.0	6.011	6.008	6.003	5.992	5.975	5.955	5.927
75.9	5.878	5.874	5.869	5.859	5.845	5.828	5.806
82.8	5.754	5.750	5.744	5.736	5.724	5.712	5.695
89.7	5.638	5.633	5.628	5.621	5.613	5.604	5.593
96.6	5.529	5.524	5.520	5.515	5.509	5.504	5.498
100.1	5.477	5.472	5.468	5.464	5.460	5.457	5.453

Table S19. Solubility parameter and molar volume as function of temperature and pressure for BR2 dead oil

T / K	333.15	343.15	353.15	363.15	373.15	383.15	393.15
P / Mpa	$\delta / \text{MPa}^{1/2}$						
3.5	18.6	18.4	18.1	17.8	17.6	17.3	16.9
7.0	18.6	18.3	18.1	17.9	17.6	17.3	17.0
13.9	18.5	18.3	18.1	17.9	17.6	17.3	17.0
20.8	18.5	18.3	18.1	17.9	17.6	17.4	17.1
27.7	18.4	18.3	18.1	17.9	17.6	17.4	17.2
34.6	18.4	18.2	18.1	17.9	17.7	17.5	17.2
41.5	18.4	18.2	18.0	17.9	17.7	17.5	17.3
48.4	18.3	18.2	18.0	17.9	17.7	17.5	17.4
55.3	18.3	18.1	18.0	17.9	17.7	17.6	17.4
62.2	18.2	18.1	18.0	17.8	17.7	17.6	17.5
69.0	18.2	18.1	17.9	17.8	17.7	17.6	17.5
75.9	18.1	18.0	17.9	17.8	17.7	17.6	17.6
82.8	18.1	18.0	17.9	17.8	17.7	17.7	17.6
89.7	18.0	17.9	17.9	17.8	17.7	17.7	17.6
96.6	18.0	17.9	17.8	17.8	17.7	17.7	17.7
100.1	17.9	17.9	17.8	17.8	17.7	17.7	17.7
	$v \cdot 10^4 / \text{m}^3/\text{mol}$						
3.5	2.91	2.93	2.96	2.98	3.00	3.03	3.05
7.0	2.90	2.92	2.95	2.97	2.99	3.02	3.04
13.9	2.89	2.91	2.93	2.95	2.97	3.00	3.02
20.8	2.87	2.89	2.91	2.93	2.96	2.98	3.00
27.7	2.86	2.88	2.90	2.92	2.94	2.96	2.98
34.6	2.85	2.87	2.89	2.90	2.93	2.95	2.97
41.5	2.84	2.85	2.87	2.89	2.91	2.93	2.95
48.4	2.82	2.84	2.86	2.88	2.90	2.92	2.93
55.3	2.81	2.83	2.85	2.87	2.88	2.90	2.92
62.2	2.80	2.82	2.84	2.85	2.87	2.89	2.91
69.0	2.79	2.81	2.83	2.84	2.86	2.88	2.89
75.9	2.78	2.80	2.82	2.83	2.85	2.87	2.88
82.8	2.77	2.79	2.81	2.82	2.84	2.85	2.87
89.7	2.77	2.78	2.80	2.81	2.83	2.84	2.86
96.6	2.76	2.77	2.79	2.80	2.82	2.83	2.85
100.1	2.75	2.77	2.78	2.80	2.81	2.83	2.84

Table S20. Cohesive energy as function of temperature and pressure for BR2 dead oil

T / K	333.15	343.15	353.15	363.15	373.15	383.15	393.15
P / Mpa	<i>E</i> / kJ/mol						
3.5	100.4	98.7	96.9	94.8	92.6	90.2	87.5
7.0	99.9	98.3	96.6	94.6	92.4	90.1	87.6
13.9	99.0	97.5	95.9	94.1	92.2	90.0	87.8
20.8	98.2	96.8	95.3	93.6	91.9	90.0	87.9
27.7	97.3	96.0	94.7	93.2	91.6	89.9	88.0
34.6	96.4	95.3	94.1	92.7	91.3	89.8	88.2
41.5	95.6	94.5	93.4	92.2	91.0	89.7	88.3
48.4	94.7	93.8	92.8	91.8	90.7	89.6	88.4
55.3	93.9	93.1	92.3	91.3	90.4	89.5	88.6
62.2	93.0	92.3	91.6	90.9	90.1	89.4	88.7
69.0	92.2	91.6	91.0	90.4	89.8	89.3	88.8
75.9	91.4	90.9	90.5	90.0	89.5	89.2	88.9
82.8	90.5	90.2	89.8	89.5	89.2	89.1	89.0
89.7	89.7	89.4	89.2	89.1	88.9	89.0	89.1
96.6	88.9	88.7	88.6	88.6	88.6	88.8	89.2
100.1	88.5	88.4	88.3	88.4	88.5	88.8	89.2